Halogen Bonding and Chalcogen Bonding Host Systems for Charged Guest Recognition

Yuen Cheong Tse

Lady Margaret Hall, University of Oxford

A thesis submitted for the degree of Doctor of Philosophy

Inorganic Chemistry Laboratory

University of Oxford

Trinity Term 2021

Halogen Bonding and Chalcogen Bonding
Host Systems for Charged Guest Recognition

Yuen Cheong Tse, Lady Margaret Hall, University of Oxford

Abstract of thesis submitted for the degree of D.Phil., Trinity Term 2021

This thesis describes the preparation of halogen bonding and chalcogen bonding macrocyclic and mechanically interlocked systems for the recognition of anions and ion-pairs.

Chapter 1 introduces the field of supramolecular host-guest chemistry, with particular focus on the recognition of anions and ion-pair species. The synthesis and applications of mechanically interlocked molecules are also reviewed.

Chapter 2 details the fundamental charged guest recognition properties of a novel family of σ-hole [2]rotaxanes incorporated with multiple halogen bonding and chalcogen bonding triazole-based donor motifs.

Chapter 3 investigates the anion sensing capability of halogen bonding receptors functionalised with photo- and redox-active reporter groups. This entails the construction of zinc(II) metalloporphyrin-BODIPY [2]rotaxanes for the dual optical- and electrochemical sensing of anions.

Chapter 4 describes the exploitation of halogen bonding and chalcogen bonding interactions to mediate ion-pair recognition in heteroditopic/multitopic macrocyclic and catenane host systems.

Chapter 5 summarises the conclusion of this thesis.

Chapter 6 provides the experimental procedures employed in this work, including synthetic protocols and characterisation of novel compounds.

Acknowledgement

This thesis would not have been possible without the help and support of the many people I have had the pleasure of meeting throughout my time in Oxford.

I would like to first and foremost express my deepest gratitude to Prof. Paul D. Beer for his excellent supervision, brilliant ideas and giving me a large degree of research freedom to pursue my own interests in the field. From the discussion we have had over the years, both his enthusiasm in chemistry and optimistic attitude have influenced me tremendously. Trying to realise his "crazy ideas" may have been my day-to-day routine in the labs over the past four years, but I truly savoured every moment of it.

In addition, I wish to express my deepest appreciation to all my friends and colleagues whose assistance has been indispensable during the course of my DPhil. In particular, I would like to thank Dr. Thanthapatra Bunchuay (Valentine) and Andrew Docker for their guidance and mentoring since my first day in the labs. They have always said, "You need to learn how to walk before you can run," and they have kindly taught me so many things whilst asking nothing in return. I must also express my gratitude towards Dr. Robert Hein, Jane Liew, Heike Khun, Dr. Krzysztof Bąk, Aidan Kerckhoffs and Laura Bickerton for their company inside and outside the labs, which has kept me sane and motivated especially in times when nothing seemed to work. Thanks also go to other current and past members of the Beer and Langton group, including Edward Mitchell, Dr. Jessica Pancholi, Vihanga Munasinghe, Zongyao Zhang, Arya Arun, Jamie Wilmore, Hui Min Tay, Toby Johnson and Dr. Xiaobo Shang for making my time in the group very enjoyable. Special shout-outs go to Zongyao Zhang and Heike Khun for resolving my crystal structures. I am also

most grateful to Dr. Jessica Pancholi, Dr. Krzysztof Bąk and Dr. Robert Hein for proofreading this thesis.

I have been very fortunate to have supervised a few incredibly talented students: Caspar Whitehead, who was a Part II student, had done incredibly well and shared my pain working with porphyrins; Christian Gateley, another highly gifted Part II student who kindly left behind a big pile of unscraped prep plates when he left, has contributed to some of the work in Chapter 4. I was also lucky enough to spend my last few months in Oxford guiding a first year DPhil student, Hui Min Tay, who I am relieved to know will continue some of my unfinished projects.

I would like to acknowledge the assistance I received from the staff members of CRL. My sincere gratitude goes to Dr. Nick Rees, who is a wonderful person to work with. Many thanks to Tina Jackson, Dr. Nader Amin, Dr. Victor Mikhailov, Dr. John Walsby-Tickle and Dr. Kourosh Honarmand Ebrahimi for running my NMR and mass spectrometry service samples. I am also deeply indebted to the Croucher Foundation for the scholarship. None of this would have been possible without their generous financial support.

Last but not least, I am extremely grateful to my family for their unconditional love and support over the years. I would also like to specially thank my girlfriend, Elaine bb Wong, who has been there for me throughout my time in Oxford. Spending time with her has allowed me to take my mind off stressful tasks and her unwavering encouragement has been what kept me going.

Richard Tse

October, 2021

List of Abbreviations

δ	chemical shift
Δ	change in
λ	wavelength
µ	micro
κ	Dielectric constant
°	degree
°C	degree Celsius
Å	angstrom
A	acceptor
A^-	anion
a.u.	arbitrary units
abs	absorption
AeB	aerogen bonding
aq.	aqueous
Ar	aryl
AMT	active metal template
ATP	adenosine triphosphate
B	Lewis base
$BAr^{F}{}_{4}$	tetrakis(3,5-bis(trifluoromethyl)phenyl)borate
Bn	benzyl
Boc	*tert*-butyloxycarbonyl
BODIPY	4,4-difluoro-4-bora-3a,4a-diaza-s-indacene
br	broadened
Bu	butyl
cat.	catalytic
Ch	chalcogen
ChB	chalcogen bonding
conc.	concentration
COSY	correlation spectroscopy
CuAAC	copper(I)-catalysed azide-alkyne cycloaddition
CV	cyclic voltammetry
d	doublet
D	donor

DFT	density functional theory
DTT	dithieno[3,2-b;2',3'-d]thiophenes
DABCO	1,4-diazabicyclo[2.2.2]octane
DiPEA	*N*,*N*-diisopropylethylamine
DMAP	4-dimethylaminopyridine
DMF	*N*,*N*-dimethylformamide
DMSO	dimethyl sulfoxide
DNA	deoxyribonucleic acid
E	energy
e.g.	*exempli gratia*
em	emission
eq., equiv.	equivalent
ex.	excess, excitation
$E_{1/2}$	half-wave potential
Et	ethyl
EDTA	ethylenediaminetetraacetic acid
ESI	electrospray ionisation
Fc	ferrocene
Fc^+	ferrocenium
g	gram
G	Gibbs free energy
Grubbs' I/II	Grubbs' first/second generation catalyst
h	hour
Hz	hertz
HB	hydrogen bonding
HOMO	highest occupied molecular orbital
HRMS	high-resolution mass spectrometry
i	iso
i.e.	*id est*
J	joule
J	coupling constant
k	kilo
K	Kelvin
K_a	association constant
L	litre

LLE	liquid-liquid extraction
LUMO	lowest unoccupied molecular orbital
m	multiplet, milli
M	molar (mole per litre)
m	*meta*
m/z	mass to charge ratio
min	minute
mol	mole
Me	methyl
Mes	1,3,5-trimethylbenzene (mesityl)
Ms	methanesulfonyl
MALDI	matrix assisted laser desorption/ionization
MD	molecular dynamics
MIM	mechanically interlocked molecule
MLCT	metal-to-ligand charge transfer
MOM	methoxymethyl acetal
MS	mass spectrometry
MW	microwave
n	nano
n	normal
NDI	1,4,5,8-naphthalenediimide
NMR	nuclear magnetic resonance
OAc	acetate
O/N	overnight
p	*para*
Ph	phenyl
pH	$-\log [H_3O^+]$
pK_a	$-\log K_a$
PnB	pnictogen bonding
ppm	parts per million
Pr	propyl
Pyr	Pyridine
PET	photoinduced electron transfer
q	quartet
quin.	quintet

Q_{zz}	quadruple moment
R	chemical substituent
r	ionic radius
R_f	retention factor
RCM	ring-closing metathesis
RNA	ribonucleic acid
ROESY	rotating-frame nuclear overhauser effect spectroscopy
RT	room temperature
s	second, singlet
s, *sec*	secondary
sat.	saturated
sept.	septet
SLE	solid-liquid extraction
SWV	squarewave voltammetry
t	triplet
t, *tert*	tertiary
T	temperature
Ts	tosyl
TBA	tetrabutylammonium
TBTA	tris[(1-benzyl-1H-1,2,3-triazol-4-yl)methyl]amine
TLC	thin layer chromatography
TrB	tetrel bonding
UV	ultra-violet
vis.	visible
vs.	versus
v/v	volume by volume
V	volt
$V_{s,max}$	local maxima electrostatic potential
VT	variable temperature
wt.	weight
X	halogen
XB	halogen bonding

TABLE OF CONTENTS

Chapter 1

Introduction

Chapter 1 Introduction

1.1 Supramolecular Chemistry: Chemistry Beyond the Molecule

Over the past half-century, the field of supramolecular chemistry has thrived and flourished, consolidating its role as one of the most fundamental concepts across many disciplines of research. Before the inception of this field, chemists had been devising methodologies to construct molecules to their hearts' desire via the precise breaking and forming of covalent bonds between atoms. These decades' worth of reactions paved the way for the birth of supramolecular chemistry, which revolves around the concept of *self-assembly* between different molecules driven by *non-covalent interactions*. This allows chemists to gain a more profound and in-depth understanding of numerous biological processes, such as protein folding, enzyme-substrate interactions and membrane transport,[1] all of which fall under the realm of supramolecular chemistry. However, the real beauty of this field manifests itself in the possibility to construct synthetic supramolecular assemblies that can display properties and applications rivalling or even surpassing those of natural biotic systems.

The origins of supramolecular chemistry can be traced back to the 1960s, in which a plethora of host molecules (receptors) were synthesised for the purpose of metal cation recognition. In particular, the pioneering work on the development of crown ethers, cryptands and spherands for Group 1 metal cation recognition (Figure 1.1a–c) led by Pedersen, Lehn and Cram respectively revolutionised this field and eventually earned them the 1987 Nobel Prize for Chemistry.[2] Almost three decades later, in 2016, the importance of the supramolecular chemistry field was once again recognised with the Nobel Prize in Chemistry being awarded to Sauvage, Stoddart and Feringa for their design and production of molecular machines.[3] Such functional molecules require

dynamic movable constituent parts and mechanisms to convert energy into unidirectional motion. Mechanically interlocked catenanes and rotaxanes (Figure 1.1d–e), developed by Sauvage and Stoddart, are composed of discrete molecules that can move freely relative to one another and therefore aptly fulfil the roles as building blocks of molecular machines. Feringa reported the first example of a molecular rotor, in which the "rotor blade" can spin in a well-defined direction indefinitely under light irradiation (Figure 1.1f).[4] The combined work from the three Nobel laureates made it possible for the building of miniature machines such as a molecular elevator,[5] molecular muscle[6] and nanocar.[7] From cation recognition to molecular machines, the field of supramolecular chemistry remains strongly relevant to this day and its potential is only limited by one's creative imagination.

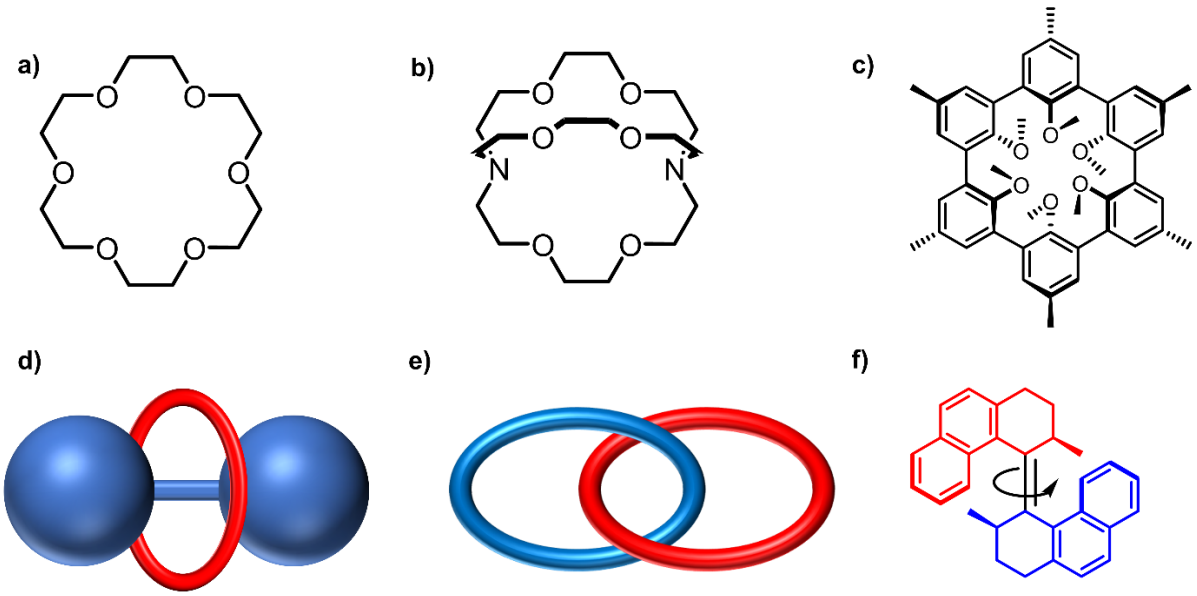

Figure 1.1 Structures of a) 18-crown-6, b) [2.2.2]-cryptand, c) spherand, d) [2]rotaxane, e) [2]catenane and f) molecular rotor.

The main theme of this thesis revolves around supramolecular host-guest chemistry, with particular focus on the recognition of anions and ion-pair species. With this in mind, this chapter begins with an introduction on the non-covalent interactions employed in host-charged guest supramolecular chemistry, followed by

examples of anion and ion-pair receptors. Lastly, different synthetic strategies and applications of mechanically interlocked molecules (MIMs) are described, in particular as switches, catalysts and host molecules for charged guest recognition.

1.2 Non-Covalent Binding Forces

Supramolecular chemistry is often described as "the chemistry of non-covalent interactions". These binding forces can be exploited in concert to facilitate host-guest recognition and the self-assembly of range of supramolecular architectures in general. An understanding of the arsenal of non-covalent interactions is of paramount importance in the judicious design of host structural frameworks for target guest species. The following section introduces some of the important interactions that are employed in biotic and synthetic host-guest systems.

1.2.1 Electrostatic Interactions

Electrostatic interactions refer to the Coulombic attraction between oppositely charged species (ions or dipoles), and can be classified into three types based on the identity of the charged partners: a) ion-ion, b) ion-dipole and c) dipole-dipole interactions. The magnitude of their stabilisation energy (E) generally decreases in the order of $E_{ion\text{-}ion}$ (non-directional and up to 250 kJ mol^{-1}) > $E_{ion\text{-}dipole}$ (50–200 kJ mol^{-1}) > $E_{dipole\text{-}dipole}$ (5–50 kJ mol^{-1}). Furthermore, they also exhibit different distance (r) dependency, with ion-pairing ($E_{ion\text{-}ion} \propto r^{-1}$) operating in significantly longer range than both ion-dipole ($E_{ion\text{-}dipole} \propto r^{-2}$) and dipole-dipole ($E_{dipole\text{-}dipole} \propto r^{-3}$) interactions.

The utilisation of electrostatic interactions in anion recognition was demonstrated in an early example by Schmidtchen and co-workers.[8] They prepared a positively charged tetrahedral cage (Figure 1.2) with four quaternary ammonium groups at the corners oriented towards the centre of its cavity. ^{1}H NMR titrations conducted in D_2O

revealed the capability of this receptor to selectively bind Br^- and I^- over Cl^- via the formation of 1:1 host-guest complexes mediated by favourable electrostatic interactions.

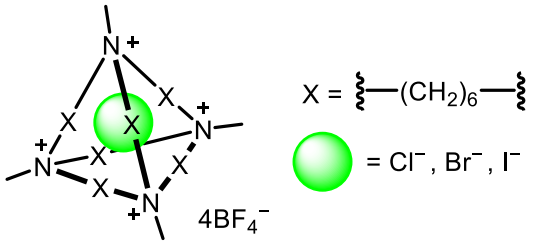

Figure 1.2 Schmidtchen's quaternary ammonium cage.[8]

1.2.2 Hydrogen Bonding

Hydrogen bonding (HB) is described as the attractive interaction between a hydrogen atom covalently linked to an electronegative donor atom (D–H) and a Lewis basic acceptor (A).[9] The bond strength of HB typically ranges from 5 to 120 kJ mol^{-1} and its formation is primarily electrostatically-driven. The directional nature of this readily accessible interaction has prompted its incorporation into a plethora of anion receptors reported to-date (Section 1.3.4.1).

In solution, solvent plays a key role in modulating HB strength. Stronger HB is commonly observed in solvents with lower polarity and dielectric constant (κ) (e.g. CH_2Cl_2, $CHCl_3$). More importantly, protic solvent (e.g. CH_3OH, H_2O) capable of forming HB interactions with either D–H or A greatly weakens the HB strength of D–H···A, as a larger amount of energy is needed to desolvate both HB partners prior to their HB formation. In one example, Hunter and co-workers measured the association constants between perfluoro-*tert*-butyl alcohol (D–H) and tri-*n*-butylphosphine oxide (A) in 13 different organic solvents.[10] Significantly higher K_a was observed in non-competitive solvents such as cyclohexane and CCl_4 ($K_a > 10^4$ M^{-1}), while polar solvents such as DMSO and *N*-methyl formamide (NMF) greatly attenuated the association

constants ($K_a < 1\ M^{-1}$). Impressively, the experimentally determined binding constants in the various organic solvents could be accurately predicted using a solvent competition model previously developed by the same group.[11]

1.2.3 Sigma-Hole Interactions

Sigma(σ)-hole interactions refer to the attractive interactions between atoms of Group 14–18 and a Lewis base (B).[12–14] This may seem counter-intuitive, especially for halogens as they are usually treated as Lewis bases with negative charge character. To explain this enigmatic attraction between halogens and negative sites, the concept of σ-hole was introduced in 2007 by Clark *et. al.*[15]

For an unbound halogen atom, its charge distribution is found to be spherically symmetrical and the electrostatic potential is positive across the surface of the atom. The formation of a covalent bond to the halogen, R—X, where R is an electron-withdrawing group and X is typically iodine or bromine, polarises the electronic charge towards the bonding region, lowering the electron density along the extension of the σ-bond, while at the same time increasing the electron density around the equatorial area of the halogen atom. The region of diminished electron density at the halogen atom's pole is termed a σ-hole, and through its interaction with Lewis base (R—X···B) gives rise to halogen bonding (XB).[16] This concept was later extended to include σ-hole interactions involving elements from Group 16 (chalcogen bonding, ChB),[17] Group 15 (pnictogen bonding, PnB),[18] Group 14 (tetrel bonding, TrB),[19] and more recently, Group 18 (aerogen bonding, AeB).[20] Representative examples of each type of σ-hole donors with their calculated electrostatic potential surfaces are shown in Figure 1.3. Among the family of σ-hole interactions, XB and ChB are the mostly widely studied and will be discussed in more detail below. Examples of anion receptors based on these two interactions will also be introduced in Section 1.3.4.2 and 1.3.4.3.

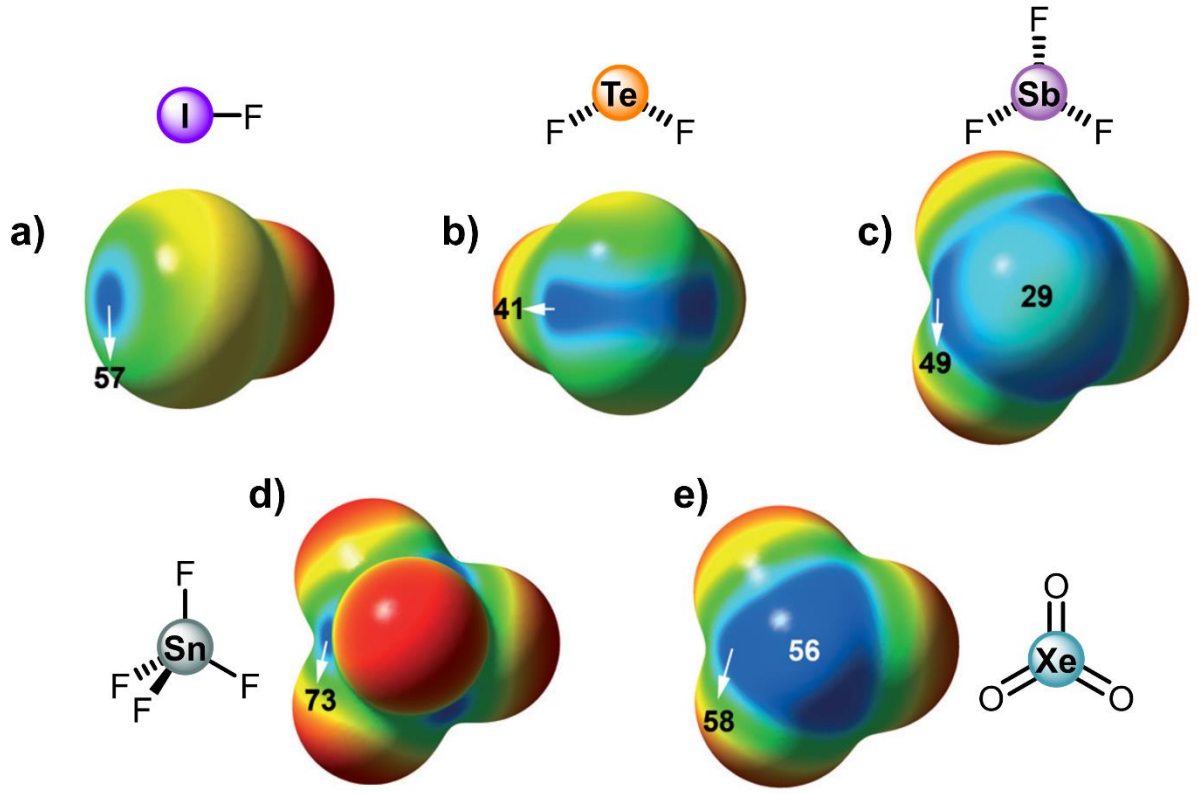

Figure 1.3 Computed molecular electrostatic potential (MEP) surfaces for a) IF, b) TeF_2, c) SbF_3, d) SnF_4 and e) XeO_3 at the MP2/aug-cc-pVTZ level of theory. MEP energy values (kcal mol^{-1}) are indicated. Blue and red represent positive and negative electrostatic potential respectively.[20] Figures reproduced from reference 20.

1.2.3.1 Halogen Bonding (XB)

In recent decades, XB has found widespread applications in areas such as crystal engineering,[21–23] drug discovery,[24–26] material sciences,[27,28] molecular recognition[29,30] and catalysis.[31,32] In comparison to HB, the localised nature of the σ-hole endows a stringent linear directionality to XB, with R–X···B bond angle ≈ 180° (R = electron-withdrawing substituent; X = halogen atom; B = Lewis base). The strength of XB increases when the halogen donor atom becomes more polarisable and less electronegative, and when it is covalently bonded to more electron-deficient fragments. For example, as shown in Table 1.1, calculated local maxima electrostatic potential $V_{s,max}$ of X in XCH_3 increases in the order of F < Cl < Br < I.[33] In addition, when the methyl group is replaced by the more electron-withdrawing trifluoromethyl motif, the $V_{s,max}$ becomes more positive for a given halogen atom.

Table 1.1: Computationally determined electrostatic potentials $V_{s,max}$ values (kcal mol^{-1}) associated with σ-holes on the halogen atoms.[33]

	Halogen	**$V_{s,max}$ (kcal mol^{-1})**
F–CH_3	F	–25
Cl–CH_3	Cl	–1
Br–CH_3	Br	6
I–CH_3	I	13
F–CF_3	F	–3
Cl–CF_3	Cl	20
Br–CF_3	Br	25
I–CF_3	I	32

1.2.3.2 Chalcogen Bonding (ChB)

Chalcogen bonding (ChB) is the sister σ-hole interaction of XB involving Group 16 elements as donors.[34] In parallel to XB, the strongest ChB is observed for the heavier chalcogen atoms down the Group (O < S < Se < Te) and in the presence of electron-withdrawing covalently-bonded motifs.

Despite the many common features shared by XB and ChB, one striking difference is the number of σ-holes on the donor atom — while halogen atoms can only have one σ-hole (Figure 1.3a), chalcogen atoms can possess up to two σ-holes when the chalcogen atom is divalently bonded (Figure 1.3b). Conceivably, this gives rise to contrasting binding geometry between a polarised chalcogen atom and a Lewis base. Interestingly, the electrostatic potential of these two σ-holes can be different if the chalcogen atom is asymmetrically substituted. For example, in Se(CH_3)CN, the electrostatic potential values of the σ-hole on the Se along the extension of NC–Se ($V_{s,max}$ = 35 kcal mol^{-1}) is more than twice than that of H_3C–Se ($V_{s,max}$ = 17 kcal mol^{-1}).[14] This contrasting yet unique feature of ChB has stimulated its exploitation and application in material science research,[35–37] anion recognition and transport[38–41] and drug discovery.[42]

1.2.4 π-π Interactions

Aromatic compounds such as benzene possess quadrupole moments, in which their two faces and edge have negative and positive electrostatic potentials respectively. This allows two benzene molecules to interact favourably either in a T-shaped or displaced conformations (Figure 1.4a).[43] Interestingly, when benzene is mixed with an equimolar solution of perfluorobenzene at room temperature (both are liquid with melting points of ca. 5 °C), the formation of a solid is immediately observed.[44] The melting point of this solid was found to be 24 °C, significantly higher than either one of the components. Further studies showed that the quadrupole moment of the electron-deficient perfluorobenzene is inverted in sign compared to that of benzene, and is of approximately the same magnitude (Figure 1.4b). This allows the two aromatic compounds to stack right on top of each other and interact through the favourable π-π interactions.

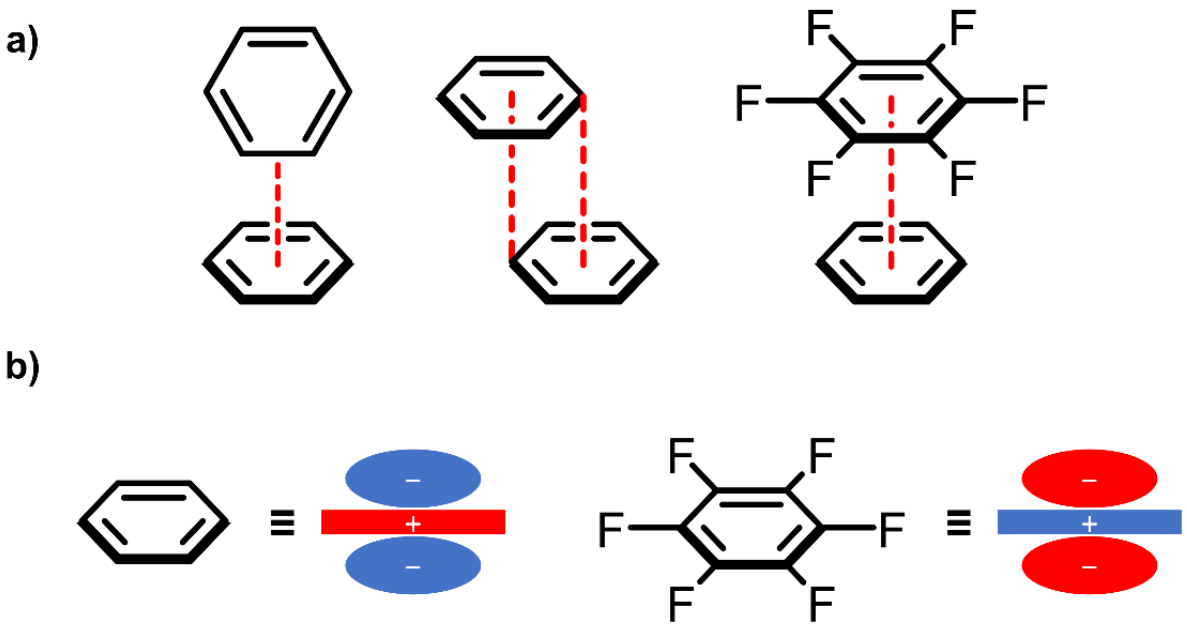

Figure 1.4 a) Location and sign of the quadrupole moment of benzene and perfluorobenzene. b) Different conformations of π-π interactions (left: T-shaped; middle: displaced; right: stacking).

1.2.5 Ion-π Interactions

Cation-π and anion-π interactions occur when the ions associate with electron-rich and electron-deficient aromatic rings respectively (Figure 1.5).

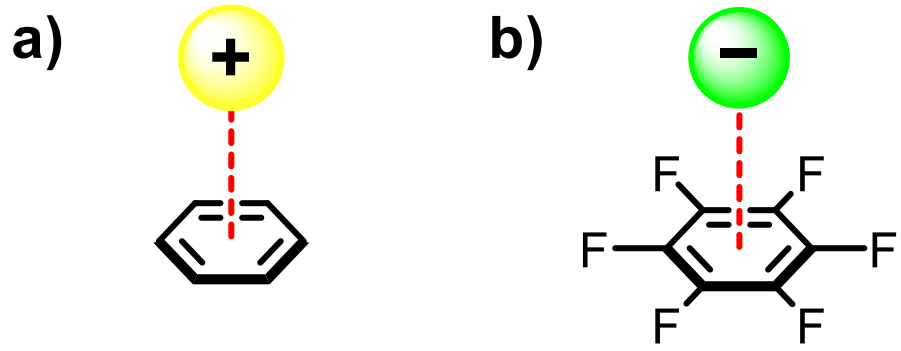

Figure 1.5 a) Cation-π interaction between a cation (yellow sphere) and benzene. b) Anion-π interaction between an anion (green sphere) and perfluorobenzene.

1.2.5.1 Cation-π Interactions

Cation-π interactions are amongst the strongest of non-covalent interactions. For example, in the gas phase the interaction energy between K^+ and benzene (19 kcal mol^{-1}) is even stronger than that between K^+ and H_2O (18 kcal mol^{-1}).[45] Electrostatically, this interaction can be viewed as the cation interacting with the quadrupole moment of the aromatic ring. This explains the stronger cation-π interaction observed for more charge-dense cations (e.g. $Li^+ > Na^+ > K^+ > Rb^+$) and more electron-rich aromatic compounds (e.g. benzene > fluorobenzene > 1,3,5-trifluorobenzene). However, this electrostatic model needs to be viewed with caution because other contributions such as cation-induced dipole, charge-transfer and dispersion forces all play key roles.[45]

1.2.5.2 Anion-π Interactions

Interactions between anions and aromatic compounds are stronger with the more electron-deficient π systems, possessing higher and more positive quadrupole

moments (Q_{zz}).[46] For example, while triazine with small Q_{zz} = 0.90 displays a modest binding with chloride in the gas phase ($E_{interaction}$ = –5.2 kcal mol^{-1}), its more electron-deficient analogue trifluorotriazine (Q_{zz} = 8.23) demonstrates significantly stronger halide binding ($E_{interaction}$ = –15.0 kcal mol^{-1}).[47] In addition to the electrostatic component of this interaction, anion induced polarisation has also been shown to play a key role in modulating anion-π strength. Higher anion affinity is usually found for an aromatic ring that is more polarisable.

In one example, the exploitation of anion-π interactions in anion recognition was reported by Wang and co-workers in their preparation of a bis-tetrazine-functionalised macrocycle (Figure 1.6).[48] This receptor bound linear anions such as N_3^- and SCN^- selectively with concomitant quenching of its emission intensity in CH_3CN. Computational studies revealed the formation of a bridge-like complex between the macrocycle and the bound linear anions, with each end of the guest interacting with the face of a tetrazine ring via the formation of anion-π interactions.

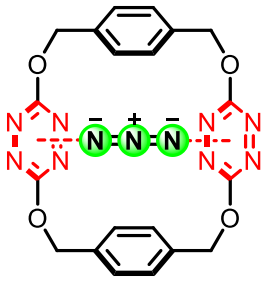

Figure 1.6 Wang's tetrazine-functionalised macrocycle.[48]

1.2.6 The Hydrophobic Effect

The hydrophobic effect refers to the tendency for organic molecules to aggregate in water to minimise unfavourable interactions between the polar water molecules and apolar hydrophobic surfaces. This interaction plays a crucial role in regulating protein folding, protein-substrate interactions and in the self-assembly of

membranes/micelles. The exact origin of the hydrophobic effect is still under debate but both entropic and enthalpic contributions can occur.[1,49]

Water molecules surrounding organic compounds are found to be more rigid and possess a low entropy. Upon aggregation of organic fragments, some of these rigid water molecules are liberated to the bulk solvent due to a decrease in total surface area of the aggregated complex, and this process is entropically favourable. At the same time, the released water molecules can now engage in more extensive HB interactions with the bulk water, which was previously inaccessible due to being on the surface of the organic compounds. This releases a significant amount of energy and contributes enthalpically to the overall hydrophobic effect.

In one example, Pittelkow and co-workers described the preparation of a new class of macrocycle, biotin[6]uril, consisting of six biotin subunits (Figure 1.7).[50] The receptor was capable of binding a range of singly charged anions in water, with selectivity towards SCN^- (log K_a = 4.5). ITC experiments revealed that anion recognition was enthalpically driven (non-classical hydrophobic effect), with the release of encapsulated water molecules from the receptor cavity upon anion complexation.

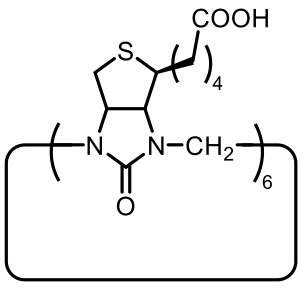

Figure 1.7 Pittelkow's biotin[6]uril.[50]

1.3 Anion Recognition

1.3.1 Importance of Anions

Anions are omnipresent and are fundamentally indispensable in numerous biological processes. For example, many biologically important molecules such as DNA and ATP are polyanionic in nature. Iodide is required for the production of hormones in the thyroid glands,[51] and people at risk to radioactive exposure often take potassium iodide (KI) tablets to pre-saturate their thyroid glands with regular iodine (^{127}I), thereby preventing the internal uptake of any radioactive form of the element (^{131}I).[52] Cystic fibrosis is caused by malfunctioning or insufficient production of chloride transport channels in our bodies.[53] Fluoride is a common additive to toothpaste and drinking water because of its effectiveness in preventing tooth decay.[54]

Environmentally, certain anions pose great threats to the ecosystems. The over-use of nitrate- and phosphate-rich fertilisers in intensive arable farming has led to high concentrations of nitrate and phosphate in soil water and surrounding lakes and rivers leading to eutrophication, characterised by an excessive growth of algae.[55] Cyanide is a highly toxic and lethal anion that can be found in industrial waste and cigarette smoke.[56] Pertechnetate is a radioactive anion present in nuclear waste. Its long half-life (>200 000 years) and high water solubility have raised significant concerns to its disposal and storage.[57] In addition to the anthropogenic release of potentially harmful anions, some naturally occurring anions are also detrimental to human health. Arsenic, in the form of $H_2AsO_4^-$ or $HAsO_4^{2-}$, is a major contaminant of groundwater, affecting over 300 million people worldwide.[58,59] Long-term exposure to arsenic can lead to diseases such as skin lesions, cancer and adverse pregnancy outcomes.[60]

The importance of anions in biological and environmental processes has now been widely recognised and this has expedited the development of the field of anion recognition. Over the years, a burgeoning number of anion receptors have been reported, with applications in numerous areas such as sensing, extraction and catalysis.[61–63] In the following sections, the challenges of anion recognition are considered, followed by a review of seminal examples of HB- and σ-hole-based anion receptor systems reported to date.

1.3.2 Challenges in Anion Recognition

Since the first report of an abiotic anion host system in 1968,[64] the advancement of research in anion recognition has, until the last couple of decades or so, been relatively slow in comparison to the parallel field of cation recognition. This may be attributed to the inherent properties of anions, which render the design of potential receptors challenging.

(i) Anions are larger in size and more charge-diffuse than isoelectronic cations and therefore possess lower electronic charge density (Figure 1.8). For example, the ionic radius of Cl^- is 1.67 Å while that of K^+, its isoelectronic counterpart, is 1.52 Å.[65] The significantly larger size and charge-diffuse nature of anions essentially weakens the attractive electrostatic interactions between anions and a positively charged receptor.

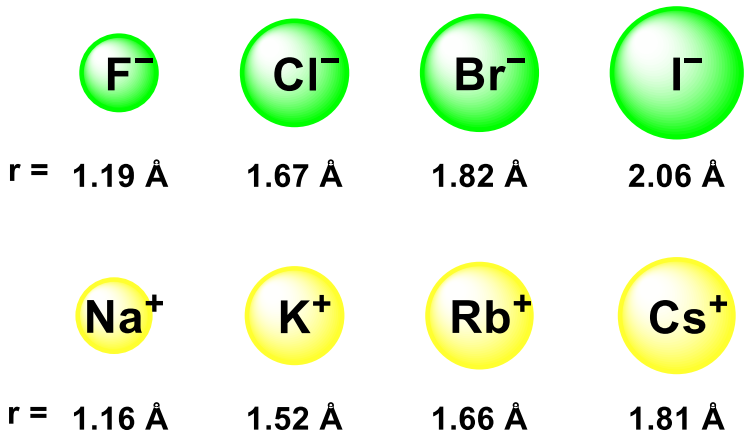

Figure 1.8 Crystal ionic radii r (Å) of halide anions (F^-, Cl^-, Br^- and I^-) and their isoelectronic alkali metal cations (Na^+, K^+, Rb^+ and Cs^+).[65]

(ii) Anions exhibit high solvation energies, especially in protic solvents due to their capabilities to act as HB acceptors.[66] Taking Cl^- and K^+ as examples, in water the experimentally determined standard Gibbs free energy of hydration ($\Delta_{hyd}G$) of Cl^- (–340 kJ mol^{-1}) is much higher than that of the K^+ (–295 kJ mol^{-1}). Hence more energy is required to desolvate anions prior to their interaction with a receptor in aqueous solvent media. In the context of anion recognition in water, the Hofmeister

effect is a frequently cited phenomenon to rationalise anion guest selectivity. First reported in 1888 by Franz Hofmeister,[67] his observation of how certain salts influenced the solubility of proteins in water led to the proposal of the "Hofmeister series", $CO_3^{2-} > SO_4^{2-} > F^- > Cl^- > Br^- > NO_3^- > I^- > ClO_4^- > SCN^-$. Early members of the series, known as kosmotropes (water-structure makers), strengthen the hydrophobic effect and decrease the solubility of protein, while chaotropes (water-structure breakers) appearing late in the series induce the opposite. The origin of this Hofmeister effect was historically related the modulation of the HB networks in bulk water,[68–70] but the importance of ion-solute interactions have also been recognised.[71,72] Water-soluble anion hosts containing hydrophobic cavities typically demonstrate selectivity bias towards the least hydrated chaotropic anions such as iodide.[73,74]

(iii) Anions display a range of geometries from spherical, linear, trigonal planar, tetrahedral, to octahedral (Figure 1.9). As a consequence, complementary size-matching shaped cavities need to be incorporated into host structural design for the selective recognition of target anions.

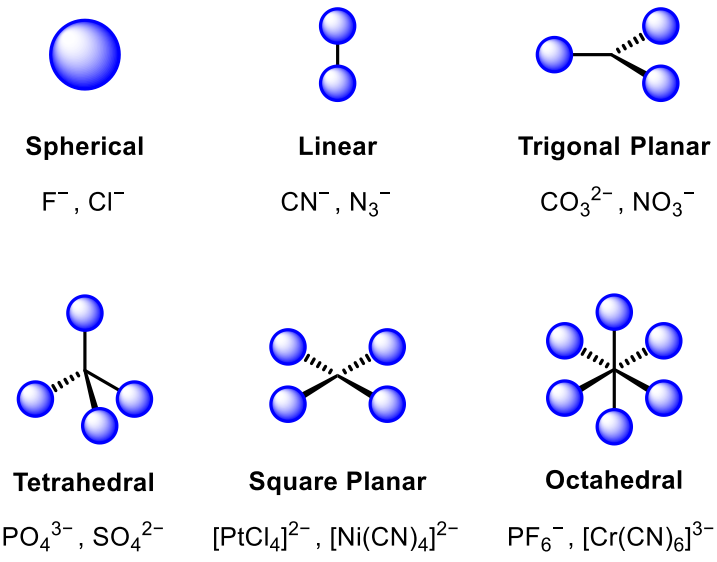

Figure 1.9 Diverse geometries of anions.

(iv) Anions are pH sensitive and can involve multiple acid-base equilibria depending on the pH of the solvent. For example, in water various phosphate anion species exist ($H_2PO_4^-$, HPO_4^{2-} and PO_4^{3-}) at different pH values.[75] This makes the binding of a specific anion more challenging because of potential competition from other anions in solution. In addition, for pH dependent receptors such as polyammonium-based systems, anion binding can only take place in a specific pH window where the target anion dominates and the receptor remains protonated.

1.3.3 Biotic Anion Receptors

Years of evolution have conferred biological systems phenomenal specificity to anions in the highly competitive aqueous cellular environment. For example, both of the naturally occurring sulphate- (SBP)[76] and phosphate-binding proteins (PBP)[77] (Figure 1.10) demonstrate prodigious affinity towards sulphate and phosphate anions respectively, capable of the highly selective uptake of the target complementary oxoanion even in the presence of structurally and electronically similar substrates such as arsenate. This remarkable anion recognition property is attributed to the complete encapsulation of the tetrahedral anions, thereby burying them deep within the protein architecture and shielding them from the bulk solvent. Specifically, each of the bound anion is held tightly by an array of exquisitely disposed HB interactions originating from the surrounding amino acid residues. It is this extensive network of non-covalent interactions that endows the anion binding proteins with unparalleled selectivity.

Mimicking Nature's design, the synthesis of anion receptors rivalling or surpassing the extraordinary anion binding properties of biological hosts have always been the Holy Grail in the field of anion supramolecular chemistry.

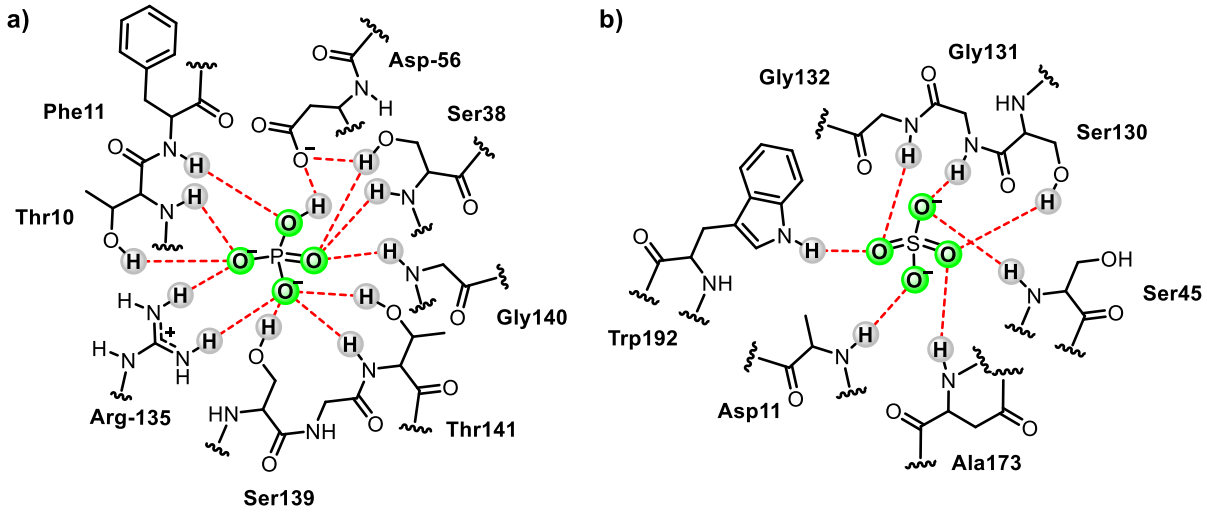

Figure 1.10 Structures of the anion binding domains of a) sulphate-binding protein[76] and b) phosphate-binding protein.[77] HB interactions between the amino acid residues and the anions are shown as red dashed lines.

1.3.4 Synthetic Anion Receptors

Despite the challenges of recognising anions mentioned in Section 1.3.2, the development of many ingeniously designed receptors have been reported over the years. This section gives an overview of receptors employing HB and σ-hole (XB and ChB) interactions as the major driving forces for anion binding in organic and aqueous solvent media.

1.3.4.1 Hydrogen Bonding-based Anion Receptors

A wide range of HB donors have been incorporated into various anion receptor structural frameworks. Common neutral HB donors include amide, urea, thiourea, squaramide, pyrrole and triazole, while charged motifs such as imidazolium and triazolium have also found applications in competitive protic solvent media. Representative HB receptors are discussed below.

(A) *Neutral HB Receptors*

Amide: Due to its synthetic accessibility, amide has frequently been incorporated into acyclic and macrocyclic anion receptor design in particular. Following the seminal

work by Crabtree and co-workers in 1997,[78] who reported a simple acyclic isophthalamide motif capable of selective Cl^- binding in CD_2Cl_2 with $K_a = 6.1 \times 10^4$ M^{-1} (Figure 1.11a), amide motifs have since been incorporated into higher-order, more preorganised anion receptor frameworks.

In one example, Kubik and co-workers reported the synthesis of a neutral cyclic hexapeptide, consisting of alternating L-proline and 6-aminopicolinic acid subunits (Figure 1.11b).[79] Impressively, the macrocyclic receptor bound I^- and SO_4^{2-} selectively with $K_a > 10^5$ M^{-2} in the competitive aqueous solvent mixture 80% D_2O in CD_3OH via the formation of a 2:1 host-guest sandwich complex.[80] The preference for these anions was attributed to their size complementarity with the cyclopeptide cavity, allowing them to simultaneously engage in six HB interactions with the amide residues of the two rings.

Urea and Thiourea: The bidentate nature of a urea functional group allows for donation of two parallel, convergent HB for complementary Y-shaped anions such as acetate.[81] For example, Gale prepared a bis-urea receptor capable of strongly binding OAc^- in 0.5% D_2O in DMSO (Figure 1.11c).[82] Thiourea is the more acidic analogue of urea (pK_a = 21.1 and 26.9 respectively for thiourea and urea in DMSO),[83] capable of forming stronger HB interactions with anions. In 2011, Jolliffe and co-workers reported the synthesis of a cyclopeptide-based cryptand, functionalised with a thiourea HB donor motif on each of the three covalent linkers (Figure 1.11d).[84] In 0.5% D_2O in DMSO-d_6, the cryptand selectively bound the basic anions F^- and AcO^- ($K_a > 10^4$ M^{-1}), while no appreciable binding was observed for charge-diffused anions such as I^- and NO_3^-.

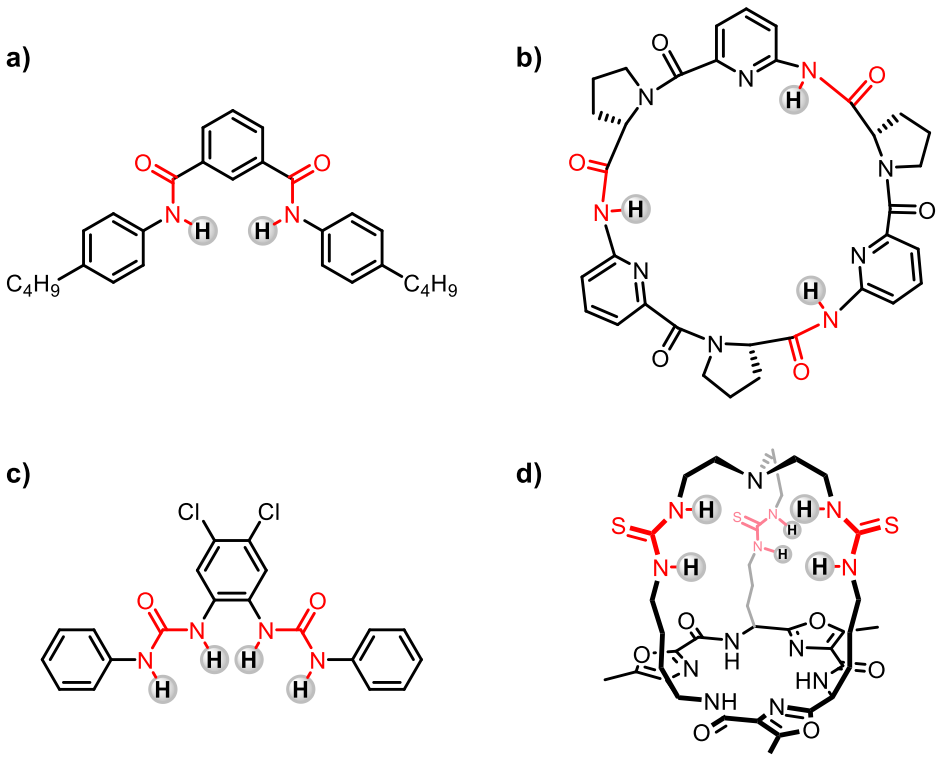

Figure 1.11 a) Crabtree's isophthalamide receptor.[78] b) Kubik's cyclic hexapeptide.[79,80] c) Gale's bis-urea transporter.[82] d) Jolliffe's cyclopeptide-based thiourea cryptand.[84]

Squaramide and Thiosquaramide: The potency of squaramide in anion binding has been linked to its enhanced aromaticity upon forming HB with anions.[85] Recently, Caltagirone and co-workers prepared a squaramide-based receptor capable of the selective binding of $H_2PO_4^-$ in the competitive solvent mixture 25% D_2O in DMSO-d_6 (Figure 1.12a).[86] The receptor was also found to function as an efficient Cl^- transmembrane transporter. In 2016, Jolliffe and Elmes reported a tris-squaramide-based macrocycle (Figure 1.12b) demonstrating high selectivity for SO_4^{2-} ($K_a > 10^4$ M^{-1}) over other tetrahedral anions in 1:2 D_2O/DMSO-d_6, owing to the better size-match between the macrocycle cavity and the dianion.[87] Impressively, the receptor was capable of discriminating between SO_4^{2-} and CrO_4^{2-} ($K_a(SO_4^{2-})/K_a(CrO_4^{2-}) > 60$) with a significantly higher degree of efficiency than that of the sulphate-binding protein ($K_a(SO_4^{2-})/K_a(CrO_4^{2-}) = 2.5$).

Thiosquaramide is more acidic than squaramide, and often displays an enhanced solubility in organic solvents likely due to a disruption of the head-to-tail ladder conformation adopted by squaramide self-aggregates.[88,89] In 2014, Gale reported pH switchable thiosquaramide-based anion transporters.[90] At physiological pH, deprotonation was observed for the acidic thiosquaramide, which switched off the chloride transport (Figure 1.12c). However, in a more acidic medium (pH = 4.0), transport of the anion was switched on when thiosquaramide deprotonation did not occur.

Pyrrole: The pyrrole motif has been exploited as a potent N–H donor group for anion recognition, especially when integrated into a cyclic framework as a calix[4]pyrrole macrocycle consisting of four pyrrole subunits. Sessler, the pioneer of such receptors, has reported a pyrrole-strapped calix[4]pyrrole that binds Cl^- strongly relative to benzene- and furan-strapped analogues in CH_3CN with $K_a = 1.8 \times 10^7\ M^{-1}$ (Figure 1.12d).[91] The solid-state structure of the receptor·Cl^- complex revealed the formation of five N–H···Cl^- HB interactions from the pyrrole subunits.

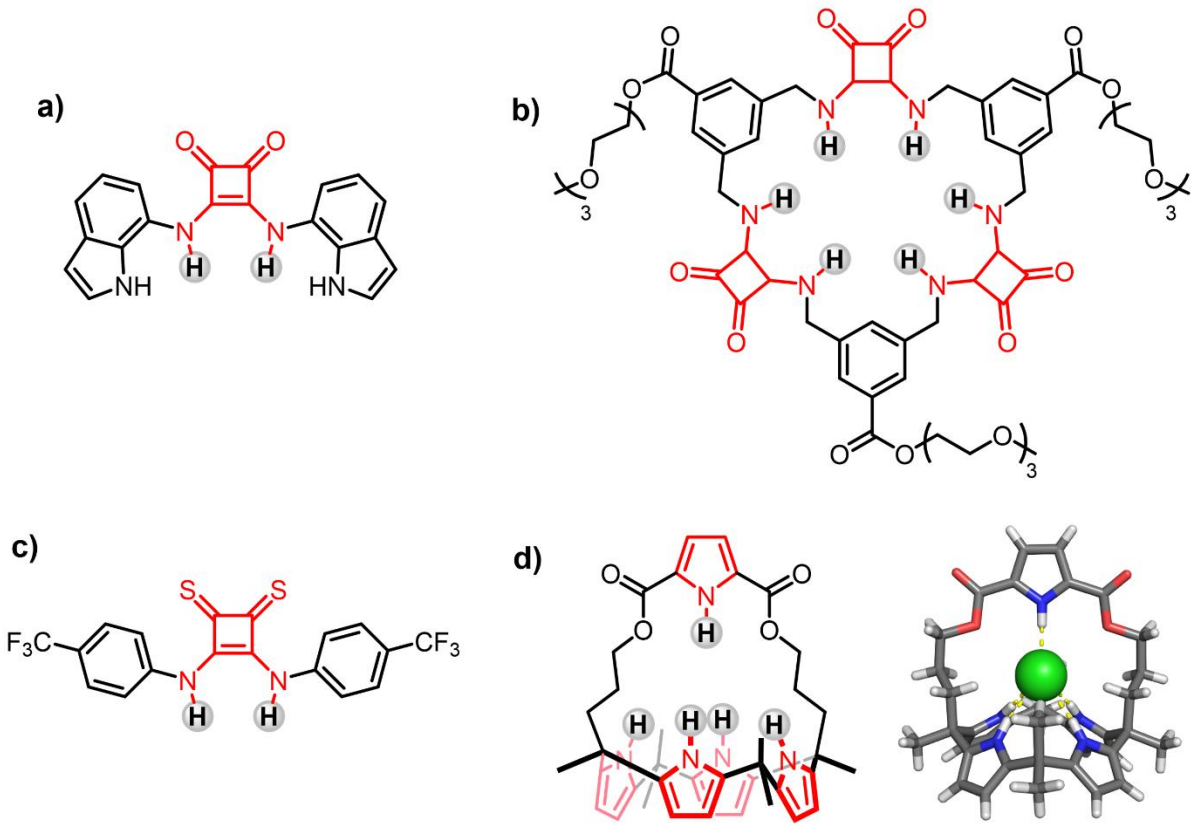

Figure 1.12 a) Caltagirone's squaramide-based anion receptor.[86] b) Jolliffe's sulphate selective squaramide macrocycle.[87] c) Gale's thiosquaramide anion transporter.[90] d) Sessler's pyrrole-strapped calix[4]pyrrole and the crystal structure of the receptor·Cl^- complex.[91]

C–H Donors: Carbon-hydrogen HB interactions are traditionally regarded as a secondary interaction that assist anion binding instead of acting as the main driving force. However, through judicious receptor design, strong anion binding can also be achieved employing C–H···anion interactions only. Flood and co-workers in 2008 reported a shape-persistent "triazolophane" macrocycle (Figure 1.13a),[92] consisting of alternating proto-triazole and phenyl motifs. This highly preorganised and rigid C–H HB macrocycle selectively bound Cl^- and Br^- ($K_a > 10^6$ M^{-1}) in CH_2Cl_2, while F^- and I^- were too small and too big respectively to fit in the binding cavity.[93] Building on this seminal work, Flood in subsequent years reported other shape-persistent macrocycles, including the cyanostilbene-based campestarene macrocycle "cyanostar" (Figure 1.13b)[94] and proto-triazole-carbazole-functionalised macrocycle "tricarb" (Figure 1.13c),[95] both of which demonstrated strong binding to charge-diffuse anions such as

PF_6^- in organic solvents by virtue of the preorganised C–H HB donors. Taking things one step further, recently, they prepared a cryptand that displayed exceptional selective binding of Cl^- ($K_a \approx 10^{17}$ M^{-1}) in CH_2Cl_2 (Figure 1.13d).[96] Solid-state analysis of the receptor·NaCl complex revealed the encapsulated Cl^- was bound by nine convergent HB interactions arising from triazole and phenyl C–H protons.

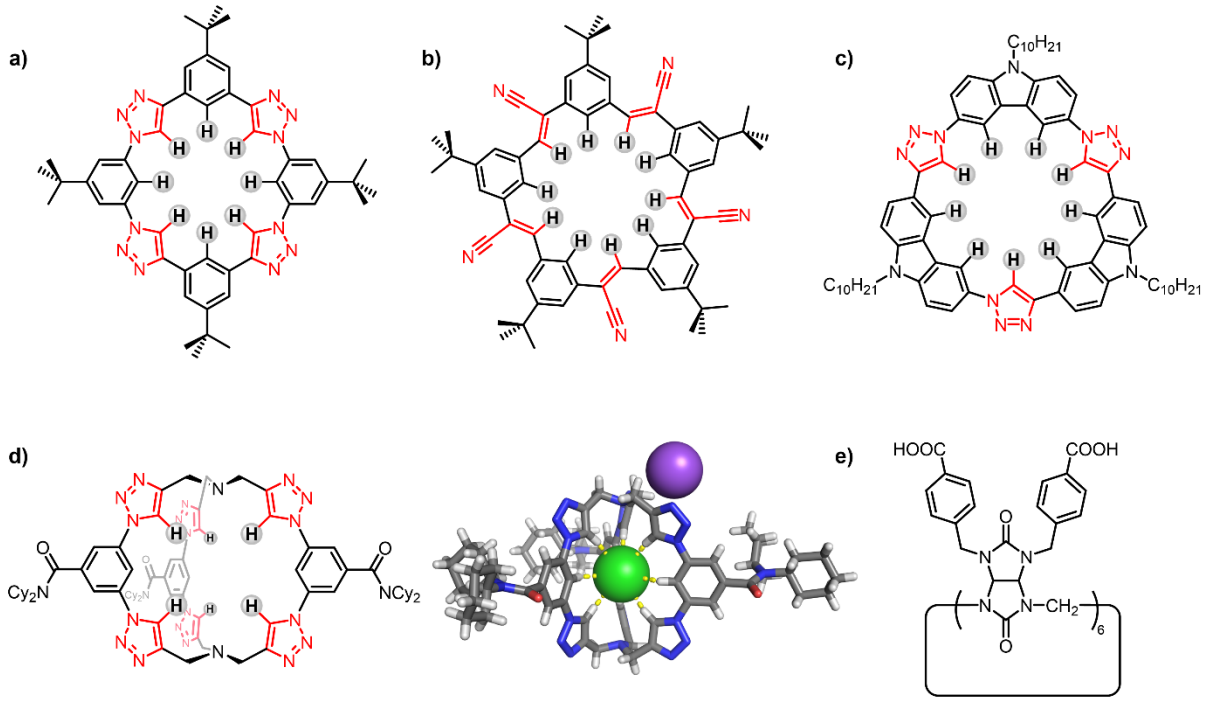

Figure 1.13 Flood's a) triazolophane,[92,93] b) cyanostar,[94] c) tricarb[95] and d) triazole-cage and its crystal structure of the cage·Cl– complex.[96] e) Sindelar's water-soluble bambus[6]uril.[97]

Bambusuril is a special class of glycoluril-based macrocycle developed by Sindelar and co-workers.[98] By introducing solubilising benzoate substituents to the outer-rims of the bambus[6]uril (Figure 1.13e), the resulting receptor bound anions in water in accordance to the Hofmeister series, with the strongest binding observed for the least solvated ClO_4^- ($K_a > 10^7$ M^{-1}) while the hydrophilic F^- was only bound weakly (K_a = 10^2 M^{-1}).[97] Anion recognition was found to be mediated by the multiple C–H HB interactions between the methine protons of the glycoluril units and the anions, as well as the non-classical, enthalpy-driven hydrophobic effect.

(B) Cationic HB Receptors

Cationic HB receptors benefit from the highly potent electrostatic attractions with anions, and have therefore been frequently designed to function in competitive protic solvent media.

Ammonium: Polyammonium compounds are among the earliest examples of HB anion receptors.[99] In water with propyl group separation, the secondary amino groups are protonated at physiological pH, forming multiple favourable charge-assisted HB electrostatic interactions with anions. For example, the hexa-protonated polyammonium macrocycle shown in Figure 1.14a was capable of binding the hydrophilic SO_4^{2-} dianion with log K_a = 4.05 in water.[100]

Guanidinium: Guanidinium is another charged HB donor motif. Compared to ammonium, it possesses a lower charge density due to charge delocalisation, but remains protonated in a much wider range of pH values by virtue of its higher pK_a value of 13.6.[101] For example, the tri-guanidinium macrocycle binds PO_4^{3-} in 9:1 CH_3OH/H_2O with a modest log K_a = 2.4, determined by pH titration (Figure 1.14b).[102]

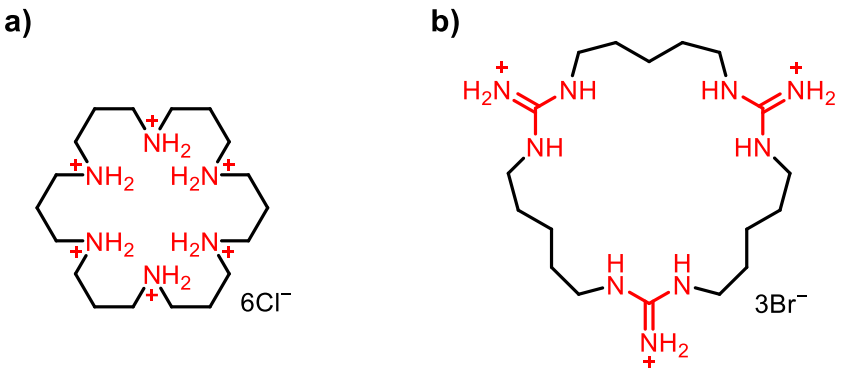

Figure 1.14 a) Polyammonium[100,103] and b) tri-guanidinium anion receptor.[102]

Imidazolium: Imidazolium is a popular motif for anion recognition due to its potent charge assisted C–H donor and its insensitivity to pH. In 2013, Gao and You reported the synthesis of a tetrakisimidazolium macrocycle (Figure 1.15a) which displays high

selectivity towards the hydrophilic SO_4^{2-} anion via formation of a 2:1 host-guest complex with $K_a > 10^9\ M^{-2}$ in water.[104] The solid-state structure of the receptor·anion sandwich complex reveals the two macrocycles align themselves orthogonally to encapsulate the SO_4^{2-} anion via formation of eight HB interactions from the imidazolium protons to the four oxygens of SO_4^{2-}.

Triazolium: Prepared by alkylating the click-accessible 1,2,3-triazole group, is the versatile cationic triazolium HB donor. Sessler and co-workers for example prepared a tetrakistriazolium macrocycle (Figure 1.15b) which exhibits a preference towards tetrahedral oxoanions (HSO_4^-, $HP_2O_7^{3-}$ and $H_2PO_4^-$) over trigonal planar and spherical anions (OAc^-, NO_3^-, Cl^- and Br^-) in polar solvent media such as CH_3OH and 2:3 acetone/H_2O.[105]

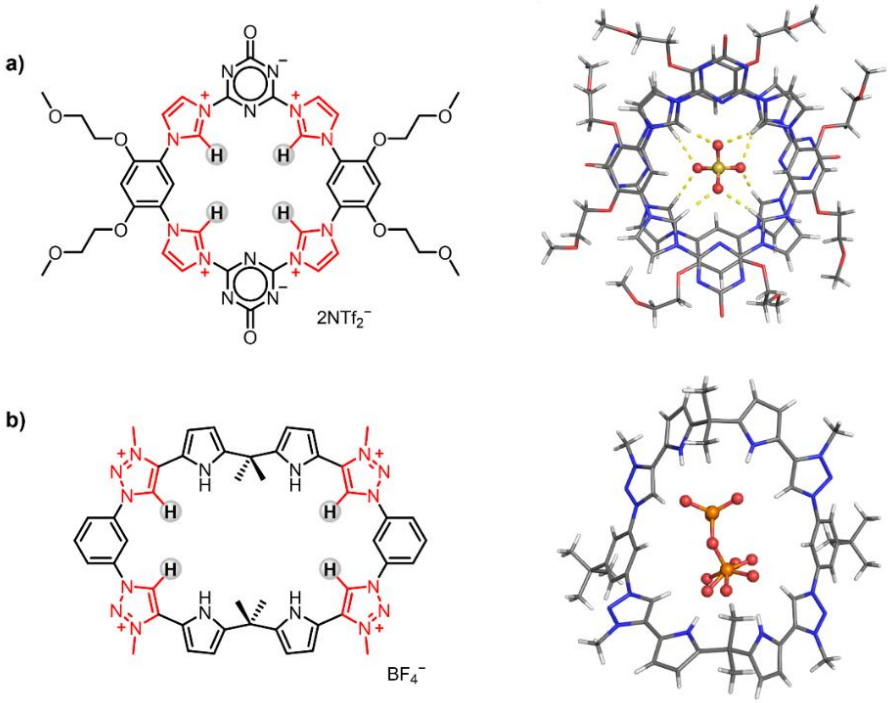

Figure 1.15 a) Gao and You's tetrakisimidazolium anion receptor and the crystal structure of the 2:1 receptor:SO_4^{2-} complex.[104] b) Sessler's tetrakistriazolium anion receptor and the crystal structure of the 1:1 receptor:$HP_2O_7^{3-}$ complex.[105] (counterions are omitted for clarity)

1.3.4.2 Halogen Bonding-based Anion Receptors

(A) *Neutral XB Receptors*

One of the earliest examples of employing XB in the binding of anions was demonstrated by Resnati and co-workers in 2005 (Figure 1.16a).[106] They reported a tripodal ion-pair receptor, consisting of anion binding XB iodo-pentafluorobenzene substituents attached to the cation binding tris[2-(2-hydroxyethoxy)ethyl]amine. This iodinated XB receptor was found to exhibit a binding constant of NaI (K_a = 2.6 × 10^5 M^{-1}) 20 times higher than its perfluorinated analogue in $CDCl_3$, which does not participate in XB interaction with iodide. Six years later, Taylor reported a urea-based receptor appended with XB iodo-pentafluoroaryl groups (Figure 1.16b).[107] Interestingly, the presence of XB donors was found to enhance the halide affinities of the receptor, yet provided minimal changes to the binding of oxoanions in CD_3CN.

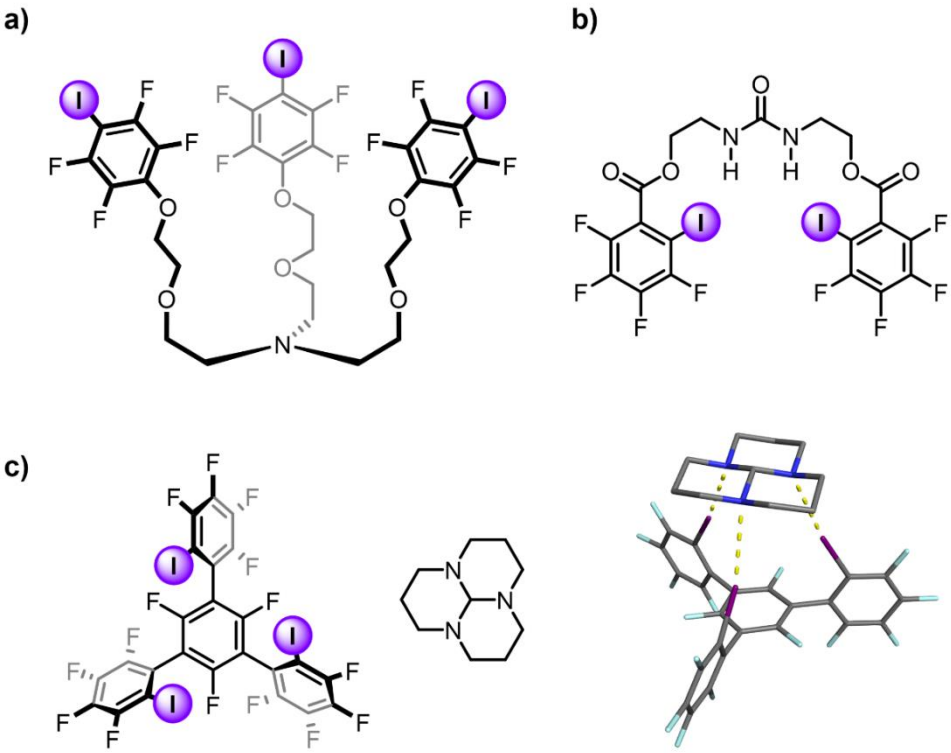

Figure 1.16 a) Resnati's ion-pair receptor for NaI.[106] b) Taylor's mixed HB/XB receptor.[107] c) Huber's tridentate three-point XB receptor, the triamine designed guest and crystal structure showing the three-point XB intereaction between them.[108]

Utilising the same XB donor motif, Huber reported a tridentate XB receptor capable of binding a neutral triamine guest through three-point XB interactions in the solid state (Figure 1.16c).[108] Titration studies conducted in toluene-d_8 revealed the XB host binds the triamine (K_a = 6.3 × 10^2 M^{-1}) significantly stronger than a series of structurally comparable mono-, bi- and tridentate amines, highlighting the importance of host-guest complementarity in exploiting linear XB interactions for guest binding.

During the past decade the 5-iodo-1,2,3-triazole motif has gained popularity due to its synthetic accessibility via CuAAC click reactions.[109] Schubert reported a carbazole-based bis(iodo-triazole) receptor with a hydroxyl group *ortho* to each triazolyl unit (Figure 1.17a).[110] Intramolecular HB interactions between the O–H and the adjacent triazole N restricts the rotational degree of freedom of the iodo-triazole motifs, leading to enhancement in anion affinity compared to the O–H free receptor analogue. Kubik and co-workers prepared a pseudo-cyclopeptide containing three XB iodo-triazole donors (Figure 1.17b).[111] In the aqueous solvent mixture (2.5% D_2O in DMSO-d_6), the XB cyclopeptide displayed strong halide binding with selectivity towards Cl^- (log K_a = 3.3) while no binding of halides was observed for the proto-triazole congener. Direct comparison between the anion binding capabilities of XB and HB receptors was also demonstrated by Beer and co-workers in their "picket-fence" porphyrin receptors, with each arm functionalised with either iodo- or proto-triazole donors (Figure 1.17c).[112] UV–visible absorption titration experiments carried out in $CHCl_3$ revealed XB interaction led to a significant increase in halide association yet attenuated the binding of OAc^-.

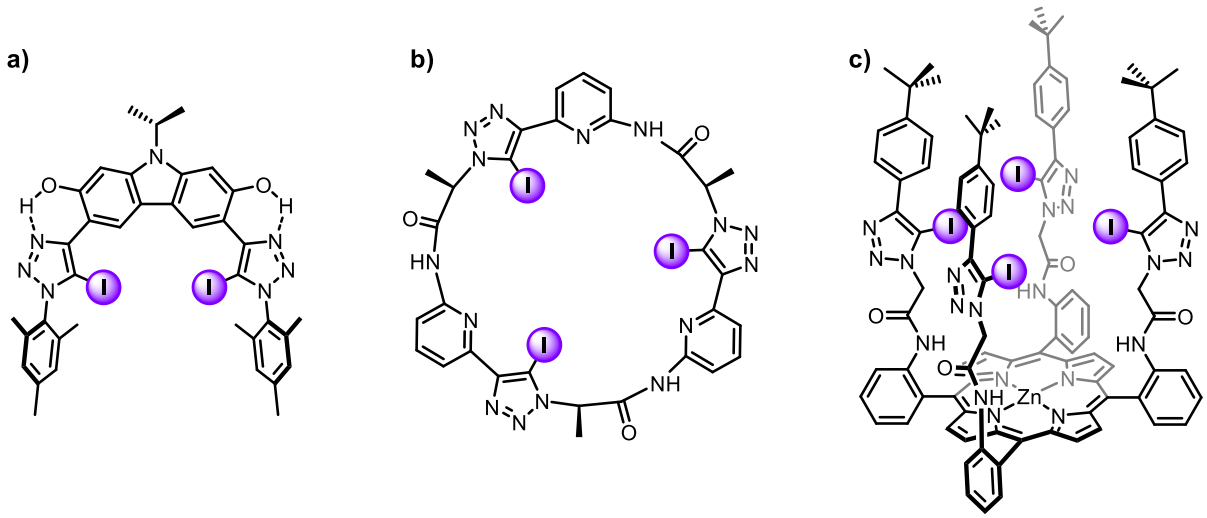

Figure 1.17 a) Schubert's HB preorganised XB receptor.[110] b) Kubik's XB pseudo-peptide receptor.[111] c) Beer's picket fence XB porphyrin receptor.[112]

(B) Cationic XB Receptors

The utilisation of cationic XB hosts benefits from the more potent charge-assisted XB donor interactions. In 2018, Berryman described the use of HB interactions to enhance the anion binding capability of a pyridinium XB receptor (Figure 1.18a).[113] Intramolecular HB between the amino group of a central fluoroaniline unit and the iodine atoms of proximal iodo-pyridinium donors preorganised the recognition site and rendered each iodine atom σ-hole more electrophilic. In 2:3 $CDCl_3/CD_3NO_2$, this preorganisation effect led to a 9-fold improvement in halide binding strength compared to a control system with benzene in place of fluoroaniline. In 2012, Beer reported the first examples of XB cyclophanes capable of fluorescence anion sensing in aqueous methanolic mixtures (Figure 1.18b).[114] In 9:1 CH_3OH/H_2O, the bromo- and iodo-imidazoliumophanes bind iodide and bromide anions selectively, with concomitant naphthyl group fluorescence turn-on. Huber and co-workers carried out comprehensive ITC studies on the anion binding thermodynamics of a 1,3-bis(iodo-imidazolium)benzene XB receptor in CH_3CN (Figure 1.18c).[115] In particular, an entropic contribution was found to be crucial to anion chelation, accounting for over 50% of the overall binding free energy ΔG.

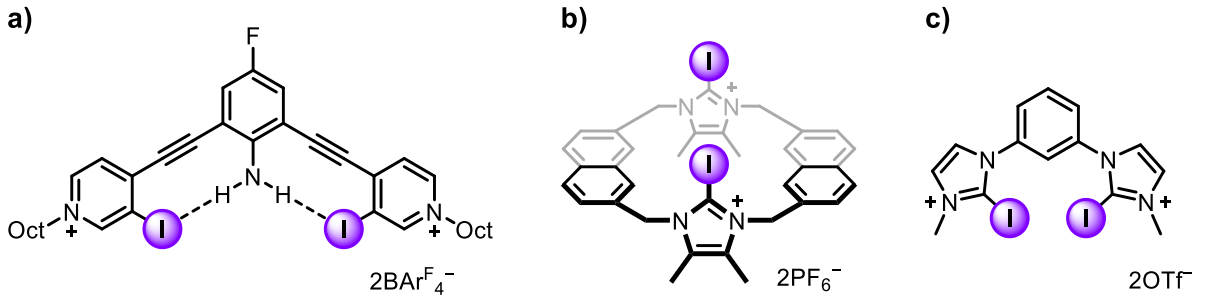

Figure 1.18 a) Berryman's HB-preorganised XB receptor.[113] b) Beer's bis(iodo-imidazolium) cyclophane receptor.[114] c) Huber's bis(iodo-imidazolium)benzene receptor.[115]

Molina and co-workers developed a pyrene-based receptor decorated with two 5-iodo-triazolium XB donors (Figure 1.19a).[116] Convergent binding of hydrogen pyrophosphate ($H_3P_2O_7^{3-}$) mediated by the two XB donor motifs in acetone brought the two fluorogenic pyrene in close proximity, leading to excimer emission intensity enhancement. Schubert and Hager reported a XB polymeric system consisting of bis(iodo-triazolium)benzene as donor motifs (Figure 1.19b).[117] When mixed with a carboxylate-based acceptor co-polymer, XB induced cross-linking between these systems endowed self-healing properties to these polymeric networks.

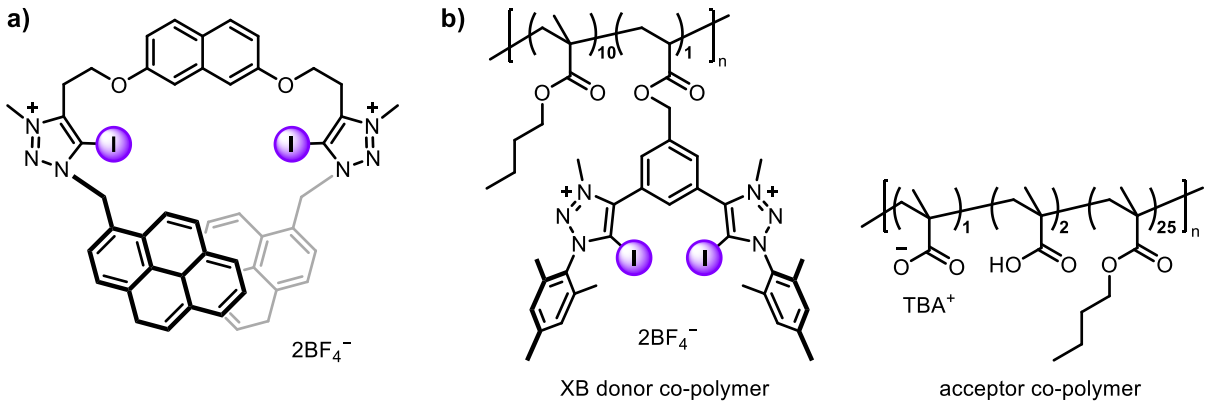

Figure 1.19 a) Molina's pyrene-based bis(iodo-triazolium) receptor.[116] b) Schuber and Hager's XB donor and carboxylate acceptor co-polymers.[117]

1.3.4.3 Chalcogen Bonding-based Receptors

The number of reported ChB-based anion receptors are relatively scarce compared to the above-mentioned XB hosts. This is in part attributed to the inherent chemical instability of the C–Te bond,[118] making ChB donors susceptible to moisture

and air, as well as more prone to decomposition by oxidation, nucleophilic attack and metal insertion.[119,120] Nevertheless, through judicious design of receptor, neutral and cationic ChB donors capable of anion binding in solution have been reported in the last decade.

(A) Neutral ChB Receptors

Taylor reported a new class of ChB receptors based on benzotelluradiazoles motifs (Figure 1.20a).[119] UV–visible absorption titration studies in THF showed that all receptors displayed a preference for Cl^-, with stronger anion binding demonstrated by the more electron-deficient derivatives. Later, the same group prepared another type of ChB receptor consisting of one or two perfluoroaryl-appended tellurophene motifs (Figure 1.20b). The bidentate ChB receptor showed stronger anion binding in organic solvents compared to the monodentate analogue.[121] Recently, Beer reported a ChB-based foldamer containing four 5-telluromethyl-1,2,3-triazoles as ChB donors (Figure 1.20c).[122] Impressively, the acyclic receptor was found to be stable in water and bind I^- very strongly with $K_a = 2.64 \times 10^7\ M^{-2}$ as a 2:1 stoichiometric host-guest complex. The much larger anion association constant value exhibited by the σ-hole receptor compared to the proto-foldamer derivative was attributed to involvement of multiple Te···I^- ChB interactions, as well as the hydrophobic collapse favouring the formation of the 2:1 host-guest sandwich complex in water.

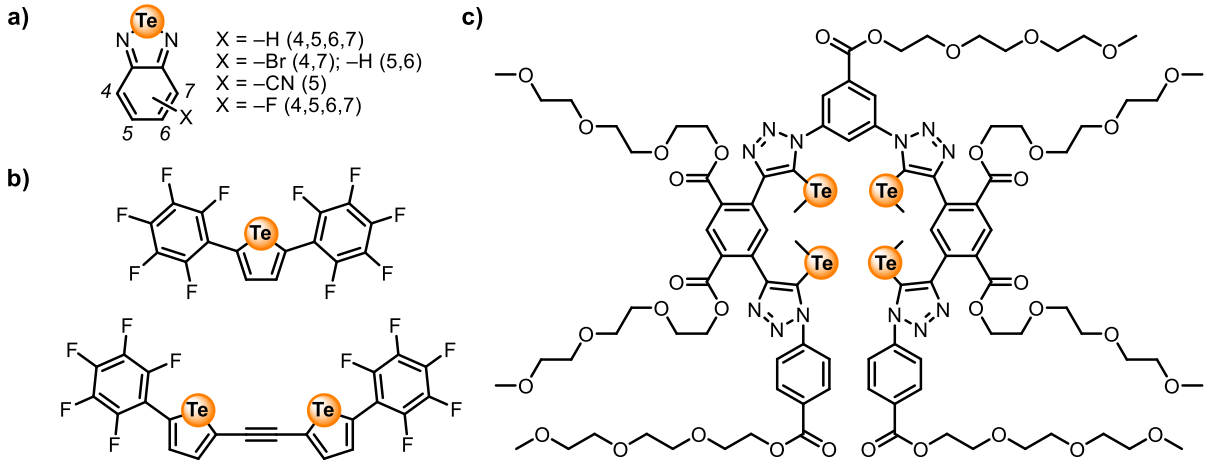

Figure 1.20 a) Taylor's monodentate benzotelluradiazoles ChB receptor.[119] b) Taylor's tellurophene-based mono- and bidentate receptors.[121] c) Beer's 5-telluromethyl-1,2,3-triazole-based ChB foldamer.[122]

The more stringent linear directionality of bonding and hydrophobic character of ChB compared to HB, has prompted the development of ChB-based organocatalysts and anion tranporters. In one example, Matile investigated the catalytic potential of a family of dithieno[3,2-b;2',3'-d]thiophenes (DTTs) in the reduction of quinoline and imine (Figure 1.21a).[123] The diimide derivative of DTT displayed the highest activity and led to a 1 290-fold enhancement in reaction rate compared to the uncatalysed reaction. In 2019, the same group also studied the anion transport abilities of perfluoroaryl-appended PnB, ChB and XB receptors (Figure 1.21b).[124] Among the three types of σ-hole transporters, the ChB tellanes were found to be the most active, attributed to the two in-plane σ-holes on the Te atoms and the extra anion-π interactions with the two covalently attached pentafluorobenzene groups.

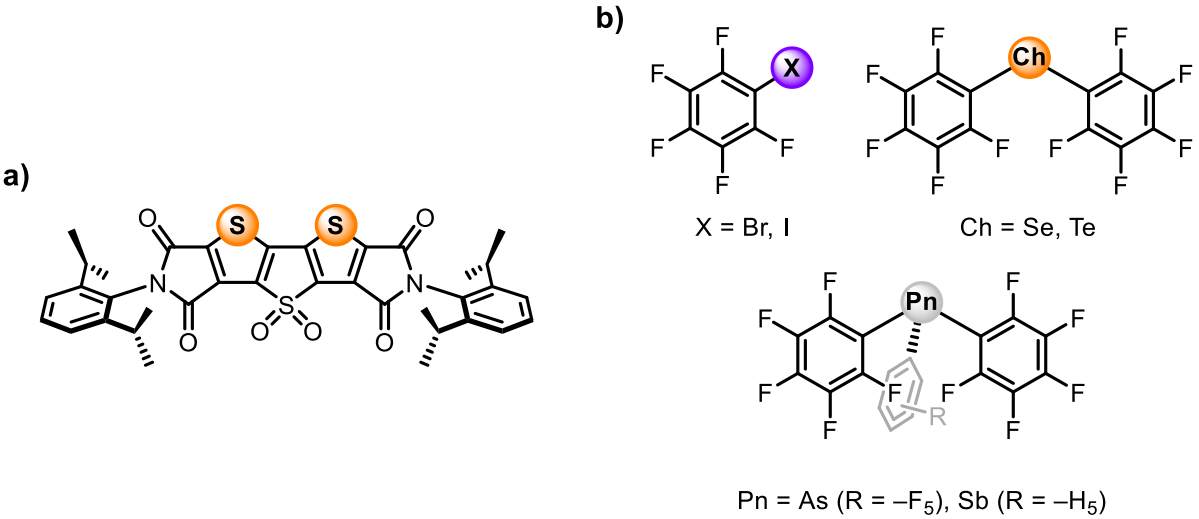

Figure 1.21 a) Matile's DTT-based ChB catalyst.[123] b) Matile's perfluoroaryl-appended XB, ChB and PnB anion transporters.[124]

(B) Cationic ChB Receptors

The first example of a cationic ChB anion receptor was reported by Gabbaï in 2010.[125] The receptor, containing both Lewis acidic boron and telluronium centres, was capable of selectively binding F^- in methanol (K_a = 750 M^{-1}) (Figure 1.22a). The anion was found to be stabilised by both B and Te atoms, with significant electron transfer character from the lone pairs of F^- to the σ* orbital of C–Te. Building on this work, Gabbaï very recently prepared a dicationic bis(telluronium) Lewis acid (Figure 1.22b), which exhibited much higher chloride affinity than its monodentate analogue.[126] In particular, the addition of the bidentate ChB compound to both [Ph_3PAuCl] and *cis*-[$(Ph_3P)_2PtCl_2$] significantly improves their activities in catalysing cycloisomerisation reactions.

In 2017, Huber described the use of selenated bis(benzimidazolium)-based ChB compounds as promoters for organic reactions (Figure 1.22c).[120] In a benchmark Ritter reaction, the use of a stoichiometric amount of the *syn* ChB isomer activates the C–Br bond of benzhydryl bromide, resulting in a 34-fold rate enhancement to yield the amide product. Beer incorporated the ChB selenomethyl-triazolium motif into a

rotaxane binding pocket (Figure 1.22d) and investigated the anion binding properties of the interlocked receptor in an aqueous-organic solvent mixture (4:1 acetone-d_6/D_2O).[127] In stark contrast to the all-protic rotaxane host analogue, which displayed a preference for Br^-, the cationic ChB rotaxane receptor was selective for the iodide anion.

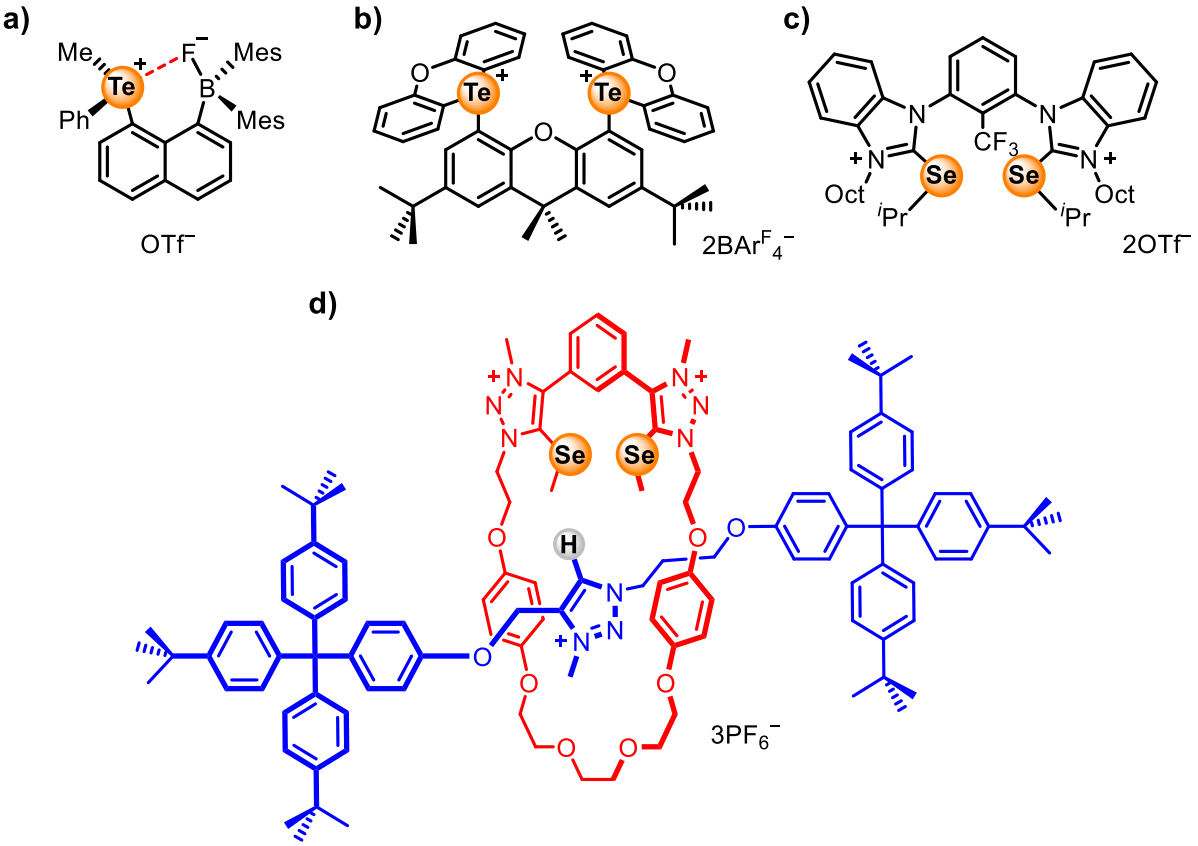

Figure 1.22 Gabbaï's a) monodentate[125] and b) bidentate[126] telluronium-based ChB receptors. c) Huber's selenated bis(imidazolium)-based ChB promoter.[120] d) Beer's bis(selenomethyltriazolium)-based ChB [2]rotaxane.[127]

1.4 Ion-Pair Recognition

Monotopic host systems for charged guest species require an energetic cost to be overcome to separate the guest ion from its ion-pair counterion.[128,129] A common strategy to lower this energetic penalty and enhance binding strength is through the use of lipophilic and non-coordinating counterions, such as for cation recognition, the tetrakis[3,5-bis(trifluoromethyl)phenyl]borate ($BAr^{F}{}_{4}^{-}$) anion and the tetraalkylammonium cation for anion binding. Despite this, the identity of the counterion still greatly influences the binding strength and selectivity of the target ion.[130,131] To help circumvent this problem, ion-pair recognition entailing the design of heteroditopic receptors capable of the simultaneous complexation of both a cation and anion has, since the early 1990s, emerged as an intense field of research.[132–137]

Stimulated by the potential wide scope of applications including salt solubilisation, salt extraction and membrane transport,[138] heteroditopic ion-pair host systems are designed to exhibit cooperative ion-pair binding, where the binding of one ion by the ditopic receptor enhances the binding of the oppositely charged counter-ion.[139,140] The origin of this cooperativity is typically due to favourable proximal ion-pair electrostatic interactions and/or allosteric effects.[141]

The variety of heteroditopic or multitopic receptors reported to date can be classified according to their binding modes (Figure 1.23).[142] When the two bound ions are in close proximity as revealed by X-ray diffraction studies or there is evidence of non-covalent interactions such as hydrogen bonding between them, this type of binding is known as contact ion-pair (Figure 1.23a). On the contrary, if the two co-bound ions are not in direct contact but are separated by solvent or the host framework, the binding modes are known as solvent-separated (Figure 1.23b) and host-separated

(Figure 1.23c), respectively. This section will discuss the representative examples of ion-pair receptors for the recognition of alkali metal salts (section 1.4.1), transition metal salts (section 1.4.2) and organic salts (section 1.4.3), followed by examples of applications (section 1.4.4).

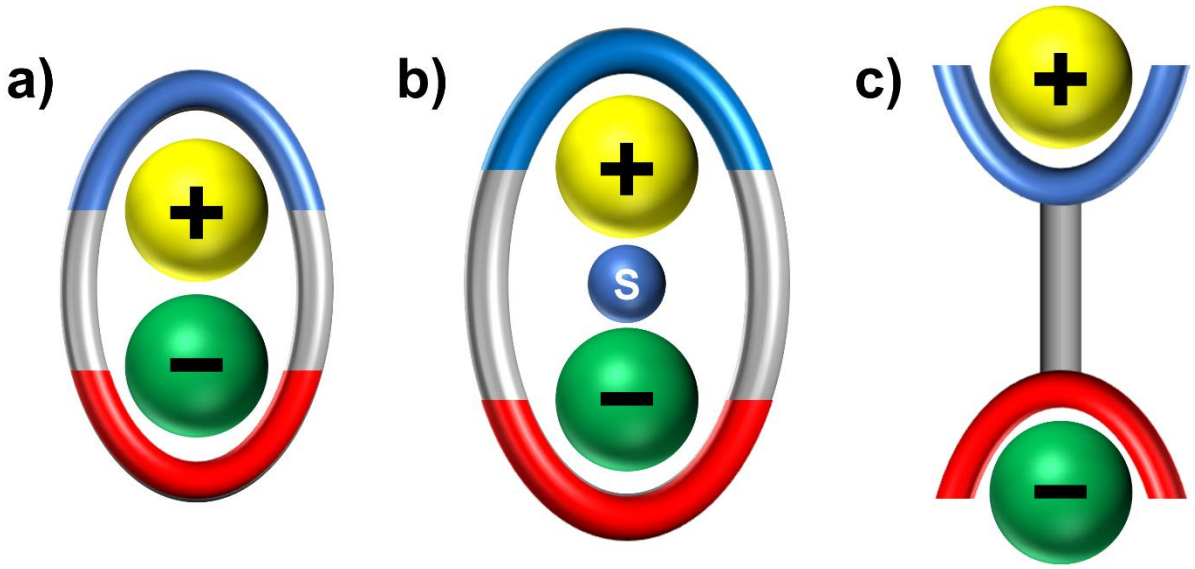

Figure 1.23 Schematics of different ion-pair binding modes: a) contact ion-pair, b) solvent-separated ion-pair and c) host-separated ion-pair. Blue and red arcs represent cation and anion binding sites respectively. Yellow, green and blue spheres represent cation, anion and solvent molecule respectively.

1.4.1 Alkali Metal Salt Binding

The established affinity and selectivity of crown ethers for alkali metal cations has resulted in their incorporation into ion-pair receptors as the cation binding site. In 2001, Smith and co-workers reported the first example of a heteroditopic bicyclic receptor capable of the cooperative binding of KCl as a contact ion-pair (Figure 1.24a).[143] In DMSO-d_6, the simultaneous binding of K^+ and Cl^- was found to be stronger than the binding of either of the free ions. Recently, Lacour reported a series of polyamide-crown ether receptors, which were prepared from 1,4-dioxane in three steps.[144] Interestingly, in the presence of alkali metal cation (Na^+, K^+), these ditopic

receptors bound linear triatomic anions (N_3^-, NCO^-, SCN^-) cooperatively in 4:1 $CDCl_3$/DMSO-d_6 but not spherical halides (Cl^-, Br^-, I–) (Figure 1.24b).

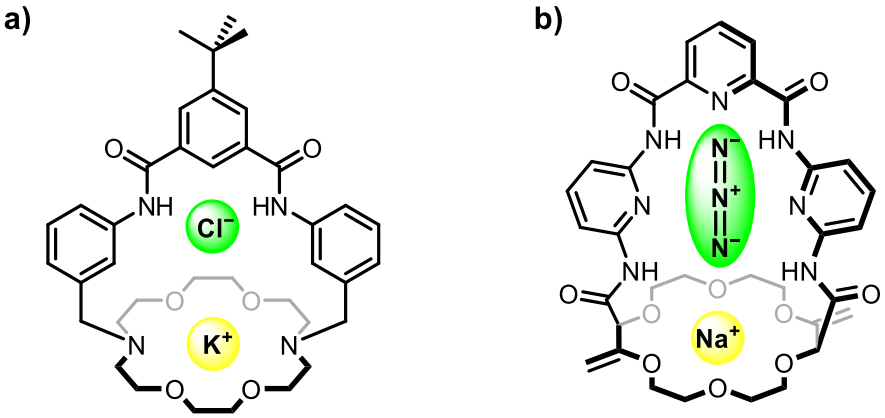

Figure 1.24 a) Smith's azacrown ether-based macrobicyclic ion-pair receptor binding KCl as contact ion-pair,[143] and b) Lacour's polyamide-crown ether heteroditopic receptor binding NaN_3 as contact ion-pair.[144]

In addition to contact ion pairs, Sessler and co-workers reported a crown-6-calix[4]arene-capped calix[4]pyrrole capable of binding CsF as a host-separated ion-pair (Figure 1.25a).[145] Binding studies conducted in 10% CD_3OD in $CDCl_3$ revealed that F^- binding by the receptor was only observed in the presence of co-bound Cs^+, highlighting the importance of cooperativity. Later, the same group reported an oligoether-capped calix[4]pyrrole receptor which demonstrated switchable ion-pair binding modes (Figure 1.25b).[146] In 9:1 CD_3CN/CD_3OD, the receptor·F^- complex was found to form a host-separated ion-pair complex with Cs^+, in which the cation was trapped by the cone-shaped electron-rich calix[4]pyrrole. In contrast, upon addition of K^+ to the receptor·F^- complex, the alkali metal cation is bound at the oligoether region in the form of a contact ion-pair with F^-.

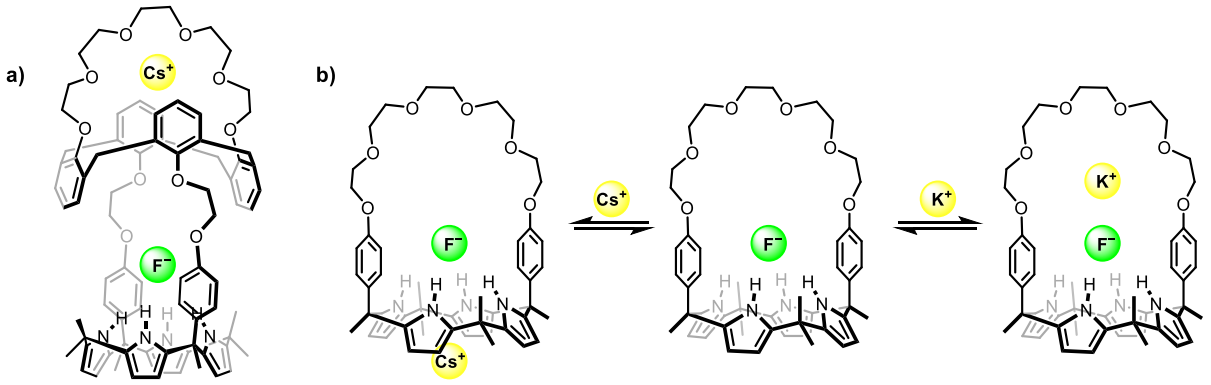

Figure 1.25 a) Sessler's calix[4]pyrrole-based receptor binding CsF as a host-separated ion-pair.[145] b) Sessler's receptor displaying switchable ion-pair binding modes: contact ion-pair with KF and host-separated ion-pair with CsF.[146]

1.4.2 Transition Metal Salt Binding

Yamato and co-workers reported a homooxacalix[3]arene appended with three triazole-linked pyrene units, which functions as a selective ratiometric sensor for the $Zn(H_2PO_4)_2$ ion-pair salt in 1000:1 CH_3CN/CH_2Cl_2 (Figure 1.26a).[147] Complexation of the receptor with Zn^{2+} via the basic triazole N led to enhancement of pyrene monomer emission with concomitant quenching of its excimer emission. However, the opposite (an increase in the excimer to monomer emission intensity ratio) was observed upon a further addition of $H_2PO_4^-$ to the Zn^{2+}-complexed receptor. In another example, Wang described the preparation of an ion-pair tripod consisting of anion binding imidazolium units and basic piperazines for transition metal cation coordination, appended with 1,8-naphthalamides as fluorescent reporter groups.[148] The receptor was found to be selective towards $Cu(ClO_4)_2$ and $Cu(NO_3)_2$, demonstrating significant fluorescence turn-on and blue-shift in emission upon addition of these two Cu^{2+} salts in CH_3CN (Figure 1.26b).

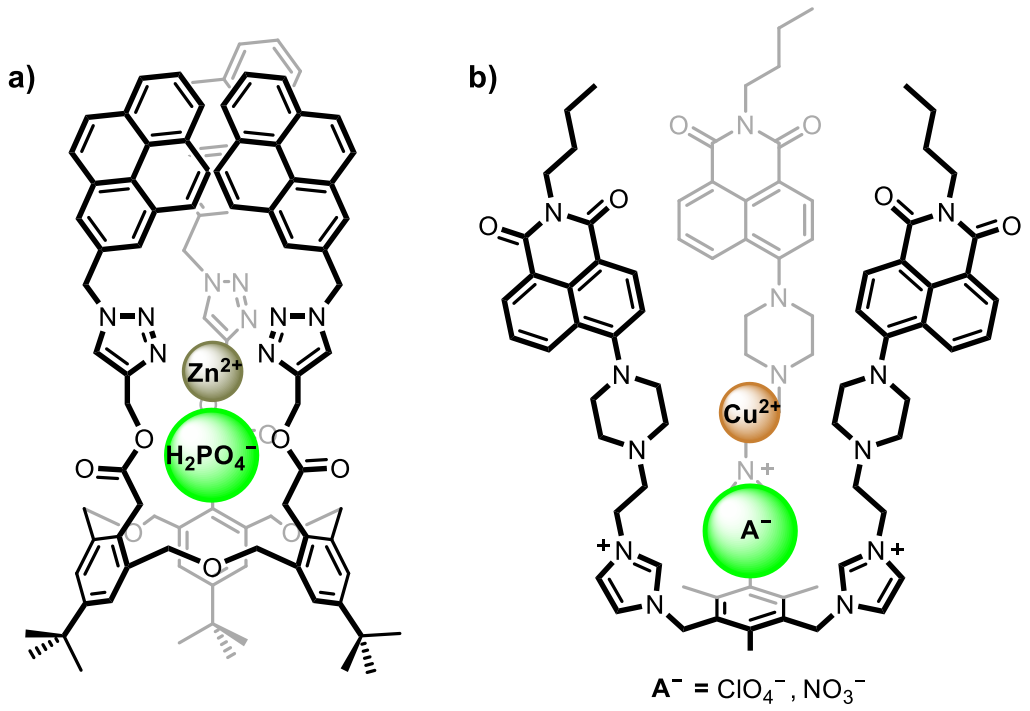

Figure 1.26 Yamato's ratiometric sensor forming ion-pair complex with Zn^{2+} and $H_2PO_4^-$.[147] Wang's tripod binding NO_3^- or ClO_4^- salt of Cu^{2+}.[148]

1.4.3 Organic Salt Binding

In contrast to metal salts, organic salts such as alkyl ammonium halides are arguably more challenging to selectively recognise due to their more diffused charge. To tackle this problem, Feng and Yuan reported a cyclo[6]aramides ion-pair receptor (Figure 1.27a) that contains six amide groups as the only functionality.[149] Intramolecular HB in the receptor framework involving four adjacent amides enforces their Lewis basic carbonyls to point towards the central cavity, constituting the cation binding site, while the remaining two amides can freely rotate and act as potential N–H HB donors to anions. The receptor was capable of binding dibutylammonium chloride in $CDCl_3$ with $K_a > 10^5\ M^{-1}$ in a pseudo-rotaxane fashion. Ballester and co-workers studied the ion-pair binding properties of a macrotricyclic receptor (Figure 1.27b), consisting of two calix[4]pyrroles separated by rigid linkers.[150] Interestingly, the host was found to form an ion-pair cascade complex in the presence of two equivalents of TBACl/TBAOCN, with one bound as contact ion pair and the other as

receptor-separated ion pair. This binding was found to be highly cooperative with a cooperativity factor of $>10^5$.

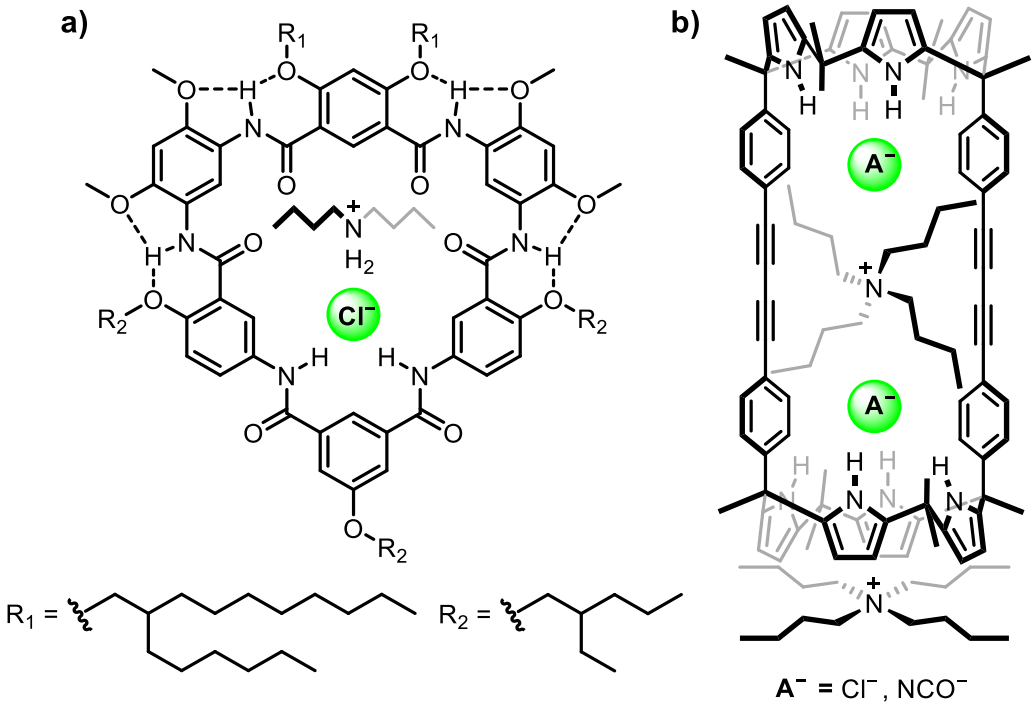

Figure 1.27 a) Feng and Yuan's cyclo[6]aramides binding dibutylammonium chloride as ion-pair.[149] b) Ballester's calix[4]pyrrole-based macrotricyclic receptor forming cascade ion-pair complex with TBACl or TBAOCN.[150]

1.4.4 Applications of Ion-Pair Receptors

The simultaneous binding of both cations and anions has promising applications in areas such as ion sensing, salt solubilisation, extraction and ion-pair membrane transport. In particular, the cooperative ion-pair binding exhibited by hetero-/multitopic receptors allows the further modulation of guest affinities and selectivities, giving them an extra advantage over monotopic host systems.

1.4.4.1 Sensing

By attaching appropriate reporting groups in the vicinity of a cation/anion binding site, ion-pair sensing can be achieved. For example, Romański reported a thiourea-based ion-pair receptor (Figure 1.28a), appended with a crown ether and a photo- and redox-active anthraquinone group.[151] By pre-complexing the receptor with Na^+, 3–4-

fold enhancement in the anion association constants of Cl^- and Br^- was observed in CH_3CN, as shown by UV–visible absorption titrations and cyclic voltammetric studies. Rurack and Costero appended both cation-complexing crown ether and anion binding calix[4]pyrrole to a boron-dipyrromethane (BODIPY) core (Figure 1.28b) and studied its ion-pair binding properties in CH_3CN.[152] UV-visible absorption and fluorescence experiments demonstrated, in addition to alkali halide salts, the receptor was capable of binding zwitterionic amino acids such as γ-aminobutyric acid (GABA).

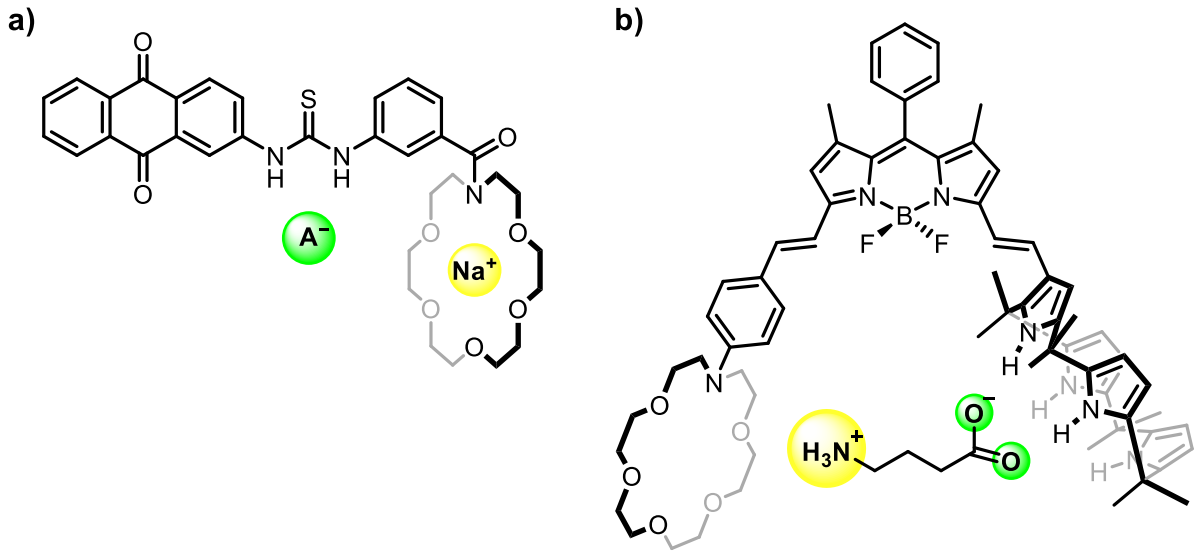

Figure 1.28 a) Romański's anthraquinone-appended ion-pair receptor.[151] b) Rurack and Costero's receptor with BODIPY core appended with crown ether and calix[4]pyrrole for binding of zwitterionic γ-aminobutyric acid (GABA).[152]

1.4.4.2 Salt Extraction

Efficient extraction and recovery of precious metal salts has huge potential in various industrial and environmental processes. White and Tasker reported a salen-based ligand with two pendant morpholine motifs (Figure 1.29a).[153] Upon exposing a $CHCl_3$ solution of the receptor to an aqueous solution of $CuSO_4$ at pH = 3.8, the organic phase turned brown immediately and ICP-AES analysis revealed a 100% loading of the salt by the receptor. The cationic Cu(II) was complexed by the salen core while SO_4^{2-} was bound by the protonated morpholine HB donors. In 2018, Piątek reported a

heteroditopic receptor (Figure 1.29b) that was prepared in three steps.[154] The presence of a co-bound K^+ at the appended crown-ether greatly enhanced the anion binding strength of the adjacent urea motif, with selectivity towards OAc^- in CH_3CN. This strong ion-pair binding preference of KOAc was further exploited in the first report of the successful extraction of the hydrophilic potassium salt from D_2O into $CDCl_3$ under liquid-liquid extraction conditions with near quantitative efficiency.

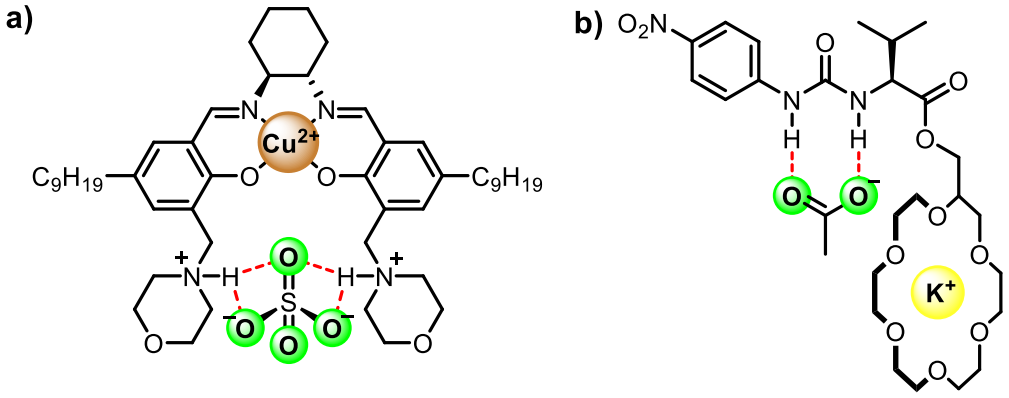

Figure 1.29 a) White and Tasker's salen-based ion-pair receptor capable of liquid-liquid extraction of $CuSO_4$ under acidic medium.[153] b) Piątek's urea-crown ether receptor binding KOAc as ion-pair.[154]

1.4.4.3 Membrane Transport

The selective recognition of ion-pair species by heteroditopic receptors has also facilitated their applications as transmembrane ion carriers. For example, de Mendoza reported a heteroditopic guanidinium-based crown ether ion-pair receptor for recognition and transport of zwitterionic amino acids (Figure 1.30a).[155] In a U-tube experiment, the chiral receptor dissolved in the central CH_2Cl_2 layer was capable of transporting tryptophan from the aqueous phase on one side (source phase) to the other (receiving phase), with an enantiomeric excess (% ee) of ca. 80%. In 2014, Jeong and co-workers prepared two mobile carriers (Figure 1.30b) capable of selectively transporting NaCl and KCl via M^+/Cl^- symport across a palmitoyl-2-oleoyl-sn-glycero-

3-phosphocholin (POPC) bilayer.[156] The efficiency of transporting the alkali metals correlates with strong cooperative salt binding in solution as contact ion-pairs.

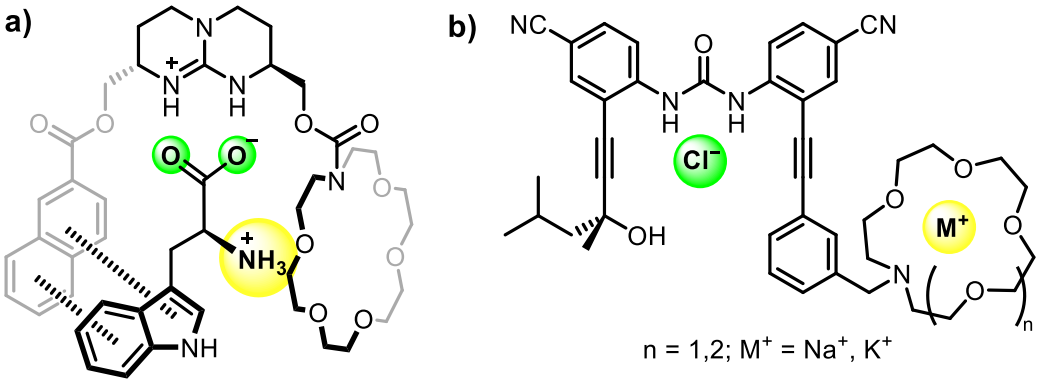

Figure 1.30 a) de Mendoza's receptor for transport of zwitterionic tryptophan.[155] b) Jeong's anion carrier capable of transporting NaCl and KCl via symport.[156]

1.5 The World of Mechanical Bonds

Paying close attention to daily objects, it is not difficult to notice signs of the ubiquitous mechanical bond. Ranging from the keychain (Figure 1.31a) in your wallet, necklace you wear, to the bicycle (Figure 1.31b) for commuting, the pervasiveness of this mechanical bond is simply astonishing.

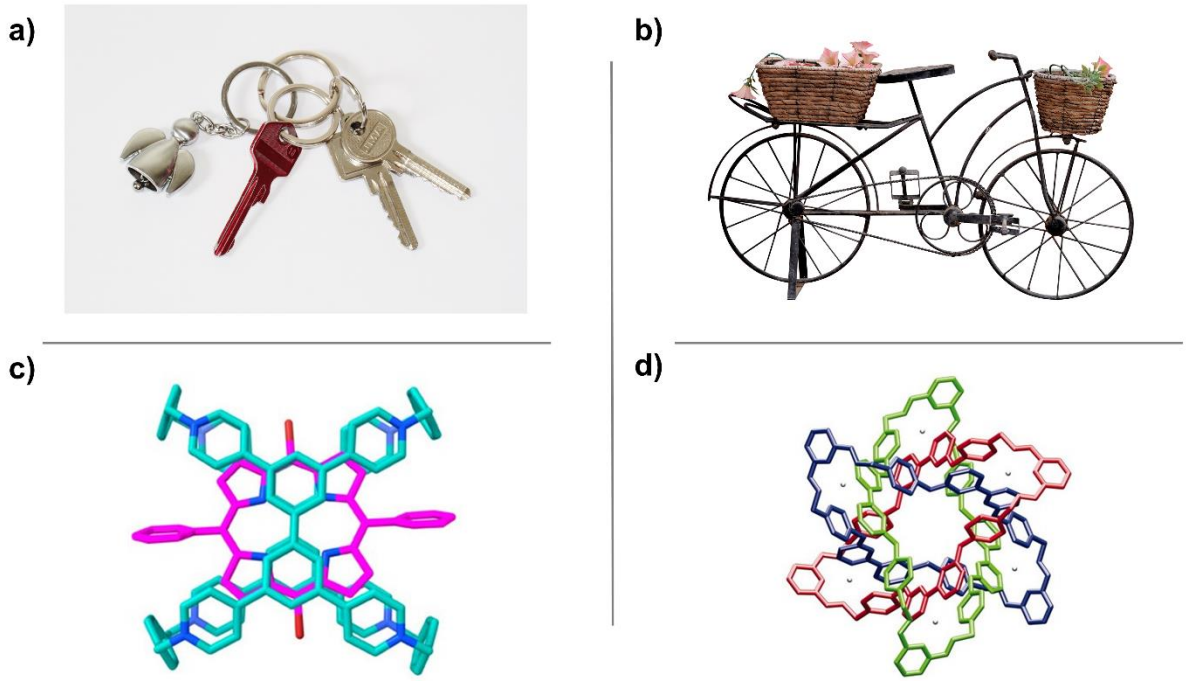

Figure 1.31 a) Interlocked key and keychains. b) Bicycle with many interlocked component parts. c) Crystal structure of suit[4]ane.[160] d) Crystal structure of Borromean rings.[162]

A mechanical bond has been aptly defined as "*an entanglement in space between two or more molecular entities such that they cannot be separated without breaking or distorting chemical bonds*".[157] In chemistry, rotaxanes and catenanes are the prototypical examples of molecules that possess mechanical bonds. Rotaxane, a compound word derived from the Latin *rota* (wheel) and *axis* (axle), consists of a macrocyclic ring threaded through by a linear axle component. Each end of the axle is capped with a bulky stopper to prevent the ring from slipping off. Catenane, derived from the Latin *catena* (chain), contains two topologically interlocked rings. These two

molecules fall under the umbrella of mechanically interlocked molecules (MIMs), which also include other notable members such as daisy chain,[158] handcuff catenane,[159] suitane (Figure 1.31c),[160] Solomon knot,[161] and Borromean rings (Figure 1.31d).[162]

1.5.1 Synthesis of MIMs

Originally stimulated by the synthetic challenge and potential intriguing molecular properties, over many years chemists have devised a variety of strategies to facilitate the preparation of MIMs. These include statistical/directed syntheses employed in the early days (Section 1.5.1.1) and later more efficient template methods (Sections 1.5.1.2 and 1.5.1.3).

1.5.1.1 Statistical and Directed Synthesis

In the 1960s, Wasserman and co-workers described the first statistical synthesis of [2]catenanes (Scheme 1.1).[163] By cyclising a large excess of bis-ester macrocyclic precursors via acyloin condensation in the presence of deuterated cycloalkane, the corresponding [2]catenane was isolated in 0.0001% yield after chromatographic purification.[164]

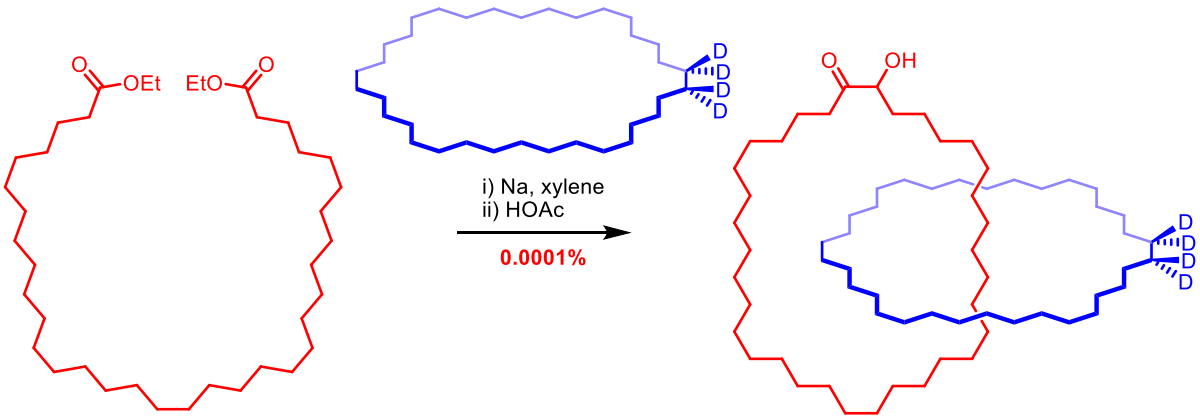

Scheme 1.1 Wasserman's statistical synthesis of [2]catenane.[163,164]

In later years, another method to construct interlocked structures known as directed synthesis was developed by Schill and Lüttringhaus.[165,166] This approach relied on cleavable covalent bonds to direct the threading necessary for the formation of mechanical bonds. Although this strategy gives a higher yields of interlocked products compared to the above-mentioned statistical method, it is characterised by long synthetic sequences. Nevertheless, this method is still employed by chemists in modern days to construct MIMs.

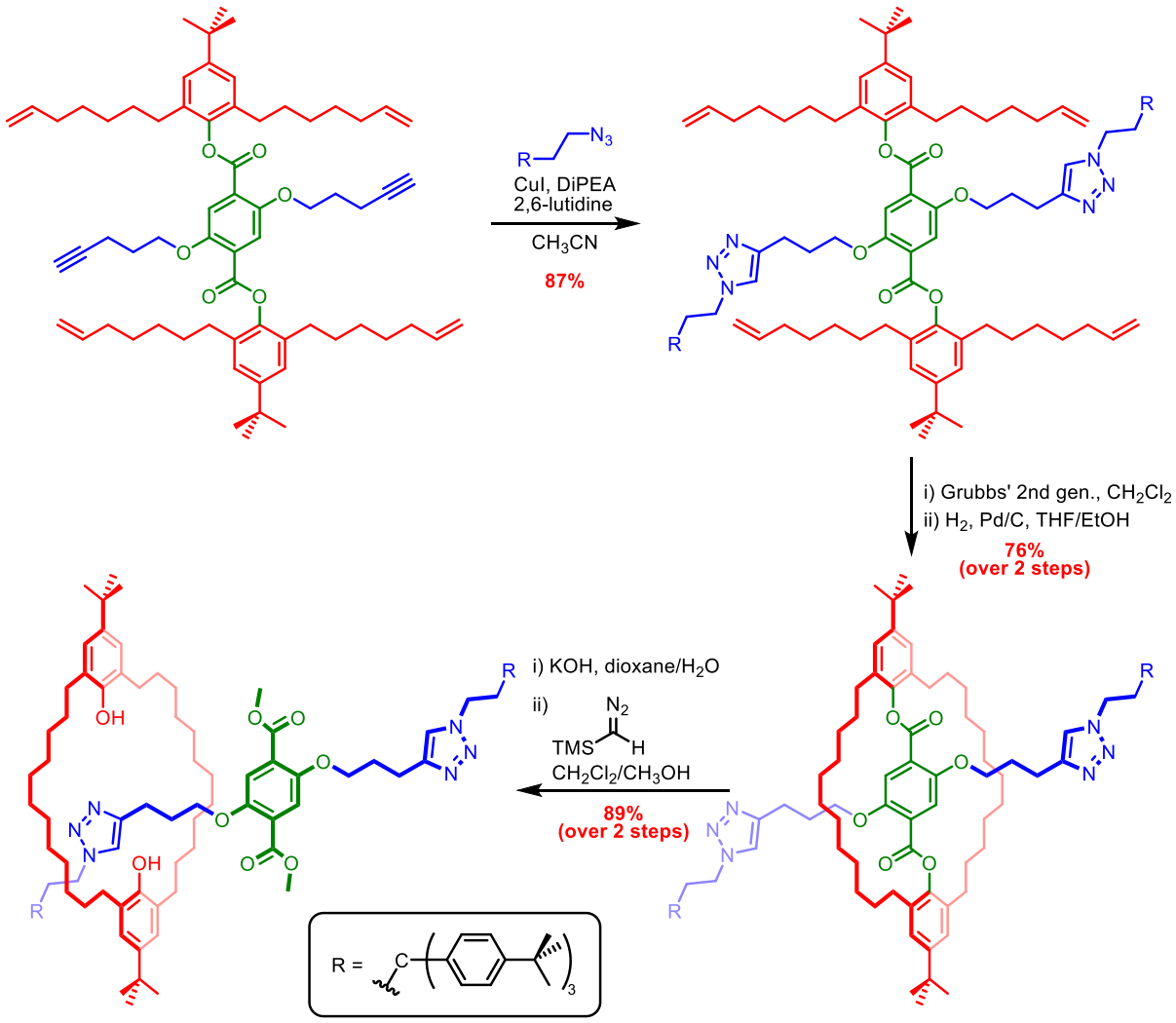

Scheme 1.2 van Maarseveen's directed synthesis of [2]rotaxane.[167]

In one example, van Maarseveen reported the synthesis of a [2]rotaxane using terephthalic acid as the covalent template (Scheme 1.2).[167] The bis-alkynyl

functionalised terephthalic acid was firstly esterified with two vinyl-appended phenols. Subsequent CuAAC end-capping with bulky stopper azide, followed by Grubbs' ring-closing metathesis (RCM) reaction between the appended vinyl groups afforded the [1]rotaxane. To liberate the macrocycle from the axle component, the ester linkers between the terephthalic core and the macrocycle were cleaved via saponification, yielding the [2]rotaxane.

These two classical approaches to making mechanical bonds granted access to some of the first examples of MIMs, prompted the development of more efficient template-directed synthesis of interlocked architectures.

1.5.1.2 Template-Directed Synthesis

The use of a templating agent facilitates the association of reagents in such a way as to favour the formation of interlocked over non-interlocked products. Through the use of suitable templates (e.g. cations, anions and ion-pairs), the yield of interlocked products can be drastically improved.

(A) Metal Cation Templation

The well-defined stereochemical coordination geometry of ligands around a transition metal centre facilitates the use of metal–ligand coordination to drive the preorganisation of precursors. This elegant concept was first demonstrated by Sauvage in 1983 in his pioneering synthesis of phenanthroline-based catenanes (Scheme 1.3).[168] The two phenanthroline cores of macrocyclic and acyclic precursors tightly wrap around the Cu(I) metal cation template in a tetrahedral geometry. Subsequent cyclisation using Williamson ether condensation afforded the [2]catenane in 42% yield, with Cu(I) being quantitatively removed via treatment with excess KCN.

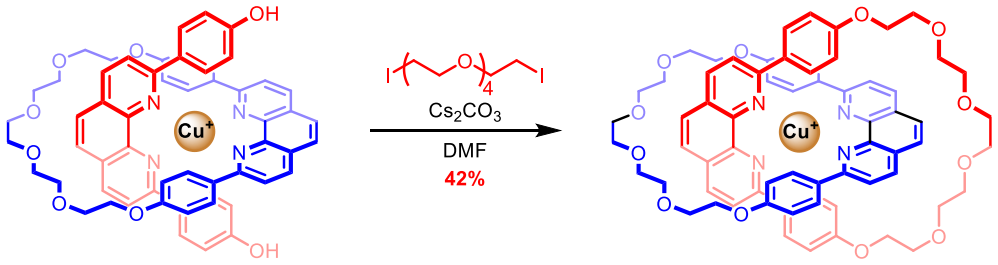

Scheme 1.3 Sauvage's Cu(I)-templated synthesis of [2]catenane.[168]

This report of the efficient synthesis of [2]catenanes completely revolutionized the field and a variety of transition metal template-directed syntheses of MIMs have been reported since.[169–174] For example, Siegel used Fe(II) and Ru (II) to template two terpyridine-functionalised macrocycle precursors together and subsequent double RCM cyclisation afforded the [2]catenanes (Scheme 1.4a).[175] In 2001, the capability of two 2,6-bis(benzylic imino)pyridine motifs to octahedrally coordinate to a wide range of transition metals (e.g. Mn(II), Fe(II), Co(II)) was exploited in the synthesis of [2]catenanes via single or double RCM reactions in yields of up to 81% (Scheme 1.4b).[176]

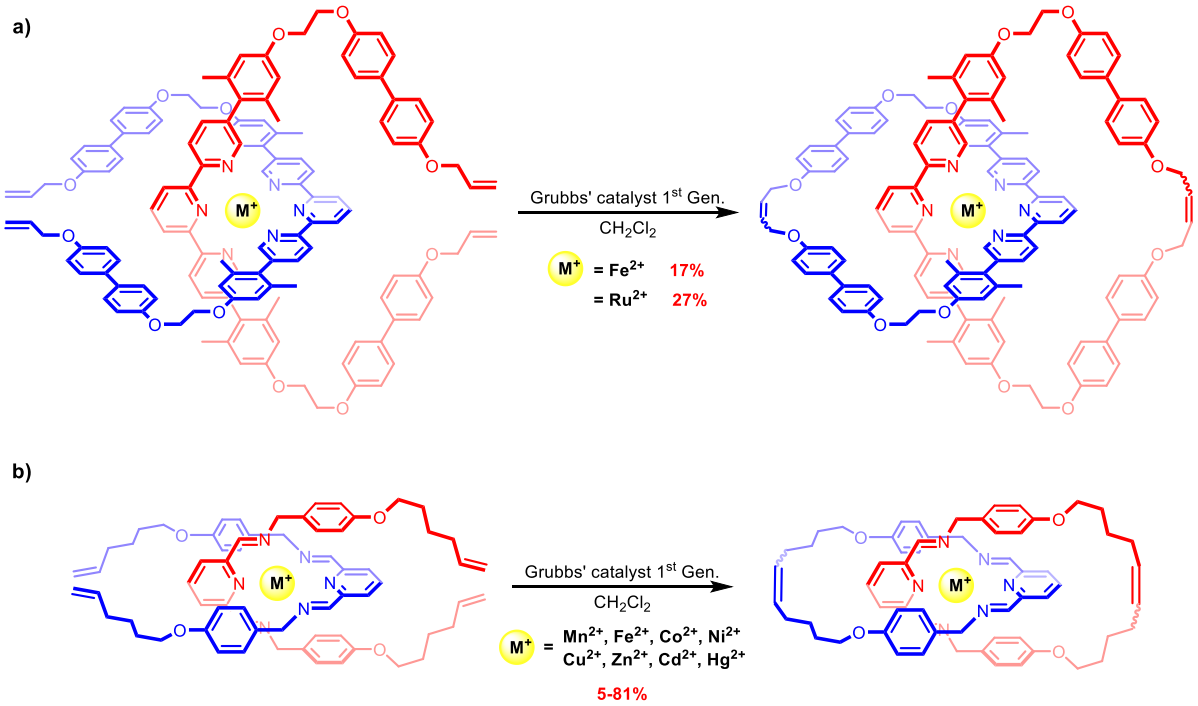

Scheme 1.4 a) Siegel's Fe(II)/Ru(II) template-directed synthesis of [2]catenane.[175] b) Leigh's synthesis of [2]catenane using a range of metal cations as passive template.[176]

In addition to transition metals, alkali metal cations have also been utilized as templates.[177] For example, capitalising on the affinities of diethylene glycols towards Na^+, Chiu reported the Na^+ templated synthesis (Scheme 1.5) of [2]rotaxanes[178] and [2]catenanes.[179]

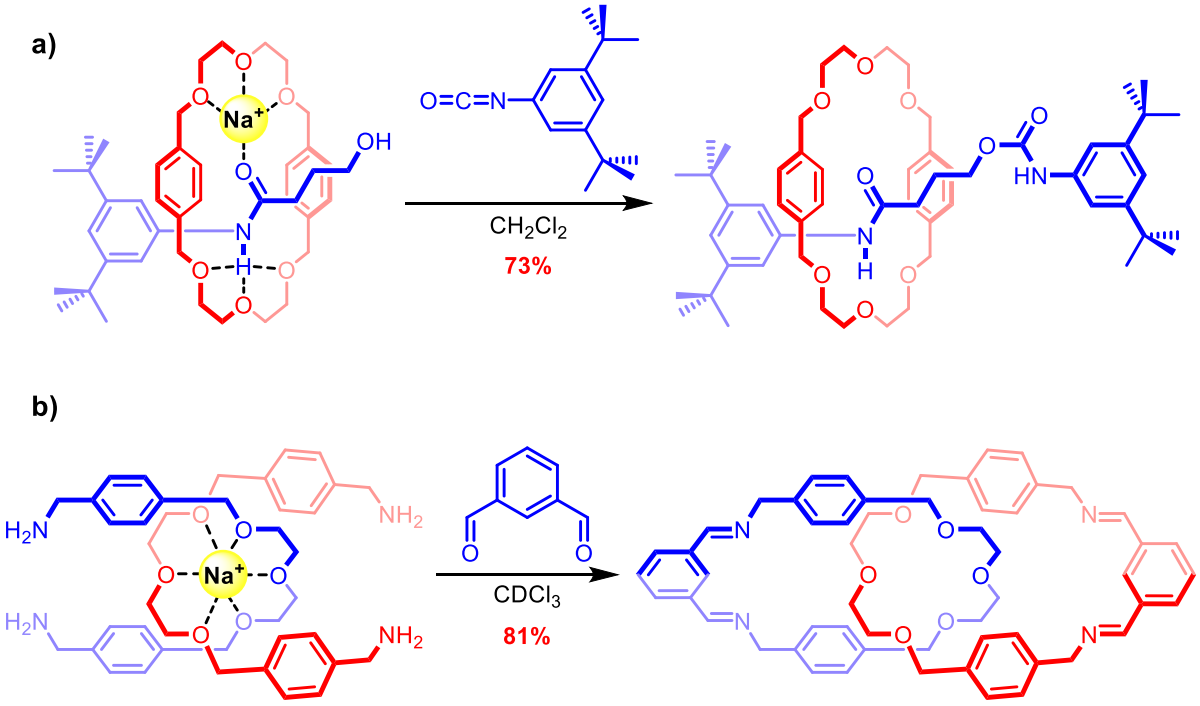

Scheme 1.5 Chiu's Na^+ templated synthesis of a) [2]rotaxane[178] and b) [2]catenane.[179]

(B) Anion Templation

Despite the challenges in recognising anions (Section 1.3.2), high yielding synthesis of MIMs using a negatively charged template was first demonstrated by Vögtle in 1999.[180] In their rotaxane synthesis, the bulky 4-tritylphenolate generated in situ is bound tightly by the tetralactam amide N–H macrocycle in CH_2Cl_2, blocking one face of the macrocycle and favouring the bromo axle precursor to approach the nucleophilic phenolate from the other side of the ring. By virtue of the strong phenolate oxygen affinity of the macrocycle, the [2]rotaxane was isolated in an excellent 95% yield (Scheme 1.6).

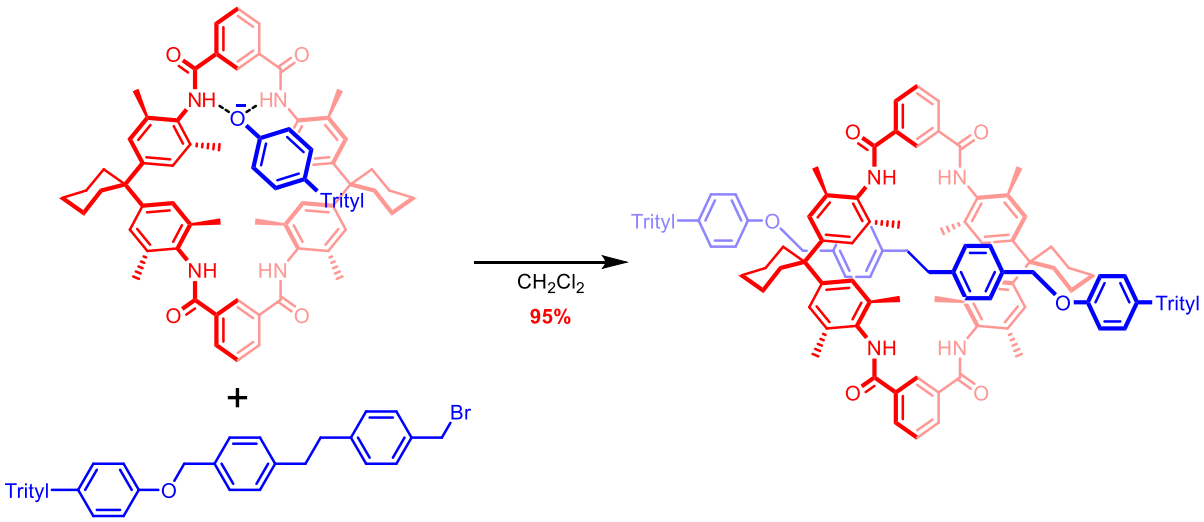

Scheme 1.6 Vögtle's first example of anion-templated synthesis of [2]rotaxane.[180]

A few years later, Beer reported the synthesis of a [2]rotaxane[181] and [2]catenane[182] utilising external halide anions as templates. This halide templation strategy in combination with the potent anion binding capability of XB donors, has recently led to a [2]rotaxane being prepared in 91% yield using a chloride template (Scheme 1.7).[183] In 2013, Flood and co-workers prepared a shape-persistent cyanostilbene macrocycle, which forms stable a 2:1 host-guest stoichiometric complex with phosphate utilising multiple convergent C–H hydrogen bonds.[94] Using a bis-alkynyl-functionalised phosphate template reagent, a [3]rotaxane containing two cyanostilbene macrocycles was synthesised after CuAAC-mediated stoppering reaction with bulky azides (Scheme 1.8). The initial reported yield was 24% but was later improved to 80% after optimising the reaction conditions.[184]

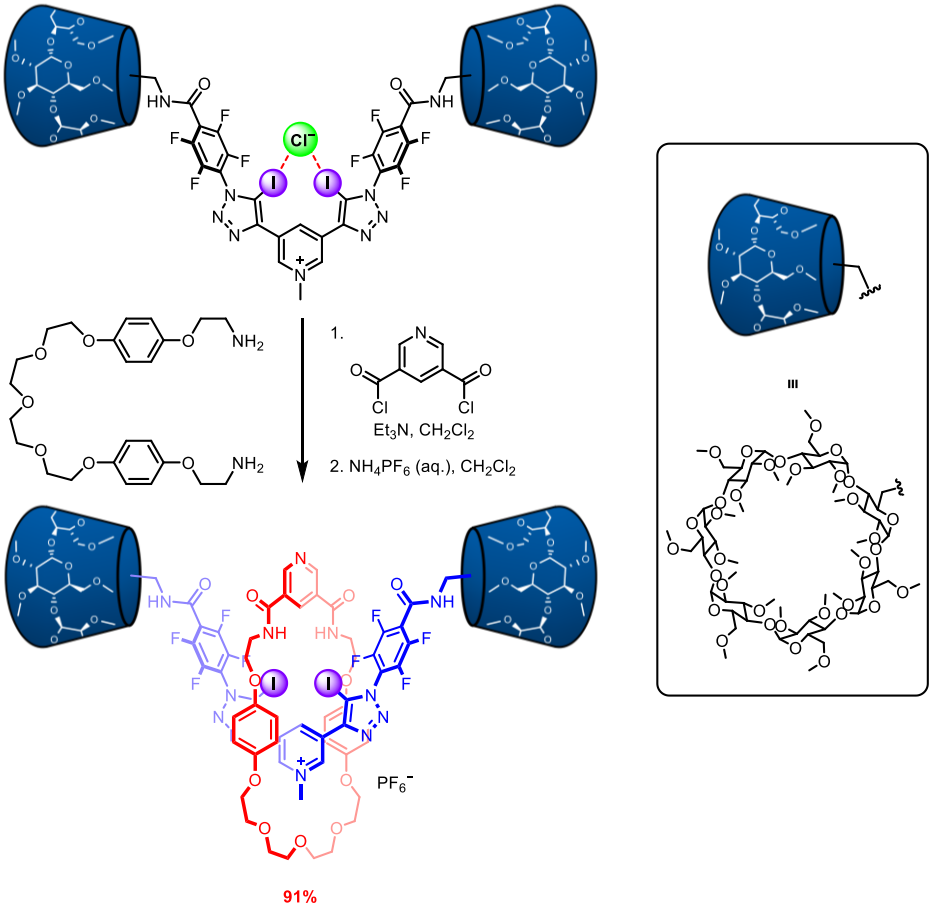

Scheme 1.7 Beer's anion-templated synthesis of [2]rotaxane via addition of Cl^-.[183]

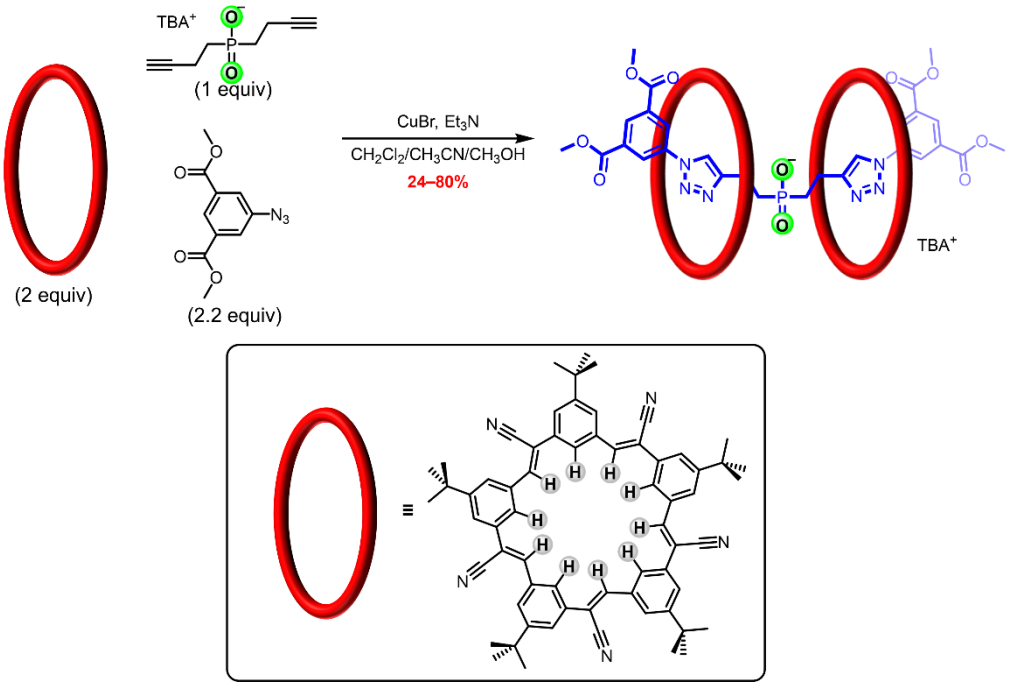

Scheme 1.8 Flood's synthesis of [3]rotaxane.[94,184]

(C) Ion-Pair Templation

Given the legion of MIMs constructed by cation and anion templates, one may question whether the same feat could be achieved via the use of an ion-pair template. However, this necessitates the presence of strong cation/anion binding motifs in the component parts of MIMs to stabilise the oppositely charged ions and prevent salt recombination. Unsurprisingly, examples of ion-pair template MIM syntheses in which both bound ions act synergistically, are scarce.

In one rare example reported by Leigh and co-workers in 2008 (Scheme 1.9), upon mixing a Pd(II)-complexed macrocycle and pyridinium chloride embedded axle, the ancillary CH_3CN ligand of Pd(II) is replaced by Cl^-, and the resulting negatively charged Pd(II)-macrocycle-Cl complex is held strongly at the axle pyridinium site, forming a pseudo-rotaxane assembly.[185] A subsequent CuAAC click stoppering reaction afforded the [2]rotaxane in 64% yield.

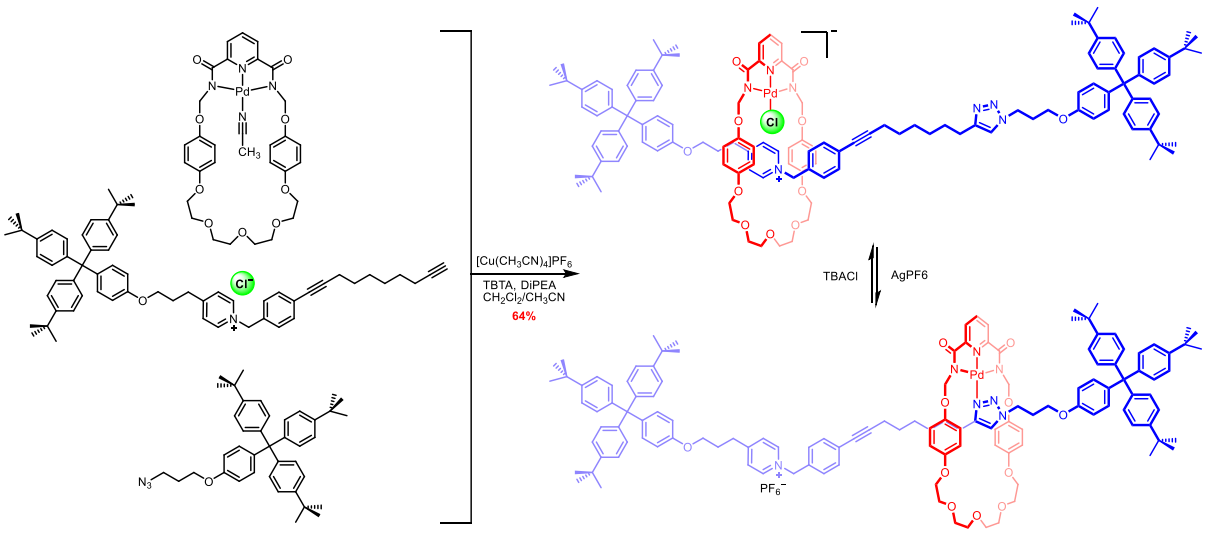

Scheme 1.9 Leigh's ion-pair templated synthesis of [2]rotaxane using pyridinium chloride functionalised axle precursor. Addition of $AgPF_6$ translocates the macrocycle from the pyridinium station to triazole station. This process could be reversed via addition of TBACl.[185]

Recently, Smith reported an alkyl ammonium-chloride ion-pair template preparation of a rotaxane (Scheme 1.10).[186] The macrocycle component was capable of

binding the quarternary ammonium chloride template using the electron-rich anthracene aromatic spacer groups for cation association in combination with amide HB interaction with chloride to prepare the [2]rotaxane, albeit in a low yield of 8%.

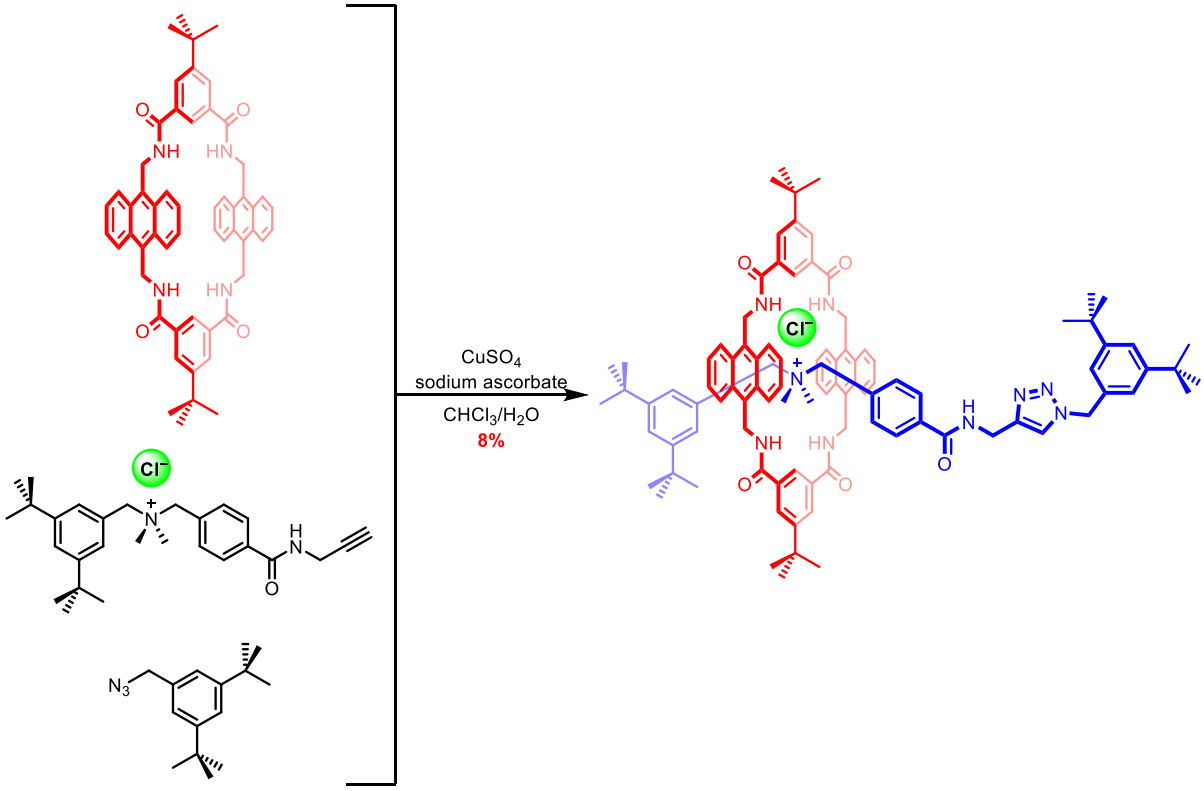

Scheme 1.10 Smith's ion-pair templated synthesis of [2]rotaxane with tetraalkylammonium chloride functionalised axle precursor.[186]

1.5.1.3 Active Metal Template Synthesis

Transition metals, in addition to forming strong metal–ligand coordinate bonds, possess rich catalytic properties. Exploiting these features, the active-metal template approach to MIM synthesis involves the utilisation of transition metal cations to both preorganise, in a passive template fashion (as in the Sauvage Cu(I) template preparation of a phenanthroline [2]catenane shown in Scheme 1.3), the precursors of MIMs and catalytically mediate mechanical covalent bond formation between the precursor components. This active metal template (AMT) strategy was first introduced by Leigh and co-workers in 2006 to synthesise rotaxanes (Scheme 1.11a).[187] Taking

advantage of the capability of pyridyl-containing macrocycles to bind Cu(I) endotopically, a CuAAC reaction between alkyne- and azide-terminated stoppers was found to occur through the ring annulus, leading to formation of [2]rotaxanes. This synthetic methodology proved to be very efficient and gave rise to rotaxanes in 94% yield when stoichiometric amounts of Cu(I) were used, or 82% yield when 20 mol% of Cu(I) was used. Later, this CuAAC-AMT method was extended by the same group to synthesise [2]catenanes (Scheme 1.11b).[188]

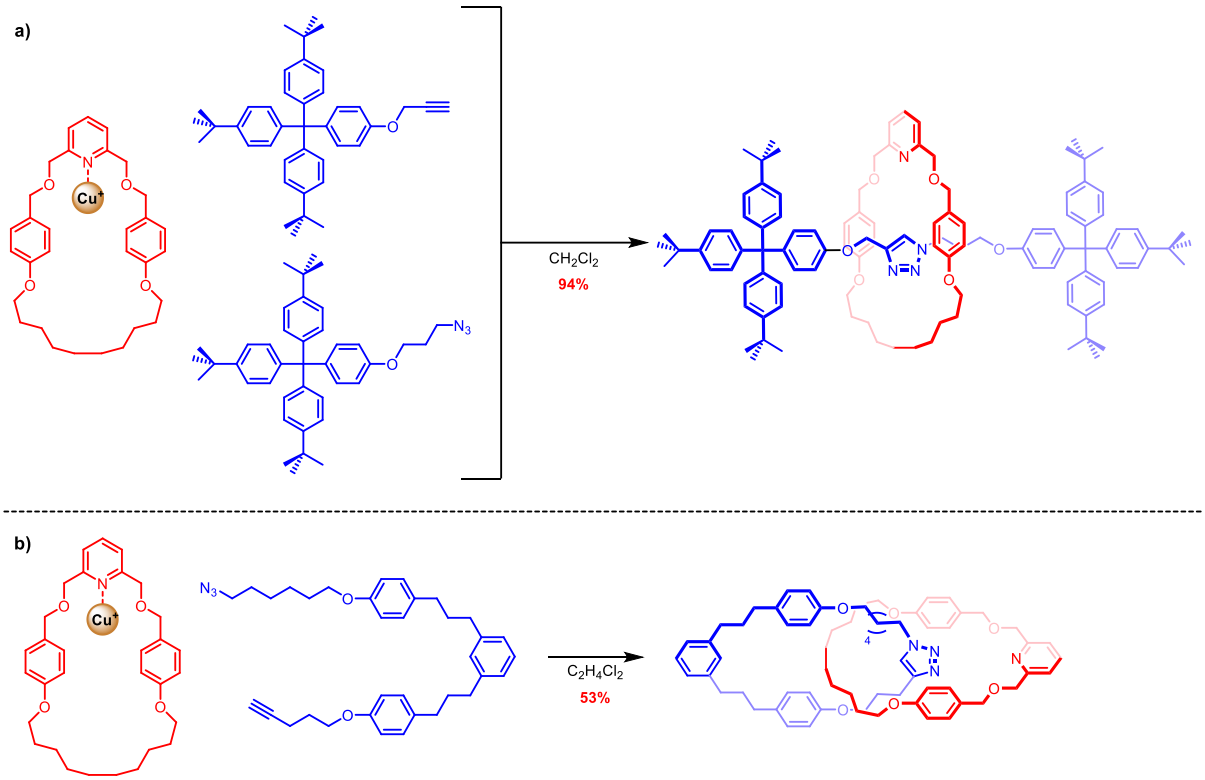

Scheme 1.11 Leigh's CuAAC-mediated active metal template synthesis of a) [2]rotaxane[187] and b) [2]catenane.[188]

In addition to Cu(I), other metals such as Ni(II),[189,190] Pd(II)[191–193] and Zn(II)[194] have also been utilised in analogous active template synthesis of MIMs. In one example (Scheme 1.12), Leigh and co-workers reported a quantitative active template formation of [2]rotaxanes utilising successive Michael additions of ethyl cyanoacetate to vinyl ketone terminated stoppers, promoted by a Pd(II)-chelated macrocycle.[193]

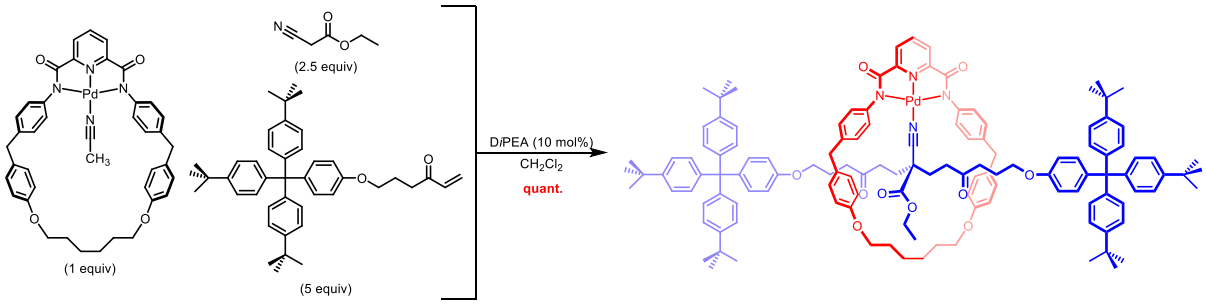

Scheme 1.12 Leigh's active template synthesis of [2]rotaxane utilising Pd(II)-catalysed Michael addition reaction.[193]

1.5.2 Applications of MIMs

With the numerous synthetic strategies developed to produce sufficient amounts of MIMs for investigation, the field has progressed from pure aesthetic interest to functionalising MIMs for wide scope of applications, including molecular switches and machines, catalysis and molecular recognition.

1.5.2.1 Molecular Switches

Molecular switches are bistable rotaxanes or catenanes in which the macrocycle can reside at either one or the other 'station' (recognition sites) located on the axle (rotaxanes) or macrocycle (catenanes). The population of rings at each station can be biased via the use of external stimuli, such as redox, light, charged species and acid/base.

Stoddart reported a [2]catenane (Scheme 1.13) consisting of electron-deficient tetracationic cyclo-bis(paraquat-*p*-phenylene) ($CBPQT^{4+}$) and another macrocycle with two electron-rich stations – tetrathiafulvalene (TTF) and 1,5-dioxynaphthalene.[195] In the reduced state (neutral TTF), the $CBPQT^{4+}$ preferentially resides at the TTF station. Upon chemical or electrochemical oxidation of TTF to $TTF^{+/2+}$, the Coulombic repulsion between paraquat and $TTF^{+/2+}$ drives the shuttling process such that the electron-poor $CBPQT^{4+}$ occupies the 1,5-dioxynaphthalene site.

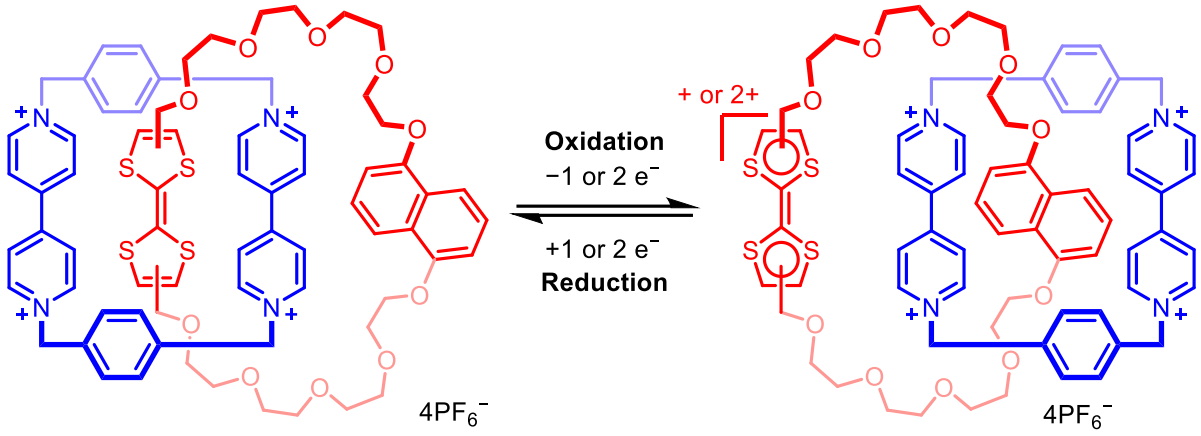

Scheme 1.13 Stoddart's molecular switch capable of redox and chemical induced shuttling.[195]

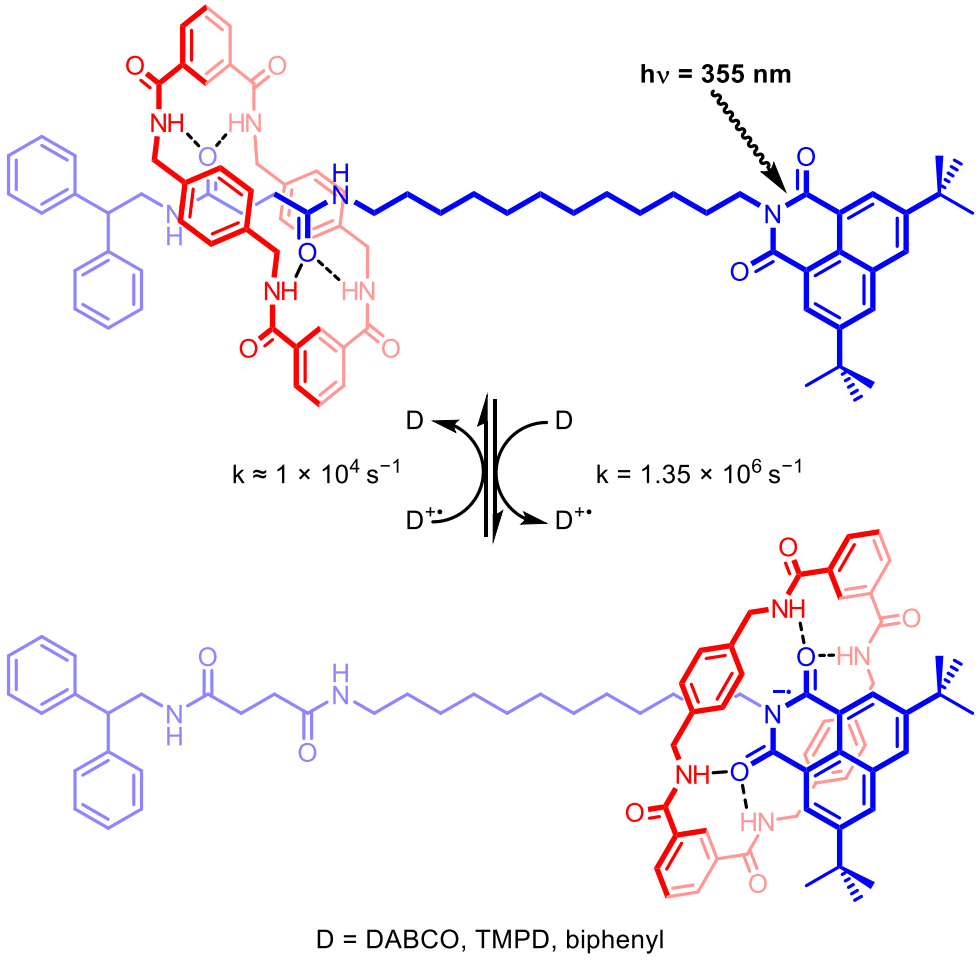

Scheme 1.14 Leigh's [2]rotaxane displaying photo-induced shuttling.[196]

Leigh and co-workers demonstrated that light can also be utilised as a stimulus to drive translational motion in MIMs.[196] They prepared a [2]rotaxane (Scheme 1.14) consisting of tetralactam macrocycle (HB donors) and axle made up of succinimide

and naphthalimide stations (HB acceptors). In the ground state, the macrocycle resides at the succinimide site due to formation of two intercomponent HB interactions. Upon photo-induced reduction of naphthalimide using 1,4-diazabicyclo[2.2.2]octane (DABCO) as electron donor in CH_3CN, the macrocycle shuttles to the naphthalimide radical anion station, and moves back to the original site after charge recombination.

1.5.2.2 Catalysis

The incorporation of catalytically active sites into the component parts of MIMs allows the preparation of supramolecular catalysts with unique dynamic character.[197] For example, Leigh reported a bistable [2]rotaxane that functions as an organocatalyst, controlled via addition of acid or base (Scheme 1.15).[198] The interlocked molecule consists of a dibenzo-24-crown-8 macrocycle and an axle component composed of a catalytically active dibenzylamine motif flanked by two triazolium groups. In the protonated state, the crown ether preferentially resides at the axle ammonium station, thereby sterically hindering the reactants from approaching the secondary amine active site. Upon deprotonation to amine, the crown ether ring translocates to the preferred triazolium station, exposing the amino group and allowing it to catalyse the Michael addition of aliphatic thiol to *trans*-cinnamaldehyde.

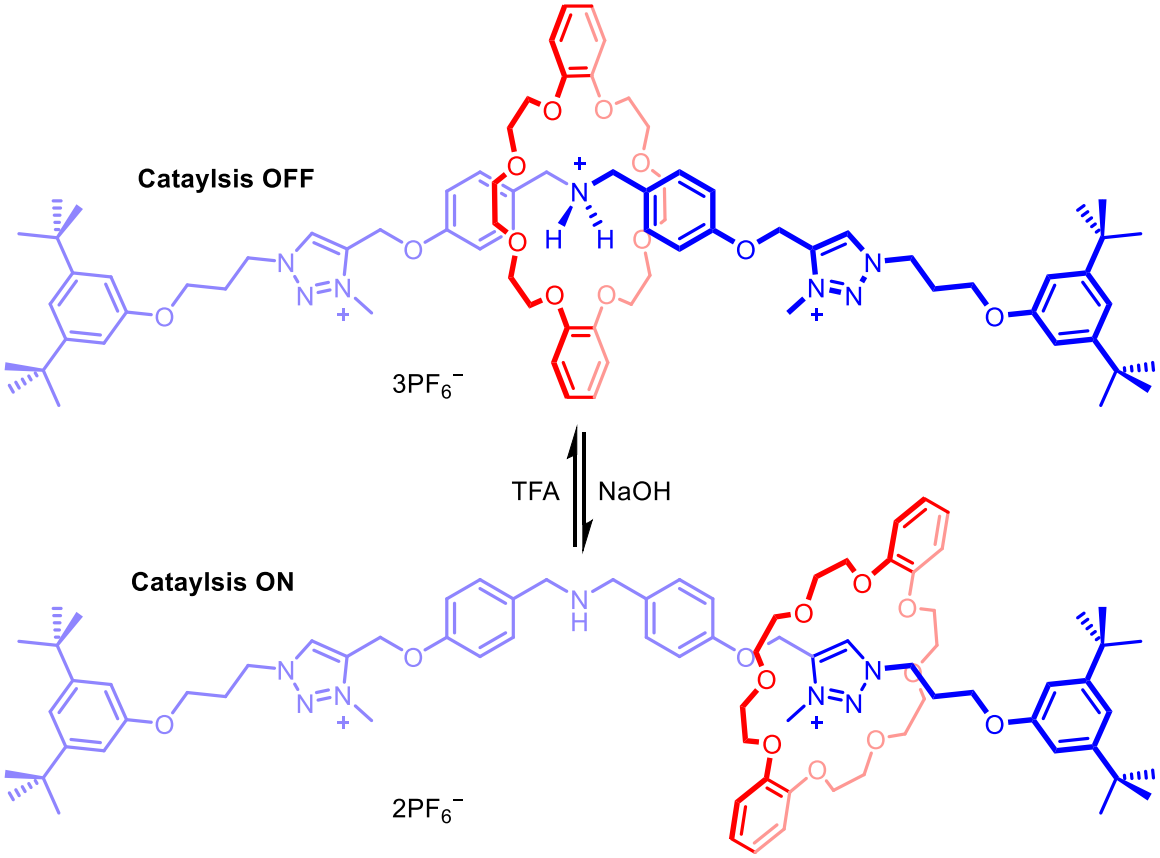

Scheme 1.15 Leigh's acid/base-switchable [2]rotaxane catalyst.[198]

1.5.2.3 Molecular Recognition

By virtue of their unique shielded three-dimensional cavities, MIMs have been demonstrated to exhibit superior cation and in particular anion selective recognition properties compared to non-interlocked acyclic and macrocyclic host analogues.[199–202] In 2019, Goldup and Rossler prepared a series of [2]rotaxane hosts (Figure 1.32) with tri-, tetra- and pentadentate nitrogenous donors around decorating the interlocked binding pockets.[203] The rotaxane hosts' sterically congested three-dimensional binding sites enforced unusual metal cation coordination, such as the formation of penta-coordinated Ni(II) or Co(II). In addition to transition metals, Ghosh and co-workers reported the synthesis of a [2]catenane for the recognition of Eu^{3+} and Gd^{3+} (Figure 1.33).[204] Binding of the trivalent lanthanide ions by the interlocked host was

found to be mediated by the two 1,10-phenanthroline-bis-ester motifs located on each of the two interlocked macrocycles.

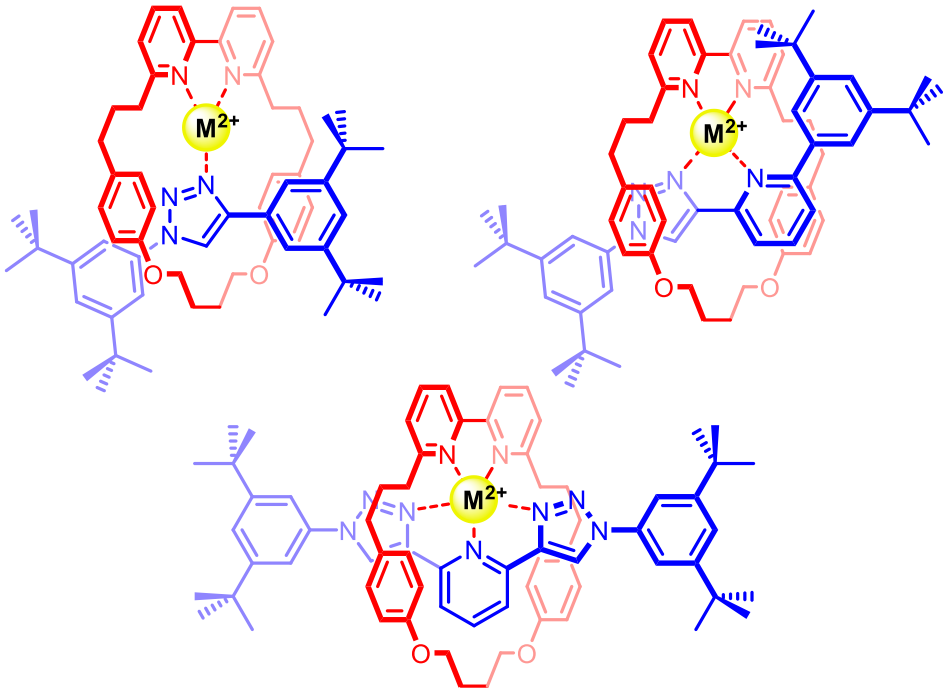

Figure 1.32 Goldup's tri-, tetra- and pentadentate [2]rotaxane binding a range of transition metal ions.[203]

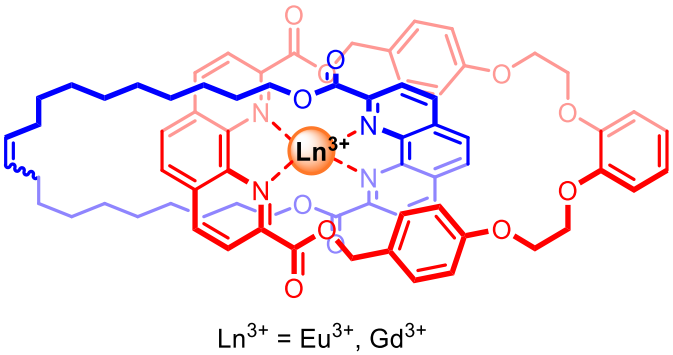

Figure 1.33 Ghosh's lanthanide-binding [2]catenane.[204]

1.6 Project Outline

Influenced by the promising and contrasting anion binding properties exhibited by the relatively few XB and ChB donor host systems reported to date (see Sections 1.3.4.2 and 1.3.4.3), the theme of this project was to design and synthesise a range of novel σ-hole based macrocyclic and interlocked host molecules for cation, anion and ion-pair recognition investigation.

Chapter 2: This chapter seeks to study the fundamental charged guest binding properties of an unprecedented family of σ-hole [2]rotaxanes consisting of tri- or tetra-dentate XB/ChB donors lining the interlocked host cavities. These rotaxanes are prepared via an active metal template CuAAC-mediated MIM synthetic methodology utilising appropriate azide and alkyne axle coupling partners. The anion and cation binding properties of these receptors are explored, followed by preliminary ion-pair recognition studies with metal halide salts.

Chapter 3: The chapter describes the incorporation of photo- and redox-active reporter groups into XB macrocyclic and rotaxane receptor frameworks for anion sensing investigations. This entailed the initial preparation of XB strapped porphyrins followed by the construction of XB BODIPY-porphyrin [2]rotaxanes via an active metal templation strategy. The dual optical- and electrochemical anion sensing properties of these BODIPY-porphyrin interlocked hosts is investigated using fluorescence and voltammetric techniques.

Chapter 4: The use of XB and ChB donors to mediate ion-pair recognition in heteroditopic phenanthroline-based macrocyclic systems is explored and discussed in this chapter. The preparation of the target heteroditopic macrocycles is first described, followed by investigation into their capability to bind lithium halide salts as ion-pairs

in organic media. In addition, the synthesis of the first examples of all-XB neutral tritopic [2]catenanes via adaptation of an alkali metal cation template strategy is described. The ion-pair recognition properties of these interlocked systems in organic solvents are investigated. Finally, the application of these ditopic/multitopic σ-hole macrocyclic and interlocked catenane receptors in salt solubilisation is also studied by extraction experiments.

Chapter 2

Halogen Bonding and Chalcogen Bonding Rotaxanes for Recognition of Charged Species

Chapter 2 Halogen Bonding and Chalcogen Bonding Rotaxanes for Recognition of Charged Species

2.1 Introduction

Halogen bonding (XB) and chalcogen bonding (ChB) are the attractive interactions between electron-deficient atoms of Groups 17/16 respectively and Lewis bases.[9,34] The electrophilicity of the halogen and chalcogen atoms originate from the anisotropic distribution of their electron density induced by covalently attached electron-deficient molecular fragments, resulting in confined regions of diminished electron density (σ-holes) along the extension of the covalent bonds.[13] Compared with hydrogen bonding (HB), these two unconventional interactions feature comparable anion binding strength but with more stringent preference for linearity due to the locality of the σ-holes.[14] These attributes are desirable to exploit in the design of preorganised anion receptors with spatially well-defined binding sites.

While the halogen atom is limited to the possession of one σ-hole, the divalent character of a chalcogen donor allows the accommodation of up to two σ-holes, conferring a more diversified anion complexation geometry for ChB receptors.[205] Furthermore, the strength of ChB is intimately related to the intrinsically more electropositive nature of chalcogen atoms relative to halogen atoms, and is influenced by the identity of their covalently appended substituents, giving ChB potentially a greater degree of tunability in anion affinity. Despite these advantageous properties of ChB, the application of such interactions in anion recognition is still largely in its infancy,[119,121,122,125–127,206–208] partly due to the inherent chemical instability of the heavier ChB donor motifs.[118–120]

One consequence of the formation of electrophilic σ-holes in halogen and chalcogen atoms is the amplified electron density in their encompassing regions, which can conceivably interact with Lewis acids. Indeed, solid state crystal structure evidence demonstrates the amphoterism of polarised iodine[209–212] and tellurium[213,214] atoms simultaneously behaving as Lewis acids and bases, with notable preferences towards "soft" metal cations such as Ag(I), Hg(II) and Pd(II).

In this context of amphoteric Lewis acid and base σ-hole molecular recognition, this chapter describes the incorporation of multiple convergent iodo- and telluro-triazole donor motifs into [2]rotaxane host frameworks and study of their anion, cation and ion-pair binding behaviours. The topologically interlocked host architecture serves to provide a highly shielded and preorganised recognition environment,[199,201,215] envisaged to preserve and strengthen the attractive σ-hole non-covalent interactions between the rotaxane's polarised iodine/tellurium atoms and charged guest species.

The CuAAC-mediated active metal template (AMT) mechanical bond forming synthetic protocol[216–218] employed to prepare the target XB/ChB [2]rotaxanes is introduced in the following section.

2.1.1 CuAAC-Mediated Active Metal Template (AMT) Synthesis of Mechanically Interlocked Structures

Active metal template synthesis is a versatile methodology used to access a myriad of interlocked structures. In a typical AMT reaction, a catalytically active metal cation endotopically coordinated to a macrocyclic ligand facilitates the covalent bond formation between axle precursors through the ring cavity, thereby capturing the final interlocked rotaxane structure (Scheme 2.1a).[218] In principle, the concept of AMT can be applied to any metal cation capable of the dual role of preorganising the axle

precursor fragments and catalysing the covalent bond coupling reaction between them. Indeed, active template synthesis of rotaxanes and catenanes has been realised with Cu(I),[187,188,219] Ni(II),[189,190,220] Zn(II),[194] and Pd(II)[191–193] via various kinds of organic coupling reactions. In particular, the CuAAC "click" reaction between azide- and alkynyl-functionalised axle precursor stopper units is by far the most widely employed coupling reaction in AMT by virtue of its mild reaction conditions, excellent yields and high functional group tolerance.[217]

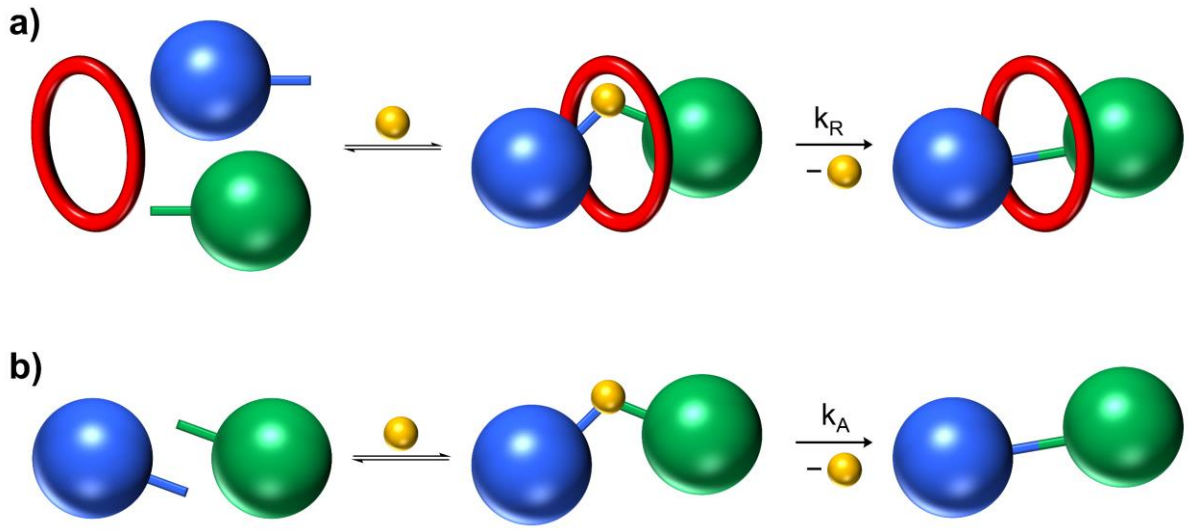

Scheme 2.1 Schematic representations of a) active metal template synthesis of [2]rotaxane and b) axle formation. Yellow sphere: catalytically ative metal cation; blue and green dumbells: axle precursors; red ring: macrocycle. (k_R and k_A represent the reaction rate constants for [2]rotaxane and axle formation respectively)

2.1.1.1 Kinetic Considerations of AMT

In traditional passive metal templation for MIM construction, pioneered by Sauvage, the yield of interlocked product depends largely on the thermodynamic stability of the preorganised pseudorotaxane assembled complex, that consists of the macrocycle, metal cation and axle precursor. In contrast, the AMT approach is to a greater extent kinetically driven,[218] with the ratio of interlocked to non-interlocked products determined by the relative rates of rotaxane (k_R) and axle (k_A) formation (Scheme 2.1). Detailed kinetic studies conducted by the pioneering group of this

methodology, Leigh and co-workers, revealed that CuAAC reactions catalysed by the free and unbound Cu(I) in the bulk solvent proceed significantly faster than those mediated by the Cu(I) endotopically immobilised by a macrocycle ($k_A > k_R$).[221] This was attributed to the necessity of the Cu(I)-catalysed triazole-forming reaction in the latter to occur through the sterically encumbered ring cavity. In addition, metal chelation by the macrocycle was postulated to disfavour certain reactive pathways of CuAAC reaction by limiting the geometric variation of the metal centre, forcing the coupling reaction to proceed via a slower mechanism. Therefore, the presence of even a small amount of unbound Cu(I) in the solution can adversely impact the yields of rotaxane by promoting the formation of non-interlocked axle. In other words, the rotaxane yields in CuAAC-AMT reaction can be improved by utilisation of macrocycles capable of strong Cu(I) coordination.

2.1.1.2 Macrocycle Structure Variation

To investigate how the structure of the macrocycle influences the AMT synthetic efficacy of rotaxanes, Leigh and co-workers prepared a series of pyridyl-based macrocycles with varying nature and number of donor atoms, and subjected them to the standard CuAAC-AMT conditions (see Figure 2.1).[221] In general, mono- and bi-dentate pyridyl macrocycles possessing relatively unhindered metal cation binding sites were capable of producing the corresponding [2]rotaxanes in reasonable yields (13–60%). In contrast, tri-dentate donor macrocycles inhibited the AMT reaction by preventing the simultaneous chelation of both azide and alkyne stopper axle precursor units to the Cu(I) metal centre.

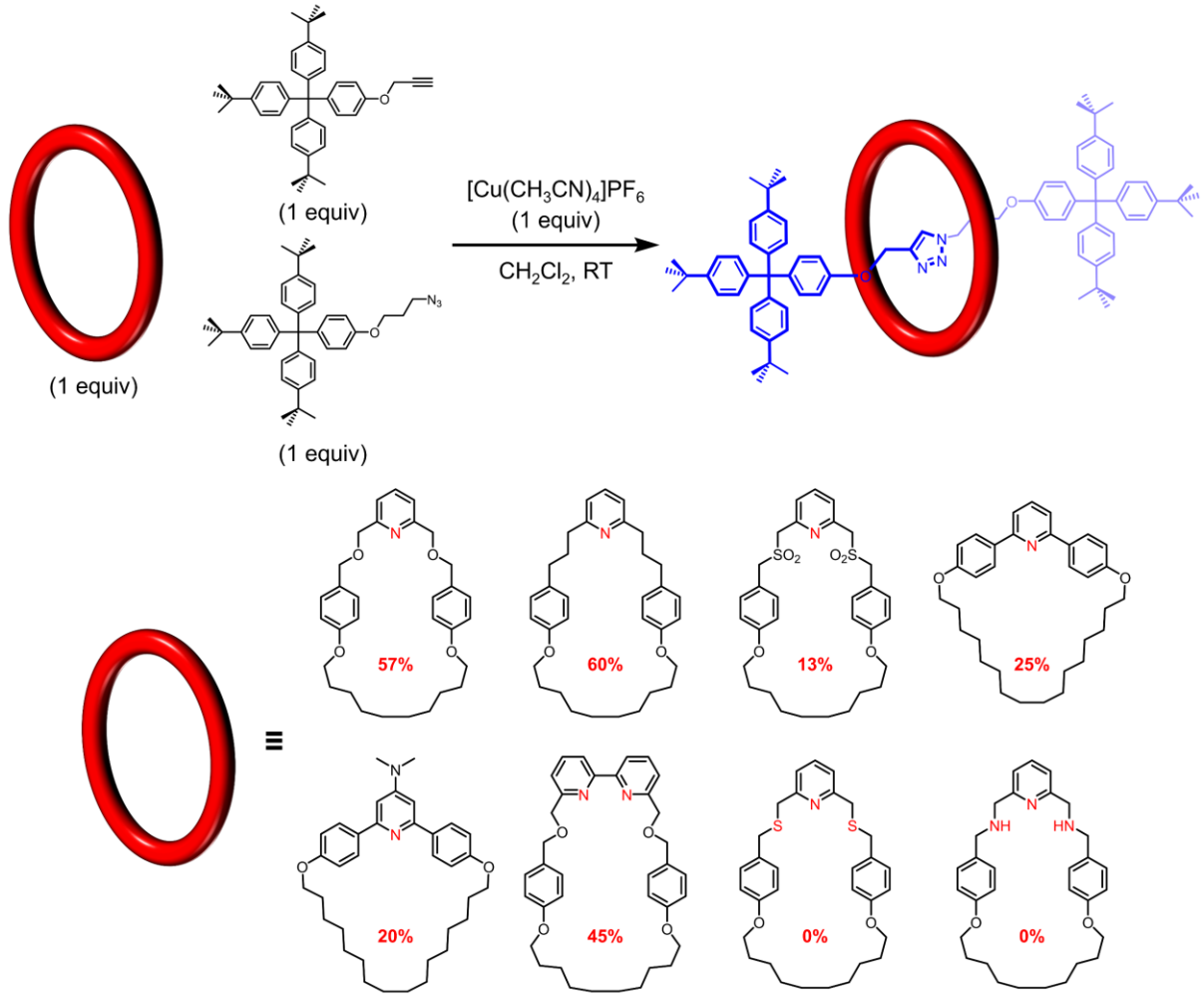

Figure 2.1 Effect of macrocycle structures on the yields of [2]rotaxane in CuAAC-AMT reaction.[221] The percentage yields are indicated in red. Reaction conditions: macrocycle (1 equiv), stopper azide (1 equiv), stopper alkyne (1 equiv), $[Cu(CH_3CN)_4]PF_6$ (1 equiv), CH_2Cl_2, RT, 24–72 hours, [macrocycle] = 10 mM. (Donor atoms of macrocycles are highlighted in red)

Furthermore, the size of the macrocycle also strongly affects the rotaxane yields in AMT reactions. Goldup and co-workers systematically varied the length of the alkyl linker of bipyridyl macrocycles and investigated their efficacy in mediating CuAAC-AMT rotaxane synthesis (Scheme 2.2).[222] A decrease in macrocyclic ring size was found to increase the isolated yields of [2]rotaxanes, with practically quantitative conversion of all axle precursors into interlocked structures observed for the smallest macrocycle (n = 2) studied.

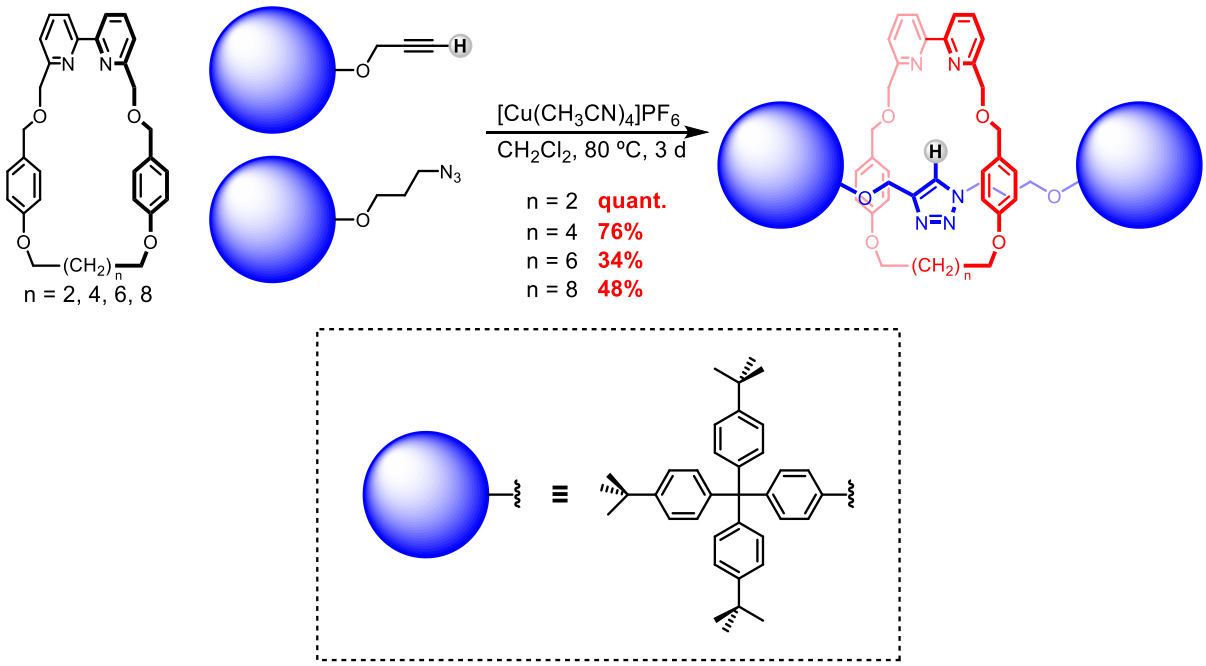

Scheme 2.2 Effect of macrocycle size on the yield of [2]rotaxane in CuAAC-AMT reactions.[222]

2.1.1.3 Effect of Increasing Macrocycle:Cu(I) Ratios and Mechanistic Insights

Recognising the fact that any unbound Cu(I) may efficiently facilitate "unproductive" non-interlocked axle forming CuAAC reactions, to circumvent this an excess of macrocycle would ensure all the Cu(I) in the reaction mixture was sequestered. Indeed, by increasing the amount of macrocycle from 1 to 10 equivalents in the presence of 1 equivalent of Cu(I), Leigh and co-workers observed a significant increase in the isolated yield of [2]rotaxane (from 57% to 90%) (Scheme 2.3).[221] Interestingly, the CuAAC-AMT reaction in the presence of excess macrocycle was found to proceed much more slowly than when a stoichiometric amount of macrocycle was employed; the reaction time increased from 24 to 72 hours to go to completion. In addition, the corresponding [3]rotaxane, which was not observed previously, was isolated in 5% yield. The lower reaction rate, together with the formation of [3]rotaxane, strongly hinted at the involvement of a bimetallic Cu(I) complex as the reactive intermediate in the CuAAC-AMT reactions (Scheme 2.4).

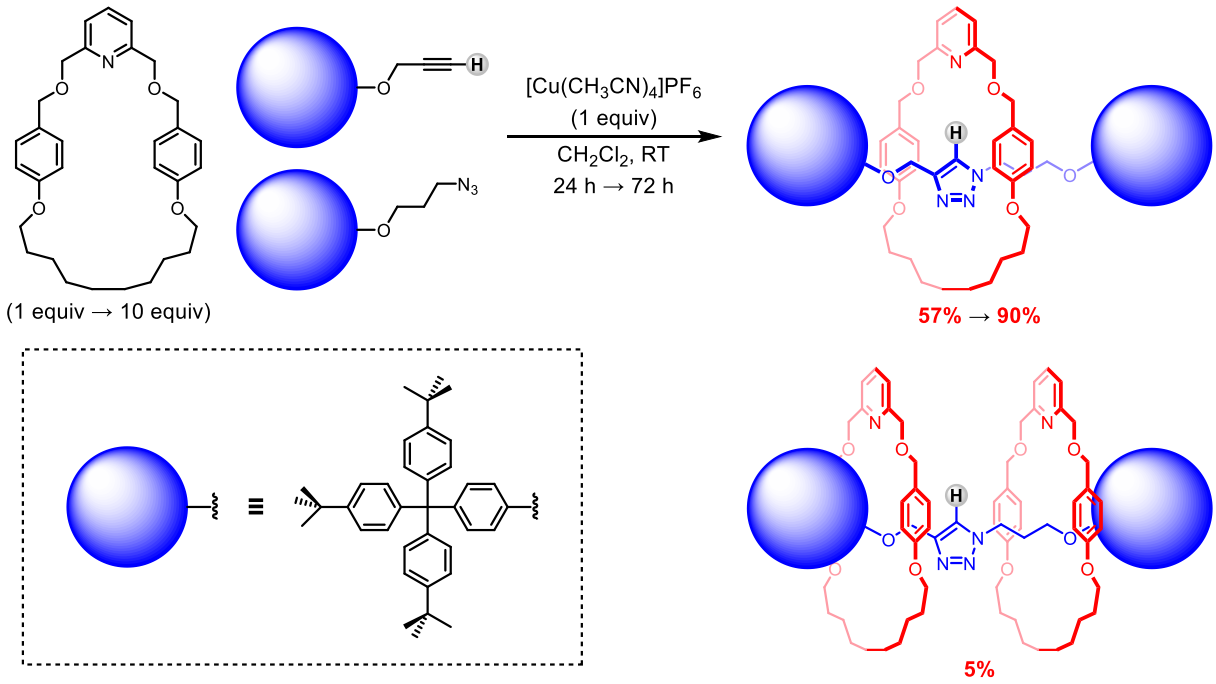

Scheme 2.3 Effect of increasing the macrocycle:$[Cu(CH_3CN)_4]PF_6$ ratio in CuAAC-AMT reaction from 1:1 to 10:1.

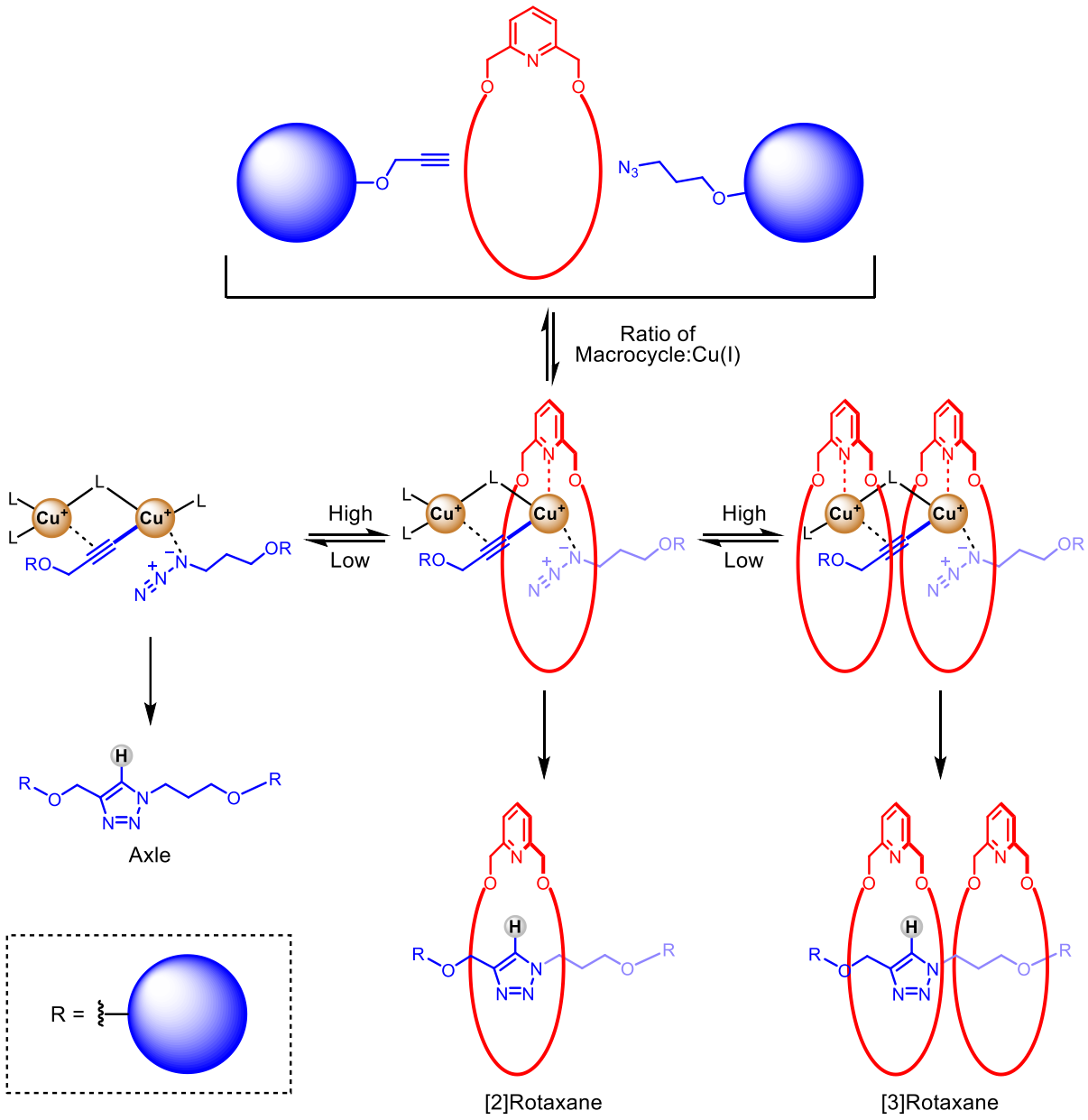

Scheme 2.4 Proposed CuAAC-AMT reaction mechanism involving bimetallic Cu(I) intermediates and the effect of varying the macrocycle:Cu(I) ratio on the distribution of products.[221]

2.1.2 Active Metal Template Synthesis of Halogen Bonding and Chalcogen Bonding [2]Rotaxanes

The synthesis of interlocked host molecules for cation and anion guest species typically use the respective charged ion passive template for their construction; i.e. anion binding interlocked hosts are prepared utilising an anion template (see Section 1.5.1.2). More recently, the AMT strategy has begun to be utilised for the synthesis of rotaxane anion receptors, although examples remain relatively rare.[201,205]

2.1.2.1 CuAAC-AMT Synthesis of XB [2]Rotaxanes

The CuAAC-AMT synthesis of interlocked anion receptors was first employed by Beer and co-workers in 2015 to prepare the first example of a neutral all-XB [2]rotaxane.[223] As shown in Scheme 2.5, the incorporation of an ambidentate bis(iodo-triazole) motif into a macrocycle enabled the facile endotopic binding of Cu(I) via the triazole nitrogen donors, facilitating the CuAAC reaction between terphenyl-based iodoalkynyl and azide stoppers to afford the XB [2]rotaxane in 25% yield. Exotopic bi-dentate triazole complexation of the rotaxane with the larger, sterically demanding Re(I) metal enforced the two XB iodine donor atoms to point towards the central rotaxane cavity for convergent anion binding. The resulting Re(I)-[2]rotaxane demonstrated a pronounced selectivity towards Cl^- over other halide anions and OAc^- in $CHCl_3$ compared with an analogous acyclic receptor. To further augment anion binding affinity, the same bis(iodo-triazole)-based macrocycle was later exploited in the synthesis of a series of cationic all-XB [2]rotaxanes via a similar CuAAC-AMT methodology,[224] for the recognition of anions via charge-assisted XB interactions.

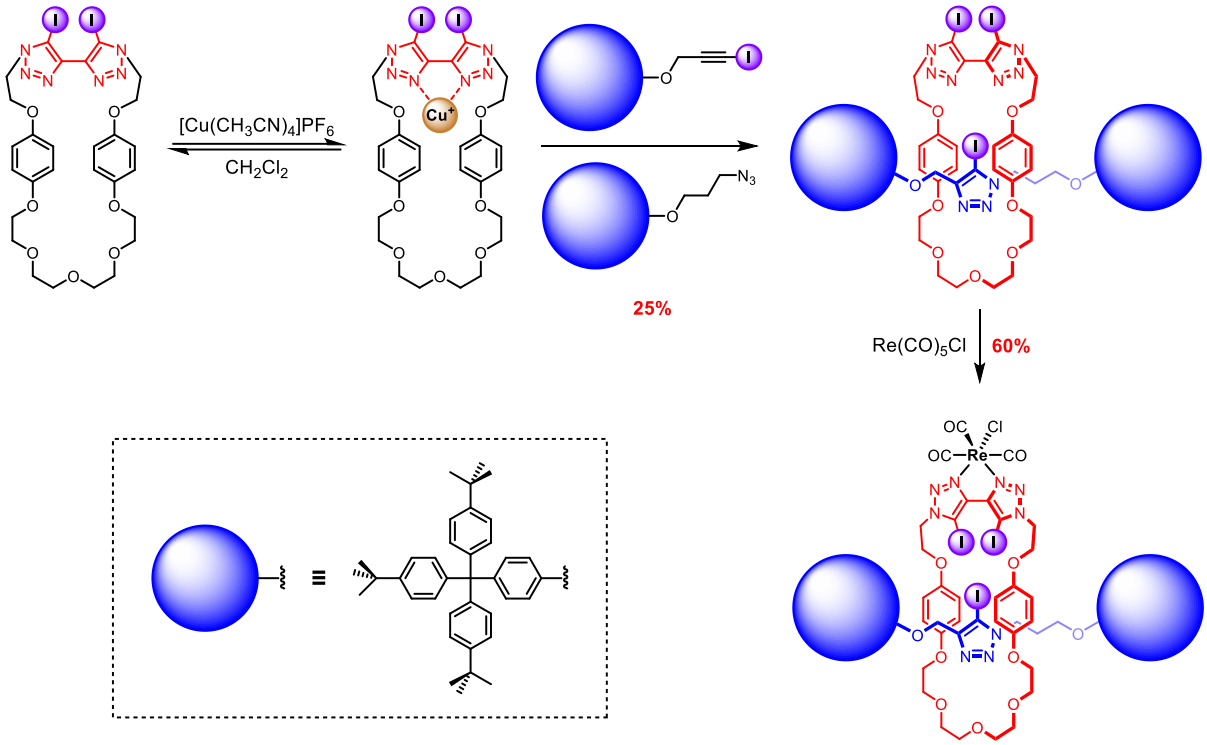

Scheme 2.5 CuAAC-AMT synthesis of XB [2]rotaxanes with bis(iodo-triazole)-functionalised macrocycle.[223]

Two years later, the same group reported the incorporation of 1,2- or 1,3-bis(iodo-triazole)benzene motifs into macrocyclic systems to endotopically bind Cu(I) in a bi- and mono-dentate fashion respectively (Scheme 2.6).[225] Utilising these macrocycles, CuAAC-AMT reactions with appropriate axle precursors afforded a series of [2]rotaxanes with two, three or four XB iodo-triazole donors in 18–41% yields. [2]Rotaxanes consisting of *meta*-substituted bis(iodo-triazole)benzene moiety in the macrocyclic components demonstrated significantly stronger anion affinity than the *ortho*-substituted analogue in acetone-d_6, attributed to the relief of steric hindrance by placing the two bulky iodo-triazole units further apart and optimisation of bite angle for anion recognition. The potency of this receptor design was further attested by the capability of the neutral tetra-dentate XB [2]rotaxane to recognise I^- selectively in 5% D_2O/acetone-d_6 mixture, while no appreciable binding was observed for all other [2]rotaxanes studied. Later, exploiting the efficacy of bis(iodo-triazole)benzene in

anion binding and mediating CuAAC-AMT reactions, a series of cationic chiral[226] and ferrocene-appended[227] all-XB [2]rotaxanes were reported for the enantioselective and electrochemical recognition of anion guest species respectively.

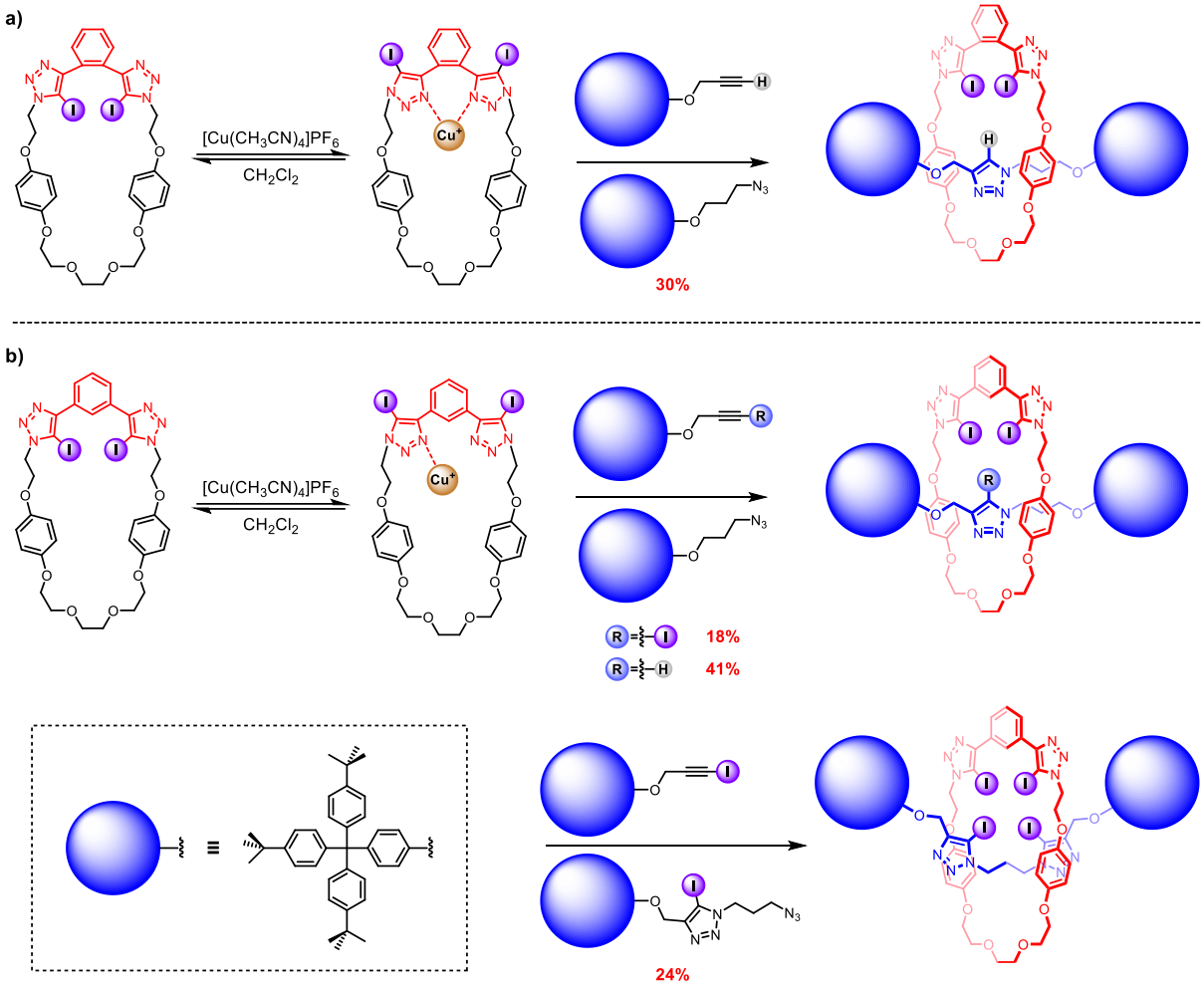

Scheme 2.6 CuAAC-AMT synthesis of XB [2]rotaxanes with a) 1,2- and b) 1,3-bis(iodo-triazole)benzene-functionalised macrocycles.[225]

In 2018, another novel macrocycle consisting of two iodo-triazole groups separated by a Lewis basic dimethylamine spacer was developed (Scheme 2.7).[228] Under the standard CuAAC-AMT conditions, an XB tetradentate [2]rotaxane incorporated with secondary amine-bis(iodo-triazole) motifs on both the macrocyclic and axle components was prepared in 34% yield. Interestingly, charged guest ion binding behaviour of the XB [2]rotaxane could be controlled orthosterically utilising acid as a trigger. In the neutral state, the [2]rotaxane exhibited pronounced affinity

towards the metal cations Zn^{2+} and Cu^{2+} in the solvent mixture 1:1 CH_2Cl_2/CH_3OH but relatively weak Cl^- anion binding was observed in acetone-d_6. However, protonation of the rotaxane's two secondary amine groups resulted in strong and selective Cl^- anion binding in the competitive aqueous solvent mixture 45:45:10 $CDCl_3/CD_3OD/D_2O$ and negated metal cation recognition.

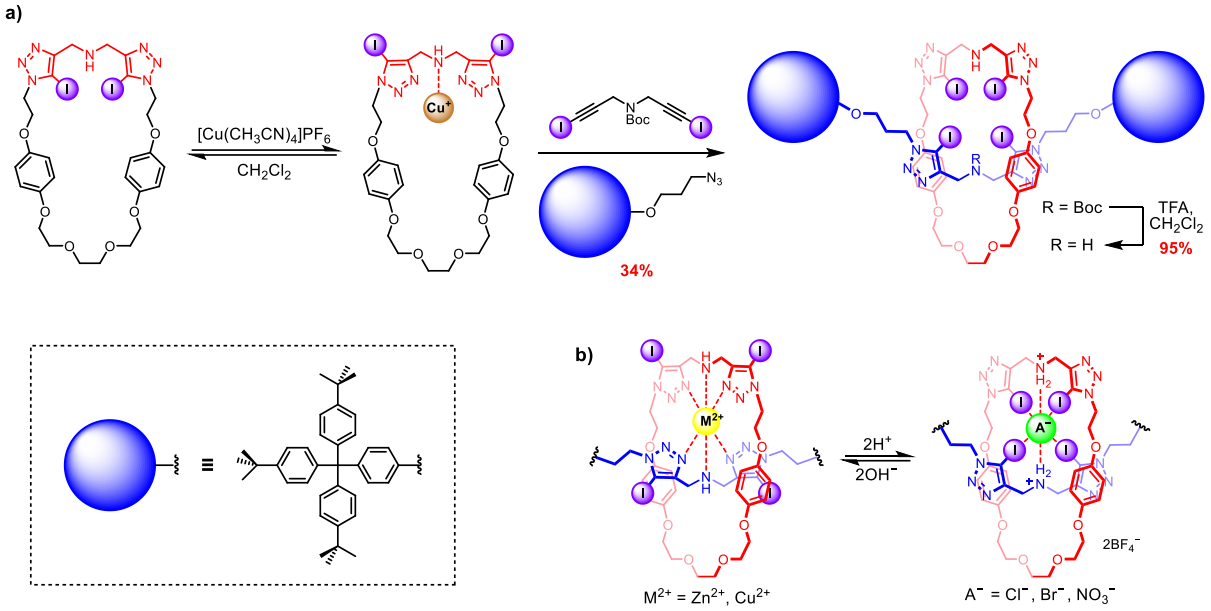

Scheme 2.7 a) CuAAC-AMT synthesis of XB [2]rotaxane with macrocycle functionalised with bis(iodo-triazole) group separated by dimethylamine spacer.[228] b) Acid/base-regulated orthosteric switching of cation and anion binding property of the XB [2]rotaxane.

2.1.2.2 CuAAC-AMT Synthesis of ChB [2]Rotaxanes

The incorporation of ChB donor motifs into anion receptor frameworks has been hampered by their inherent chemical instability, in particular of the labile C–Te bond[118] which has a propensity to decompose via oxidation, hydrolysis or metal insertion reactions.[119,120] In 2017 Beer and co-workers reported the first examples of ChB [2]rotaxanes, prepared from macrocycles incorporated with two chemically robust ChB 5-seleno-/telluro-methyl-1,2,3-triazoles covalently linked to a central benzene spacer at the 1,3-positions (Scheme 2.8a).[127] In contrast to the above-mentioned iodo-triazole-functionalised macrocycles (Scheme 2.6), in which Cu(I) binding was mediated by the triazole N atoms, these ChB macrocycles endotopically

coordinate to Cu(I) via the two chalcogen atoms in a bidentate manner. This facilitated the subsequent CuAAC reactions between axle coupling partners through the cavity of the macrocycle, affording the corresponding ChB [2]rotaxanes in 46–56% yields. In comparison to the all-protic rotaxane analogue, the telluromethyl-triazole-functionalised [2]rotaxane displayed an enhanced anion affinity in acetone-d_6, with selectivity towards the dianion SO_4^{2-}. Although no appreciable binding was observed for the analogous selenium rotaxane in the same solvent, converting the triazole groups to triazolium using trimethyloxonium tetrafluoroborate ($(CH_3)_3O{\cdot}BF_4$) (Scheme 2.8b), gave the tricationic [2]rotaxane which was capable of selectively binding SO_4^{2-} in 20% D_2O in acetone-d_6 with K_a = 3530 M^{-1}.

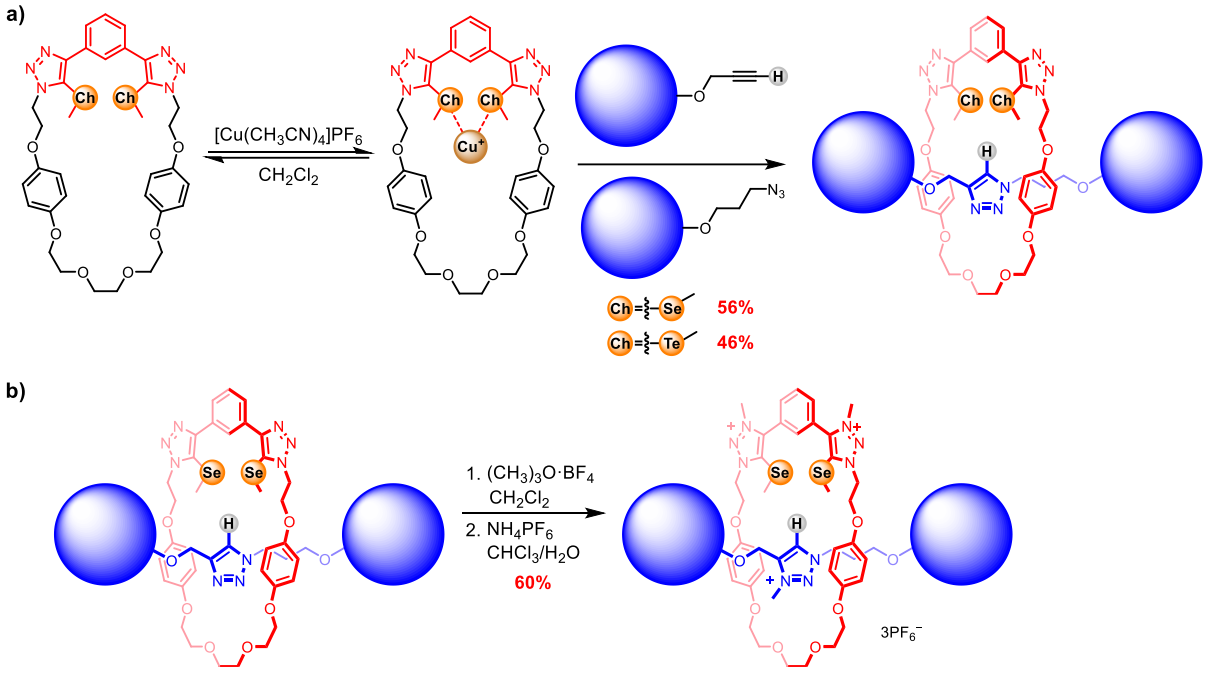

Scheme 2.8 a) CuAAC-AMT synthesis of ChB [2]rotaxane with macrocycles incorporated with 1,3-bis(seleno-/telluro-methyltriazole)benzene motif. b) Methylation of selenated [2]rotaxane.

2.2 Chapter Aims

This chapter aims to investigate the fundamental charged guest recognition properties of sigma-hole [2]rotaxanes integrated with multiple iodo-/telluro-triazole donor motifs. By virtue of the amphoteric nature of the anisotropically polarised iodine and tellurium atoms, these interlocked hosts are envisaged to recognise *both* anions and cations in solution via the same donor atoms (Figure 2.2). A novel family of tri- and tetra-dentate XB, ChB and unprecedented mixed XB/ChB [2]rotaxanes are synthesised via the CuAAC-mediated AMT approach, employing appropriately functionalised alkynyl and azide axle precursors. The anion, cation, and ion-pair recognition properties of these interlocked hosts were investigated by extensive ^{1}H NMR titration studies.*

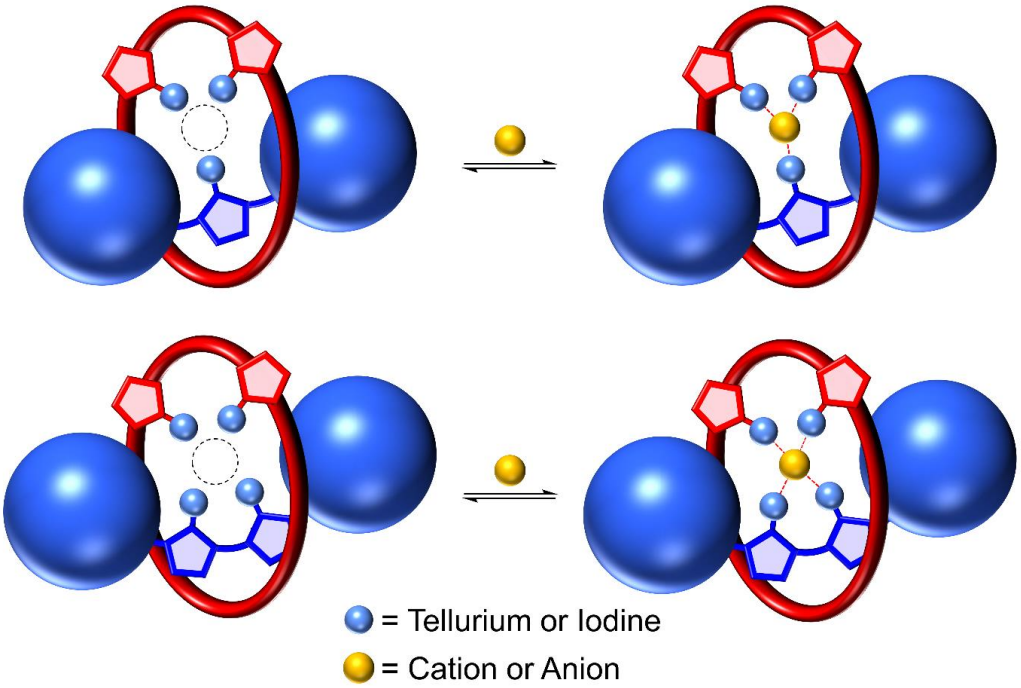

Figure 2.2 Schematic representation of target tri- and tetra-dentate σ-hole [2]rotaxanes for cation and anion recognition. Sky blue spheres: iodine or tellurium donors; yellow sphere: cation or anion.

* This work was undertaken in collaboration with fellow graduate student Andrew Docker, who synthesised the requisite telluro-alkyne functionalised axle precursors **2.8·Te$^{Me/Ph/pCF3}$** and **2.9·Te^{Me}** (Scheme 2.13 and Scheme 2.14) and assisted in the titration experiments.

2.3 Design and Synthesis of Halogen Bonding and Chalcogen Bonding [2]Rotaxanes

The target tri-/tetra-dentate σ-hole [2]rotaxanes are retrosynthetically prepared from XB/ChB macrocycles, and appropriately functionalised stopper alkynes and stopper azides via CuAAC-AMT synthesis (Scheme 2.9). The macrocycles are equipped with the 5-*tert*-butyl-1,3-bis(iodo-/telluromethyl-triazole)benzene motifs for the dual role of endotopic Cu(I) coordination (for rotaxane synthesis via CuAAC-AMT) and anion binding (via XB/ChB interactions). The synthesis of the requisite macrocycles and axle precursors are first described, followed by the construction of target multi-dentate σ-hole [2]rotaxanes via CuAAC-AMT reactions.

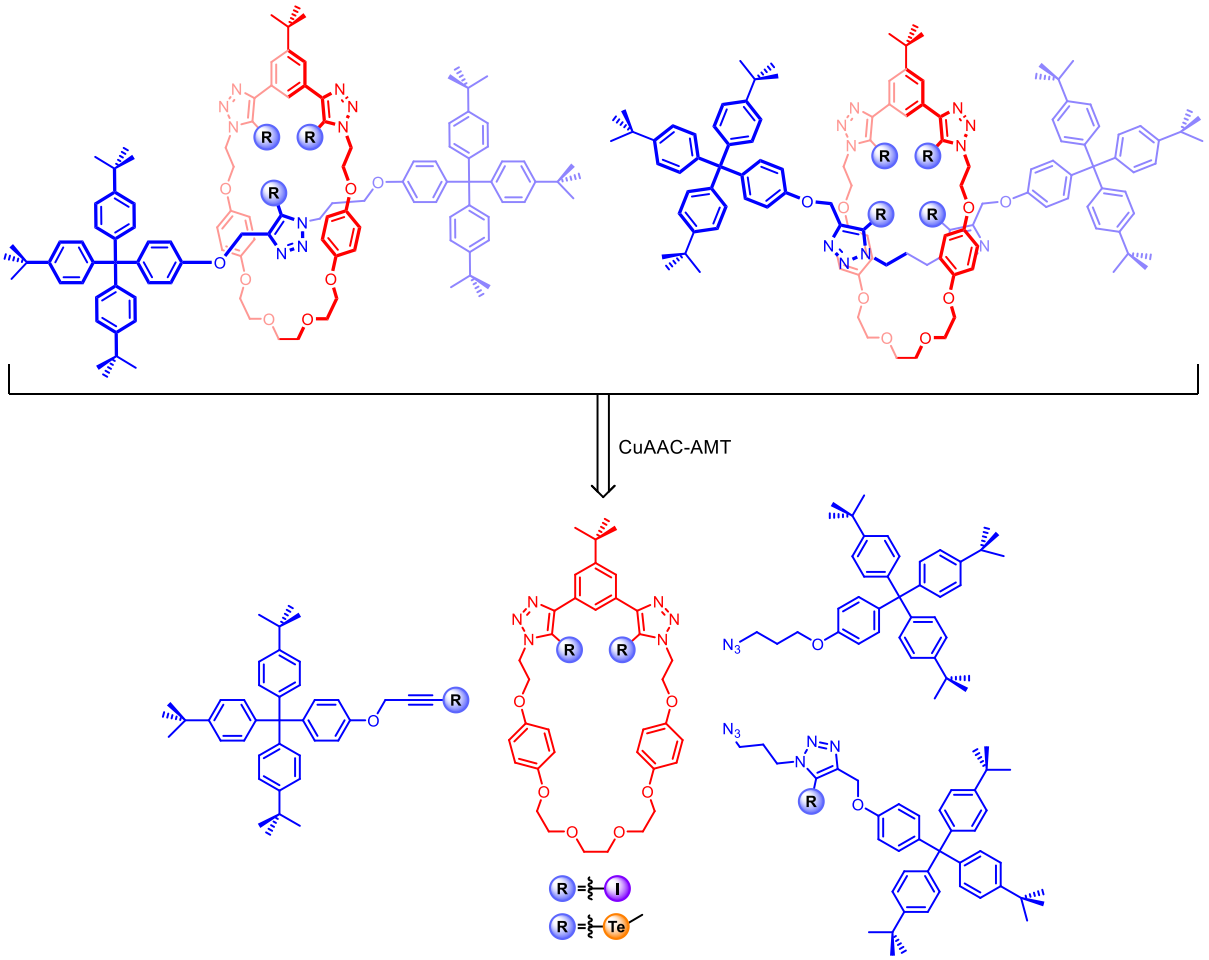

Scheme 2.9 Retrosynthesis of target tridentate and tetradentate [2]rotaxanes.

2.3.1 Synthesis of XB and ChB Macrocycles

The target XB and ChB macrocycles (**2.1·I** and **2.1·Te^{Me}**), and their HB analogues (**2.1·H**) were prepared by CuAAC-mediated macrocyclisation reactions between appropriately appended bis-alkyne and bis-azide precursors (Scheme 2.10).

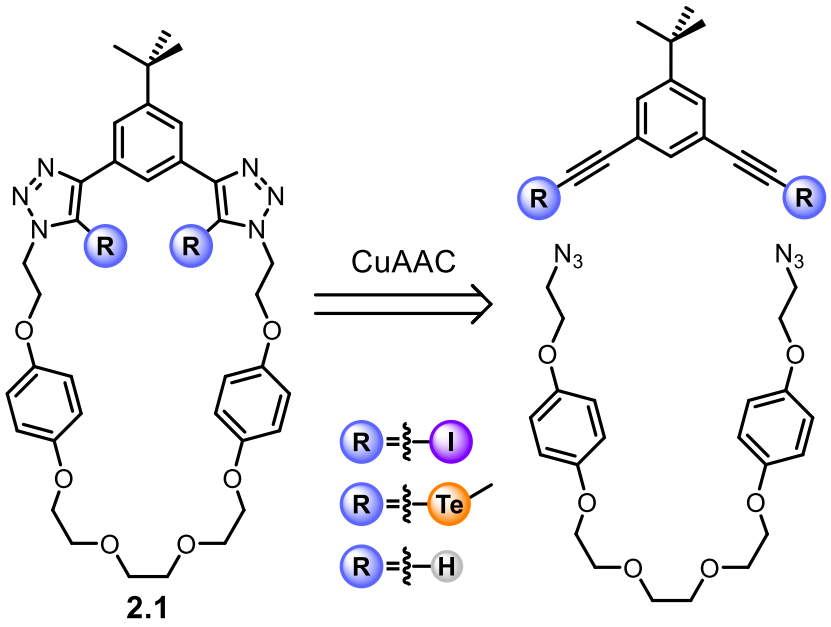

Scheme 2.10 Retrosynthesis of target XB/ChB/HB macrocycles **2.1·I/Te^{Me}/H**.

The synthetic routes to the requisite bis-alkynyl precursors **2.3·I/Te^{Me}/H** are shown in Scheme 2.11a. Initially, Sonagashira coupling reaction between commercially available 5-*tert*-butyl-1,3-dibromobenzene and ethynyltrimethylsilane in the presence of a catalytic amount of [Pd(PPh$_3$)$_2$Cl$_2$] and CuI afforded the TMS-protected bis-alkyne **2.2** in 60% yield.[229] By treating compound **2.2** with *N*-iodosuccinimide (NIS) in the presence of a catalytic amount of AgNO$_3$, bis(iodo-alkyne) **2.3·I** was obtained in 95% yield.[230] The telluromethyl analogue **2.3·Te^{Me}** was prepared by firstly reacting **2.2** with AgF and converting it into corresponding silver acetylide, which was subsequently exposed to CH$_3$TeBr to give the tellurium product after chromatographic purification in 77% yield.[231] The proto-alkyne **2.3·H** was obtained by cleavage of the TMS protecting groups using K$_2$CO$_3$ in CH$_3$OH/THF in 93% yield.[232]

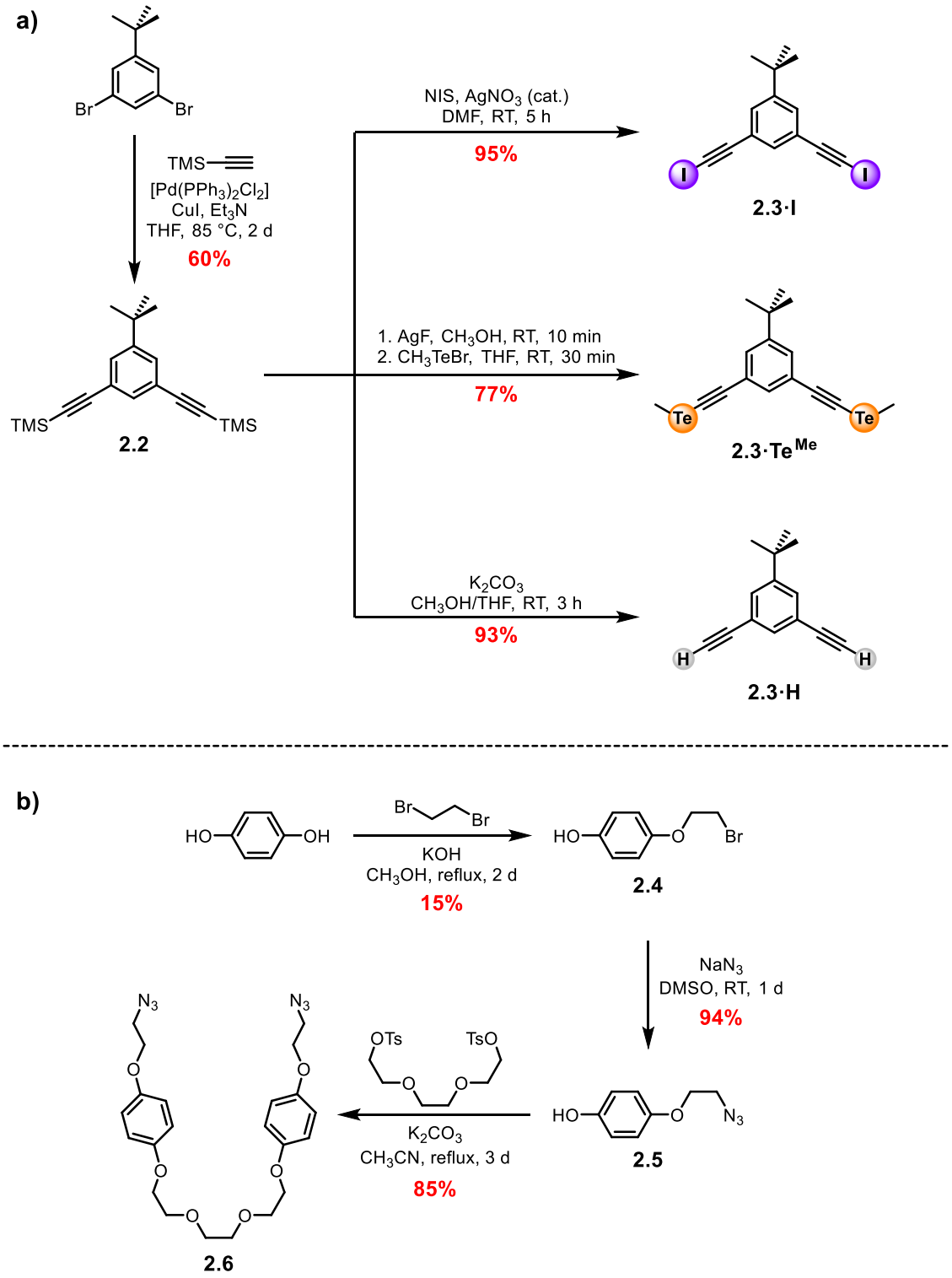

Scheme 2.11 Synthetic routes of a) iodo-, tellouromethyl- and proto-appended bis-alkynes **2.3**, and b) tri(ethylene glycol)-based bis-azide **2.6**.

Scheme 2.11b outlines the synthesis of the tri(ethylene glycol)-based bis-azide precursor **2.6**.[127] Mono-alkylation of hydroquinone with 1,2-dibromoethane in the presence of basic KOH in CH_3OH afforded the phenol **2.4** in 15% yield after

chromatographic purification. Nucleophilic substitution of bromide in **2.4** with NaN_3 gave the corresponding azide **2.5** in 94% yield. Williamson ether condensation between **2.5** and tri(ethylene glycol)-bis-tosylate under basic conditions afforded the bis-azide **2.6** in 85% yield.

To prepare the target macrocycles (Scheme 2.12), bis-alkynyl precursors **2.3·I/Te^{Me}/H** and bis-azide **2.6** were dissolved in anhydrous CH_2Cl_2 under high dilution conditions in the presence of a catalytic amount of $[Cu(CH_3CN)_4]PF_6$ and TBTA, and the reaction mixtures were stirred at room temperature over the period of 24–48 hours. Subsequent aqueous work-up with basic aqueous EDTA/NH_4OH and purification by column chromatography afforded the target macrocycles **2.1·I**, **2.1·Te^{Me}** and **2.1·H** in yields in the range of 21–43%.

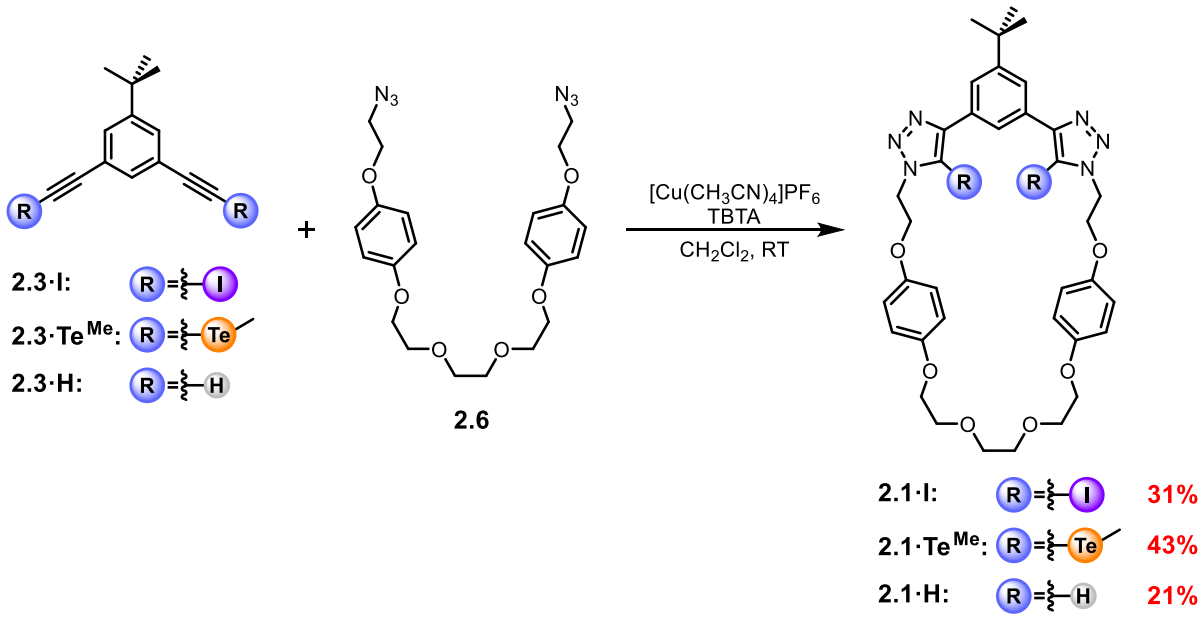

Scheme 2.12 CuAAC-mediated macrocyclisation synthesis of XB/ChB/HB macrocycles.

2.3.2 Synthesis of Axle Precursors

The synthesis of the iodo- and telluro-functionalised alkyne CuAAC-AMT coupling partners is summarised below in Scheme 2.13.

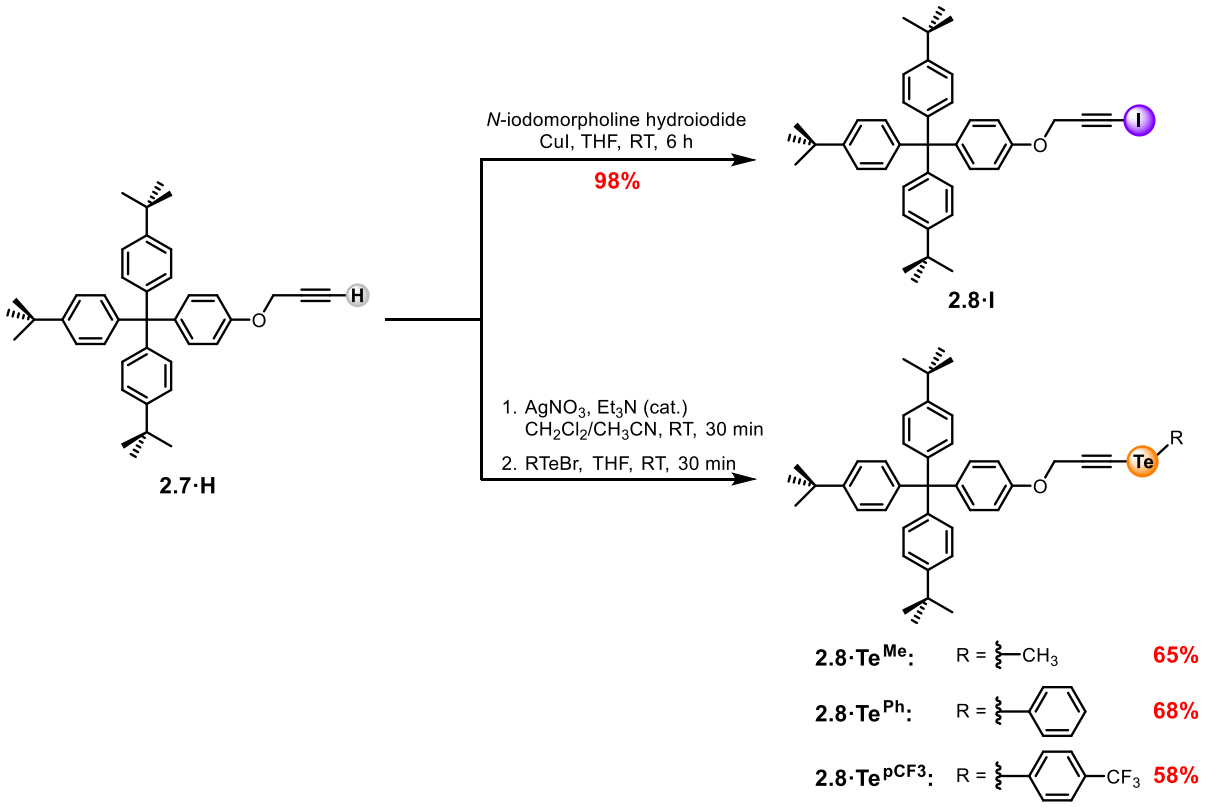

Scheme 2.13 Synthesis of iodo- and telluro-alkynyl axle precursors **2.8**.

Following a reported procedure,[233] the iodo-alkynyl stopper **2.8·I** was obtained by iodination of proto-alkyne **2.7·H** using *N*-iodomorpholine hydroiodide and CuI in THF, followed by aqueous work-up. The novel stopper telluro-alkynes **2.8·Te$^{Me/Ph/pCF3}$** were synthesised in two steps, with initial conversion of the proto-alkyne **2.7·H** into the corresponding silver acetylide via the addition of $AgNO_3$ to a solution of the compound dissolved in 1:1 CH_2Cl_2/CH_3CN in the presence of catalytic amount of triethylamine. The isolated acetylide was suspended in THF and reacted with corresponding Te(II) bromide (RTeBr) species, generated via treatment of the parent diorgano ditelluride (R_2Te_2) with Br_2 in CH_2Cl_2, to afford the respective organotelluro-alkyne appended stopper derivatives **2.8·Te$^{Me/Ph/pCF3}$** in yields in the range of 58–68%.

To access the higher-order tetradentate XB and ChB [2]rotaxanes with two σ-hole donors in the axle component, **2.8·I/Te^{Me}** was reacted with excess 1,3-diazidopropane

in CH_2Cl_2 under standard CuAAC conditions, followed by chromatographic purification, to afford azide precursors consisting of a pre-formed iodo-/telluromethyl-triazole (**2.9·I**[225] and **2.9·Te^{Me}**) in 85–90% yields (Scheme 2.14).

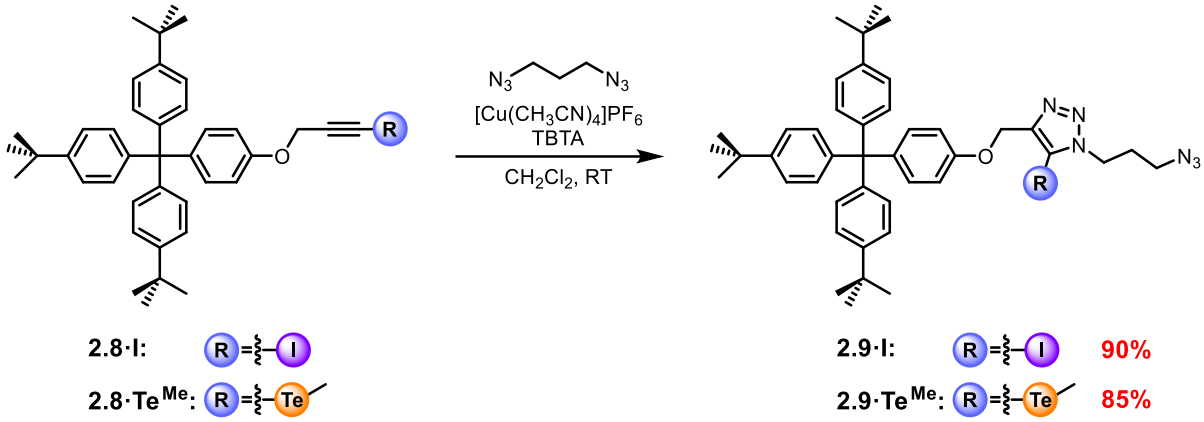

Scheme 2.14 Synthesis of azide axle precursors **2.9** consisting of a pre-formed iodo-/telluromethyl-triazole.

2.3.3 CuAAC-AMT Synthesis of XB and ChB [2]Rotaxanes

To construct the target [2]rotaxanes with different permutations of σ-hole donors around the binding pocket, CuAAC-AMT reactions were performed between various combinations of macrocycles (**2.1·I/Te^{Me}/H**), stopper alkynes (**2.7·H** and **2.8·I/Te^{Me}/Te^{Ph}/Te^{pCF3}**) and stopper azides (**2.9·I/Te^{Me}** and **2.10**[221]) (Scheme 2.15).

In a typical reaction, an equimolar mixture of the macrocycle and $[Cu(CH_3CN)_4]PF_6$ in anhydrous CH_2Cl_2 was stirred at room temperature for 30 minutes to facilitate metal complexation. Subsequently, five equivalents excess of alkynyl and azide coupling partners were added. The reaction mixture was then left stirring for 48 hours, during which the CuAAC reaction between the axle precursors catalysed by the endotopically bound Cu(I) in the macrocycles captured the interlocked products. If after which time TLC and mass spectrometry analysis of the crude mixture indicated the persistence of unreacted azides or alkynes, an additional equivalent of Cu(I) was added and the reaction was allowed to stir for an extended period of 24 hours. This process of addition of metal catalyst was repeated until complete consumption of the axle precursors was observed. The reaction mixture was then subjected to aqueous work-up by washing with basic EDTA/NH_4OH and purification by preparative TLC afforded the target σ-hole [2]rotaxanes in various yields. The individual reaction conditions for each rotaxane is summarised in Table 2.1. All novel [2]rotaxanes were characterised by ^1H, ^{13}C NMR and high-resolution ESI mass spectrometry. Tridentate (**2.11·X$_n$Y$_m$**) and tetradentate (**2.12·X$_n$Y$_m$**) [2]rotaxanes are named by indicating the nature of the anion binding donors (XB/ChB/HB) they possess, with X and Y indicating the donors on the macrocycle and axle respectively.

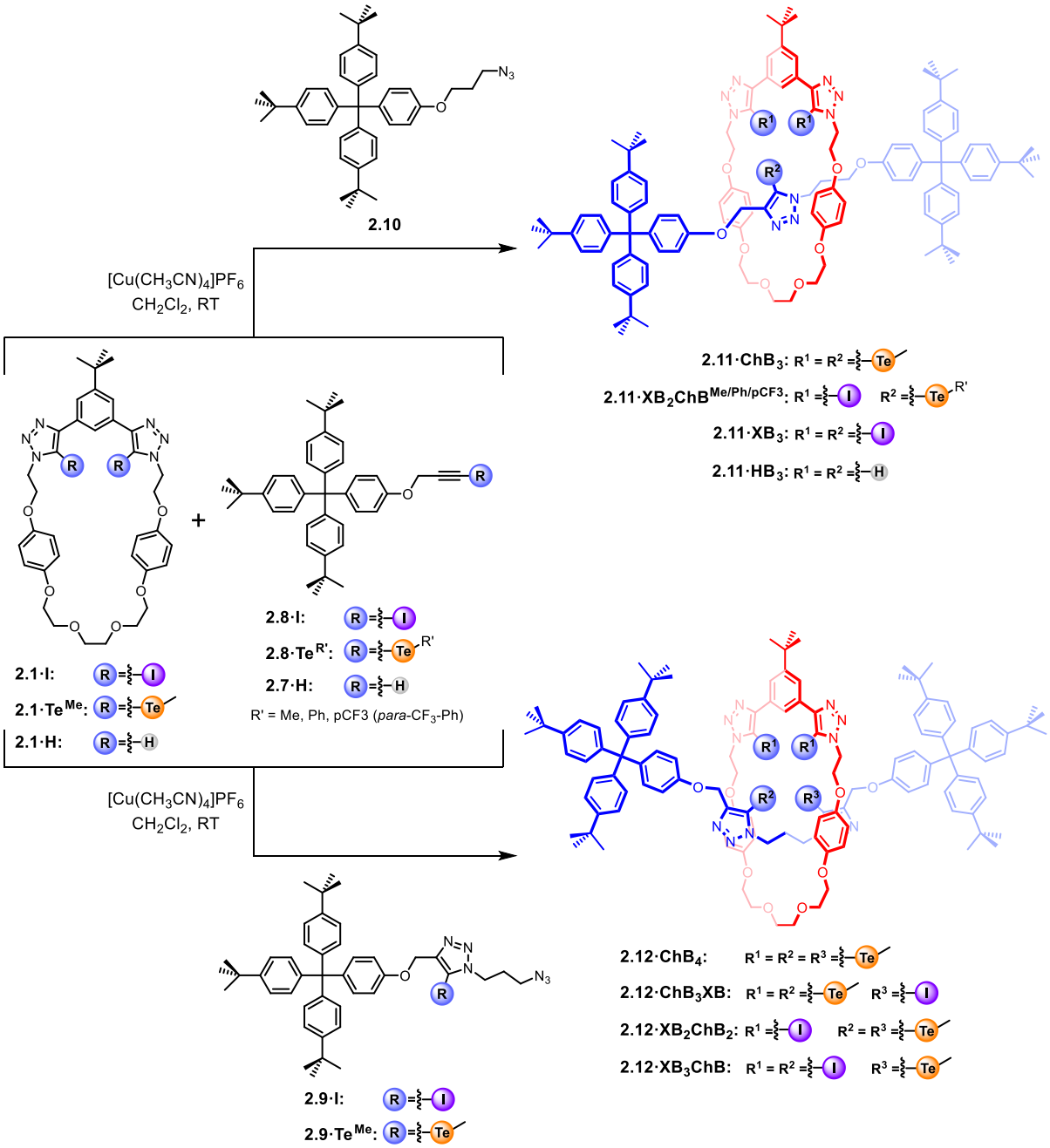

Scheme 2.15 General CuAAC-AMT synthesis of a) tridentate and b) tetradentate σ-hole [2]rotaxanes.

Table 2.1: Reaction conditions and yields for the synthesis of the tri- and tetradentate [2]rotaxane series by CuAAC-mediated active metal templation.[a]

Entry	[2]Rotaxanes	Macrocycle	Alkyne	Azide	Cu(I)[b]	Time	Yield[c]
1	**2.11·ChB$_3$**	**2.1·Te^{Me}**	**2.8·Te^{Me}**	**2.10**	1 equiv	2 d	24%
2	**2.11·ChB$_2$XB**	**2.1·Te^{Me}**	**2.8·I**	**2.10**	1 equiv	2 d	—[d]
3[e]	**2.11·XB$_3$**	**2.1·I**	**2.8·I**	**2.10**	3 equiv	5 d	31%
4	**2.11·XB$_2$ChB^{Me}**	**2.1·I**	**2.8·Te^{Me}**	**2.10**	1 equiv	2 d	25%
5	**2.12·ChB$_4$**	**2.1·Te^{Me}**	**2.8·Te^{Me}**	**2.9·Te^{Me}**	5 equiv	7 d	18%
6	**2.12·ChB$_3$XB**	**2.1·Te^{Me}**	**2.8·Te^{Me}**	**2.9·I**	1 equiv	2 d	23%
7	**2.12·XB$_2$ChB$_2$**	**2.1·I**	**2.8·Te^{Me}**	**2.9·Te^{Me}**	5 equiv	7 d	10%
8	**2.12·XB$_3$ChB**	**2.1·I**	**2.8·Te^{Me}**	**2.9·I**	1 equiv	2 d	17%
9	**2.11·XB$_2$ChB^{Ph}**	**2.1·I**	**2.8·Te^{Ph}**	**2.10**	2 equiv	3 d	20%
10	**2.11·XB$_2$ChB^{pCF3}**	**2.1·I**	**2.8·Te^{pCF3}**	**2.10**	3 equiv	4 d	13%
11	**2.11·HB$_3$**	**2.1·H**	**2.7·H**	**2.10**	1 equiv	2 d	18%

[a]Ratio of macrocycle:alkyne:azide = 1:5:5. Reactions were carried out in CH_2Cl_2 at room temperature with concentration of 5 mM with respect to the macrocycle. [b]$[Cu(CH_3CN)_4]PF_6$ was added portionwise at 1 equivalent. [c]Isolated yield after chromatographic purification. [d]No rotaxane formed. [e]Reaction was performed at 35 °C.

Inspection of Table 2.1 reveals a number of synthetic milestones and trends. The exploitation of CuAAC-AMT reactions with various combinations of σ-hole macrocycles and axle coupling partners allows access to a family of [2]rotaxanes, including the unprecedented all-ChB and mixed XB/ChB interlocked structures with up to four σ-hole donors (Table 2.1 entries 1, 4–10). It is noteworthy that a minor persistent side product in the synthesis of ChB-based [2]rotaxanes was the respective corresponding proto-triazole rotaxane derivative. The decomposition of the telluromethyl-triazole motif to proto-triazole is postulated to occur via the formation of a copper triazolide intermediate (Scheme 2.16), possibly facilitated by the lability of the weak C–Te bond and the metal coordinating environment generated in the rotaxane interlocked cavity.

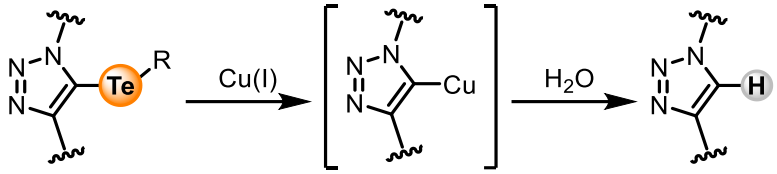

Scheme 2.16 Proposed Cu(I)-mediated decomposition pathway of telluro-triazole into proto-triazole.

In addition, the use of azide precursor **2.9·Te^{Me}**, which consists of a pre-formed telluromethyl-triazole moiety, evidently suppressed the catalytic activity of Cu(I), leading to a significantly retarded reaction rate (Table 2.1 entries 5 and 7). This necessitated the addition of up to a five-fold excess of Cu(I) and subjecting the reaction mixture to a prolonged reaction time of 168 hours for complete consumption of starting materials. This was attributed to the presence of the five-fold excess telluromethyl-triazole-containing axle precursor **2.9·Te^{Me}** in the reaction mixture, which sequestered the Cu(I) and/or occupied the free coordination site of the endotopically bound Cu(I) in the macrocycle, via direct Te···Cu(I) interactions (Figure 2.3). In contrast, a reduction in reaction rate was not observed when the iodo-triazole-containing precursor **2.9·I** was used (Table 2.1 entries 6 and 8), which only required one equivalent of Cu(I) catalyst and a reaction time of 48 hours. This further attests to the involvement of Te donor atoms in hindering the reaction rate, highlighting their Cu(I) coordinating ability.

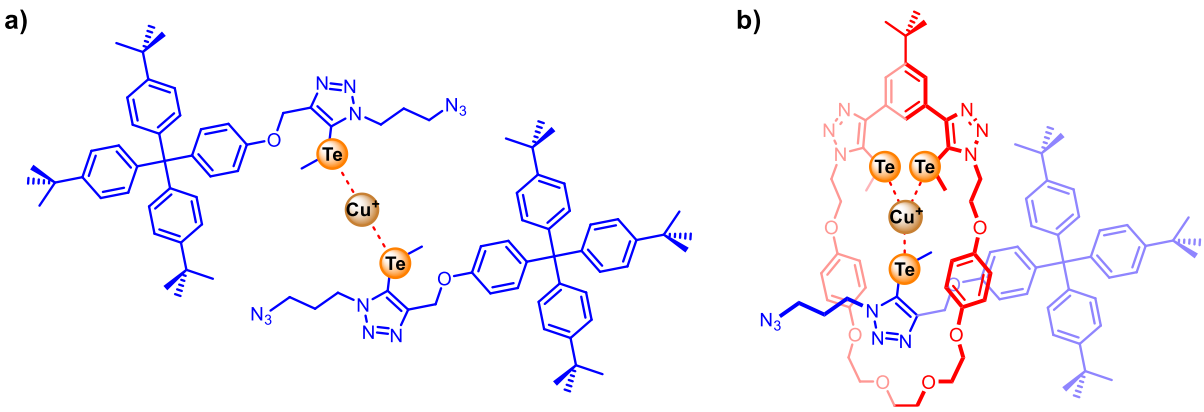

Figure 2.3 Proposed Cu(I) binding mediated by telluromethyl-triazole-containing axle precursor **2.9·Te^{Me}**.

The series of mixed XB/ChB rotaxanes synthesised potentially allows a systematic modulation of anion affinity and selectivity, while maintaining a highly hydrophobic binding environment in the rotaxane cavities (Table 2.1 entries 4, 6–10). In one attempt, ChB macrocycle **2.1·Te^{Me}** and axle precursors **2.8·I** and **2.10** were subjected to the standard CuAAC conditions to prepare the corresponding [2]rotaxane **2.11·ChB$_2$XB** (Table 2.1 entry 2 and Scheme 2.17). However, formation of the interlocked structure was not observed. One major side product was isolated in 30% yield, which surprisingly was identified by ^{1}H NMR and ESI-MS analyses to be the XB macrocycle **2.1·I**, with both telluromethyl-triazole groups in the reactant macrocycle **2.1·Te** converted into iodo-triazoles. Initially, it was suspected that a trace amount of residual I_2 in stopper **2.8·I,** originating from the previous iodination step, was responsible for the iodination of **2.1·Te**. However, despite thoroughly washing **2.8·I** with $Na_2S_2O_{3(aq)}$ and repeating the reaction, the direct transformation of **2.1·Te^{Me}** to **2.1·I** was still observed. The mechanism for ChB macrocycle to XB macrocycle conversion may tentatively involve the formation of the above-mentioned copper triazolide reactive intermediate, promoted by the lability of the C–Te bond (Scheme 2.16).

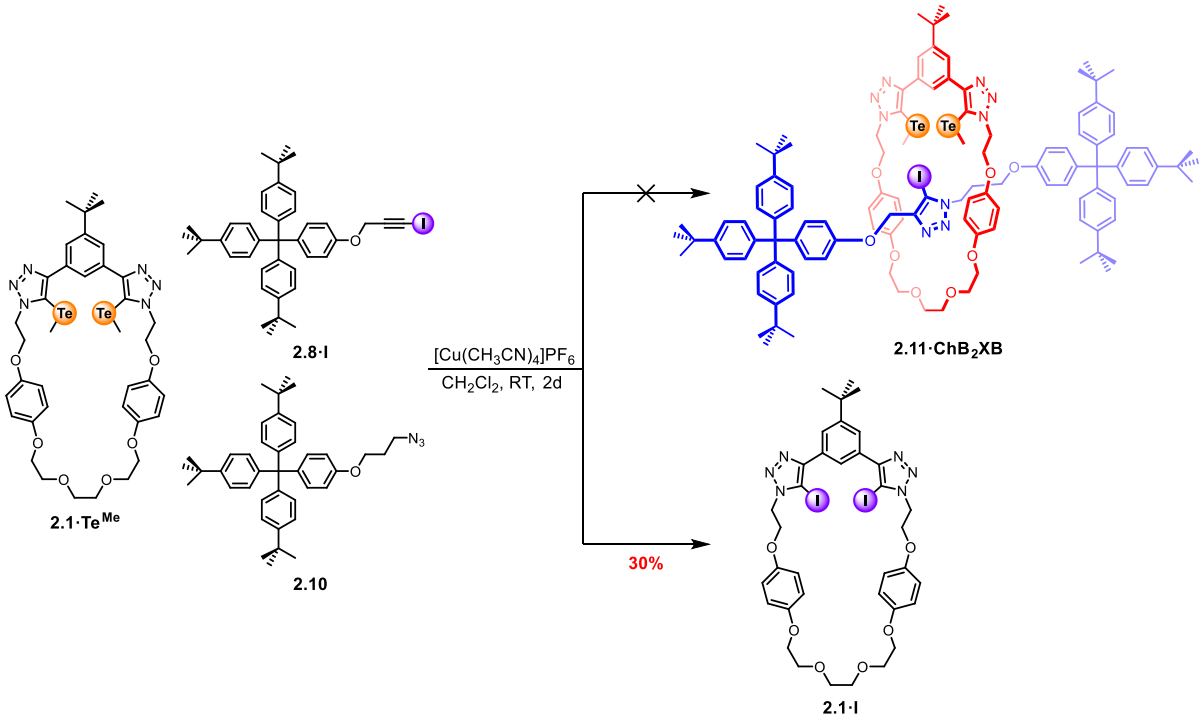

Scheme 2.17 Attempted CuAAC-AMT synthesis of [2]rotaxane **2.11·ChB$_2$XB** and the unexpected formation of **2.1·I**.

Influenced by a recent demonstration that Te atom substituent variation of telluro-triazole units can significantly alter the anion binding properties of ChB donors,[234] efforts were made to prepare [2]rotaxanes incorporated with aryl-appended telluro-triazoles as ChB donors. Specifically, [2]rotaxanes **2.11·XB$_2$ChB^{Ph}** and **2.11·XB$_2$ChB^{pCF3}** were synthesised from aryl-functionalised stopper telluroalkynes **2.8·Te^{Ph}** and **2.8·Te^{pCF3}** respectively, in the presence of XB macrocycle **2.1·I** and stopper azide **2.10** (Table 2.1 entries 9 and 10). In comparison with the synthesis of methyl-analogue **2.11·XB$_2$ChB^{Me}** (Table 2.1 entry 4), the increase in Te substituent size evidently hinders the CuAAC reaction rate, with reaction time increases in the order of **2.11·XB$_2$ChB^{Me}** < **2.11·XB$_2$ChB^{Ph}** < **2.11·XB$_2$ChB^{pCF3}**. Nevertheless, the successful isolation of [2]rotaxanes **2.11·XB$_2$ChB^{Ph}** and **2.11·XB$_2$ChB^{pCF3}** in 20% and 13% yields respectively highlights the synthetic versatility of the CuAAC-AMT methodology in constructing interlocked receptors.

2.4 Anion Recognition Studies

2.4.1 Tridentate Sigma-Hole [2]Rotaxanes

To assess the anion recognition properties of the novel tridentate mixed XB/ChB (**2.11·XB$_2$ChB^{Me}**) and all-ChB (**2.11·ChB$_3$**) [2]rotaxanes, quantitative ^{1}H NMR anion titrations were undertaken in acetone-d_6 with TBA halide salts. Upon addition of Cl^- to a solution of **2.11·XB$_2$ChB^{Me}** (Figure 2.4a), progressive downfield shifts of the rotaxane macrocycle component internal benzene proton *a* and axle $TeCH_3$ protons 6^{Te} were observed, confirming the encapsulation of the halide anion by the interlocked host via the formation of both XB (I···Cl^-) and ChB (Te···Cl^-) interactions. In the case of all-ChB **2.11·ChB$_3$** (Figure 2.4b), increasing the concentration of Cl^- in the receptor solution led to downfield perturbations of both the macrocycle and axle $TeCH_3$ protons (h^{Te} and 6^{Te}), indicative of anion binding mediated by the three convergent ChB donors in the vicinity of the rotaxane binding pocket. Similar proton perturbations were observed in the titrations of these two [2]rotaxanes with the heavier halides (Br^- and I^-), implying analogous anion binding conformations. By monitoring the shifts of the internal benzene (*a*) and macrocycle $TeCH_3$ (h^{Te}) protons of **2.11·XB$_2$ChB^{Me}** and **2.11·ChB$_3$** respectively as a function of anion concentration (Figure 2.4 insets), Bindfit[235,236] analysis of the resulting binding isotherms using a 1:1 host-guest stoichiometric model determined the halide anion association constants (Table 2.2). For comparison, the binding constants of the relevant tridentate σ-hole [2]rotaxanes (**2.13·ChB$_2$HB**, **2.13·XB$_3^H$** and **2.13·XB$_2$HB**) and their proto-analogue (**2.13·HB$_3^H$**) (Figure 2.5) previously reported by the Beer group are also tabulated.[127,225]

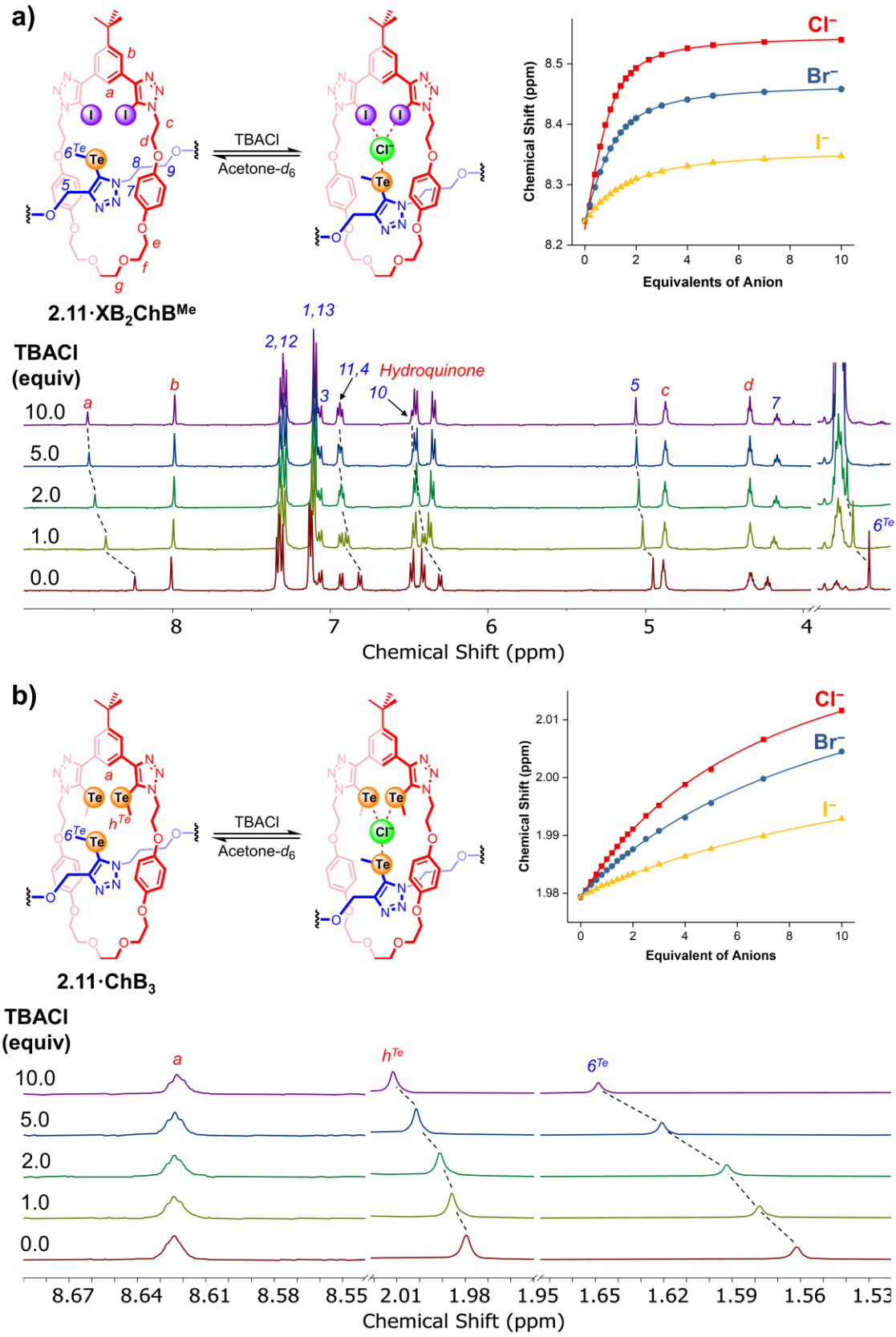

Figure 2.4 Truncated ^{1}H NMR titration spectra of a) **2.11·XB_2ChB^{Me}** and b) **2.11·ChB_3** upon addition of 1.0, 2.0, 5,0 and 10.0 equivalents of TBACl. Inset: Binding isotherms showing changes in chemical shift of proton a) *a* and *b)* h^{Te} with increasing equivalents of halide anions. Filled dots represent the experimental data while the solid lines show the calculated isotherms. ([Rotaxane] = 1.0 mM, 500 MHz, 298 K, acetone-d_6)

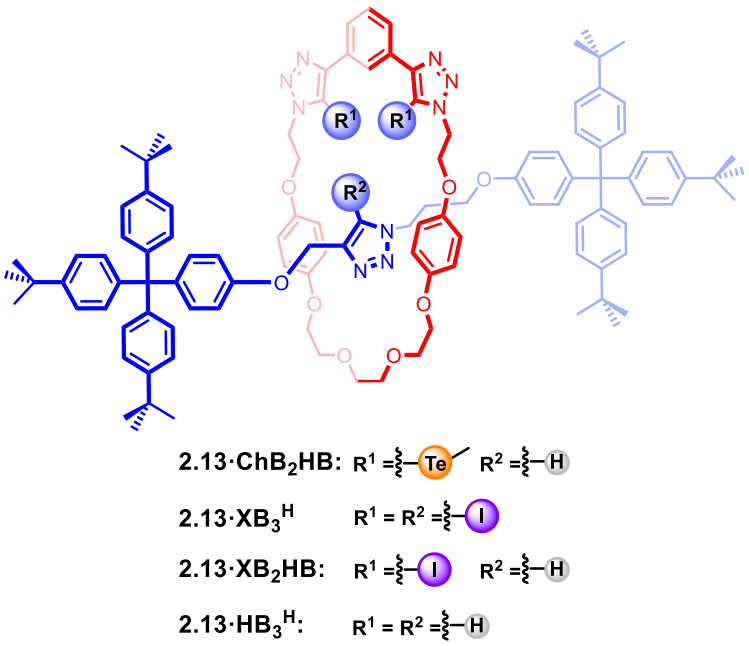

Figure 2.5 Structures of previously reported tridentate [2]rotaxanes.

Table 2.2: Anion association constants (K_a/M^{-1}) for tridentate [2]rotaxanes with TBA halide salts in acetone-d_6 determined by ^{1}H NMR titrations.[a]

Anion	**2.13·XB$_3$^{H}**	**2.11·XB$_2$ChB^{Me}**	**2.13·XB$_2$HB**	**2.11·ChB$_3$**	**2.13·ChB$_2$HB**	**2.13·HB$_3$^{H}**
Cl$^-$	>10^4	4 090 (351)	4 380 (322)	130 (1)	127 (2)	81 (3)
Br$^-$	/[b]	2 330 (41)	2 140 (68)	80 (1)	110 (2)	65 (5)
I$^-$	/[b]	977 (24)	902 (57)	46 (<1)	34 (3)	43 (1)

[a]K_a values calculated using Bindfit with a 1:1 host-guest binding model.[235,236] Errors (±) are in parentheses and are all <10%. Solvent = acetone-d_6. T = 298 K. [Rotaxane] = 1.0 mM. Data for **2.13·XB$_3$^{H}** and **2.13·XB$_2$HB** are reported from reference 225. Data for **2.13·ChB$_2$HB** and **2.13·HB$_3$^{H}** are reported from reference 127. [b]Not performed.

Table 2.2 reveals a general preference of all the tridentate σ-hole [2]rotaxanes for the more charge-dense halide anions (Cl$^-$ > Br$^-$ > I$^-$) in acetone-d_6. In addition, XB-based [2]rotaxanes (**2.13·XB$_3$^{H}**, **2.11·XB$_2$ChB^{Me}** and **2.13·XB$_2$HB**) display significantly larger K_a values (by at least an order of magnitude) for all the halides. This suggests increasing the number of XB iodo-triazole donors around the binding pockets of rotaxanes has the most noticeable effect on enhancing their halide anion affinities. The incorporation of ChB telluromethyl-triazole moieties into the rotaxane framework of **2.11·ChB$_3$** and **2.13·ChB$_2$HB** led to a modest but notable improvement

(up to 1.7-fold increase in K_a) in the binding of Cl^- and Br^- in comparison with the all-HB congener **2.13·HB$_3^H$**.

While the presence of XB iodo-triazole groups notably endow the rotaxane receptors with strong halide affinity, the incorporation of ChB telluro-triazole motifs offers the unique opportunity to further modulate the anion recognition properties of the hosts by varying the steric and electronic nature of the substituents directly attached to the Te donor atoms. To illustrate, [2]rotaxanes **2.11·XB$_2$ChB^{Ph}** and **2.11·XB$_2$ChB^{pCF3}** were prepared, each containing an axle aryl-functionalised telluro-triazole motif. Preliminary anion binding studies were probed by ^{1}H NMR titrations with TBACl in the more competitive aqueous solvent mixture 2% D_2O in acetone-d_6 (chloride binding in acetone-d_6 was too strong to quantify for **2.11·XB$_2$ChB^{pCF3}** with $K_a[Cl^-] > 10^4\ M^{-1}$) (Figure 2.6), and the corresponding Bindfit[235,236] determined anion association constants are tabulated in Table 2.3. In comparison with the telluromethyl-analogue **2.11·XB$_2$ChB^{Me}** ($K_a[Cl^-]$ = 89 M^{-1}), replacing the methyl group with a phenyl substituent in **2.11·XB$_2$ChB^{Ph}** attenuated the binding of Cl^- ($K_a[Cl^-]$ = 69 M^{-1}), attributed to the steric demand imposed by the bulky aryl ring. However, the direct attachment of an even bulkier *p*-trifluoromethylphenyl group to the Te atom in **2.11·XB$_2$ChB^{pCF3}** augmented chloride anion affinity by almost two-fold ($K_a[Cl^-]$ = 173 M^{-1}) relative to the methyl-appended rotaxane. This suggests the electron-deficient *p*-trifluoromethylphenyl group strongly polarises the σ-holes on the Te donor atom, which more than compensates for the steric repulsion in guest binding. Given the established superior anion recognition properties exhibited by interlocked hosts compared to their non-interlocked congeners,[201,237] it is noteworthy that ChB-functionalised [2]rotaxanes have the additional design potential to fine-tune their anion affinity and selectivity via modulation of Te donor atom substituent.

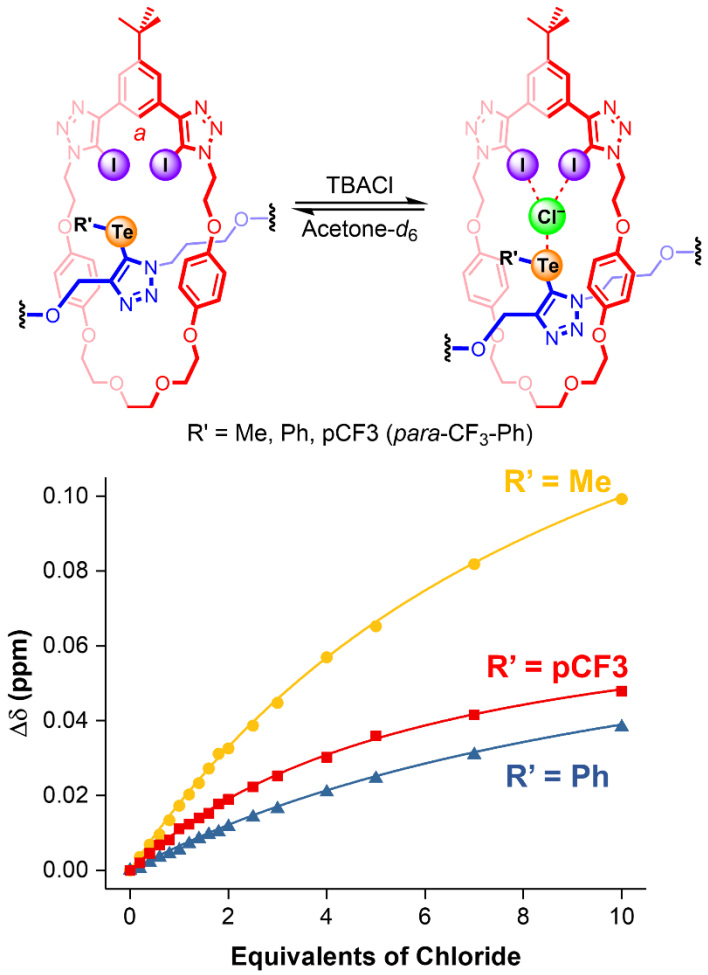

Figure 2.6 Anion binding isotherms of **2.11·XB$_2$ChB^{Me}**, **2.11·XB$_2$ChB^{Ph}** and **2.11·XB$_2$ChB^{pCF3}** generated by monitoring the change in chemical shift (Δδ) of internal benzene proton *a* as a function of chloride concentration. Filled dots represent the experimental data while the solid lines show the calculated isotherms. ([Rotaxane] = 1.0 mM, 500 MHz, 298 K, 2% D_2O in acetone-d_6)

Table 2.3: Anion association constants (K_a/M^{-1}) for tridentate [2]rotaxanes with TBACl in 2% D_2O in acetone-d_6 determined by ^{1}H NMR titrations.[a]

Anion[a]	**2.11·XB$_2$ChB^{Me}**	**2.11·XB$_2$ChB^{Ph}**	**2.11·XB2ChB^{pCF3}**
Cl^-	89 (1)	69 (1)	173 (3)

[a]K_a values calculated using Bindfit with a 1:1 host-guest binding model.[235,236] Errors (±) are in parentheses and are all <5%. Chloride added as its TBA salt. Solvent = 2% D_2O in acetone-d_6. T = 298 K. [Receptor] = 1.0 mM.

2.4.2 Tetradentate Sigma-Hole [2]Rotaxanes

Analogous ^{1}H NMR halide anion titration studies were conducted on the series of higher-order tetradentate σ-hole [2]rotaxanes **2.12·ChB$_4$**, **2.12·ChB$_3$XB**, **2.12·XB$_2$ChB$_2$** and **2.12·XB$_3$ChB** in acetone-d_6. The representative titration spectra of each rotaxane upon the addition of 1, 2, 5 and 10 equivalents of TBACl are shown in Figure 2.7. Interestingly, these [2]rotaxanes exhibit two different binding modes of Cl^- as a result of the varied combinations of σ-hole donors around their anion recognition pockets.

For both **2.12·XB$_3$ChB** and **2.12·XB$_2$ChB$_2$**, addition of Cl^- led to significant downfield shifts of their internal benzene proton *a*, indicative of anion binding inside the shielded rotaxane cavities. Downfield perturbations of axle methylene protons adjacent to triazole donors (*5* and *10* for **2.12·XB$_3$ChB**; *5* for **2.12·XB$_2$ChB$_2$**) were also observed, which likely arise from their proximity to the bound anion inside the rotaxane cleft. In particular, diastereotopic splitting of macrocycle methylene protons *c* and *d* were seen for the mixed XB/ChB [2]rotaxane **2.12·XB$_3$ChB**. This can be ascribed to the restriction of the methylene protons' rotational degrees of freedom induced by the tightly bound Cl^- anion, where the two protons of each methylene group are on opposite sides of the plane of macrocycle, facing different environments of the asymmetric axle component.

In stark contrast, addition of 10 equivalents of Cl^- to **2.12·ChB$_3$XB** and **2.12·ChB$_4$** resulted in negligible shifts to the respective macrocycle internal benzene proton *a*, suggesting the halide did not penetrate into the binding cavity, but was likely to be perching between the plane of the macrocycle and one of the bulky stoppers due to the higher number of sterically demanding telluromethyl-triazole motifs present in the binding domains. For **2.12·ChB$_3$XB**, the downfield shifts observed for axle

methylene proton *10* (adjacent to iodo-triazole) but not for *5* (adjacent to telluromethyl-triazole) indicated the chloride anion was bound proximal to the side of the axle XB donor. Minimal perturbations to the ^{1}H NMR spectra were seen in the case of **2.12·ChB$_4$** except for downfield shifts to both $TeCH_3$ peaks on the macrocycle (h^{Te}) and axle (6^{Te}).

By monitoring the chemical shifts of protons in the vicinity of anion binding sites (proton *a* for **2.12·XB$_3$ChB** and **2.12·XB$_2$ChB$_2$**; proton *10* for **2.12·ChB$_3$XB**; proton h^{Te} for **2.12·ChB$_4$**) as a function of halide anion concentration (Figure 2.7 insets), Bindfit[235,236] analysis with a 1:1 host-guest stoichiometric model determined the corresponding association constants (Table 2.4).

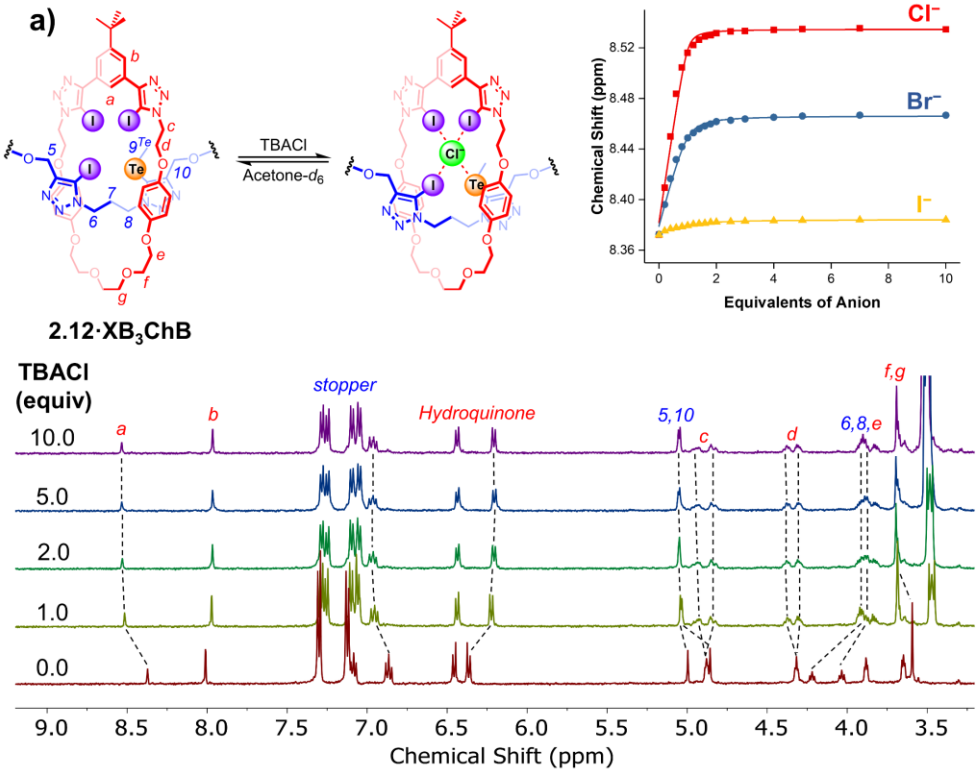
a)
TBACl
Acetone-d_6
Cl⁻
Br⁻
I⁻
Chemical Shift (ppm)
Equivalents of Anion
2.12·XB$_3$ChB
TBACl (equiv)
10.0
5.0
2.0
1.0
0.0
stopper
Hydroquinone
Chemical Shift (ppm)

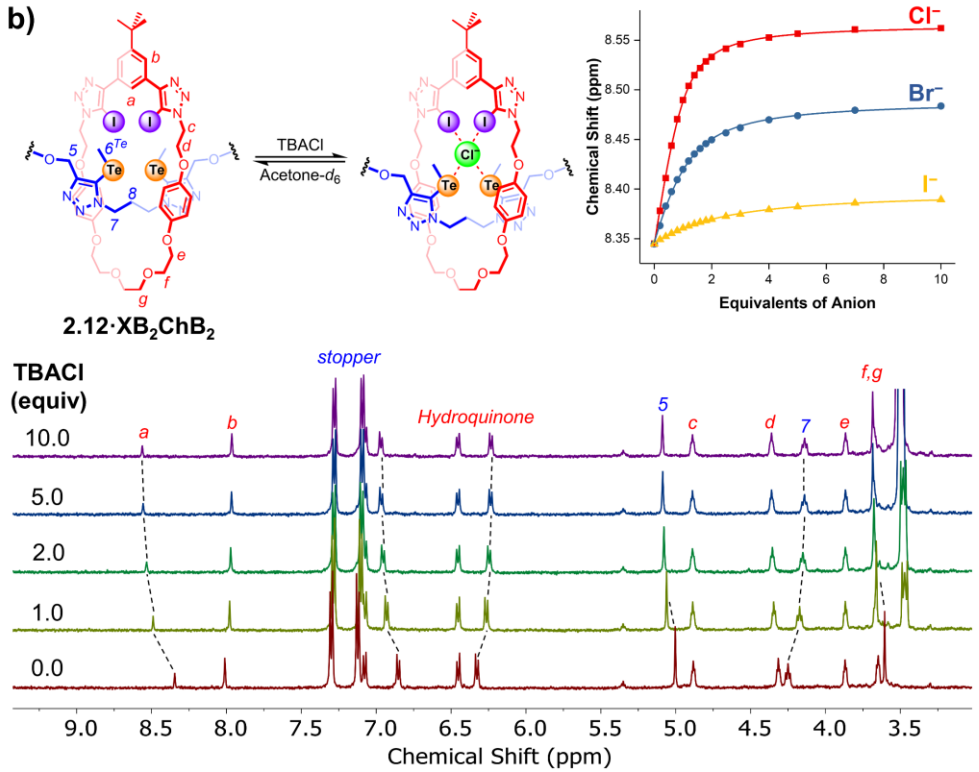
b)
TBACl
Acetone-d_6
Cl⁻
Br⁻
I⁻
Chemical Shift (ppm)
Equivalents of Anion
2.12·XB$_2$ChB$_2$
TBACl (equiv)
10.0
5.0
2.0
1.0
0.0
stopper
Hydroquinone
Chemical Shift (ppm)

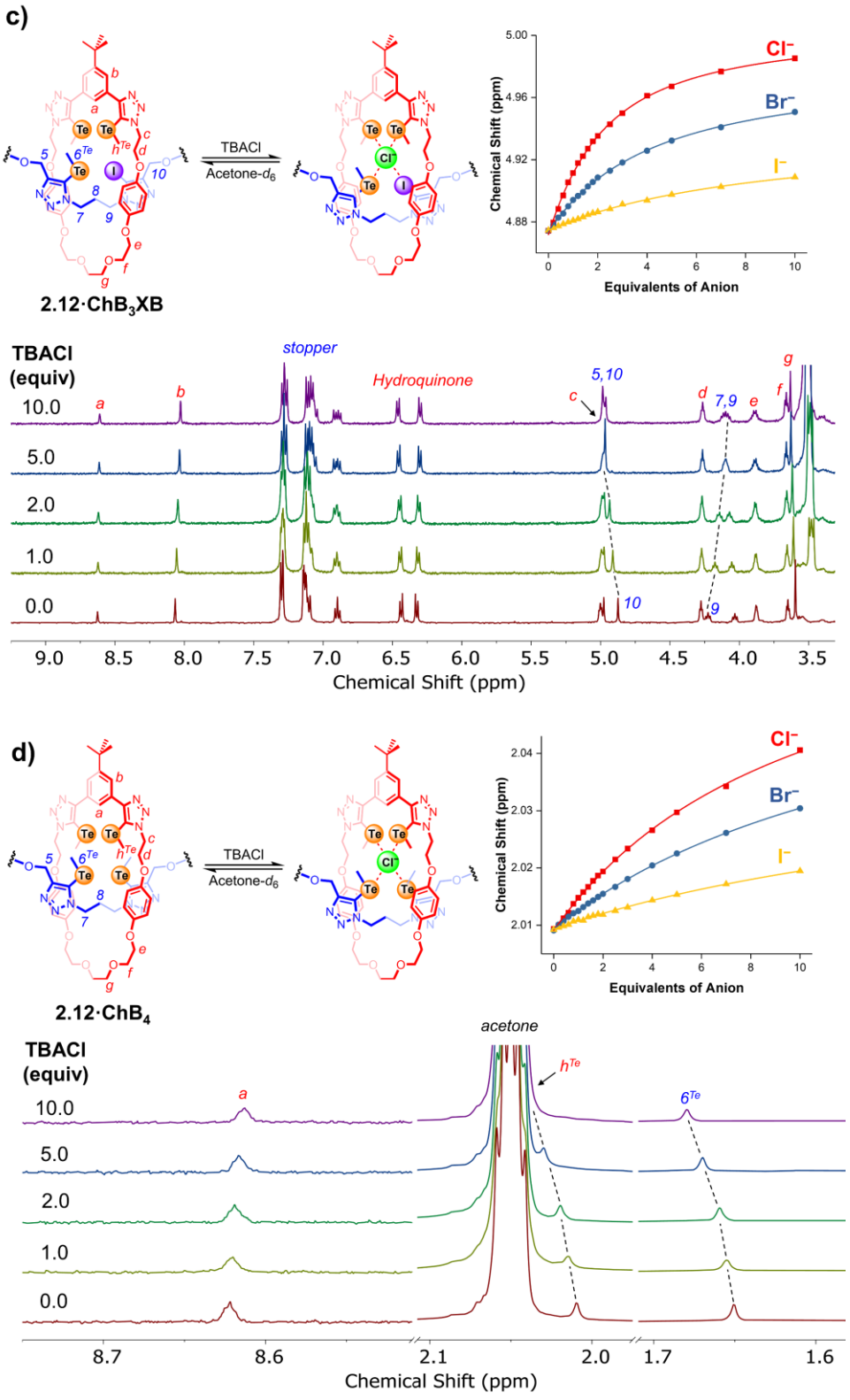

Figure 2.7 Truncated ^{1}H NMR titration spectra of a) **2.12·XB$_3$ChB**, b) **2.12·XB$_2$ChB$_2$**, c) **2.12·ChB$_3$XB** and d) **2.12·ChB$_4$** upon addition of increasing equivalents of TBACl. Inset: Binding isotherms showing changes in chemical shift of proton a) *a, b) a*, c) *10* and d) h^{Te} with increasing equivalents of halide anions. Filled dots represent the experimental data while the solid lines show the calculated isotherms. ([**2.12·ChB$_4$**] = [**2.12·XB$_2$ChB$_2$**] = 0.5 mM, [**2.12·ChB$_3$XB**] = [**2.12·XB$_3$ChB**] = 1.0 mM, 500 MHz, 298 K, acetone-d_6)

Table 2.4: Anion association constants (K_a/M^{-1}) for tetradentate [2]rotaxanes with TBA halide salts in acetone-d_6 determined by ^{1}H NMR titrations.[a]

Anion	**2.12·XB$_3$ChB**	**2.12·XB$_2$ChB$_2$**	**2.12·ChB$_3$XB**	**2.12·ChB$_4$**
Cl$^-$	>10^4	10 600 (394)	557 (13)	172 (2)
Br$^-$	>10^4	4 220 (137)	253 (4)	100 (1)
I$^-$	3 080 (153)	1 090 (21)	99 (2)	56 (1)

[a]K_a values calculated using Bindfit with a 1:1 host-guest binding model.[235,236] Errors (±) are in parentheses and are all <5%. Solvent = acetone-d_6. T = 298 K. [**2.12·ChB$_4$**] = [**2.12·XB$_2$ChB$_2$**] = 0.5 mM. [**2.12·ChB$_3$XB**] = [**2.12·XB$_3$ChB**] = 1.0 mM.

The tetradentate [2]rotaxanes exhibit the same halide anion binding trend as the tridentate analogues, with selectivity towards the most basic Cl$^-$ over Br$^-$ and I$^-$. The incorporation of XB donors into the rotaxane binding sites substantially enhances the binding of halide anions, with the largest increase in K_a seen for Cl$^-$ > Br$^-$ > I$^-$. For example, by replacing one of the axle telluromethyl-triazoles in **2.12·ChB$_4$** with an iodo-triazole moiety, the association constants of the resulting **2.12·ChB$_3$XB** with Cl$^-$, Br$^-$ and I$^-$ increased by 3.2-, 2.5- and 1.8-fold respectively.

In conclusion, the adaptability of the CuAAC-AMT mechanical bond synthesis strategy facilitated the construction of higher order, tetradentate all-ChB and mixed XB/ChB [2]rotaxanes, which displayed tunable halide anion affinity based on the combination, nature and arrangement of incorporated sigma-hole donors.

2.5 Metal Cation Recognition Studies

The incentive to integrate multiple iodo- or telluro-triazole donors into a receptor structural framework stems from the unique property of the anisotropically polarised iodine and tellurium atoms to function as either Lewis acids forming XB/ChB interactions with anions via their electrophilic σ-holes, or Lewis bases to coordinate metal cations. Regarding the latter, ^{1}H NMR titration experiments with diamagnetic Cu(I), Ag(I) and Tl(I) metal cations and the series of σ-hole macrocycles and interlocked [2]rotaxanes were undertaken in CD_3CN.

Initial efforts were directed towards confirming the nature of Cu(I) binding modes by the series of XB and ChB receptors. The addition of $[Cu(CH_3CN)_4]PF_6$ aliquots to a ChB macrocycle **2.1·Te^{Me}** solution elicited progressive upfield shifts of the internal benzene proton signal *a* and downfield perturbations of the $TeCH_3$ signal. These observations, together with the negligible shifts seen for the macrocycle polyether region proton signals, suggested Cu(I) binding occurred in the vicinity of the bis(telluromethyl-triazole)benzene motif. Bindfit[235,236] analysis of the corresponding titration isotherm determined a 1:1 host-guest stoichiometric K_a[Cu(I)] of 22 M^{-1}. In contrast, no Cu(I) binding was observed for XB macrocycle **2.1·I**. Analogous $[Cu(CH_3CN)_4]PF_6$ titration experiments conducted on the σ-hole rotaxane series (**2.11·ChB$_3$**, **2.11·XB$_3$** and **2.12·ChB$_4$**) led to similar upfield shifts of macrocycle internal benzene proton signal *a*, and importantly for ChB rotaxanes **2.11·ChB$_3$** and **2.12·ChB$_4$**, strong perturbations of both macrocyclic and axle $TeCH_3$ signals. Analysis of the resulting binding isotherms with Bindfit[235,236] software revealed 1:1 host-guest stoichiometric K_a[Cu(I)] of 98, 40 and 113 M^{-1} for **2.11·ChB$_3$**, **2.11·XB$_3$** and **2.12·ChB$_4$** respectively (Table 2.5). The significantly higher Cu(I) affinity of ChB receptors relative to XB systems strongly suggested their different Cu(I) binding

modes, either through tellurium (for ChB hosts) or triazole-N atom coordination (for XB hosts). This was further supported by the fact that proto-triazole HB analogue **2.11·HB$_3$**, which could conceivably coordinate to Cu(I) only via triazole-N ligation, exhibited a K_a[Cu(I)] of 40 M^{-1}, identical to that of XB rotaxane **2.11·XB$_3$**.

Encouraged by these promising results, efforts were made to quantify the affinity of the σ-hole receptor series to other "soft" metal cations, namely Ag(I) and Tl(I). Analogous to [Cu(CH$_3$CN)$_4$]PF$_6$ titration experiment, the addition of AgPF$_6$ and TlPF$_6$ to the respective XB and ChB host solutions elicited strong perturbations of proton signals in the triazole-decorated cavities, most noticeable for ChB receptors. In particular, significant line broadening was seen in the cases of tri- and tetradentate ChB rotaxanes **2.11·ChB$_3$** and **2.12·ChB$_4$** upon the addition of one equivalent of AgPF$_6$ and after which only minor shifts were observed, qualitatively implying the formation of highly stable Ag(I)·rotaxane complexes. By monitoring the cation-induced chemical shifts of the σ-hole macrocyclic and interlocked rotaxane series, Bindfit[235,236] analysis of the respective titration isotherms, using a 1:1 host-guest stoichiometric model, determined metal cation association constants (Table 2.5).

Table 2.5: Cation association constants (K_a/M^{-1}) for [2]rotaxanes and macrocycles with various metal salt in CD$_3$CN determined by ^{1}H NMR titrations.[a]

Cation	**2.12·ChB$_4$**	**2.11·ChB$_3$**	**2.1·Te^{Me}**	**2.11·XB$_3$**	**2.1·I**	**2.11·HB$_3$**
[Cu(CH$_3$CN)$_4$]PF$_6$	113 (1)	98 (1)	22 (1)	40 (2)	N.B.[c]	40 (1)
AgPF$_6$	>10^4	>10^4	7 600 (1 001)[b]	125 (1)	N.B. [c]	220 (2)
TlPF$_6$	2 350 (127)	1 570 (52)	84 (3)	318 (7)	120 (4)	282 (6)

[a]K_a values calculated using Bindfit with a 1:1 host-guest binding model.[235,236] Errors (±) are in parentheses and are all <5% unless otherwise stated. Solvent = CD$_3$CN. T = 298 K. [Receptor] = 1.0 mM. [b]Error = 13%. [c]N.B. = no binding.

Overall, the ChB hosts displayed significantly stronger metal cation affinity compared to the XB and HB analogues, with pronounced preference towards Ag(I).

Indeed, the Ag(I) affinity of the ChB macrocycle **2.1·Te^{Me}** (K_a = 7600 M^{-1}) is substantially larger than that of the XB rotaxane **2.11·XB$_3$** (K_a = 125 M^{-1}), and only surpassed by tri- and tetradentate ChB rotaxanes **2.11·ChB$_3$** and **2.12·ChB$_4$** (K_a > 10^4 M^{-1}). The superior metal cation binding capability demonstrated by the ChB macrocycles and rotaxanes is ascribed to the direct coordination of Te to the complementary "soft" Cu(I), Ag(I) and Tl(I) metal cations. In contrast, the comparable association constants and same metal cation selectivity trend of Tl(I) > Ag(I) > Cu(I) indicated both the XB and HB systems complex metal cations via triazole-N ligation. It is also noteworthy that σ-hole interlocked receptors demonstrate stronger cation affinity compared to their macrocyclic component alone, which was rationalised by the increased number of triazole donors and more preorganised, shielded coordination environment of rotaxane hosts.[201,237]

Lastly, to further attest to the role of polarised tellurium donor atoms in metal cation coordination, and to eliminate the possibility of ^{1}H NMR spectral perturbations due to non-specific interactions, ^{1}H NMR titration experiment of ChB rotaxane **2.11·ChB$_3$** and "hard" K^+ cation (as its $BAr^F{}_4$ salt) was undertaken. As expected, no binding of the alkali metal cation was observed, despite the fact that K^+ is of intermediate size (r = 1.52 Å) between Ag(I) (r = 1.29 Å) and Tl(I) (r = 1.64 Å).

In summary, these anion and metal cation recognition studies presented in Sections 2.4 and 2.5 highlight the amphoteric behaviour of electronically polarised tellurium donor atoms to function as both a Lewis acid and base. Their judicious incorporation into various host structural frameworks is envisaged to potentially endow the resulting host molecules with a rich and unique anion and cation coordination behaviour.

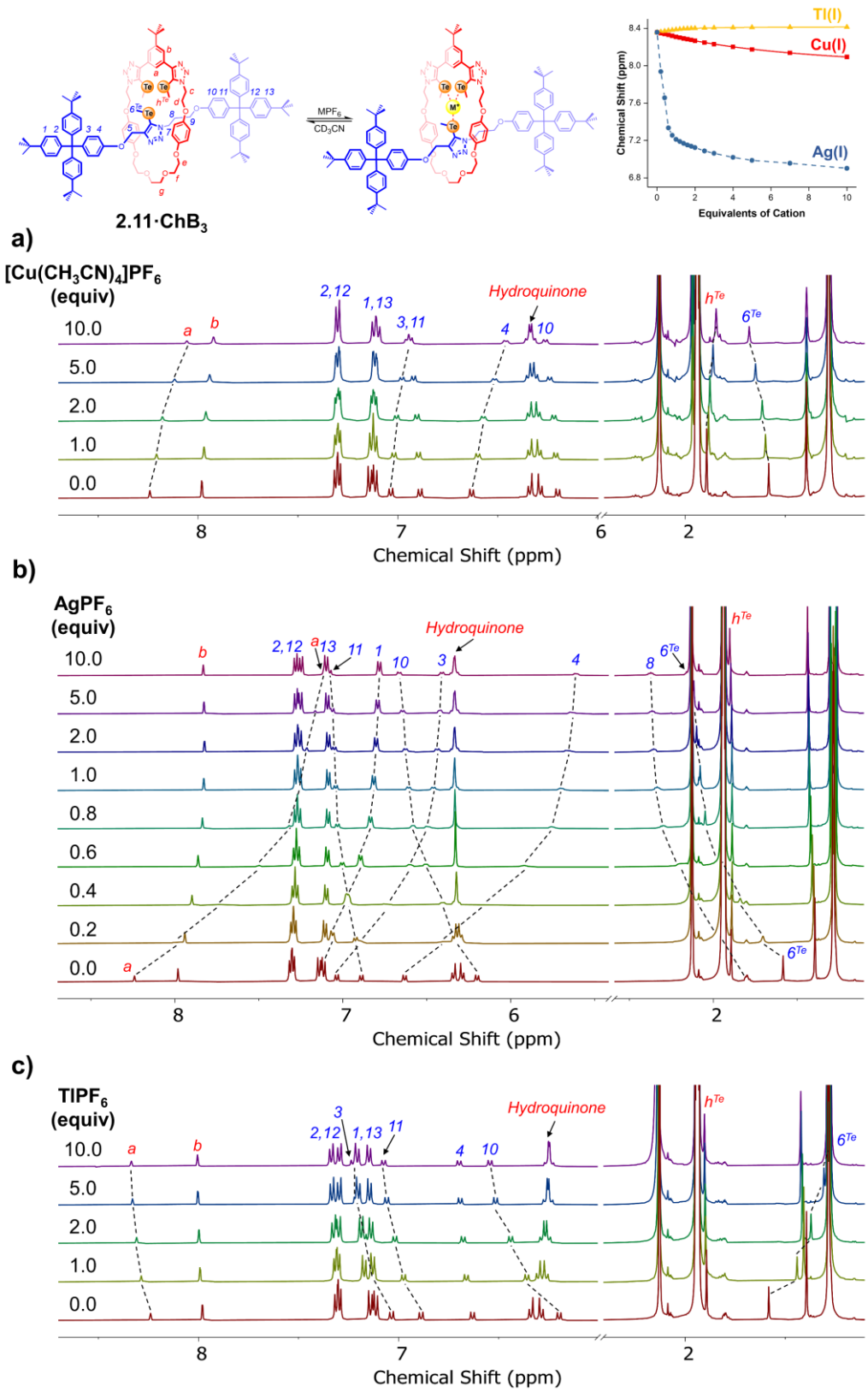

Figure 2.8 Truncated ^{1}H NMR titration spectra of **2.11·ChB$_3$** upon addition of increasing equivalents of a) $[Cu(CH_3CN)_4]PF_6$, b) $AgPF_6$ and c) $TlPF_6$. Inset: Binding isotherms showing changes in chemical shift of proton *a* with increasing equivalents of metal cations. Filled dots represent the experimental data, the solid lines show the calculated isotherms and the dashed lines are visual aid. ([**2.11·ChB$_3$**] = 1.0 mM, 500 MHz, 298 K, CD_3CN)

2.6 Preliminary Ion-Pair Recognition Studies

As introduced in Chapter 1 section 1.4, ion-pair recognition refers to the simultaneous binding of both cations and anions by designed heteroditopic receptors. Such host systems have the advantage of seeking to exploit the cooperative effect of the binding of one ion enhancing the receptor's affinity for the other oppositely charged ion.[136,137,142] Despite the demonstration of enhanced binding strength and selectivity of cation and anion recognition by mechanically interlocked receptors, their application in the field of ion-pair recognition is underexplored.[138,142] The first example of a heteroditopic [2]rotaxane was reported by Beer and co-workers in 2014.[238] The receptor was capable of binding alkali metal halide salts as an axle-separated ion-pair (Figure 2.9). Notably, Na^+ complexation by the rotaxane's calix[4]diquinone macrocycle and axle pyridine N-oxide, led to a 15- and 10-fold increase in the amide binding of Cl^- and Br^- in 4:1 $CDCl_3/CD_3OD$.

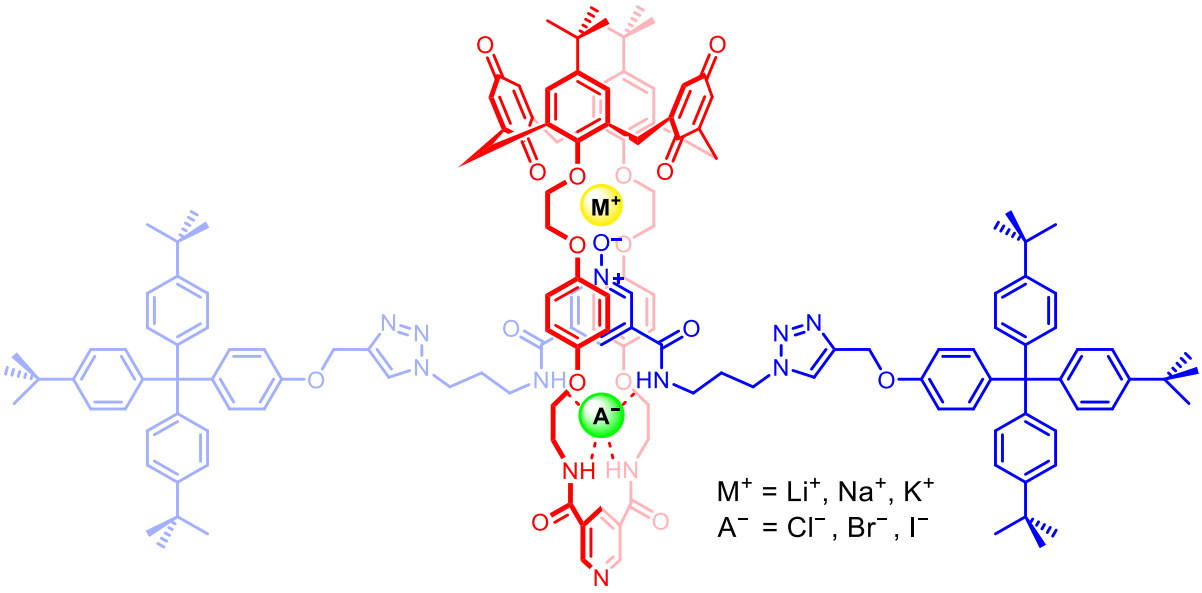

Figure 2.9 Beer's heteroditopic [2]rotaxane binding alkali metal halide salts as axle-separated ion-pairs.[238]

While the "soft" nature of ChB tellurium donors negated their ability to bind "hard" metal cations, the domain created by the macrocycle polyether oxygen and axle

triazole nitrogen atoms in the σ-hole rotaxane series could conceivably chelate to complementary metal cations such as Li^+. This is envisaged to polarise the axle σ-hole donors, allowing the simultaneous recognition of halide anion in the opposite side of the axle component. To this end, qualitative ^1H NMR lithium iodide titration experiments was initially carried out on the mixed XB/ChB [2]rotaxane **2.11·XB$_2$ChB^{Me}**. The addition of $LiClO_4$ to a rotaxane solution in 1:1 $CDCl_3/CD_3CN$ induced significant perturbations to crown ether proton signals, indicative of Li^+ binding by the array of oxygen and nitrogen donor atoms (Figure 2.10). Subsequent addition of one, two and five equivalents of I^- caused progressive downfield shifts of the internal benzene proton signal *a*, indicating cooperative halide anion binding mediated by the rotaxane's three σ-hole donors.

Encouraged by these preliminary results, attention turned to quantify the lithium iodide ion-pair recognition properties of [2]rotaxane **2.11·XB$_2$ChB^{Me}**. Notably, initial ^1H NMR TBAI titration conducted on the free rotaxane receptor in 1:1 $CDCl_3/CD_3CN$ revealed weak binding of I^- with $K_a < 10$ M^{-1}. In contrast, addition of aliquots of TBAI to a solution of rotaxane **2.11·XB$_2$ChB^{Me}** pre-complexed with an equimolar of $LiClO_4$ elicited progressive downfield shifts of internal benzene proton signal *a*. By monitoring the chemical shift of proton signal *a* as a function of anion concentration, Bindfit[235,236] analysis of the resulting binding isotherm determined a notably enhanced I^- binding constant of $K_a = 338$ M^{-1} (Table 2.6). The significantly augmented binding of I^- in the presence of a co-bound Li^+ can be attributed to both favourable electrostatic interactions between the proximal co-complexed ions, and structural rigidification of the [2]rotaxane upon cation chelation. The polarisation of the σ-holes on the axle ChB donor induced by triazole N···Li^+ ligation is also thought to play a role.[239]

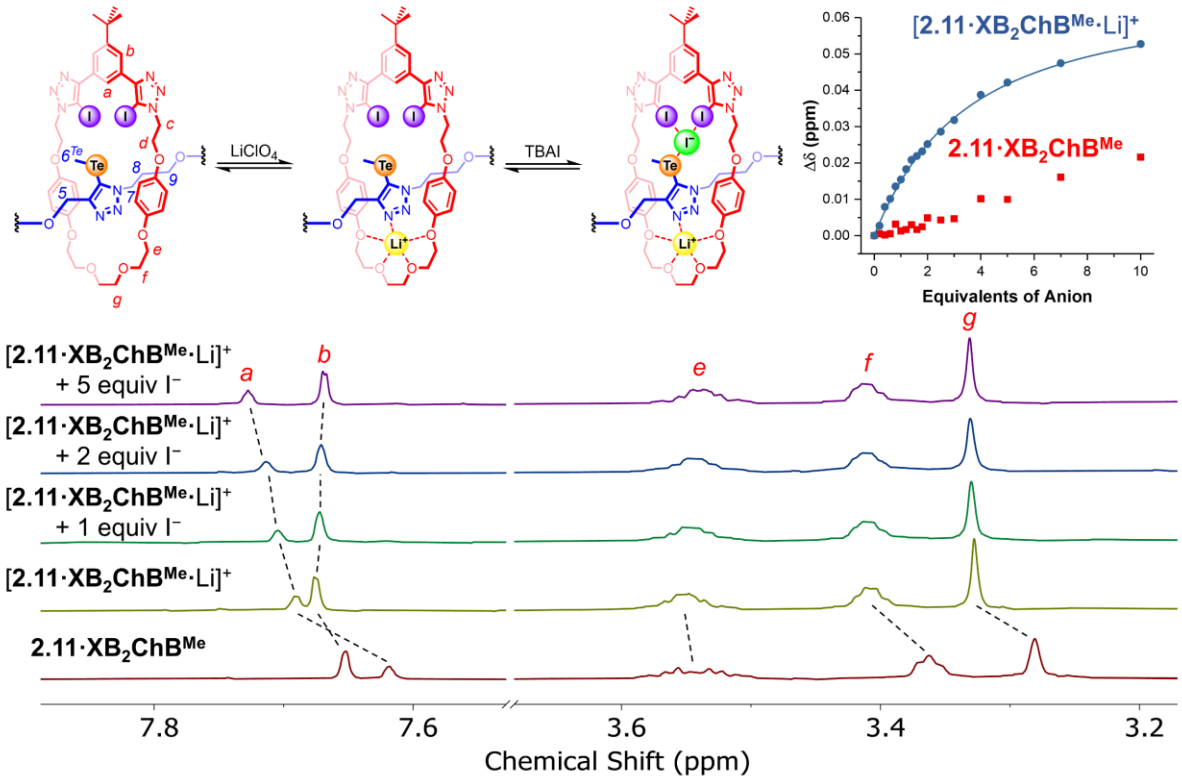

Figure 2.10 Truncated ^{1}H NMR spectra of free [2]rotaxane **2.11·XB$_2$ChB^{Me}**, upon addition of 1 equivalent of $LiClO_4$ and further addition of 1, 2 and 5 equivalents of TBAI. Inset: binding isotherms showing change in chemical shift ($\Delta\delta$) of proton *a* with increasing equivalents of iodide anion. Filled dots represent the experimental data while the solid lines show the calculated isotherms. ([**2.11·XB$_2$ChB^{Me}**] = 1.0 mM, 500 MHz, 298 K, 1:1 $CDCl_3/CD_3CN$)

Table 2.6: Anion association constants (K_a/M^{-1}) for tridentate [2]rotaxane **2.11·XB$_2$ChB^{Me}** with TBAI in the absence and presence of one equivalent of $LiClO_4$ in 1:1 $CDCl_3/CD_3CN$ determined by ^{1}H NMR titrations.[a]

Anion	Cation	**2.11·XB$_2$ChB^{Me}**
I^-	None	<10
	Li^+	338 (10)

[a]K_a values calculated using Bindfit with a 1:1 host-guest binding model.[235,236] Errors (±) are in parentheses and are all <5%. Lithium cation added as $LiClO_4$. Iodide anion added as TBAI. Solvent = 1:1 $CDCl_3/CD_3CN$. T = 298 K. [Rotaxane] = 1.0 mM.

2.7 Conclusion

To summarise, a family of ten novel [2]rotaxanes integrated with up to four iodo-/telluro-/proto-triazole motifs as XB/ChB/HB donors, were synthesised via a CuAAC-AMT strategy. In particular, alkyl- and aryl-appended telluroalkynes were utilised for the first time as one of the axle coupling partners in CuAAC-AMT reactions, granting access to the unprecedented all-ChB and mixed XB/ChB interlocked receptors. The systematic variation of the nature of σ-hole donors around the rotaxane binding pockets allowed modulation of affinity and selectivity towards charged guest species.

Extensive ^{1}H NMR halide anion titration studies conducted on the series of tri- and tetra-dentate σ-hole [2]rotaxanes revealed selectivity for the Cl^- anion. While the presence of XB iodo-triazole motifs endow the interlocked hosts with prodigious anion affinity, the incorporation of ChB telluromethyl-triazole donors into the receptor framework led to a modest improvement to the anion binding strength relative to the HB analogues. However, the attachment of an electron-deficient aryl ring to the Te donor atoms significantly augmented the Te···anion ChB interactions, demonstrating the unique tunability of ChB in the context of anion recognition.

Furthermore, the telluro-triazole-functionalised [2]rotaxanes demonstrated affinity and selectivity towards "soft" metal cations, such as Ag(I) and extremely toxic Tl(I), compared to iodo- and protic-triazole congeners. This exceptional metal cation recognition property of the tellurium containing receptors was attributed to their Lewis basic complementary Te donors. Hence the amphoteric Lewis acid and base character of the polarised Te atoms in the telluro-triazole-based [2]rotaxanes was demonstrated by these interlocked hosts' capability to recognise *both* anions and cations.

Lastly, as proof-of-concept for potential ion-pair binding, complexation of a mixed XB/ChB [2]rotaxane with a Li^+ cation switched on the affinity of the receptor for I^-, with the two co-bound ions existing as an axle-separated ion-pair. The enhancement in iodide anion affinity was ascribed to favourable electrostatics between the proximal oppositely charged ions, structural preorganisation, and triazole N-coordinated Li^+ induced polarisation of the Te σ-holes of the axle ChB donor. Importantly, this serves as the first example of σ-hole mediated ion-pair recognition in interlocked heteroditopic hosts.

2.8 Future Work

Selective sensing of charged species via tailor-made synthetic receptors has widespread industrial and biological applications such as the detection of toxic anions/cations, medical diagnosis and live-cell imaging.[62] For these reasons, future work of this project will entail the functionalisation of telluro-triazole motifs with appropriate reporter groups (e.g. anthracene, ferrocene) for sensing complementary anions, cations and ion-pairs via changes in the receptors' fluorescence/redox responses (Figure 2.11).

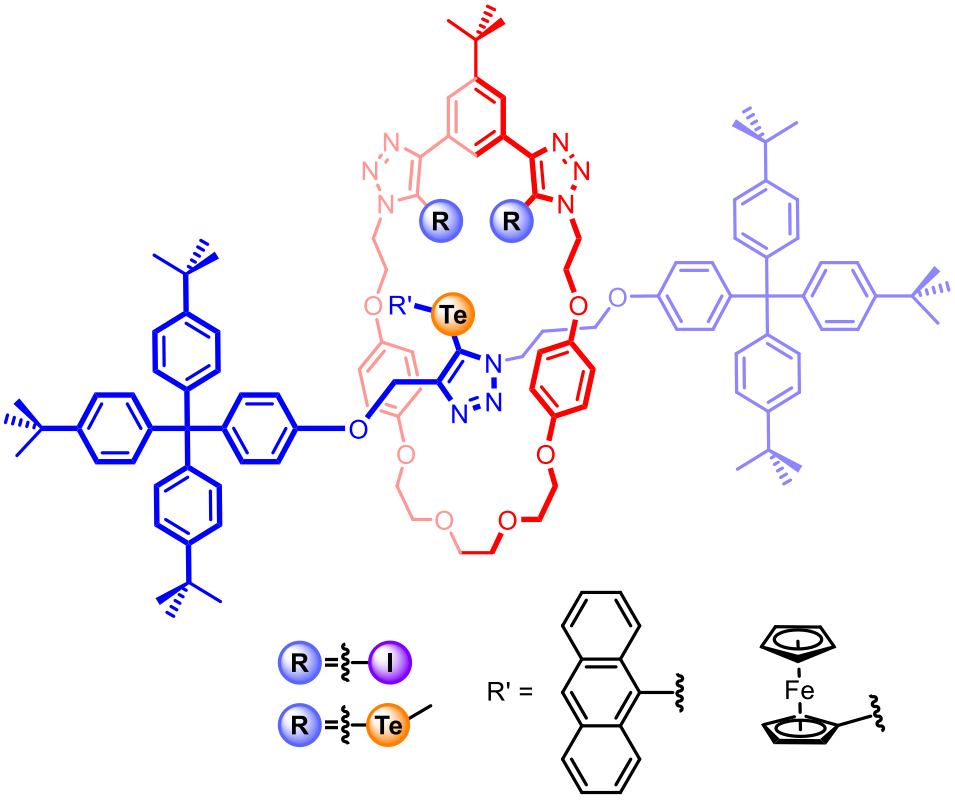

Figure 2.11 Proposed structures of σ-hole [2]rotaxanes incorporated with optical/redox reporter groups.

Chapter 3

Halogen Bonding Strapped Porphyrin BODIPY Rotaxanes for Dual Optical and Electrochemical Anion Sensing

Chapter 3 Halogen Bonding Strapped Porphyrin BODIPY Rotaxanes for Dual Optical and Electrochemical Anion Sensing

3.1 Introduction

The promising potential of mechanically interlocked molecules (MIMs) in applications such as molecular switches,[195,196,240–245] catalysis,[197,198,246–254] drug delivery[255–257] and molecular recognition[201,202,215] has drawn much research interest in their derivatisation in recent years. In particular, by virtue of their topologically shielded three-dimensional binding pockets, MIMs constructed for anion recognition have been shown to exhibit superior anion guest binding affinity and selectivity compared to non-interlocked analogues.[199,237,258] Capitalising on the improved binding properties, integration of suitable optical- or redox-responsive reporter groups proximal to an anion recognition site can allow the transduction of the anion binding event via fluorescent,[228,259–269] colourimetric[112,270–274] and electrochemical[227,274–280] methods. Among the diverse number of reporter groups, porphyrins and BODIPYs present themselves as excellent candidates for incorporation into the molecular frameworks of MIMs as signalling motifs due to their rich optical and redox properties, synthetic accessibility and ease of functionalisation.

In the following sections, the fundamental properties of porphyrins and BODIPYs are briefly discussed, followed by examples of their incorporation into MIMs as reporter groups for anion sensing. Dual-signalling receptors capable of detecting anions via two distinct readout responses will also be introduced.

3.1.1 Porphyrins

The importance of porphyrins is best illustrated by the pivotal roles they play in many biological processes. For example, haemoglobin and myoglobin are both derived from iron(II) porphyrin (haem) (Figure 3.1a) and are responsible for the transport of oxygen in the bloodstream. Photosynthesis in plants converts solar energy into chemical energy while releasing oxygen as a by-product. This vital process is carried out by chlorophyll, which consists of magnesium(II)-containing porphyrins (Figure 3.1b) and chlorins (partially reduced porphyrin).

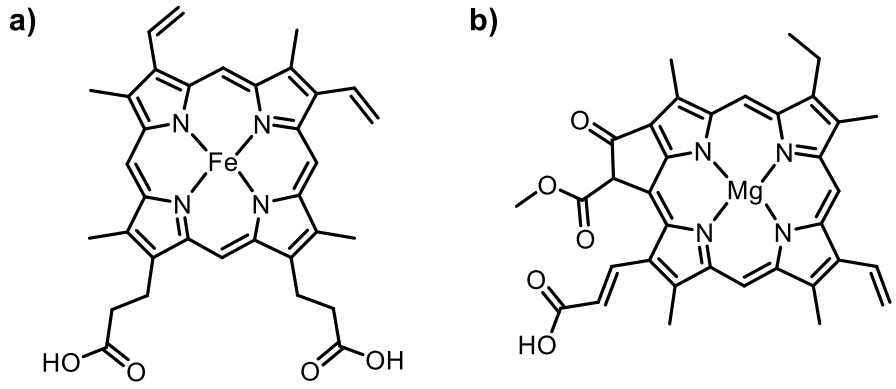

Figure 3.1 Chemical structures of a) heme b and b) chlorophyll c_1.

3.1.1.1 Properties of Porphyrins

Porphyrins are macrocycles comprised of four pyrrole groups covalently connected to each other at their α-positions via methine (CH) linkers. They are highly conjugated compounds and contain 18 delocalised π-electrons in the ring, obeying Hückel's rule of aromaticity. The central cavity created by the pyrrole subunits allows porphyrins to chelate to almost all metal cations.[281] Porphyrins are also excellent chromophores and all their derivatives are intensely coloured. Typically, porphyrins exhibit an intense higher energy band (Soret band) at ca. 400 nm, accompanied by several weaker, lower energy Q bands at ca. 450–700 nm (Figure 3.2). Electrochemically, porphyrins display two quasi-reversible $P/P^{+\bullet}$ and $P^{+\bullet}/P^{2+}$

oxidation couples, both of which are sensitive to the substitutional pattern of the porphyrin macrocycle, chelated metal centre and axially coordinated ligands of the metalloporphyrin core.[282]

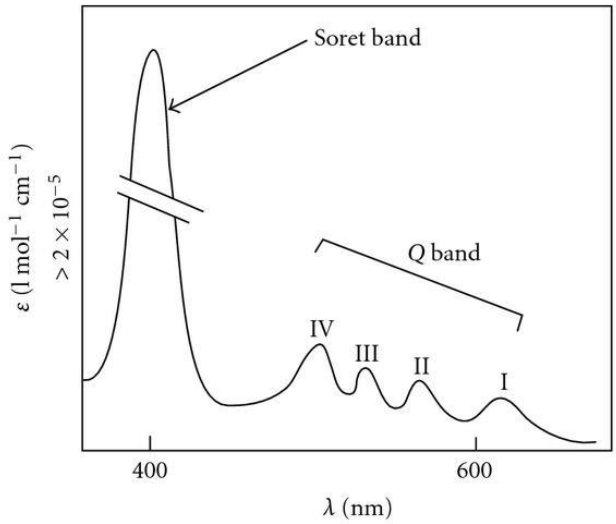

Figure 3.2 Typical porphyrin absorption spectrum showing the Soret and Q bands. Reproduced from reference 283.

3.1.1.2 Synthesis of Porphyrins

The laboratory synthesis of porphyrins can be dated back to the 1940s when Rothemund heated a pyridine solution of pyrrole and benzaldehyde at 220 °C inside a sealed tube for 48 hours to afford tetraphenylporphyrin (TPP) in ca. 10% yield.[284] This method was later improved by Alder, who refluxed both pyrrole and benzaldehyde in propionic acid at 141 °C, which, following washing with methanol and water, afforded TPP in ca. 20% yield.[285] These two procedures, however, both require harsh conditions and high reaction temperature, limiting the choice of pyrrole and aldehyde precursors. To circumvent this problem, Lindsey, in 1986, reported an alternative two-step one-pot synthetic pathway which proceeded efficiently at room temperature (Scheme 3.1).[286] The first step of this protocol involves the self-assembly of pyrrole and aldehyde precursors to form a porphyrinogen intermediate in the presence of acid catalyst (e.g. TFA or $BF_3{\cdot}OEt_2$). The porphyrinogen is subsequently oxidised via the

addition of quinone-based oxidising agents (e.g. 2,3-dichloro-5,6-dicyano-1,4-benzoquinone (DDQ), *p*-chloranil) to give the fully conjugated target porphyrin. These mild reaction conditions allow the conversion of variously functionalised pyrrole and aldehyde into corresponding porphyrins, greatly broadening the scope of the reaction.

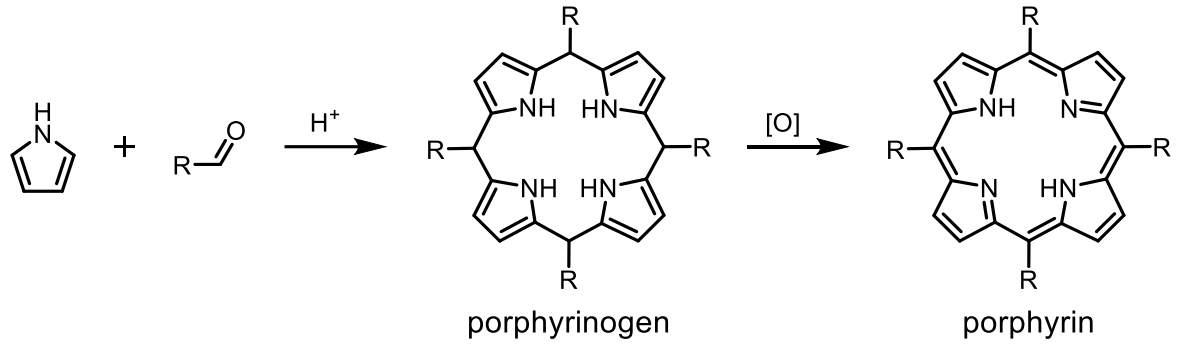

Scheme 3.1 Lindsey's one-pot synthesis of porphyrin.[286]

3.1.1.3 Porphyrin-based Anion Receptors

While porphyrins possess highly desirable optical properties, it is their unique ability to coordinate to Lewis bases via the metalloporphyrin centres that differentiate them from other reporter groups. As such, porphyrins have been incorporated into various anion receptor frameworks, such as picket fences,[112,287–296] cages[297–299] and MIMs.[270,278,300,301]

In one example, Jang and co-workers prepared a picket-fence type zinc(II) metalloporphyrin with four pendant proto-triazole groups (Figure 3.3).[292] The receptor demonstrated strong binding to halide anions, with selectivity towards Cl^- ($K_a > 10^8\ M^{-1}$) in CH_2Cl_2. ^1H NMR, UV–visible absorption and computational modelling suggested the halide anion is bound by four convergent triazole C–H HB interactions, and is additionally coordinated to the Lewis acidic zinc(II) centre in the metalloporphyrin core.

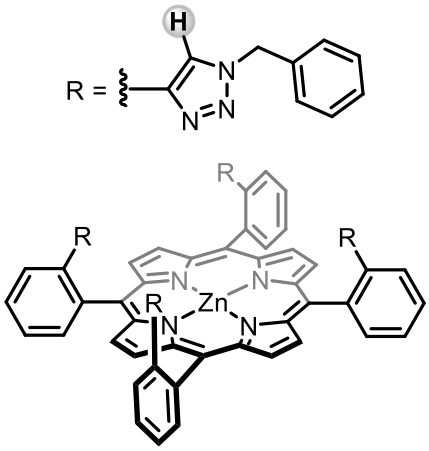

Figure 3.3 Jang's proto-triazole-based picket fence porphyrin receptor.[292]

The incorporation of porphyrins into MIMs as signalling units for anion binding events has previously been reported by the Beer group. In one study, [2]rotaxanes, with porphyrins either as stopper groups or covalently attached to the macrocycle, were prepared by a chloride-template clipping methodology (Figure 3.4a).[278] Despite the proximity of porphyrins to the anion binding site, both receptors were ineffective as optical sensors as negligible changes were observed in the porphyrin absorption and emission spectra upon anion addition. However, electrochemical studies revealed the capability of the interlocked systems to sense Cl^- via cathodic shifts of the porphyrin $P/P^{+\bullet}$ oxidation couple. In addition to these rotaxanes, the same group also reported the synthesis of a porphyrin-functionalised [2]catenane via a similar anion-template strategy (Figure 3.4b).[270] Addition of Cl^- to a solution of the receptor in DMSO induced small but significant hypsochromic shifts to porphyrin absorption peaks, indicative of Cl^- binding (K_a = 2400 M^{-1}), while no perturbations were observed for the bulkier halides (Br^- and I^-).

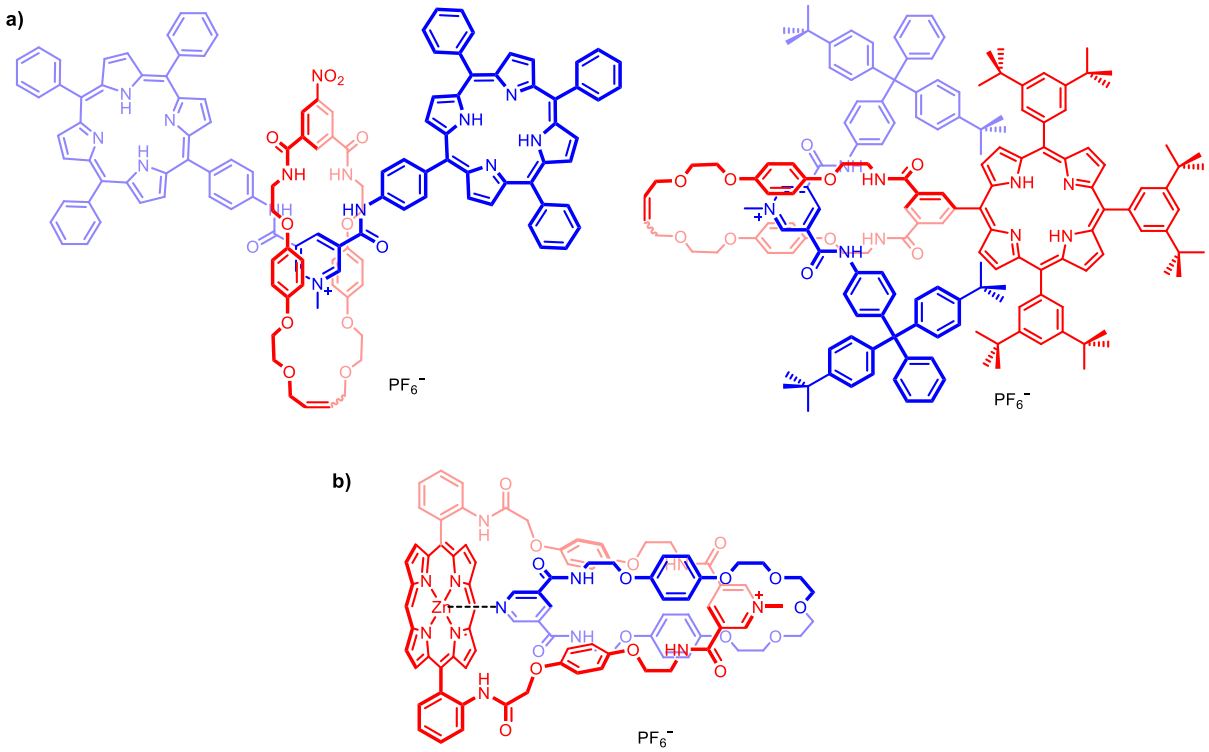

Figure 3.4 Beer's porphyrin-functionalised a) [2]rotaxanes[278] and b) [2]catenane.[270]

3.1.2 BODIPYs

3.1.2.1 Properties of BODIPYs

4-Bora-3a,4a-diaza-s-indacene (BODIPY) is a popular class of fluorophore dye that has been exploited in many areas such as bio-imaging, fluorescent sensing and photovoltaic devices.[302–304] This wide range of applications of BODIPYs is attributable to their exceptional photophysical properties,[305,306] which are characterised by large molar absorption coefficients, substituent tunable long excitation and emission wavelengths (>500 nm) and high fluorescence quantum yields.

3.1.2.2 Synthesis of BODIPYs

BODIPYs can be synthesised in a one-pot fashion similar to Lindsey's procedure for porphyrin preparation (Scheme 3.2).[307] The initial acid-catalysed condensation of pyrrole and benzaldehyde affords the corresponding dipyrromethane. To disfavour the formation of porphyrinogen or polymeric side products, excess amounts of pyrrole or

2-substituted pyrroles are generally used. The generated dipyrromethane is chemically unstable and is therefore immediately oxidised into the dipyrrin (dipyrromethene) by the addition of DDQ or *p*-chloranil. Subsequent complexation of dipyrrin with boron using $BF_3{\cdot}OEt_2$ under basic conditions yields the BODIPY dye. Alternatively, BODIPYs can also be synthesised by condensation reaction between pyrroles and acid chlorides, or via 2-ketopyrrole precursors.[305] Both of these methods enable access to asymmetric BODIPY compounds.

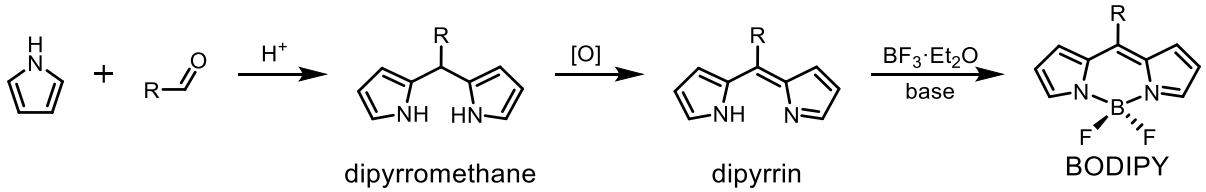

Scheme 3.2 One-pot synthesis of BODIPY dye.[307]

3.1.2.3 BODIPY-based Anion Receptors

The majority of BODIPY-functionalised anion receptors are chemodosimeters, where sensing is achieved via anion-induced irreversible chemical reactions that modulate the photophysical properties of BODIPYs.[306,308] This type of sensory mechanism, however, limits the scope of detectable guests to reactive anions (e.g. F^-, CN^-, ClO^-), and the same spectral response can potentially be elicited by the presence of other reactive impurities. Furthermore, the chemically transformed receptors cannot be recovered. These problems can be circumvented via the use of chemosensors, which reversibly bind target anions utilising non-covalent interactions. However, the incorporation of BODIPYs in such supramolecular hosts is underexploited.[309–313]

In one example, Rurack and co-workers prepared an amido-thiourea-appended BODIPY dye (Figure 3.5a), capable of sensing F^- in 50% water/DMSO via significant quenching of the BODIPY emission.[314] This spectral change was ascribed to a photo-induced electron transfer (PET) process, induced by the HB amido-thiourea mediated

F^- binding. Impressively, functionalisation of a test-strip with the probe allowed for the determination of F^- content in pure water with the aid of a fluorescence lateral flow reader.

The incorporation of BODIPY into MIM frameworks is uncommon,[315–322] and the exploitation of BODIPY as reporter groups in anion binding interlocked hosts is even rarer. Lin and co-workers prepared a BODIPY-functionalised [2]rotaxane (Figure 3.5b), capable of selectively sensing $H_2PO_4^-$ in CH_3CN with quenching of BODIPY-centred emission.[323] Anion binding was mediated by favourable electrostatic interactions, and HB interactions arising from the two triazolium C–H donor groups on the axle.

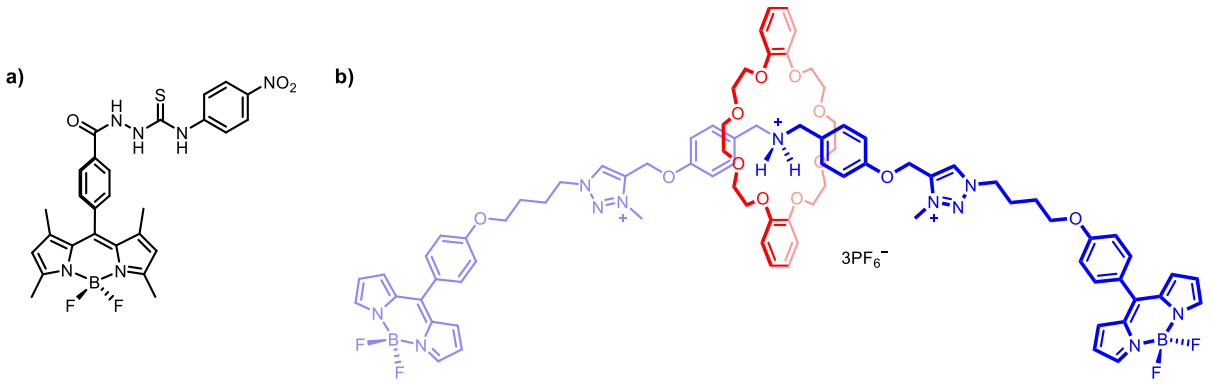

Figure 3.5 a) Rurack's BODIPY-based HB receptor.[314] b) Lin's BODIPY-stoppered [2]rotaxane.[323]

3.1.3 Dual Optical and Electrochemical Anion Sensing

Dual/multi-channel anion sensors capable of detecting guests via more than one read-out response (e.g. optical and redox) have notable advantages over traditionally employed mono-channel transducing receptors. Firstly, this type of sensor can significantly reduce the likelihood of false positives. Secondly, external interferences can be minimised. For example, if guest sensing via a change in emission of the receptor is thwarted by the presence of external fluorescence quenchers (e.g. oxygen,

iodide) in the analyte solution, electrochemical sensing can then potentially act as an alternative, or back-up, sensory mechanism.

Despite the benefits of having additional sensory output channels, the number of reported dual-/multi-signalling anion sensors is surprisingly low.[324–329] In one example by Sessler and co-workers,[330] a redox-active tetrathiafulvalene (TTF) was incorporated into the backbone of diindolylquinoxaline (DIQ) (Figure 3.6a), which functions as an optical reporter group and anion binding site. The receptor was found to be selective towards $H_2PO_4^-$ in CH_2Cl_2, capable of sensing the anion via quenching of the DIQ-centred emission. Cyclic voltammetric analysis revealed significant cathodic shifts of the first oxidative redox couple of TTF upon addition of $H_2PO_4^-$. Beer and co-workers has reported the preparation of dual signalling macrocycles consisting of photo-active Ru(II)-bipyridyl and redox-active ferrocene-/cobaltocenium motifs (Figure 3.6b).[331] Addition of Cl^- to the receptor solution in CH_3CN led to an increase in Ru(II)-bipyridyl-based MLCT emission intensity and lifetime. The same halide anion also induced significant cathodic perturbations of the ferrocene (Fc/Fc^+) or cobaltocenium (Co/Co^+) redox couples.

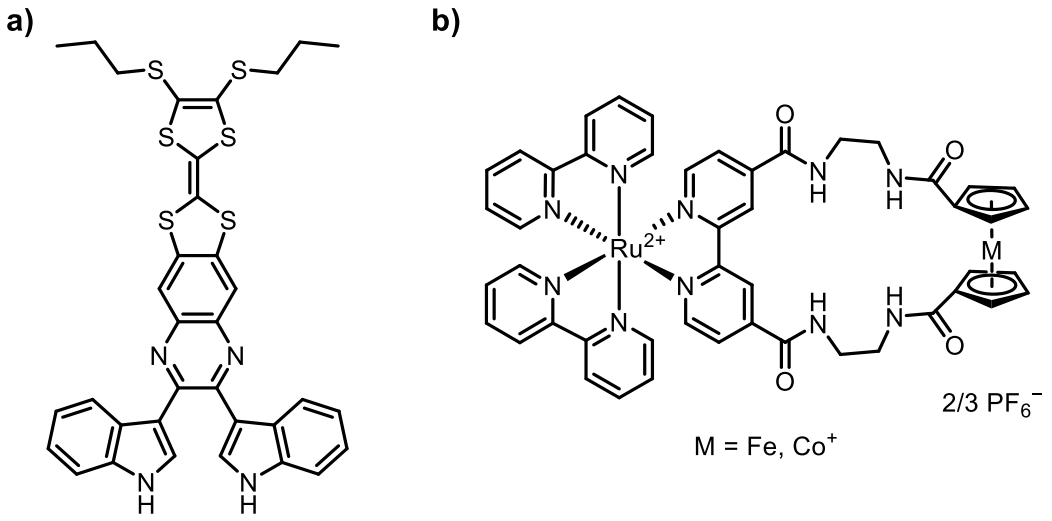

Figure 3.6 a) Sessler's DIQ-based receptor incorporated with redox-active TTF.[330] b) Beer's Ru(II)-complexed ferrocene/cobaltocenium-functionalised macrocycle.[331]

3.2 Chapter Aims

This chapter is divided into two parts:

Part I: Part I entails the incorporation of the potent XB 1,3-bis(iodotriazole)benzene donor motif into strapped zinc(II) metalloporphyrin macrocycles for anion recognition and sensing (Figure 3.7a). By virtue of the combination of XB donors on the strap, the Lewis acidity of the zinc(II) metalloporphyrin and the macrocyclic effect, it was envisaged that the target macrocycles would display superior anion binding affinity and selectivity in comparison to the strap-free zinc(II) tetraphenylporphyrin (ZnTTP) control.

Part II: Inspired by the superior anion binding properties of MIMs compared to non-interlocked analogues, Part II of this project aims to construct XB strapped porphyrin [2]rotaxanes via active metal template MIM synthesis (Figure 3.7b). To further improve the potential anion guest sensing performance, BODIPY motifs are incorporated as axle stoppers in the rotaxane host framework to facilitate dual optical and electrochemical anion sensing. Electronic absorption, fluorescence and electrochemical voltammetric titration studies are conducted to probe the capability of the [2]rotaxanes to sense anions via changes in the optical and redox responses of the porphyrin and BODIPY reporter groups.

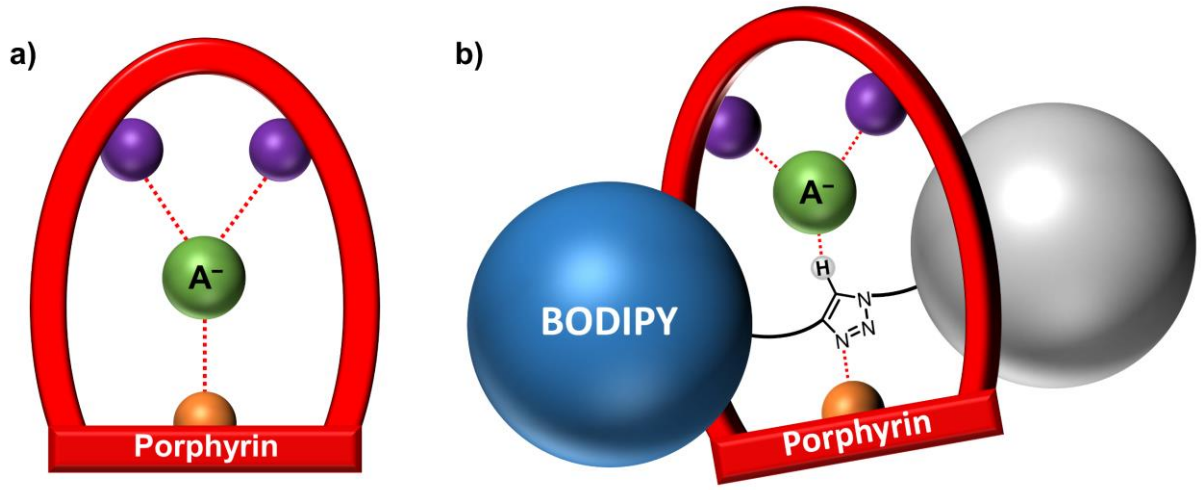

Figure 3.7 Schematics of target XB a) strapped porphyrin and b) porphyrin-BODIPY [2]rotaxane. Purple spheres represents XB donors; orange sphere represents metal centre of porphyrin; A^- represents the anion.

3.3 Halogen Bonding Strapped Porphyrins

3.3.1 Design and Synthesis of XB Strapped Porphyrins

The retrosynthesis of the target porphyrin-functionalised receptor **3.1**, containing the 1,3-bis(iodotriazole)benzene XB donor motif on the strap, is shown in Scheme 3.3. Conceivably, the strapped porphyrin can be prepared either by route a) a CuAAC click cyclisation reaction between a porphyrin-functionalised bis-azide and bis-iodoalkyne or, route b) a pyrrole-aldehyde condensation reaction between an appropriate XB bis-aldehyde derivative and dipyrromethane, forming the porphyrin core as the final reaction. Route a), however, necessitates the prior synthesis of isomerically pure α,α-atropisomer of the porphyrin precursor, which could be difficult to isolate from the crude racemic mixture. To circumvent this, route b) was therefore pursued.

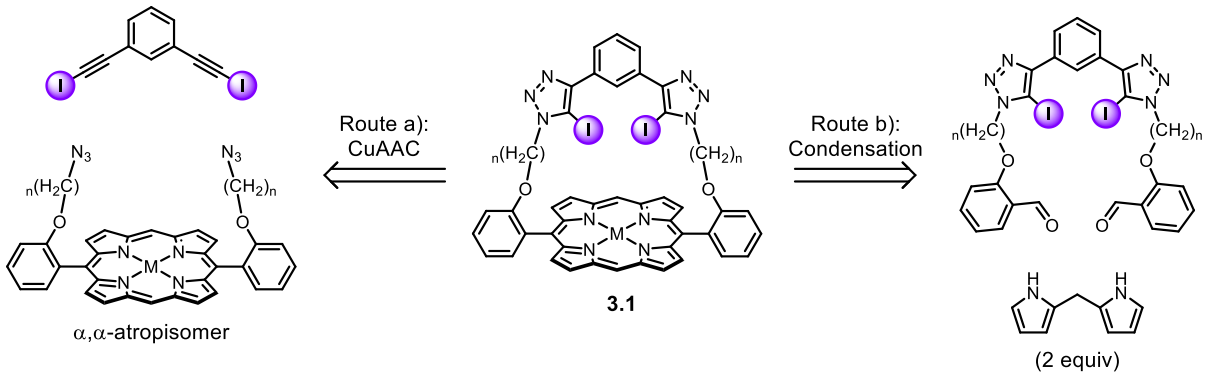

Scheme 3.3 Retro-synthesis of target XB strapped porphyrin **3.1**.

3.3.1.1 Synthesis of Bis-aldehyde and Dipyrromethane Precursors

Synthesis of XB bis-aldehyde strap component **3.5** is outlined in Scheme 3.4a. 1,3-Bis(iodo-alkynyl)benzene **3.2**[332] was prepared by first treating the proto-alkyne precursor with ^{n}BuLi at −78 °C to generate the lithium acetylide complex, which was subsequently exposed to elemental I_2 to give the iodinated alkynyl product **3.2** in 95% yield. To prepare the azide precursors **3.4a–b**,[333] commercially available salicyaldehyde was reacted with excess butyl or pentyl dibromide under basic conditions to afford **3.3a–b**. Nucleophilic substitution of the bromide with NaN_3 in DMSO gave the azides **3.4a–b** in 97% yields. The bis-aldehyde-functionalised XB strap was then prepared by CuAAC click reaction between bis-iodoalkyne **3.2** and two equivalents of azides **3.4a–b**. Chromatographic purification afforded the products **3.5a** and **3.5b** in a yield of 93% and 76%, respectively.

2,2'-Dipyrromethane **3.6** was prepared according to a literature procedure (Scheme 3.4b).[334] Specifically, paraformaldehyde was added to excess freshly distilled pyrrole in the presence of a catalytic amount of trifluoroacetic acid (TFA) at 55 °C for 3 hours. Following neutralisation by NaOH and removal of unreacted pyrrole under reduced pressure, the crude product was purified by silica gel column chromatography to afford compound **3.6** in 60% yield.

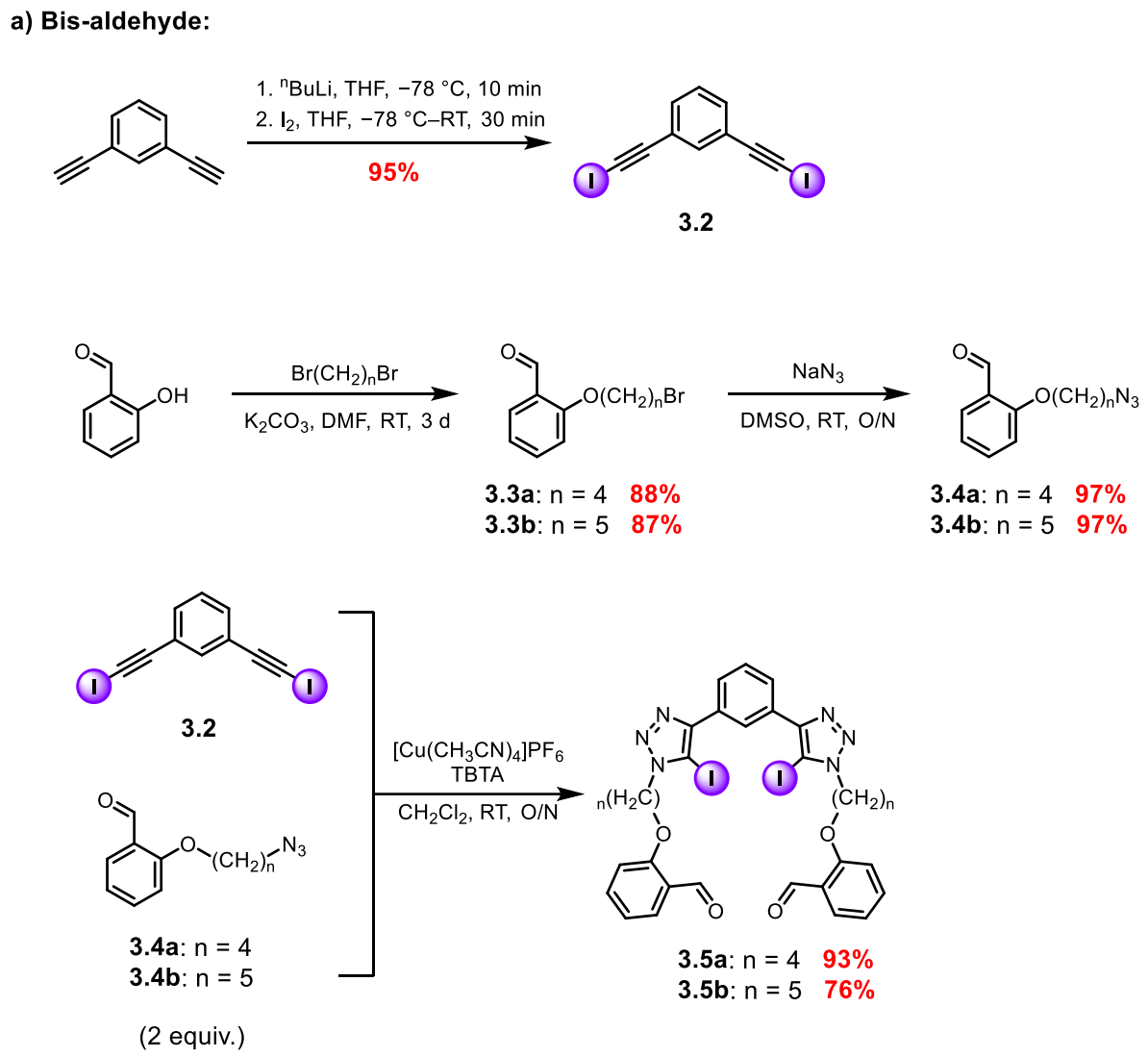

Scheme 3.4 Synthetic routes to a) bis-aldehyde **3.5a–b** and b) dipyrromethane **3.6** precursors.

3.3.1.2 Synthesis of XB Strapped Porphyrins

To prepare the target XB strapped porphyrins (Scheme 3.5), a TFA-catalysed condensation reaction between bis-aldehydes **3.5a–b** and 2,2'-dipyrromethane **3.6** was carried out, followed by in situ oxidation with DDQ to give the cyclised, strapped free-base porphyrins **3.1a·H2** and **3.1b·H2** in 43% and 21% yields respectively. The

Lewis acidic metal centre zinc(II) was introduced into the porphyrin ligand by treating the metal-free porphyrins with excess $Zn(CH_3COO)_2{\cdot}2H_2O$ to afford **3.1a–b·Zn** quantitatively.

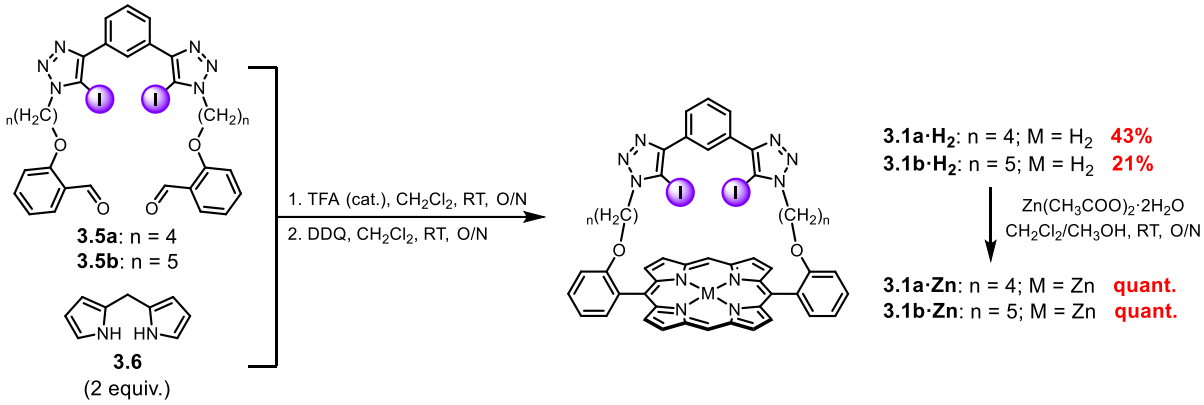

Scheme 3.5 Synthesis of target XB strapped zinc(II) porphyrins **3.1a–b·Zn**.

Both **3.1a·Zn** and **3.1b·Zn** were characterised by ^{1}H, ^{13}C NMR spectroscopies and high-resolution ESI-MS. Single crystals suitable for X-ray diffraction studies of both compounds were obtained by slow evaporation of CH_2Cl_2/*n*-hexane (**3.1a·Zn**) or CH_2Cl_2/*n*-hexane/THF (**3.1b·Zn**) receptor solutions (Figure 3.8). In both structures, the iodo-triazoles are twisted out of the plane of the central benzene unit, likely due to the bulky size of the iodine atoms. The covalent strap is also found to bend towards the porphyrin core. The longer strapped porphyrin **3.1b·Zn** co-crystallises with a THF solvent molecule, with the oxygen from THF coordinating to the Lewis acidic porphyrin zinc(II) metal.

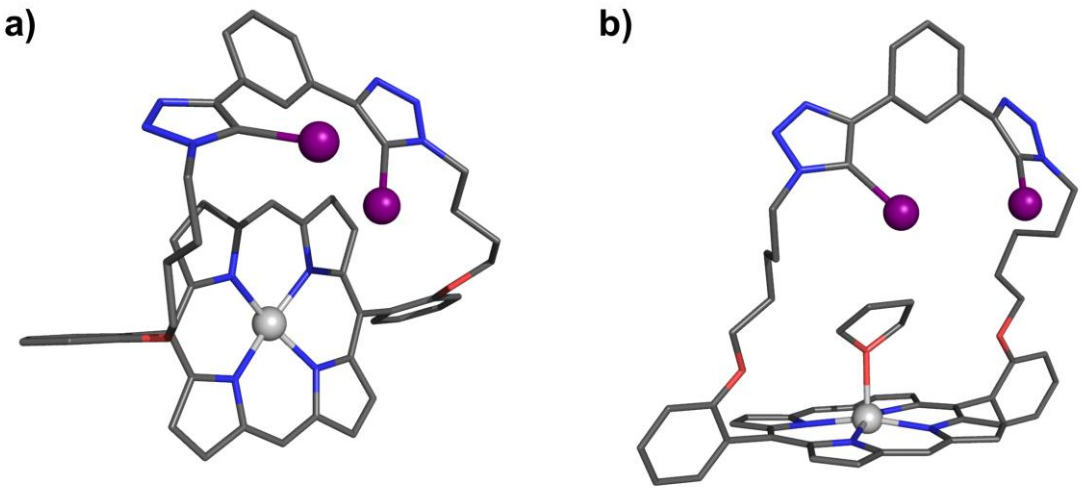

Figure 3.8 Crystal structure of a) **3.1a·Zn** and b) **3.1b·Zn**. Hydrogen atoms are omitted for clarity. Gray = carbon, blue = nitrogen, red = oxygen, purple = iodine, silver = zinc.

3.3.2 Anion Recognition Properties

3.3.2.1 ^{1}H NMR Titration Experiments

The anion binding properties of the XB strapped porphyrins were initially investigated by a preliminary ^{1}H NMR titration of **3.1a·Zn** with TBACl in acetone-d_6 (Figure 3.9). The addition of TBACl to the macrocycle solution induced significant downfield shifts of internal benzene proton *c*, accompanied by upfield perturbations to the porphyrin aromatic signals *l*, *m* and *n*. This indicates the halide anion was bound inside the strapped porphyrin cavity, stabilised by both the XB donors on the strap and axial ligation to the Lewis acidic zinc(II) metalloporphyrin.[335] Interestingly, during the addition of one equivalent of chloride, these proton signals (*l*–*n* and *c*) also experienced significant broadening and splitting, but merged again after an equivalent of anion was administered. This origin of splitting was unclear but potentially due to Cl^- binding being relatively slow on the NMR timescale. Negligible chemical shifts observed after addition of an equimolar of chloride indicated the binding site of the host was saturated by the halide guest, qualitatively implying strong anion binding. Indeed, by monitoring the chemical shift of internal benzene proton *c* as a function of

chloride concentration, Bindfit[235,236] analysis using a 1:1 host-guest stoichiometric binding model determined an association constant K_a (Cl^-) > 10^4 M^{-1}.

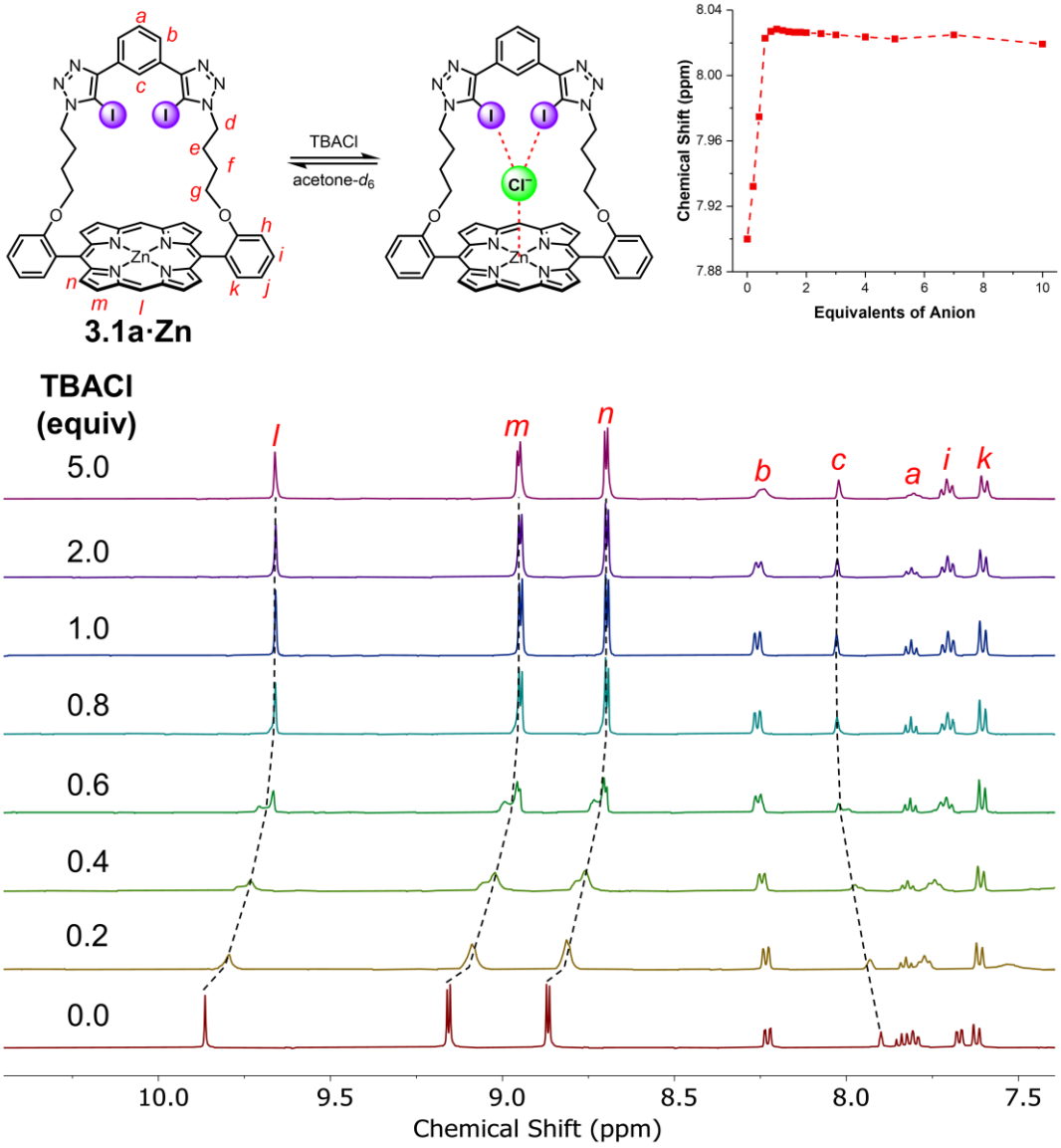

Figure 3.9 Truncated ^{1}H NMR titration spectra of **3.1a·Zn** with TBACl. Inset: Binding isotherm showing changes in chemical shift of proton signal *c* with increasing equivalents of chloride anion. Filled dots represent the experimental data while dashed lines are visual aid. (500 MHz, 298 K, acetone-d_6)

Attempts to quantify the anion binding capabilities of longer strapped porphyrin **3.1b·Zn**, however, were thwarted due to its unexpected insolubility in acetone-d_6. This is surprising considering its structural similarity to the shorter strap analogue **3.1a·Zn**. Later electrochemical studies (Section 3.5.2) revealed that, due to the presence of the longer and more flexible pentyl linkers, the triazole donor on the strap

intramolecularly coordinates to the zinc(II) porphyrin core,[336–339] explaining its altered solubility in the organic solvent.

3.3.2.2 UV–Visible Absorption Titration Experiments

To probe the anion sensing capabilities, UV–visible absorption titration experiments of XB strapped porphyrin **3.1a·Zn** and TBA halide salts in acetone were carried out. The free macrocyclic receptor exhibits typical porphyrin absorption peaks, a more intense Soret band at 412 nm and Q bands at around 500–600 nm. The addition of halides induced a red-shift to both Soret and Q bands. Specifically, the Soret band underwent a bathochromic shift from 412 nm to 423 nm, with a clear isosbestic point at 416 nm (Figure 3.10). This observation is consistent with halide coordination to Lewis acidic zinc(II) metalloporphyrin.[335] By monitoring the change in absorbance of Soret band, global analysis[235] using OriginLab with a 1:1 host-guest stoichiometric binding model determined the corresponding halide anion association constants (Table 3.1). For comparison, the halide binding constants of the strap-free zinc(II) 5,10,15,20-tetraphenylporphyrin (ZnTPP) in the same solvent system is also tabulated.[298]

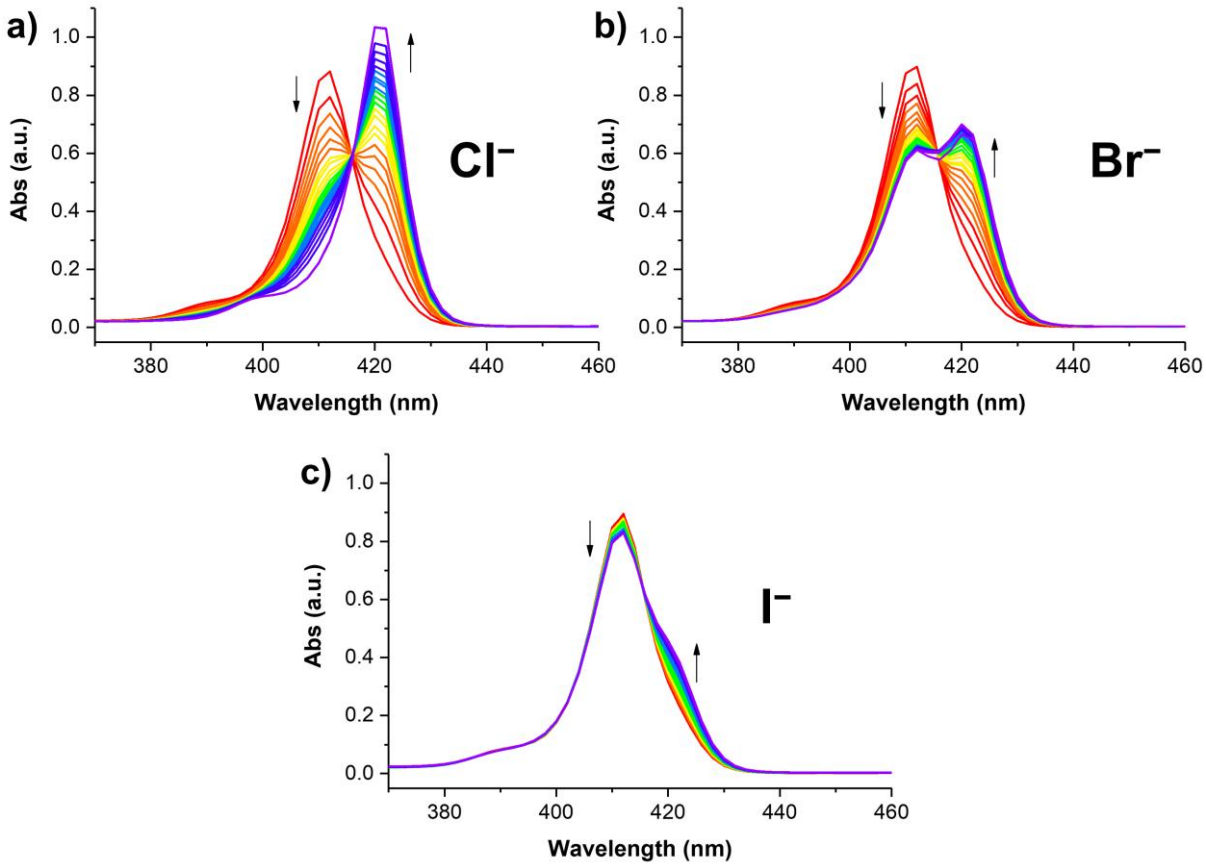

Figure 3.10 Changes in the absorbance of the Soret band of **3.1a·Zn** upon addition of 10 equivalent of (a) TBACl, (b) TBABr and (c) TBAI (298 K, acetone, [**3.1a·Zn**] = 3 μM).

Table 3.1: Anion association constants (K_a/M^{-1}) for **3.1a·Zn** and ZnTPP with TBA halide salts in acetone determined by UV–visible titrations.[a]

Anion	**3.1a·Zn**	ZnTPP^{298}	Binding Enhancement Factor K_a(**3.1a·Zn**) /K_a(ZnTPP)
Cl$^-$	4.1×10^5	8.1×10^3	5.1×10^1
Br$^-$	1.5×10^6	1.5×10^2	1.0×10^4
I$^-$	9.4×10^4	5.0×10^1	1.9×10^3

[a]K_a values calculated from global fitting of UV–visible titration data using OriginLab with a 1:1 host-guest binding model.[235] Errors (±) are all <10%. All anions added as their TBA salts. [**3.1a·Zn**] = 3 μM. Solvent = acetone. T = 298 K.

Examining Table 3.1 reveals much higher association constant values with all halides tested for strapped porphyrin **3.1a·Zn** in comparison with ZnTPP, highlighting the importance of XB strap in anion binding. The greatest enhancement

in binding is seen for Br^-, with a K_a increase by a factor of 10^4. In addition, while ZnTPP displays a selectivity trend for the smaller sized charge dense halide anions (Cl^- > Br^- > I^-), **3.1a·Zn** demonstrates a preference for bromide over chloride and iodide. This selectivity for Br^- could be rationalised by both size and shape complementarity between the anion and the strapped cavity, strengthening its XB interactions with two iodo-triazole donors, as well as its endotopic ligation to the zinc(II) metalloporphyrin centre. In conclusion, by incorporating a XB strap to the porphyrin core, anion affinities are substantially enhanced and halide selectivity can be modulated.

3.4 Halogen Bonding Strapped Porphyrin [2]Rotaxanes

Active metal templation (AMT) has presented itself as a powerful method to construct MIMs since its introduction in 2006 by Leigh and co-workers (See Section 2.1 for more discussion).[187] Macrocycles containing the 1,3-bis(iodo-triazole)benzene motif have been demonstrated to be capable of endotopically coordinating a copper(I) metal centre via one of the basic triazole nitrogen atoms (Scheme 2.6).[225–227] This allows the subsequent CuAAC click reaction between azide and alkyne axle precursors to occur through the ring annulus, assisting the formation of rotaxanes. In addition, a phenanthroline strapped zinc(II) metalloporphyrin has been recently reported to preorganise the azide precursors via zinc(II) ligation in CuAAC-AMT rotaxane reactions.[340] Therefore, XB strapped porphyrin **3.1a·Zn** was expected to be a potential candidate as a macrocyclic precursor in the AMT synthesis of [2]rotaxanes (Scheme 3.6).

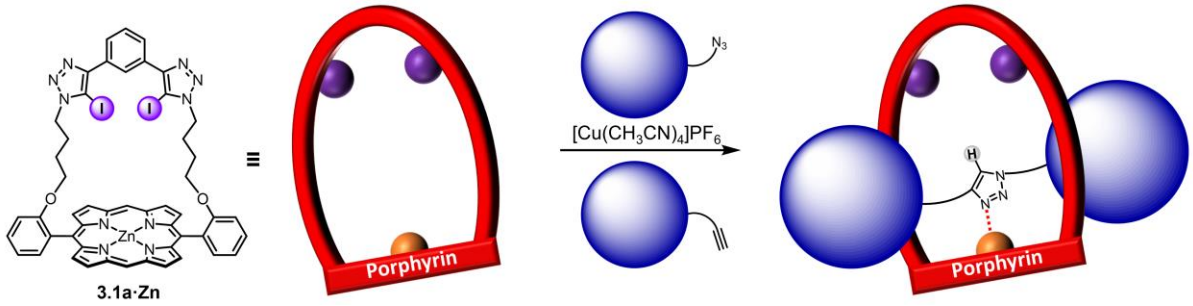

Scheme 3.6 Schematics of the general CuAAC-AMT synthesis of [2]rotaxanes with macrocyclic precursor **3.1a·Zn**.

3.4.1 Terphenyl-Stoppered XB Strapped Porphyrin [2]Rotaxanes

3.4.1.1 CuAAC-AMT Synthesis of Terphenyl-Stoppered XB Strapped Porphyrin [2]Rotaxanes

In an initial attempt (Scheme 3.7), strapped porphyrin **3.1a·Zn** was pre-complexed with an equimolar amount of $[Cu(CH_3CN)_4]PF_6$ in CH_2Cl_2 for 30 minutes. Subsequently, five equivalents of terphenyl-stoppered alkyne **3.7** and azide **3.8** in CH_2Cl_2 was added. The resulting mixture was heated at 40 °C for 2 days, whereupon TLC analysis indicated the complete consumption of both axle precursors. Preparative TLC purification afforded the target XB [2]rotaxane **3.9·Zn** in an excellent yield of 63%. This high yield is postulated to originate from the synergistic effects of endotopic Cu(I) coordination by iodo-triazole nitrogen, and azide positioning mediated by zinc(II) metalloporphyrin.[340] Longer strapped porphyrin **3.1b·Zn** was also subjected to the same CuAAC-AMT conditions. Despite complete consumption of axle precursors after heating the reaction at 40 °C for 2 days, no formation of interlocked structure was observed. This is likely due to the intramolecular strap triazole coordination to zinc(II), blocking the macrocycle cavity and preventing the triazole nitrogen from binding copper(I) endotopically. [2]Rotaxane **3.1a·Zn** was characterised by ^{1}H, ^{13}C NMR spectroscopies and high-resolution ESI-MS.

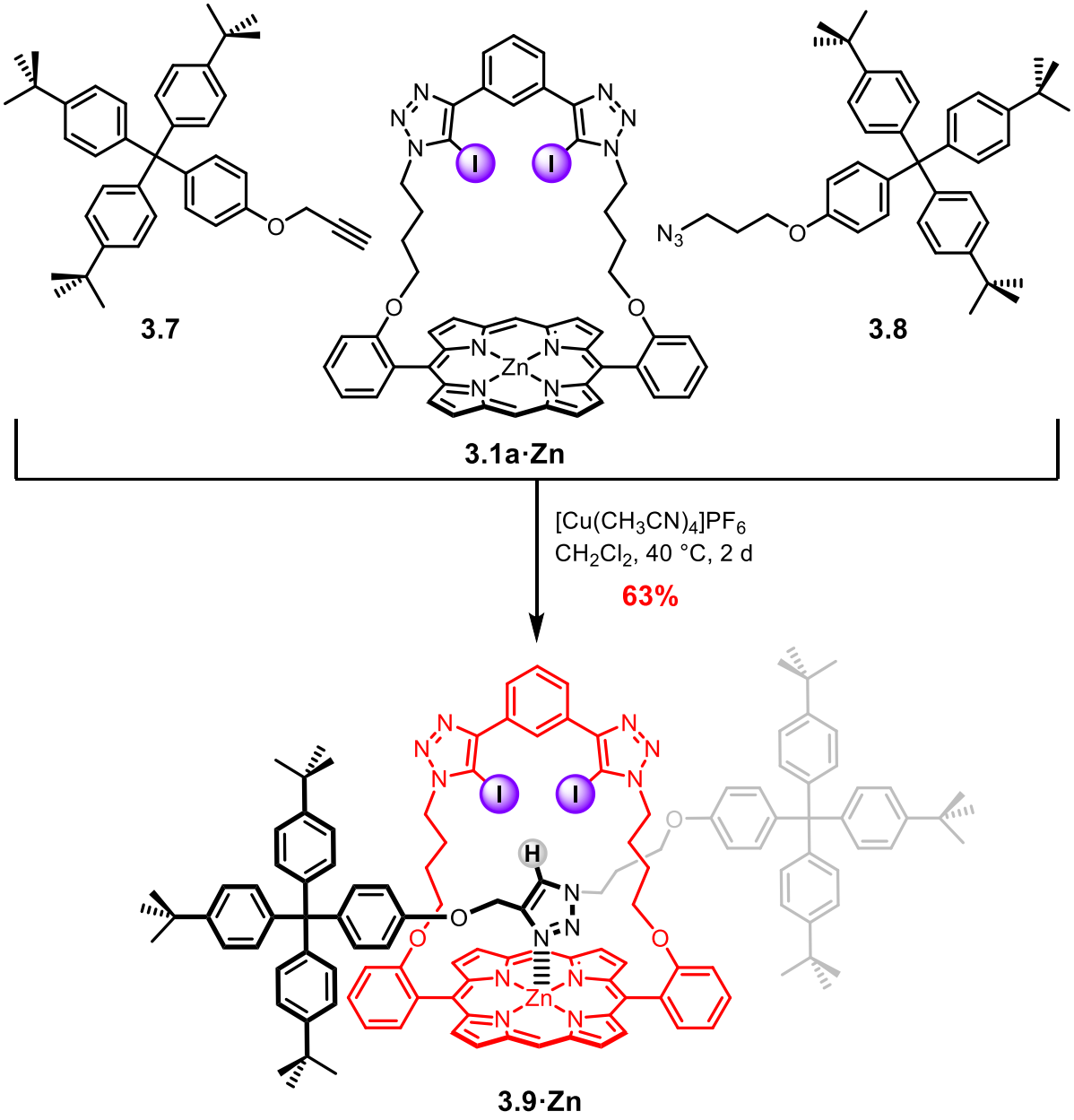

Scheme 3.7 CuAAC-AMT synthesis of terphenyl-stoppered [2]rotaxane **3.9·Zn**.

A comparison of ^{1}H NMR spectra of [2]rotaxane **3.9·Zn**, macrocycle **3.1a·Zn** and the corresponding axle is shown in Figure 3.11. A splitting of porphyrin aromatic signals *l*–*n* was observed in the [2]rotaxane spectrum, likely arising from the restricted motion of the strapped porphyrin macrocycle along the asymmetric axle at ambient temperature. In addition, large upfield perturbation of axle triazole proton signal *6* (Δδ = 1.8 ppm) was seen for **3.9·Zn** compared to the non-interlocked free axle. This strongly suggests the coordination of the axle triazole group to the macrocyclic zinc(II)

porphyrin, thereby placing the triazole proton *6* in the deshielding region of the porphyrin's aromatic ring current.[292] In summary, the ^{1}H NMR spectrum of **3.9·Zn** is fully consistent with that of a mechanically interlocked [2]rotaxane.

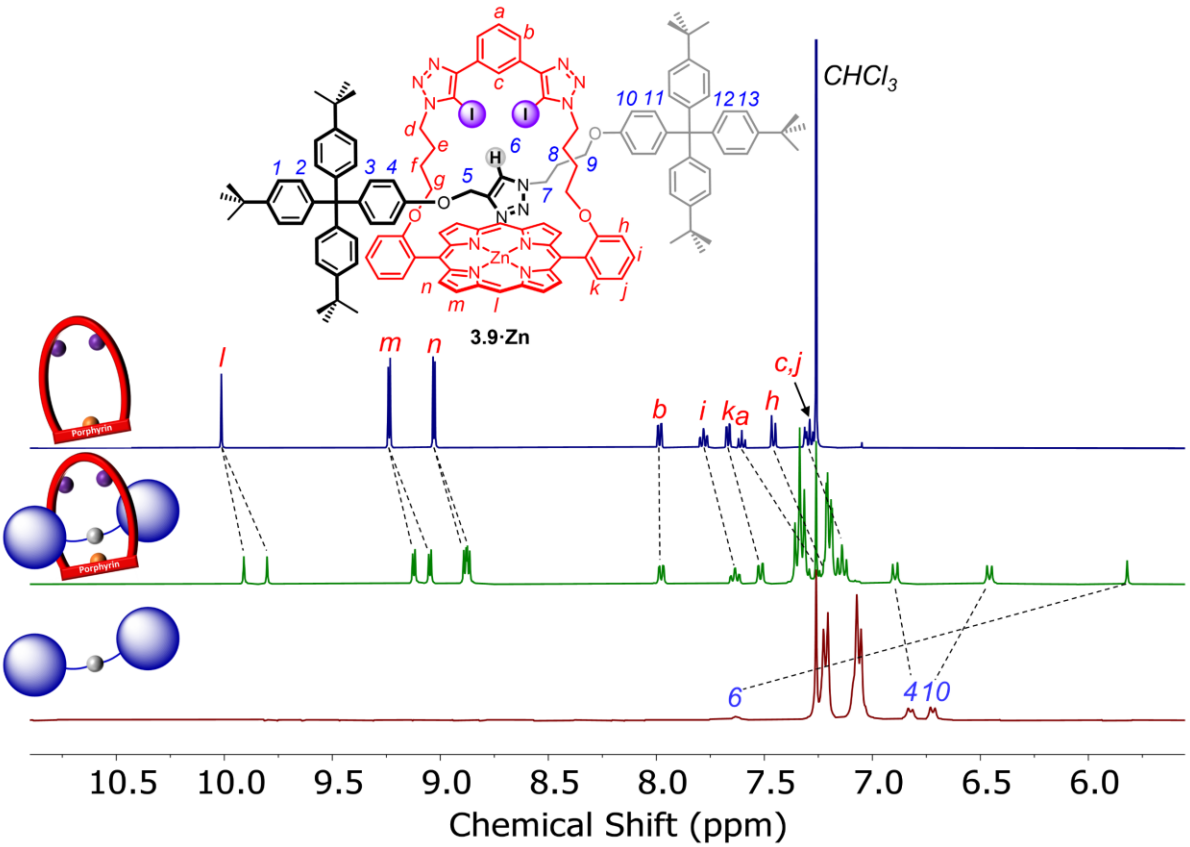

Figure 3.11 Comparative truncated ^{1}H NMR spectra of strapped porphyrin **3.1a·Zn** (top), [2]rotaxane **3.9·Zn** (middle) and the corresponding free axle (bottom) (400 MHz, 298 K, $CDCl_3$).

3.4.1.2 Intramolecular Axle Triazole Ligation to Strapped Zinc(II) Porphyrin

The ^{1}H NMR spectrum of the [2]rotaxane **3.9·Zn** shown in Figure 3.11 suggested the presence of an intercomponent coordination of axle triazole heterocycle to the zinc(II) metalloporphyrin. This metal–ligand bond is envisaged to both enhance the degree of preorganisation of the interlocked anion receptor, and polarise the triazole C–H bond to strengthen its HB donor capability.

Additional evidence for this triazole ligation interaction was obtained via UV–visible absorption experiments. A comparison of the porphyrin Soret band of strapped porphyrin **3.1a·Zn** and [2]rotaxane **3.9·Zn** is shown in Figure 3.12. While the Soret band of macrocyclic porphyrin **3.1a·Zn** appears at 411 nm, the introduction of triazole-containing axle through its cavity induced a red-shift of 6 nm (to 417 nm) to the spectrum of **3.9·Zn**, consistent with coordination of basic triazole nitrogen to zinc(II) porphyrin.[335] This is further attested by investigating the effects of pyridine addition to the resulting porphyrin absorption peaks. The addition of 1% of pyridine to the solution of strapped porphyrin **3.1a·Zn** elicited a bathochromic shift of 411 nm to 416 nm to the Soret band (Figure 3.13a), resulting from pyridine ligation to zinc(II) metalloporphyrin. In contrast, the Soret band of [2]rotaxane **3.9·Zn** appeared at slightly longer wavelength (417 nm) relative to pyridine-coordinated **3.1a·Zn** (416 nm), and displayed negligible shift upon the addition of pyridine (Figure 3.13b). This indicates the fifth coordination site of zinc(II) is already occupied by the axle triazole, and pyridine, despite being a better ligand, is unable to displace it. This is potentially due to the interlocked nature of **3.9·Zn**, which renders a higher effective concentration of the axle triazole ligand.

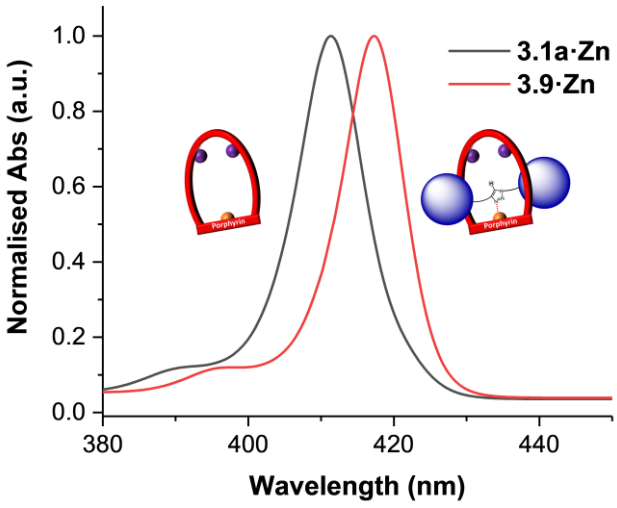

Figure 3.12 Normalised UV–visible absorption spectra of strapped porphyrin **3.1a·Zn** and [2]rotaxane **3.9·Zn** (298 K, acetone, [**3.1a·Zn**] = [**3.9·Zn**] = 3 μM).

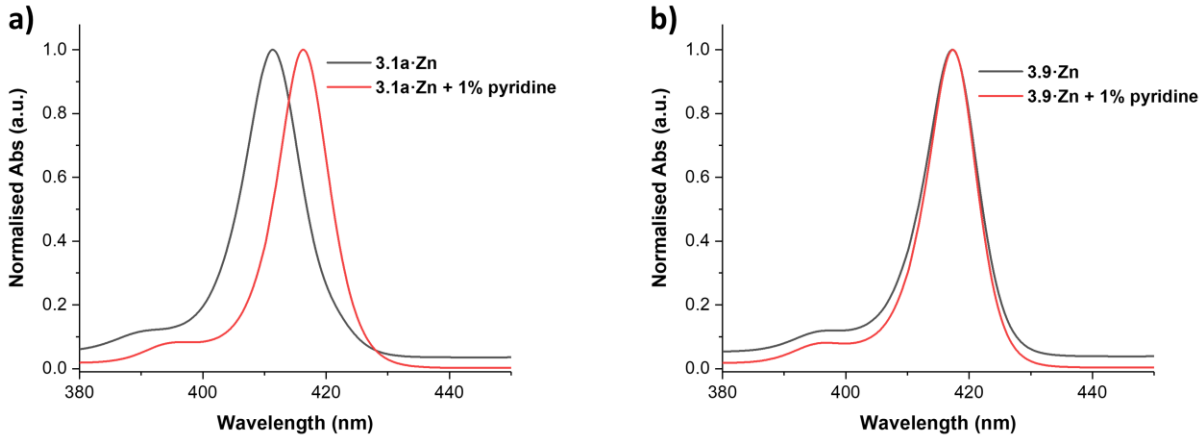

Figure 3.13 Effect of addition of 1% of pyridine to the normalised UV–visible absorption spectra of (a) **3.1a·Zn** and (b) **3.9·Zn** (298 K, acetone, [**3.1a·Zn**] = [**3.9·Zn**] = 3 μM).

In conclusion, ^{1}H NMR and UV–visible absorption studies of rotaxane **3.9·Zn** reveal the axle triazole coordination to zinc(II) porphyrin, which is also corroborated by electrochemical studies (Section 3.5.2). This non-covalent interaction anchors the macrocycle along the axle and, as will be shown later, has profound effects on strengthening the anion binding properties of the interlocked receptor.

3.4.1.3 Anion Recognition Studies

(A) ^{1}H NMR Titration Experiments

To assess its anion binding properties, quantitative ^{1}H NMR titration experiments of [2]rotaxane **3.9·Zn** and TBA halide salts were conducted in acetone-d_6. Upon addition of Cl^-, aromatic proton signals (*l'*, *m'* and *n'*) on one side of the porphyrin experienced significant upfield perturbations, while only slight shifts were observed for those on the other side (*l"*, *m"* and *n"*) (Figure 3.14). In addition, downfield shifts of peripheral stopper proton *4* were seen. These observations suggest that the anion, instead of penetrating into the rotaxane binding cavity, is perching between the plane of macrocycle and one of the stopper groups (Figure 3.15a). Evidence of axle triazole HB interaction with Cl^- arises from the significant downfield shift of triazole proton *6* ($\Delta\delta$ = 1.7 ppm). By monitoring the chemical shift of triazole signal *6* as a function of

TBA halide concentrations (Figure 3.16), anion association constants of **3.9·Zn** in acetone-d_6, and the more competitive aqueous 2% D_2O/acetone-d_6, were determined using Bindfit[235,236] with a 1:1 stoichiometric host-guest complex model (Table 3.2). For comparison purposes, the corresponding anion binding constants for an analogous porphyrin-free [2]rotaxane **3.10** (Figure 3.15b) are also tabulated.[225]

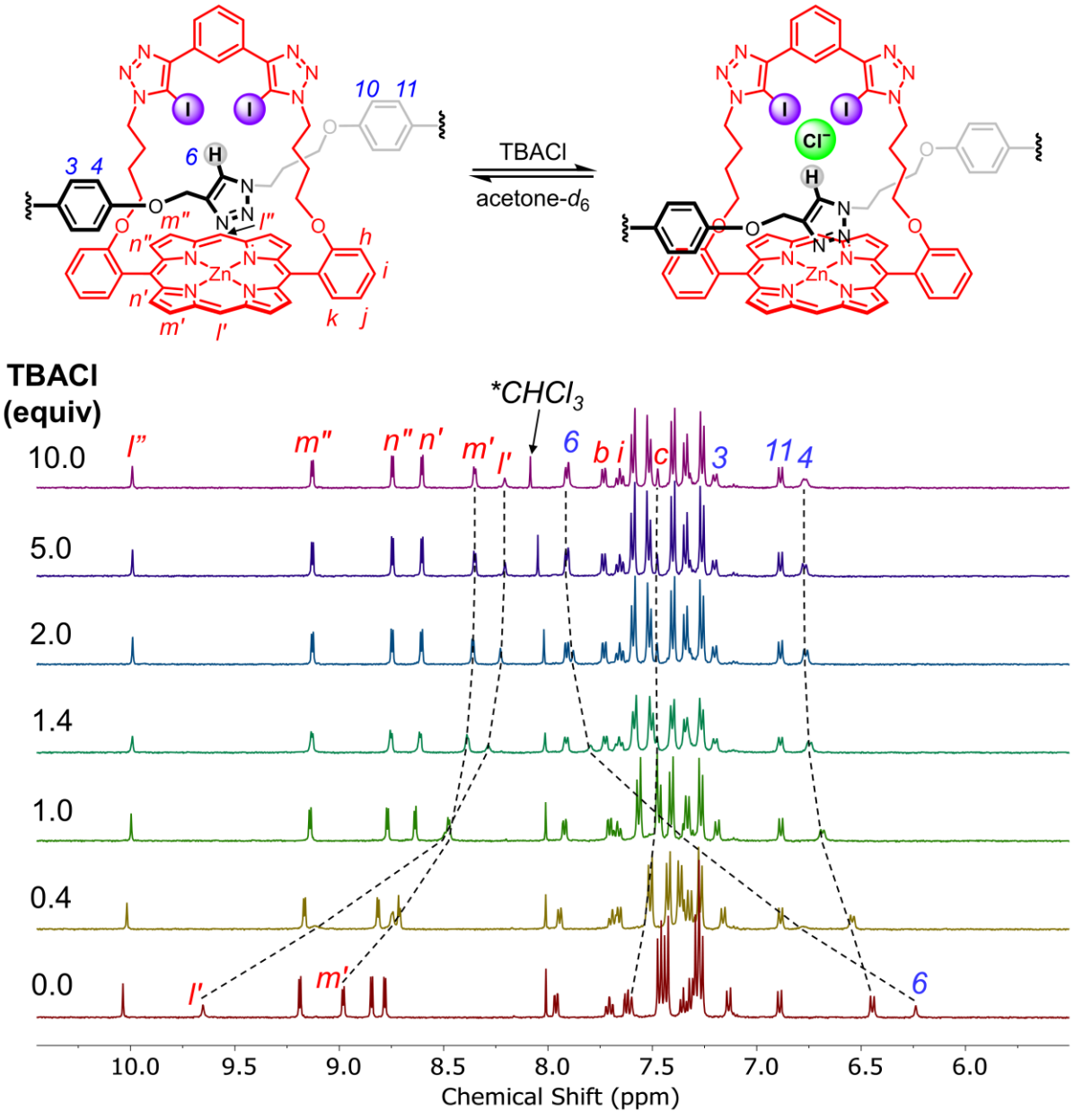

Figure 3.14 Truncated ^{1}H NMR titration spectra of [2]rotaxane **3.9·Zn** upon addition of 0.4, 1.0, 1.4, 2.0, 5.0 and 10.0 equivalents of TBACl (500 MHz, 298 K, acetone-d_6, [**3.9·Zn**] = 1.0 mM).

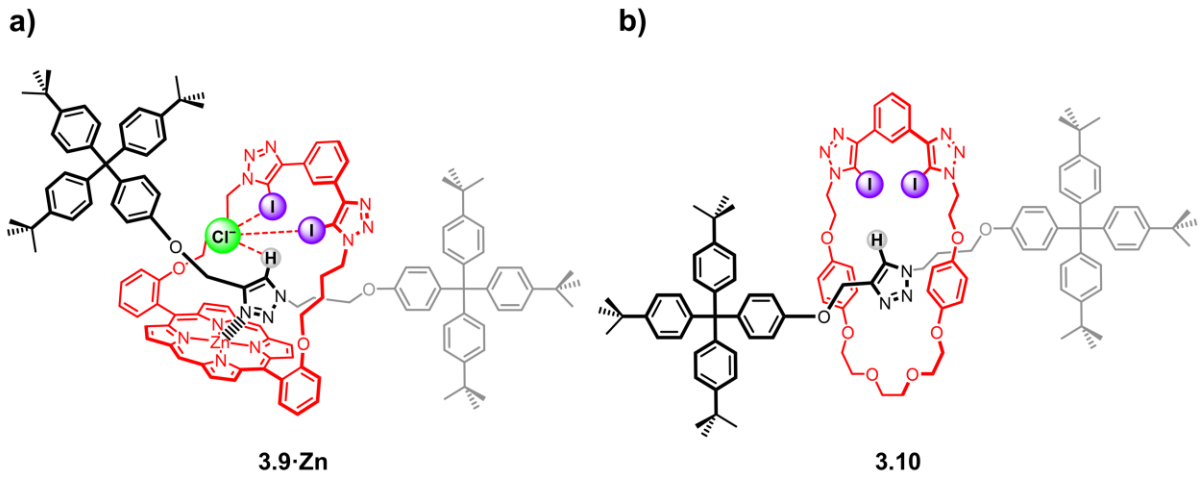

Figure 3.15 (a) Postulated Cl^- binding mode of **3.9·Zn** with anion perching on one side of the rotaxane cavity. (b) Reference [2]rotaxane **3.10** containing tri(ethylene glycol) instead of porphyrin as macrocyclic linker.

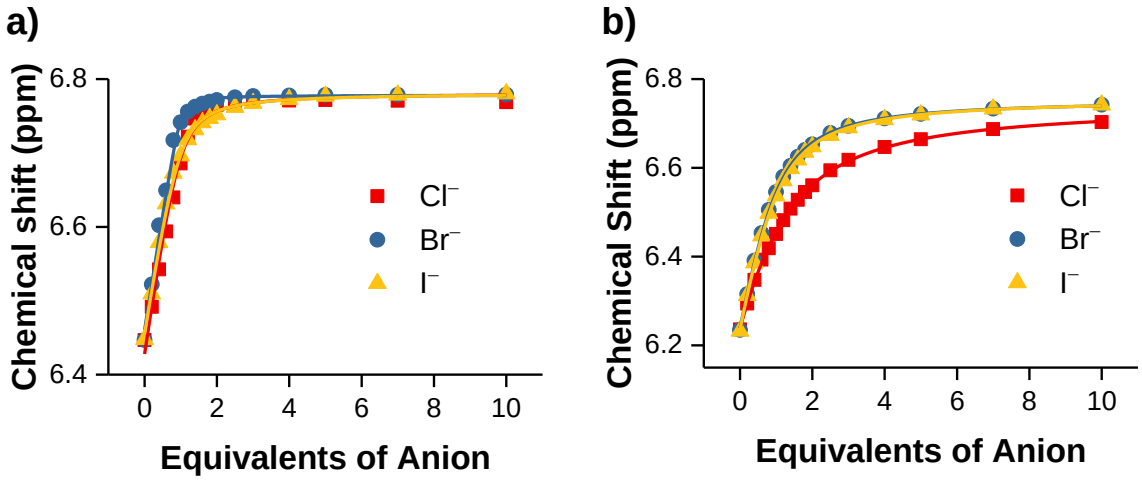

Figure 3.16 Binding isotherms of **3.9·Zn** showing changes in chemical shift of axle triazole proton *6* with increasing equivalents of anions in (a) acetone-d_6 and (b) 2% D_2O/acetone-d_6. Filled dots represent the experimental data while the solid lines show the fitted data. ([**3.9·Zn**] = 1.0 mM, 500 MHz, 298 K)

In acetone-d_6, porphyrinoid [2]rotaxane **3.9·Zn** displays strong binding to all the halide anions with $K_a > 10^4\ M^{-1}$, which are significantly higher than that of the porphyrin-free analogue **3.10**. As expected, the introduction of 2% D_2O to the solvent drastically reduces the halide association constant magnitudes for both rotaxanes studied, but **3.9·Zn** still demonstrates a 6- to 12-fold enhancement in binding. This highlights the importance of the intercomponent axle triazole coordination to zinc(II) metalloporphyrin in preorganising the binding site and augmenting the anion

affinities. In terms of anion selectivity, while **3.10** displays a clear Hofmeister bias with highest association constants towards the least hydrated I^-, **3.9·Zn** displays a preference for Br^- over I^-. This is ascribed to the presence of the rigid porphyrin, in place of the flexible tri(ethylene glycol) spacer, in the macrocycle of **3.9·Zn**, which restricts the size the binding pocket and weakens the receptor affinity towards the larger I^- guest species.

Table 3.2: Anion association constants (K_a/M^{-1}) for **3.9·Zn** and **3.10** with TBA halide salts in acetone-d_6 and 2% D_2O/acetone-d_6 determined by ^1H NMR titrations.[a]

	Acetone-d_6		2% D_2O/Acetone-d_6		
Anion	**3.9·Zn**	**3.10**	**3.9·Zn**	**3.10**	K_a**(3.9·Zn)**/K_a**(3.10)**
Cl^-	$>10^4$	4 380	1 290	110	12
Br^-	$>10^4$	2 140	3 550	370	10
I^-	$>10^4$	900	3 230	530	6

[a]K_a values calculated using Bindfit with a 1:1 host-guest binding model.[235,236] Errors (±) are all <10%. All anions added as their TBA salts. [**3.9·Zn**] = 1.0 mM. Solvent = acetone-d_6 or 2% D_2O/acetone-d_6. T = 298 K.

(B) UV–Visible Absorption Titration Experiments

To probe the anion sensing capability of interlocked **3.9·Zn**, UV–visible absorption anion titration studies were carried out with TBA halide salts in acetone. However, despite the addition of excess (>1000 equivalents) of the halide anions, no perturbation to porphyrin absorption peaks was observed. This suggests that although axle triazole coordination substantially enhances the preorganisation of binding site and increases host affinity to anions, it also saturates the zinc(II) metalloporphyrin coordination site, negating its ability to function as a UV–visible absorption reporter group to transduce the anion complexation event.

3.4.2 BODIPY-Stoppered XB Strapped Porphyrin [2]Rotaxanes

Since triazole ligation to zinc(II) metalloporphyrin in the [2]rotaxane structure appears to nullify the porphyrin's chromophoric anion sensing ability, this necessitated the incorporation of alternative reporting motifs in the vicinity of rotaxane binding cleft. BODIPY, by virtue of its excellent photophysical properties, was chosen to act as one of the rotaxane stopper groups. Despite the frequent use of BODIPY in many applications such as bioimaging and photovoltaic devices, its exploitation as a fluorescent reporter groups in supramolecular host-guest assemblies is rare. The synthesis and anion sensing investigations of the first examples of BODIPY-stoppered strapped porphyrin XB [2]rotaxanes is described in the next section.

3.4.2.1 CuAAC-AMT Synthesis of BODIPY-Stoppered XB Strapped Porphyrin [2]Rotaxanes

(A) Synthesis of BODIPY-Functionalised Stoppers[*]

The synthetic routes to the novel BODIPY-functionalised stopper alkyne and azide precursors are shown in Scheme 3.8. To prepare the alkynyl stopper, the BODIPY core **3.11** was initially synthesised in a three-step one-pot reaction.[341] A condensation reaction between 4-ethynylbenzaldehyde and 2,4-dimethylpyrrole in the presence of catalytic amount of TFA afforded the corresponding dipyrromethane intermediate, which was oxidised in situ by *p*-chloranil to give the dipyrrin intermediate. Subsequent complexation with boron via addition of $BF_3{\cdot}OEt_2$ afforded BODIPY **3.11** in 31% yield over three steps after chromatographic purification. To increase the steric bulk of the BODIPY alkyne in order for it to effectively function as a rotaxane stopper,

[*] The requisite BODIPY-functionalised precursors were synthesised by a fellow graduate student Edward J. Mitchell.

Knoevenagel condensation between **3.11** and 3,5-di-*tert*-butylbenzaldehyde was carried out, affording the BODIPY-functionalised stopper alkyne in 53% yield after purification by silica gel column chromatography. Using a similar synthetic procedure and 4-azido-tetrafluorobenzaldehyde[342] as starting material, BODIPY stopper azide **3.14** was successfully prepared.

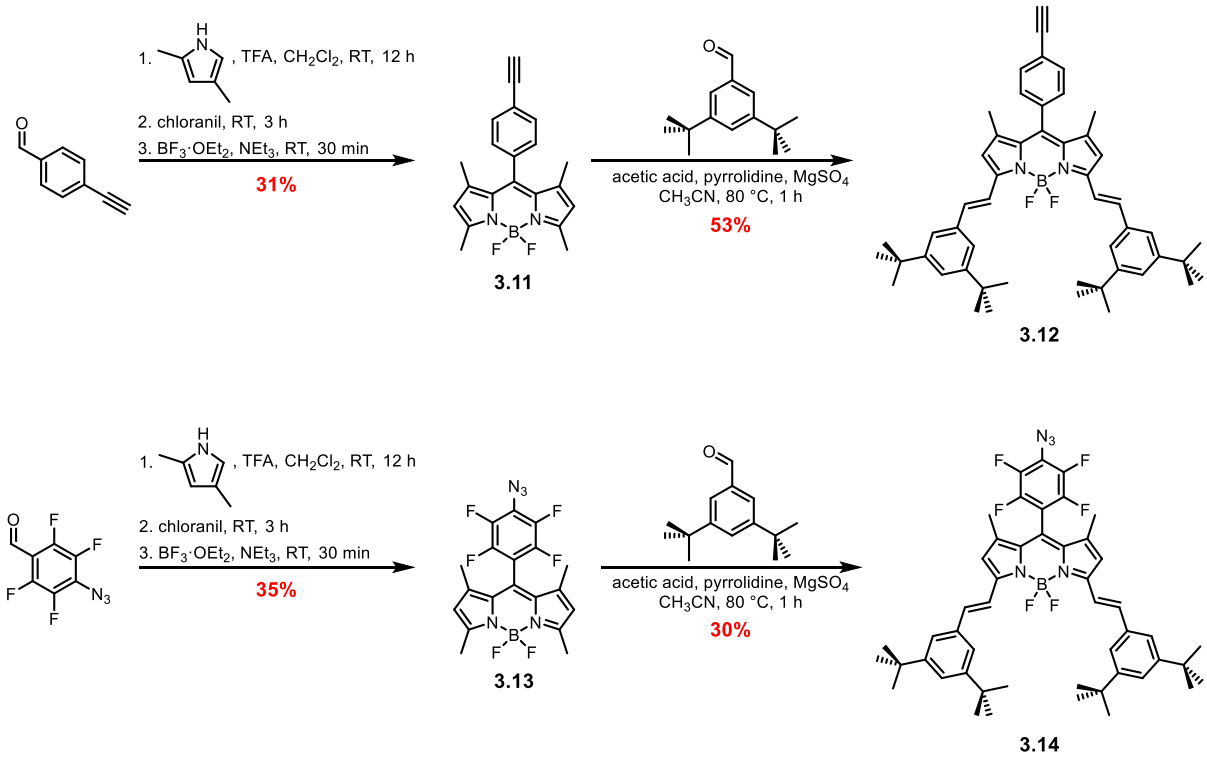

Scheme 3.8 Synthetic routes to BODIPY-functionalised stopper alkyne **3.12** and stopper azide **3.14**.

(B) *Synthesis of BODIPY-Stoppered XB Strapped Porphyrin [2]Rotaxanes*

Following the general CuAAC-AMT procedure (Scheme 3.9), BODIPY-functionalised rotaxanes **3.15·Zn** and **3.16·Zn** were constructed using BODIPY-stopper alkyne **3.12** and stopper azide **3.14** respectively in 35–37% yields after chromatographic purification. The introduction of the perfluoroaryl spacer in **3.16·Zn** instead of the phenyl group in **3.15·Zn** was expected to further polarise the axle triazole C–H and enhance its anion affinity. It is noteworthy that, similar to terphenyl-stoppered rotaxane **3.9·Zn**, upfield perturbations of triazole proton signal in the ^{1}H

NMR spectra and bathochromic shifts of porphyrin Soret band compared to macrocyclic **3.1a·Zn** were observed for these two porphyrin-BODIPY rotaxanes. This suggests the presence of metal–ligand coordination between macrocyclic zinc(II) porphyrin and axle triazole, enhancing the preorganisation of the binding sites and anion affinities of the receptors.

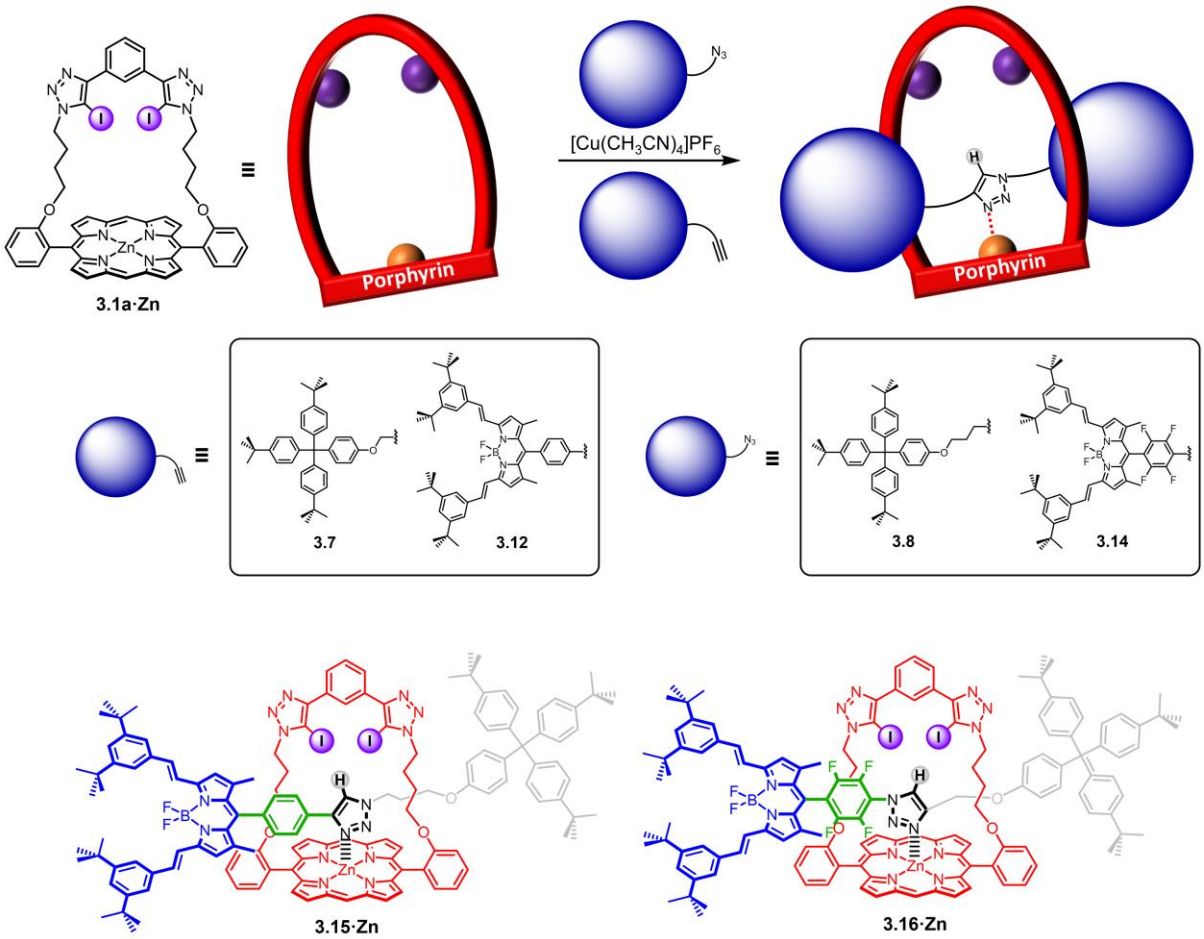

Scheme 3.9 CuAAC-AMT synthesis of BODIPY-porphyrin [2]rotaxanes **3.15–16·Zn**.

3.4.2.2 Fluorescence Anion Sensing Studies

Both BODIPY-containing rotaxanes **3.15·Zn** and **3.16·Zn** were highly emissive in acetone and displayed typical BODIPY-based emission maxima at 638 and 666 nm respectively. The longer emission wavelength of **3.16·Zn** is ascribed to the presence of the electron-deficient perfluoroaryl motif adjacent to the BODIPY fluorophore. To assess the optical anion sensing capabilities of these interlocked receptors,

fluorescence titration experiments were conducted in acetone with various anions (Cl^-, Br^-, I^-, OAc^- and SO_4^{2-}) administered as their TBA salts. In general, all anions induced quenching of the BODIPY emission bands, whereby the oxoanions (OAc^- and SO_4^{2-}) elicited larger decreases in emission intensities than the halide anions (Cl^-, Br^-, I^-) (Figure 3.17 and Figure 3.18a–e). In addition, larger magnitudes of quenching was seen upon addition of anions to the perfluoroaryl-appended **3.16·Zn** than for phenyl-appended **3.15·Zn**. By monitoring the quenching of BODIPY emission bands as a function of anion concentration, global fitting[235] analysis carried out by OriginLab determined the anion association constants with a 1:1 host-guest stoichiometric binding model (Table 3.3).

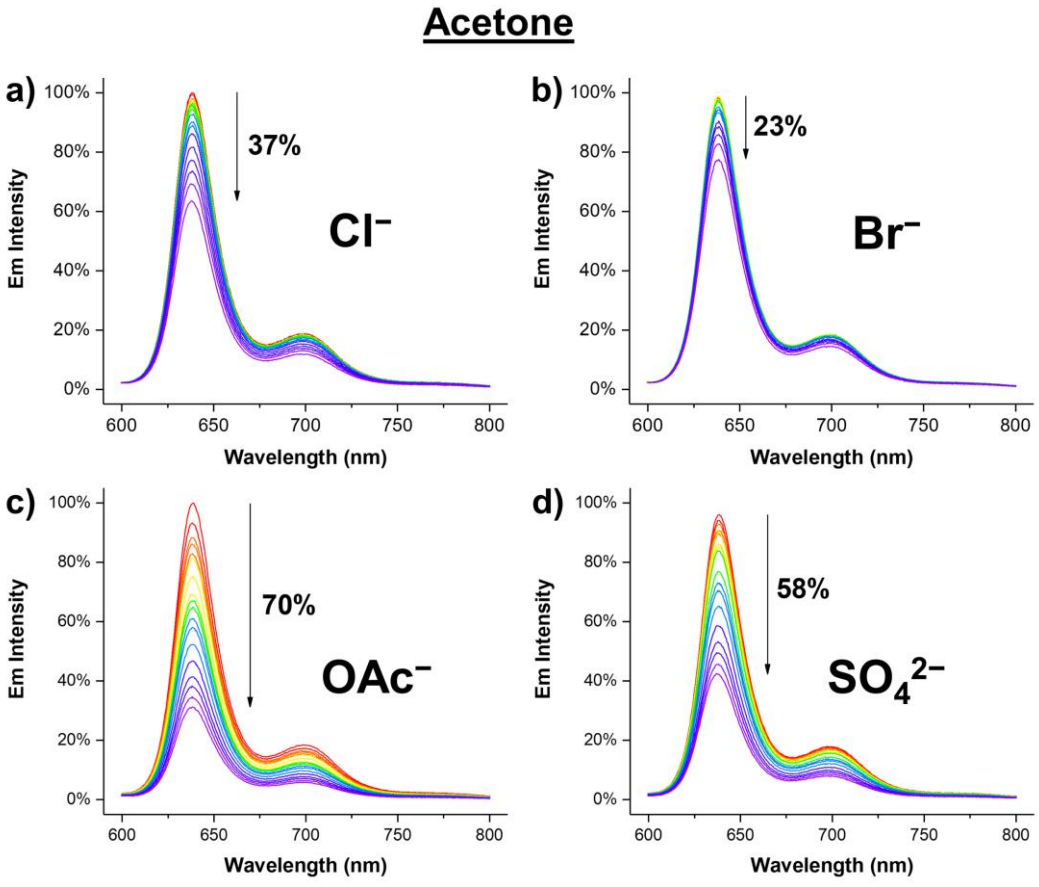

Figure 3.17 Fluorescence titration spectra of **3.15·Zn** with various TBA salts of anions. Direction and percentage change in fluorescence intensity are denoted in the figures. ([**3.15·Zn**] = 1 μM, λ_{ex} = 575 nm, 298 K, acetone).

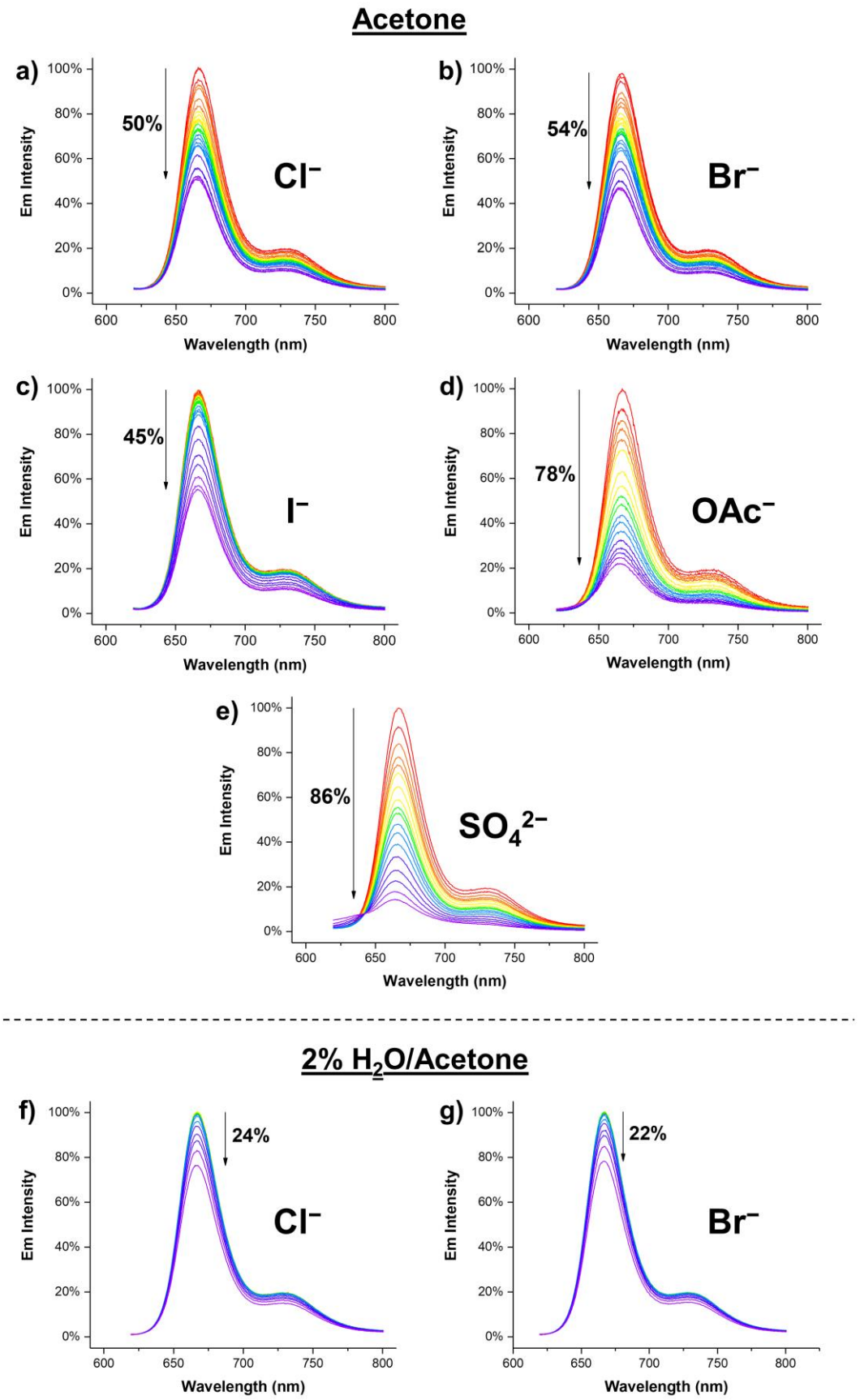

Figure 3.18 Fluorescence titration spectra of **3.16·Zn** with various TBA salts of anions. Direction and percentage change in fluorescence intensity are denoted in the figures. ([**3.16·Zn**] = 1 μM, λ_{ex} = 595 nm, 298 K, acetone (a–e) or 2% H_2O/acetone (f–g)).

Table 3.3: Anion association constants (K_a/M^{-1}) for **3.15·Zn** and **3.16·Zn** with TBA halide salts in acetone and 2% H_2O/acetone determined by fluorescence titrations.[a]

	Acetone		2% H_2O/Acetone	
Anion	**3.15·Zn**	**3.16·Zn**	**3.15·Zn**	**3.16·Zn**
Cl^-	5 440	44 910	N.B.[b]	1 090
Br^-	2 280	35 240	N.B.	650
I^-	–[c]	4 820	N.B.	N.B.
OAc^-	29 940	58 310	N.B.	N.B.
SO_4^{2-}	13 820	39 220	N.B.	N.B.

[a]K_a values calculated using global fitting of fluorescence titration spectra using OriginLab with a 1:1 host-guest binding model.[235] Errors (±) are all <10%. All anions added as their TBA salts. [Rotaxane] = 1 μM. Solvent = acetone or 2% H_2O/acetone. T = 298 K. [b]N.B. = no binding. [c]No reliable association constants could be obtained.

For the spherical halides, both receptors demonstrated a preference for the more charge-dense Cl^-, following halide anion basicity trends. In addition, perfluoroaryl-appended rotaxane **3.16·Zn** displayed an 8- to 15-fold increase in association constants for Cl^- and Br^- compared to phenyl-appended **3.15·Zn**. This is attributed to the electron-withdrawing effect of the axle perfluoroaryl group, strengthening HB donor capability of the axle triazole C–H and enhancing rotaxane receptor affinity to anions. In addition, both receptors also display strong affinity to oxoanions (OAc^- and SO_4^{2-}), with anion association constants comparable to, or stronger than that of, Cl^-. This suggests, in spite of the structural rigidification resulting from axle triazole-metalloporphyrin coordination, the receptors still possess a certain degree of flexibility to accommodate the bulky polyatomic oxoanions.

To further test the ability of these receptors to function as efficient anion sensors in aqueous environments, analogous titrations in the more competitive 2% H_2O/acetone mixture were undertaken. For phenyl-appended **3.15·Zn**, no binding to anions was observed in this solvent mixture as evidenced by the negligible perturbation to the BODIPY emission bands. In contrast, **3.16·Zn** still demonstrated

significant quenching response towards both Cl^- and Br^- (Figure 3.18f–g). Interestingly, in contrast to terphenyl-stoppered [2]rotaxane **3.9·Zn**, which displayed a stronger binding for Br^- over Cl^- in the aqueous mixture, BODIPY-stoppered **3.16·Zn** maintains a selectivity for the smaller, more hydrophilic Cl^-. This anion binding preference is tentatively ascribed to the shorter axle component and the presence of a hydrophobic perfluoroaryl group adjacent to the rotaxane cavity in **3.16·Zn**, rendering the anion binding pocket more shielded from the bulk aqueous solvent mixture, which possibly strengthens the XB and HB interactions with Cl^- and assists the desolvation of the anion.

3.5 Electrochemical Studies of XB Strapped Porphyrins and [2]Rotaxanes*

3.5.1 General Electrochemical Characterisation and Reversibility

The electrochemical properties of XB strapped porphyrins (**3.1a–b·Zn**) and [2]rotaxanes (**3.9·Zn**, **3.15·Zn** and **3.16·Zn**) were investigated by cyclic voltammetry (CV) in CH_2Cl_2. All receptors displayed two quasi-reversible porphyrin-centred one-electron oxidation couples, ($P/P^{+\bullet}$) and ($P^{+\bullet}/P^{2+}$), whereby the latter generally exhibited a poorer reversibility and was not studied in detail. For BODIPY-functionalised hosts (**3.15·Zn** and **3.16·Zn**), in addition to the above-mentioned porphyrin-centred oxidations, another quasi-reversible couple which appears at more anodic potential than the $P/P^{+\bullet}$ couple was also observed (Figure 3.19). By comparison with the voltammograms of BODIPY-based stopper alkyne **3.12** and stopper azide

* The electrochemical studies in this chapter were conducted by Dr. Robert Hein, a joint post-doctoral fellow between the Beer group and the Davis group.

3.14 (Figure 3.20), this redox couple is unambiguously assigned to be the one-electron oxidation of the BODIPY moiety (BDP/BDP$^{+\bullet}$) in the rotaxanes.

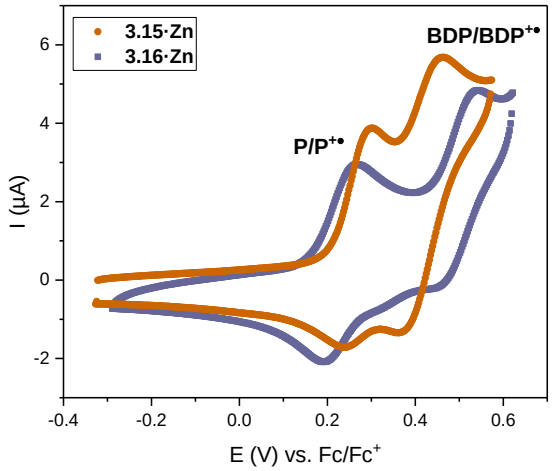

Figure 3.19 CVs of **3.15·Zn** (brown) and **3.16·Zn** (purple) in CH_2Cl_2/$TBAPF_6$ at a scan rate of 100 mV/s.

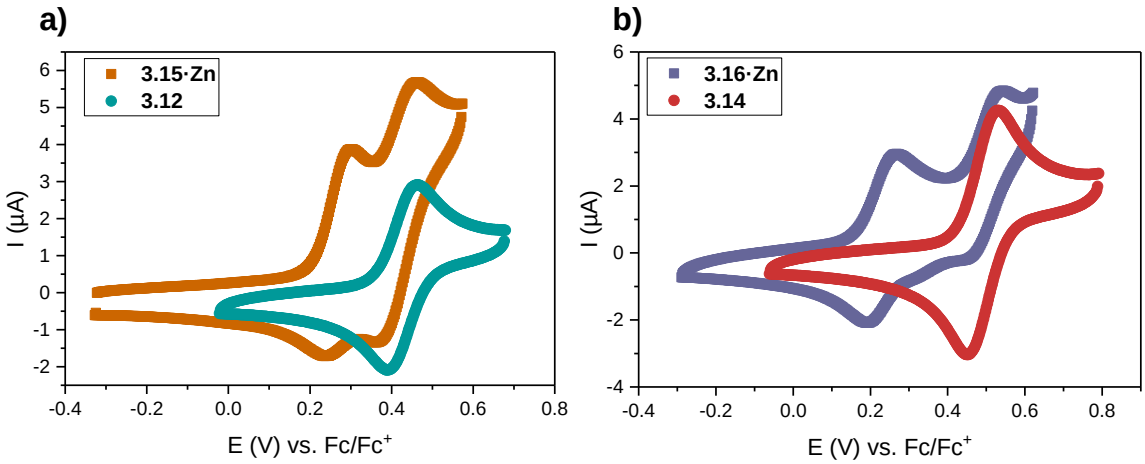

Figure 3.20 CVs of a) **3.15·Zn** (brown) and **3.12** (cyan) and b) **3.16·Zn** (purple) and **3.14** (red) in CH_2Cl_2/$TBAPF_6$ at a scan rate of 100 mV/s.

3.5.2 Comparison of Redox Potentials

The measured redox potentials ($E_{1/2}$) of all receptors in CH_2Cl_2 in the absence and presence of pyridine (1%, v/v) are tabulated in Table 3.4. Interestingly, structurally similar strapped porphyrins **3.1a·Zn** and **3.1b·Zn** exhibited significantly different $E_{1/2}$ values for the first porphyrin-centred one-electron oxidation couple P/P$^{+\bullet}$. In particular, shorter strap (butyl linker) **3.1a·Zn** displayed a $E_{1/2}$ at 0.282 V while that

of the longer strap (pentyl linker) **3.1b·Zn** appears at more cathodic potential of 0.179 V. This indicates the **3.1b·Zn** is more prone to oxidation. Structural similarity between these two strapped porphyrins suggests that the shift observed in $E_{1/2}$ does not arise from any through-bond inductive effects. Thus, it is likely that one of the triazole groups on the strap intramolecularly coordinates to the zinc(II) porphyrin centre, thereby increasing the electron density of the porphyrin and rendering its oxidation more facile. This intramolecular ligation is only possible in the case of **3.1b·Zn**, which possesses a longer and more flexible strap linker. This is further attested by repeating the experiments in the presence of pyridine (1%, v/v). For shorter strap **3.1a·Zn**, addition of pyridine led only to a slight cathodic shift of $\Delta E_{1/2}$ = –15 mV, which could be ascribed to a stabilisation effect as a result of pyridine coordination to zinc(II) porphyrin (Figure 3.21a). In stark contrast, the presence of pyridine induced a significant destabilisation of $\Delta E_{1/2}$ = +91 mV for **3.1b·Zn**, indicative of ligand displacement of triazole by the more basic pyridine (Figure 3.21b).

Table 3.4: Half-wave potentials $E_{1/2}$ (V vs. Fc/Fc^+) for all receptors in CH_2Cl_2, 100 mM $TBAPF_6$ in the absence and presence of pyridine (1%, v/v).

$E_{1/2}$ in $CH_2Cl_2/TBAPF_6$	$P/P^{+\bullet}$	$P^{+\bullet}/P^{2+}$[a]	$BDP/BDP^{+\bullet}$
3.1a·Zn	0.282 V	0.624 V	/[b]
3.1b·Zn	0.179 V	0.617 V	/
3.9·Zn	0.193 V	0.652 V	/
3.15·Zn	0.270 V	0.688 V	0.425 V
3.16·Zn	0.230 V	0.675 V	0.501 V
3.1a·Zn + pyridine (1%, v/v)	0.267 V	0.567 V	/
3.1b·Zn + pyridine (1%, v/v)	0.270 V	0.552 V	/
3.9·Zn + pyridine (1%, v/v)	0.204 V	0.550 V	/
3.15·Zn + pyridine (1%, v/v)	0.292 V	0.609 V	N.O.[c]
3.16·Zn + pyridine (1%, v/v)	0.248 V	0.579 V	≈0.47[d]

[a]Poor reversibility. [b]Not applicable. [c]N.O. = not observed. [d]Weak and broad.

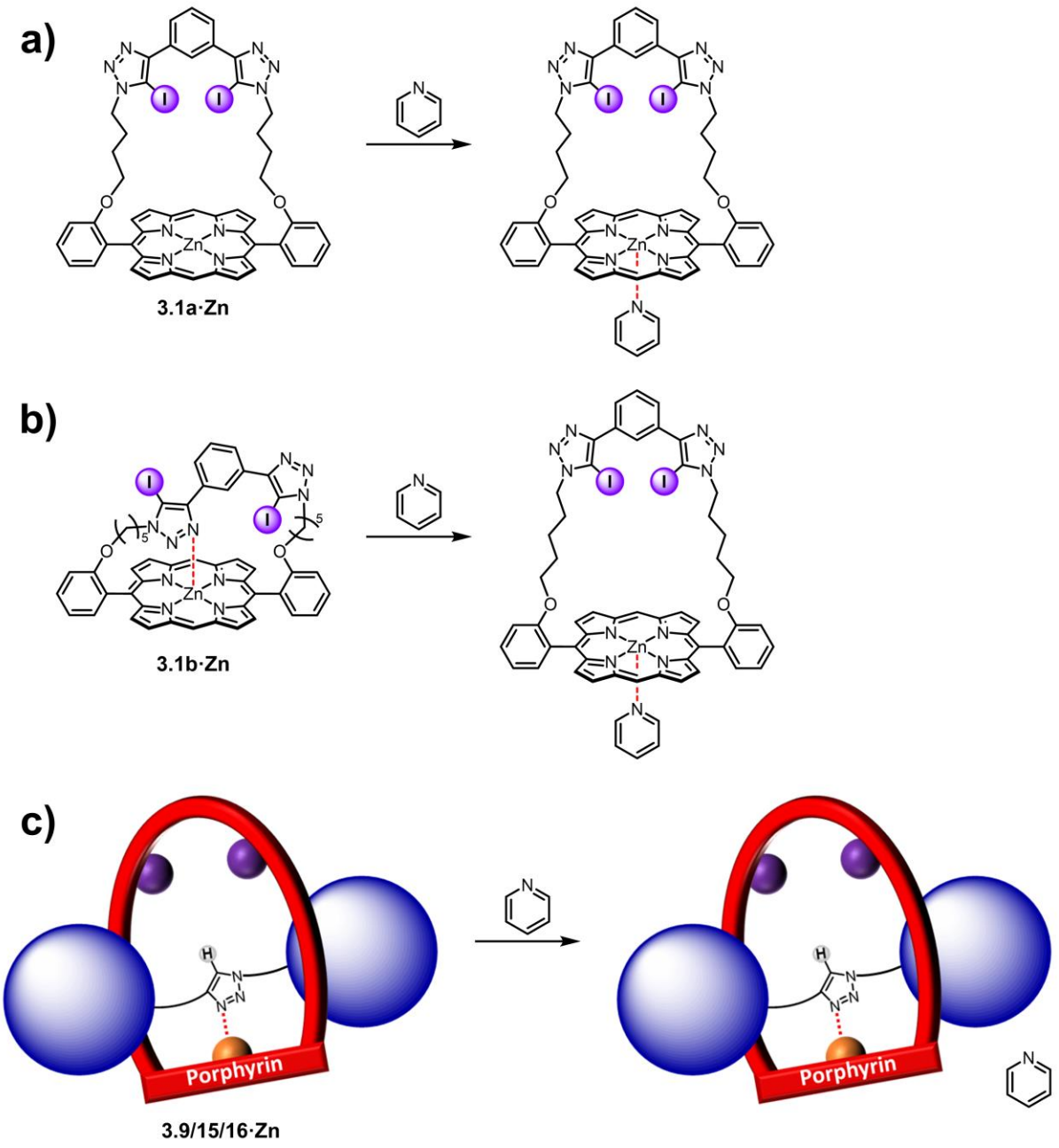

Figure 3.21 Different effects of pyridine on the conformations of a) **3.1a·Zn**, b) **3.1b·Zn** and c) **3.9/15/16·Zn**.

[2]Rotaxane **3.9·Zn** displayed a more anodic $E_{1/2}$ (0.193 V) than that of its macrocyclic component **3.1a·Zn** (0.282 V), suggestive of stabilisation of the oxidised form $P^{+\bullet}$ via metal-ligand coordination to the metalloporphyrin. However, unlike **3.1b·Zn**, coordination of macrocycle triazole to porphyrin is highly unlikely in the presence of a threaded axle. Intermolecular macrocycle triazole-zinc(II) ligation can also be ruled out as similar stabilisation effect was not observed for the free macrocycle

3.1a·Zn. Furthermore, the addition of 1% of pyridine to the CH_2Cl_2 solution of the [2]rotaxane **3.9·Zn**, only led to a modest perturbation to its $E_{1/2}$ ($\Delta E_{1/2}$ = +11 mV). Since macrocycle intramolecular triazole coordination could be easily disrupted by pyridine (i.e. in the case **3.1b·Zn**), this confirms axle triazole coordination to zinc(II) porphyrin, which for kinetic reasons cannot be displaced by pyridine (Figure 3.21c). Similar effects were also observed for BODIPY-functionalised rotaxanes **3.15–16·Zn**, with pyridine addition leading to only small anodic shifts, indicating pyridine cannot displace the axle triazole ligand.

Lastly, it is noteworthy that pyridine addition led to a consistent cathodic shift ($\Delta E_{1/2} \approx 60–70$ mV) of the second porphyrin oxidation couple $P^{+\bullet}/P^{2+}$ for all receptors studied (Figure 3.22 and Figure 3.23). This indicates, that regardless of initial triazole coordination in the reduced form, pyridine can still increase the electron density of porphyrin core for the $P^{+\bullet}/P^{2+}$ oxidation.

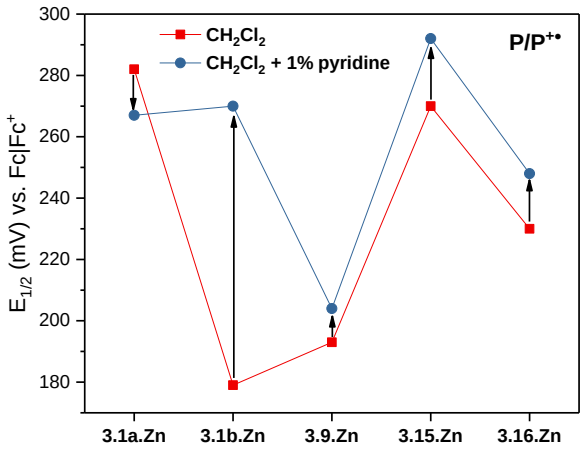

Figure 3.22 Half-wave potentials of the $P/P^{+\bullet}$ couple of all receptors in $CH_2Cl_2/TBAPF_6$ in the absence (red square) and presence (blue circles) of 1% (v/v) pyridine. Connecting lines are to guide the eye only.

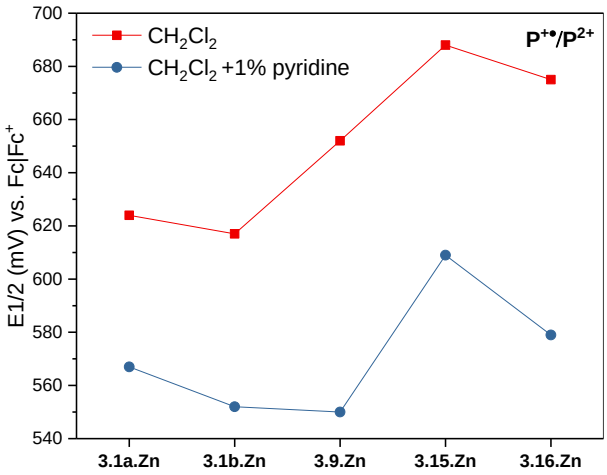

Figure 3.23 Half-wave potentials of the $P^{+\bullet}/P^{2+}$ couple of all receptors in CH_2Cl_2/$TBAPF_6$ in the absence (red square) and presence (blue circles) of 1% (v/v) pyridine. Connecting lines are to guide the eye only.

3.5.3 Electrochemical Anion Sensing

To assess the electrochemical anion sensing capabilities of the [2]rotaxanes (**3.9·Zn**, **3.15·Zn** and **3.16·Zn**), voltammetric anion titrations were undertaken with HSO_4^-, Cl^- and OAc^- in CH_2Cl_2. In a typical titration, $\Delta E_{1/2}$ of the $P/P^{+\bullet}$ redox couple of the receptor was measured upon increasing the anion concentration. All experiments were conducted at consistent ionic strength of 100 mM and monitored by square-wave voltammetry (SWV).

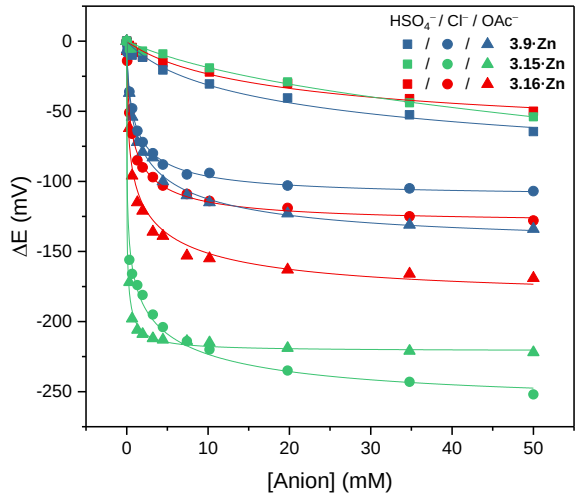

Figure 3.24 Cathodic voltammetric shifts of **3.9·Zn** (blue), **3.15·Zn** (green) and **3.16·Zn**(red) upon titration with HSO_4^- (squares), Cl^- (circles) and OAc^- (triangles) in CH_2Cl_2, 100 mM $TBAPF_6$. Solid lines represent fits to the Nernst 1:1 host-guest binding model.[280]

As shown in Figure 3.24 and Table 3.5, the addition of anions induced significant cathodic shifts for all receptors, with larger responses seen for Cl^- and OAc^- than HSO_4^-. In particular, **3.15·Zn** displays the largest cathodic shift to both Cl^- and OAc^- among all three interlocked receptors, with $\Delta E_{1/2}$ = −252 and −222 mV respectively. By fitting the voltammetric isotherms to a Nernst binding model using a 1:1 host-guest stoichiometry,[280] anion association constants were determined for the oxidised (K_{Ox}) and native (K_{red}) receptor state (Table 3.5). As expected, K_{Ox} is significantly larger than that of K_{red} by multiple orders of magnitude, indicating that electrochemical oxidation of the [2]rotaxanes substantially enhances their anion binding strength. Importantly, these results serve to highlight the capabilities of the strapped porphyrin-functionalised [2]rotaxanes in sensing anions via significant cathodic shift of the $P/P^{+\bullet}$ redox couple.

Table 3.5: Maximum cathodic shifts ΔE_{Max} (mV) of the $P/P^{+\bullet}$ couple of **3.9·Zn**, **3.15·Zn** and **3.16·Zn** upon titration with anions (at [anion] = 50 mM) and anion binding constants to the oxidised (K_{Ox}) and native receptor state (K_{Red}) in CH_2Cl_2, 100 mM $TBAPF_6$.[a]

$E_{1/2}$ in $CH_2Cl_2/TBAPF_6$	ΔE_{Max} (mV)[b]	K_{Ox} (M^{-1})	K_{Red} (M^{-1})
3.9·Zn + HSO_4^-	−65	254	5
3.9·Zn + Cl^-	−107	9 700	128
3.9·Zn + OAc^-	−134	10 900	36
3.15·Zn + HSO_4^-	−54	97	0
3.15·Zn + Cl^-	−252	80 000	31
3.15·Zn + OAc^-	−222	4 010 000	718
3.16·Zn + HSO_4^-	−50	175	11
3.16·Zn + Cl^-	−128	19 400	122
3.16·Zn + OAc^-	−169	50 500	38

[a]K_{Ox} and K_{Red} were obtained by fitting of the voltammetric isotherms according to a Nernst 1:1 host-guest binding model.[280] [b]Estimated error ≤ 5 mV.

3.6 Conclusion

In conclusion, two XB strapped porphyrins with butyl (**3.1a·Zn**) and pentyl (**3.1b·Zn**) linkers were initially prepared. UV–visible absorption titration experiments were undertaken to evaluate their anion sensing capabilities. Interestingly, while strong binding to halide anions was demonstrated for the shorter strap porphyrin, intramolecular triazole coordination to zinc(II) metalloporphyrin completely negated the anion affinity of the longer strap congener.

Employing CuAAC-mediated active metal templation, the shorter strap porphyrin **3.1a·Zn** was further exploited in the synthesis of three [2]rotaxanes, including the first examples of porphyrin-BODIPY [2]rotaxanes **3.15–16·Zn** capable of dual sensing of anions via changes in their optical and redox properties. Extensive ^{1}H NMR, electronic absorption and electrochemical studies reveal the coordination of axle triazole to macrocyclic zinc(II) porphyrin in these interlocked systems. This intercomponent interaction serves to enhance the degree of preorganisation of the rotaxane binding sites and augments their anion affinities. Fluorescence titrations conducted in acetone and the more competitive 2% H_2O/acetone (v/v) mixture demonstrated the optical anion sensing capabilities of **3.15–16·Zn** via quenching of the rotaxane axle component BODIPY-centred emission band. In particular, larger magnitudes of quenching and significantly stronger binding of anions was observed for rotaxane **3.16·Zn**, which was ascribed to the presence of the axle electron-withdrawing perfluoroaryl group, highlighting the tunability of these systems. Lastly, all three porphyrin-functionalised rotaxanes also displayed significant cathodic perturbations to the porphyrin P/P$^{+\bullet}$ oxidation redox couples upon addition of anions, illustrating their electrochemical anion sensing capabilities. These results serve to highlight the

versatility of this receptor design by incorporating optical and redox active moieties to the axle and macrocyclic components of MIMs for dual anion sensing.

3.7 Future Work

Anion recognition in aqueous environments has numerous biological, industrial and medicinal applications.[343] However, the design and synthesis of hosts capable of binding anions in water is notoriously challenging due to water being a very competitive solvent. This explains why the majority of water-soluble synthetic anion receptors reported to-date are highly positively charged and therefore benefit from the strong Coulombic attractions with the anions.[344] However, strong electrostatic attractions, in the context of anion recognition, is a double-edge sword that strengthens the anion affinity of the receptor, but also leads to selectivity towards the most highly charged anions due to the non-directional nature of this interaction. Anion complexation with cationic hosts also suffer from the presence of counterions that compete for the binding sites. These issues can be effectively circumvented with the use of charge-neutral anion receptors.[73,79,97,122,345–350]

To this end, future work building on the results of this project will entail the synthesis of electroneutral XB strapped porphyrin anion sensors that can operate in pure water. This may be achieved via the judicious incorporation of water-solubilising tri(ethylene glycol) side chains into the porphyrin core and the covalent strap to impart water solubility (Figure 3.25). Furthermore, utilising CuAAC-AMT (Scheme 3.10), water soluble [2]rotaxanes with fluorogenic BODIPY and solubilising permethylated β-cyclodextrin stoppers can be synthesised. As demonstrated by the superior anion affinity of perfluoroaryl-appended **3.16·Zn** compared to phenyl-appended **3.15·Zn**, two tetrafluorobenzene spacers can be covalently linked to the axle triazole to

strengthen the anion affinity. These water-soluble BODIPY-porphyrin-cyclodextrin systems are envisaged to be capable of dual anion sensing in aqueous media via changes in the emission intensity of BODIPY and the redox properties of porphyrin.

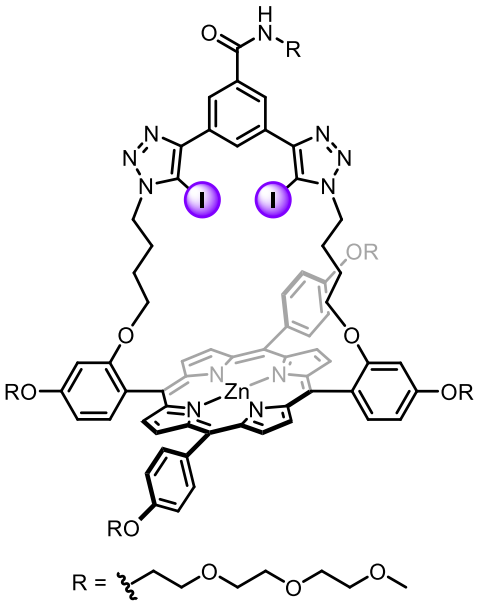

Figure 3.25 Structure of target water-soluble XB strapped porphyrin.

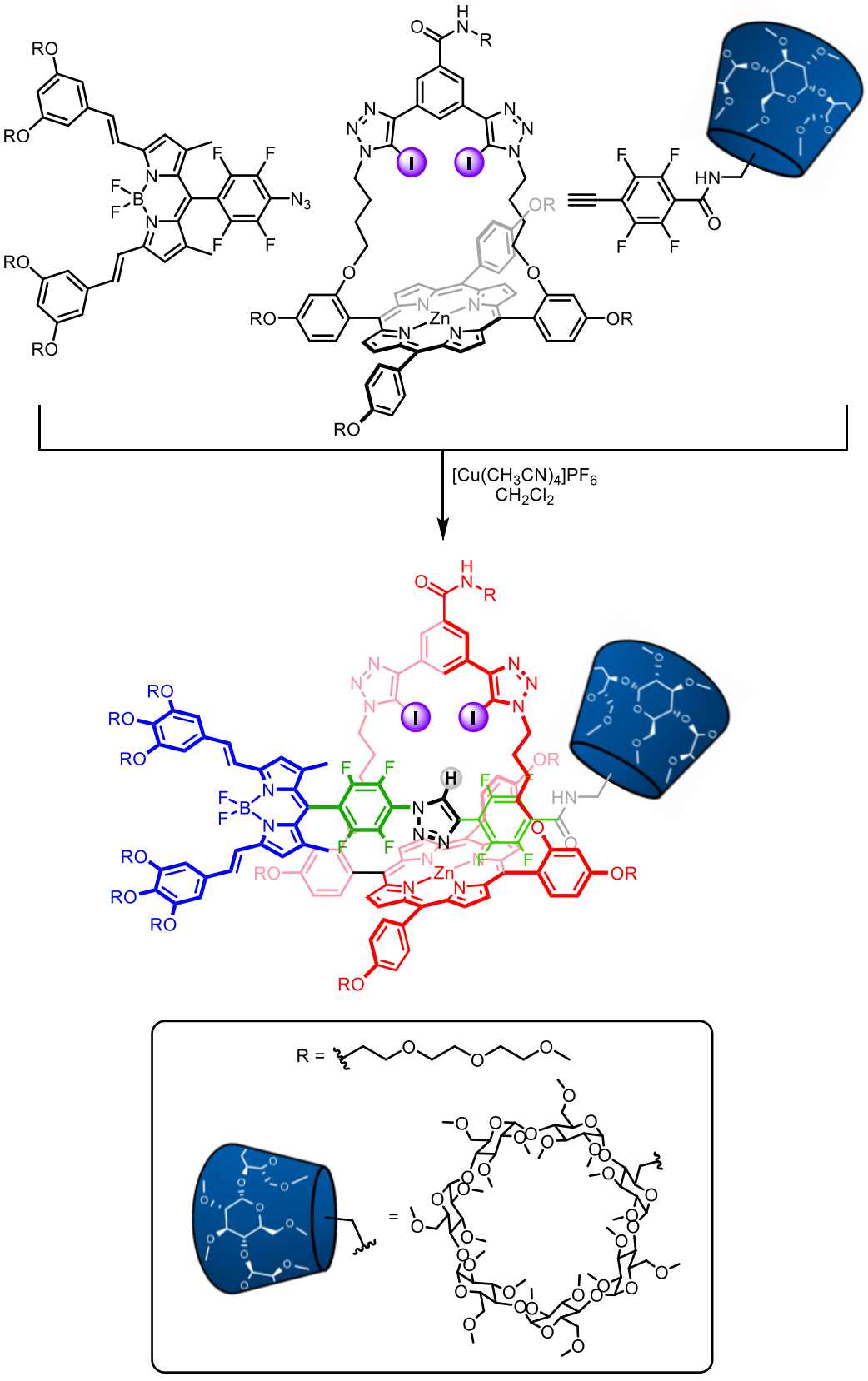

Scheme 3.10 Proposed synthesis of target water-soluble BODIPY-porphyrin-*β*-cyclodextrin XB [2]rotaxane via CuAAC-AMT.

Chapter 4

Sigma-Hole Mediated Ion-Pair Recognition in Macrocyclic and Catenane Interlocked Systems

Chapter 4 Sigma-Hole Mediated Ion-Pair Recognition in Macrocyclic and Catenane Interlocked Systems

4.1 Introduction

Ion-pair receptors designed for the simultaneous recognition of both cations and anions have been widely exploited as salt extracting/solubilising agents, membrane transporters and sensors.[136,137] To date, the majority of the heteroditopic/multitopic receptors reported contain crown ethers for Group 1 metal cation complexation, and are appended with HB donor motifs such as amide and urea for anion binding.[142,351] In recent years, XB and ChB interactions have been shown to be promising alternatives to traditionally employed HB in the context of anion recognition, by virtue of their comparable binding strength to HB, more stringent linear directionality in bonding and the intrinsic hydrophobicity of halogen and chalcogen atoms.[30,205] Despite this, heteroditopic receptors employing such σ-hole interactions to drive anion complexation are rare.[106,239,352–355]

This chapter focuses on the design and synthesis of heteroditopic/multitopic σ-hole macrocyclic and catenane interlocked systems for ion-pair recognition. The concept of cooperativity in the context of ion-pair binding is briefly introduced (Section 4.1.1), followed by examples of heteroditopic/multitopic σ-hole receptors for ion-pair recognition (Section 4.1.2).

4.1.1 Cooperativity in Ion-Pair Recognition

Cooperativity is a central concept in the binding of ion-pairs. When the recognition of one ion enhances/diminishes the heteroditopic receptor's affinity towards the other oppositely charged ion, it is described as cooperative/anti-cooperative binding. This phenomenon is usually attributed to two underlying mechanisms — a) proximal electrostatic interactions between the two co-bound ions, and b) the ion-induced allosteric conformational change.[137,142,351] For instance, Kubo and co-workers reported a crown ether based receptor appended with two HB thiourea units (Figure 4.1).[356] While the free receptor displayed a modest affinity towards diphenylphosphate (K_a = 490 M^{-1}) in CD_3CN, complexation of the receptor with one equivalent of K^+ cation led to an almost 19-fold increase in the phosphate anion association constant (K_a = 9200 M^{-1}). An energy minimised structure of the receptor·ion-pair complex suggested the receptor undergoes a significant conformational change upon K^+ crown ether complexation, bringing the two distant thiourea donors together for the convergent binding of diphenylphosphate (Figure 4.1). In addition, the close proximity of the two co-bound ions strengthens their favourable Coulombic attractions, further contributing to the observed positive cooperativity.

In contrast to the monotopic binding of a cation or anion, multiple binding equilibria co-exist in the recognition of an ion-pair, which all contribute to the observed cooperativity effect.[357] As shown in Figure 4.2, in addition to the formation of the receptor·ion-pair complex ([R·CA]), the heteroditopic receptor can also individually bind the cation ($[R·C]^+$) or anion ($[R·A]^-$). Significant ion-pairing or salt recombination (CA) can be observed in solvents of low polarity. In some cases, the ion-pair binding system is further complicated by the association of higher order stoichiometric complexes. Therefore, despite the frequent exploitation of cooperativity

in ion-pair recognition, delineation of individual contributions from electrostatic and allostery remains a challenging task and may only be limited to simplified systems.[139,140]

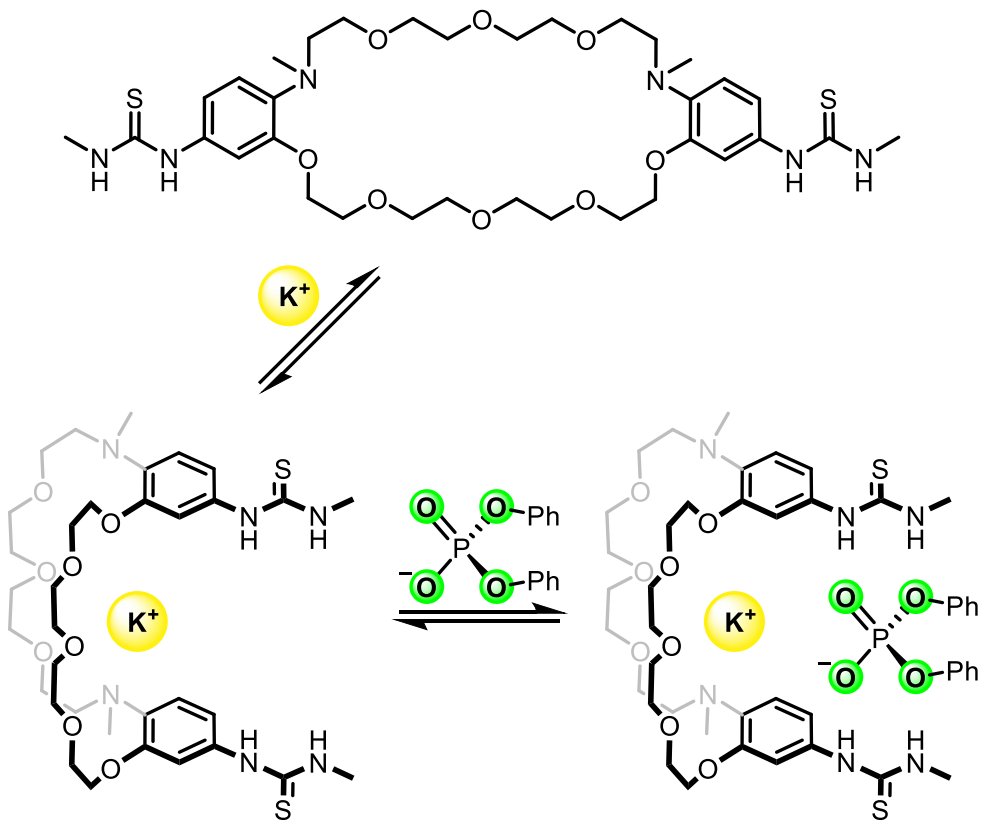

Figure 4.1 Kubo's crown ether-thiourea ion-pair receptors, showing the K^+-induced conformational change of the receptor that favours the binding of tetraphenylphosphate anion.[356] (K^+ was added as tetrakis(4-chlorophenyl)borate (TCPB) salt and tetraphenylphosphate was added as tetraethylammonium (TEA) salt)

Ion-Pair Binding: $R + C^+ + A^- \rightleftharpoons [R{\cdot}CA]$

Cation Binding: $R + C^+ \rightleftharpoons [R{\cdot}C]^+$

Anion Binding: $R + A^- \rightleftharpoons [R{\cdot}A]^-$

Ion-Pairing: $C^+ + A^- \rightleftharpoons CA$

Higher Stoichiometry: $R + 2C^+ + 2A^- \rightleftharpoons [R{\cdot}C_2A_2]$

$2R + A^- \rightleftharpoons [R_2{\cdot}A]^-$

$2R + C^+ \rightleftharpoons [R_2{\cdot}C]^+$

⋮

Figure 4.2 Multiple equilibria involved in ion-pair recognition.

In a study by Flood and co-workers,[141] they combined both experimental and computational evidence to deconvolute the electrostatic and allosteric contributions in ion-pair binding, utilising an oligo(ethylene glycol)-based macrocycle containing an anion binding bis-triazole motif as the model heteroditopic receptor (Figure 4.3). By considering the multiple ion-pair binding equilibria involved, titration experiments conducted in 4:1 CD_2Cl_2/CD_3CN allowed for the accurate determination of cooperativity factors in the binding of NaI and $NaClO_4$ salts. DFT calculations showed that both electrostatic and allostery contribute positively to the binding of sodium halide salts. In particular, allostery was found to account for ca. 30% of the overall observed binding cooperativity and the dominant electrostatic component enabled the use of Coulomb's Law to correctly predict the observed trend in the degree of cooperativity (NaCl > NaBr > NaI).

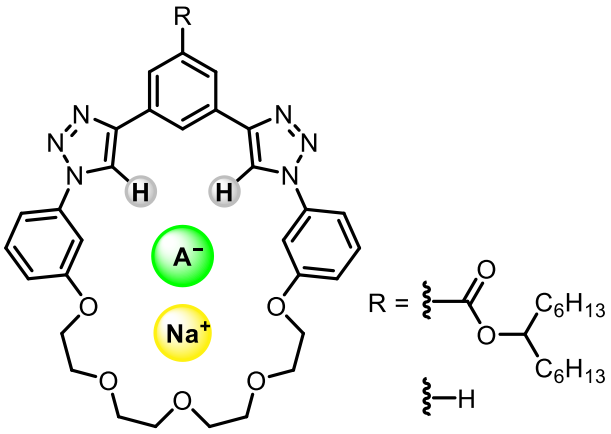

Figure 4.3 Flood's bis(proto-triazole) heteroditopic receptor for investigating the electrostatic and allosteric contributions in ion-pair recognition.[141]

4.1.2 Sigma-Hole Mediated Ion-Pair Recognition

Following the first example of XB heteroditopic receptor reported by Resnati and Metrangolo in 2005,[106] it was not until Schubert and co-workers, twelve years later in 2017, that another example appeared.[239] They described an iodo-triazole-containing polyether macrocycle for the ion-pair recognition of NaI (Figure 4.4a). ^{1}H and ^{13}C NMR titrations conducted in 3:1 CD_2Cl_2/CD_3CN revealed significant cooperativity in the binding of NaI, with Na^+ complexation greatly enhancing the receptor's affinity towards the I^- anion.

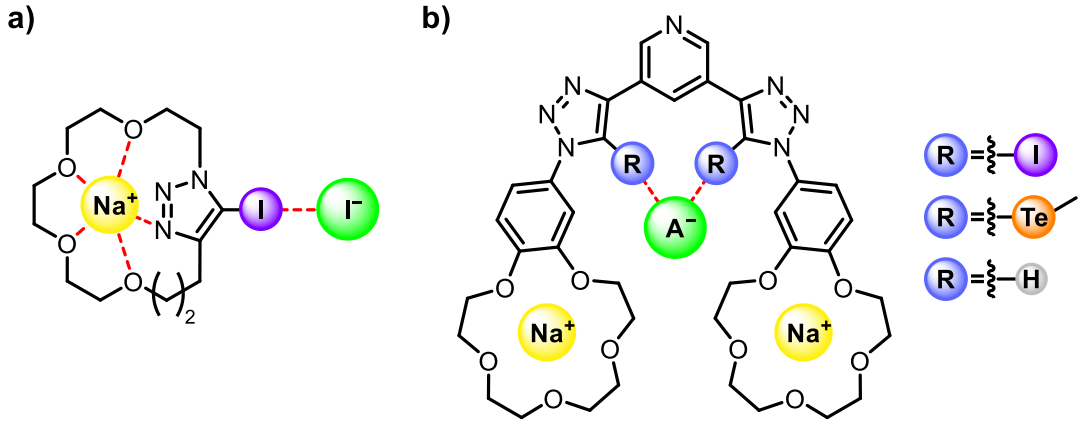

Figure 4.4 a) Schubert's iodo-triazole-containing macrocycle binding NaI as an ion-pair.[239] b) Beer's XB/ChB/HB crown-ether based heteroditopic receptors (A^- = Br^-, I^-).[354]

Recently, the Beer group reported a series of heteroditopic receptors incorporated with 3,5-bis(iodo-/telluromethyl-/proto-triazole)pyridine as the XB/ChB/HB donor motifs (Figure 4.4b).[354] Sodium cation complexation by each of the benzo-15-crown-5 groups covalently attached to the XB- and ChB-functionalised triazole units, substantially augmented the receptors' binding of Br^- and I^-. While the XB host demonstrated the strongest binding of halide anions in the presence of co-bound Na^+ cations in 1:9 DMSO/$CDCl_3$, the largest enhancement in anion association constant values (>200-fold) was observed for the ChB analogue, essentially switching on its halide anion affinity. DFT calculations suggested the higher degree of cooperativity

exhibited by the XB/ChB heteroditopic receptors relative to the HB congener originates from the Na^+ cation-induced through-bond polarisation of the σ-holes on the iodine and tellurium atoms. Importantly, these results highlighted the unique advantage of heteroditopic receptors integrated with σ-hole donors to modulate ion-pair binding strength.

4.2 Chapter Aims

This chapter is divided into two parts:

Part I: Inspired by the exciting ion-pair binding potential demonstrated by reported σ-hole heteroditopic receptors, Part I of this project aims to synthesise a series of 1,10-phenanthroline-based macrocycles, integrated with *meta*-substituted bis(iodo-/telluromethyl- triazole)benzene XB/ChB anion recognition sites, for the binding and extraction of lithium halide salts (Figure 4.5a). The respective receptor's capability to complex the lithium cation is established initially. This is followed by an extensive quantitative ^1H NMR titration study to determine halide anion association constants of the heteroditopic hosts in the absence and presence of co-bound lithium cations. Lastly, the ability of these macrocycles to extract and recover lithium salts is studied by both solid-liquid and liquid-liquid extraction experiments.

Part II: With the objective to exploit the superior charged guest recognition capability of MIMs, Part II of this project entails the preparation of the first examples of all-XB heterotritopic [2]catenanes functionalised with a cation binding polyether pocket, via adaptation of an alkali metal cation template strategy (Figure 4.5b). The ability of these interlocked catenane hosts to bind alkali metal salts as ion-pairs is investigated by ^1H NMR titration experiments. The potential of these receptors to function as

solubilising agents for alkali metal salts is probed by a preliminary solid-liquid extraction study.*

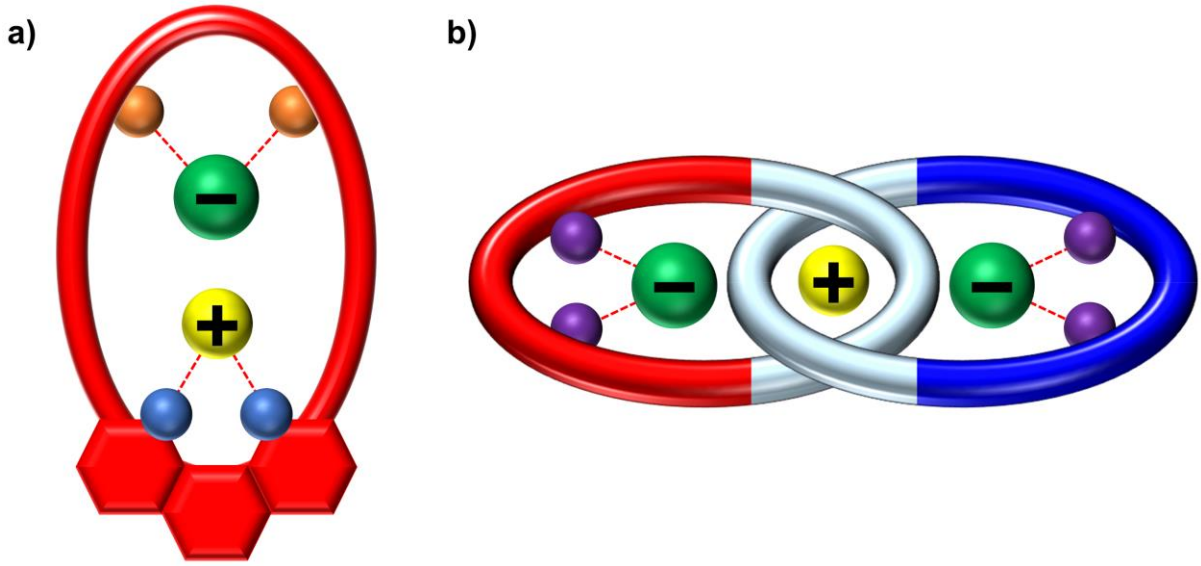

Figure 4.5 Schematic representation of the target a) phenanthroline-based heteroditopic σ-hole macrocycles, and b) all-XB tritopic [2]catenane. Orange spheres: σ-hole donors; Purple spheres: XB donors; Blue spheres: phenanthroline nitrogen donors; White arcs: polyether linkers; Yellow spheres: cations; Green spheres: anions.

4.3 Halogen Bonding and Chalcogen Bonding Heteroditopic Macrocycles

4.3.1 Design and Synthesis of XB and ChB Heteroditopic Macrocycles

The target heteroditopic σ-hole macrocycles **4.1** consist of a cation chelating 1,10-phenanthroline unit and XB/ChB 5-*tert*-butyl-1,3-bis(iodo-/telluromethyl-triazole)benzene motifs as the anion binding site. Scheme 4.1 outlines the retrosynthesis of the target macrocycles **4.1**. Route a) involves the CuAAC-mediated cyclisation reaction between a phenanthroline-functionalised bis-azide derivative and bis(iodo/telluromethyl)alkynes, forming the σ-hole donor bis-triazoles in the final step. However, CuAAC click reactions in the presence of a phenanthroline-containing

* This project was undertaken in collaboration with a final year Part II student Christian Gateley and fellow graduate student Hui Min Tay.

precursors may prove challenging due to the strong Cu(I)-chelating capability of the nitrogenous ligand, which can significantly inhibit the catalytic activities of the metal centre.[358] This synthetic obstacle could be circumvented by employing route b), in which the bis(iodo/telluromethyl)triazoles are pre-formed and incorporated into a bis-phenol precursor. Under basic conditions, a Williamson ether reaction between the bis-phenol and phenanthroline-based bis-tosylate affords the target heteroditopic macrocycles **4.1**.

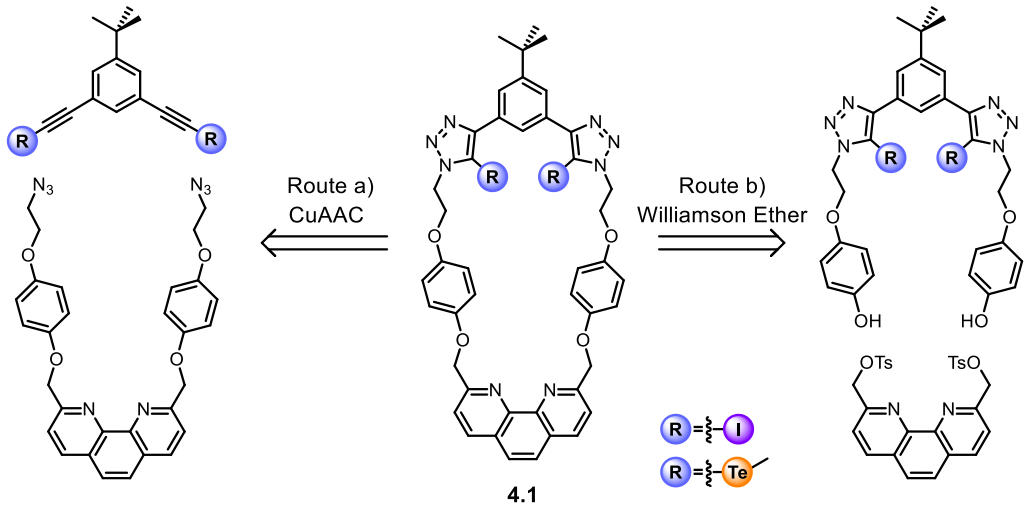

Scheme 4.1 Retro-synthesis of target heteroditopic σ-hole macrocycles **4.1**.

The synthetic route to phenanthroline-based bis-tosylate precursor **4.4** is shown in Scheme 4.2. Commercially available neocuproine was formylated via a SeO_2-mediated oxidation reaction in 1,4-dioxane/H_2O to afford the bis-aldehyde **4.2** in 80% yield.[359] $NaBH_4$ was then added to a solution of **4.2** in EtOH to reduce the aldehyde groups to alcohol and obtain diol **4.3**.[359] Treatment of **4.3** with tosyl chloride under basic conditions at 0 °C afforded bis-tosylate **4.4** in 85% yield after aqueous work-up and chromatographic purification.[360] It is noteworthy that in the tosylation reaction, prolonged reaction times (>3 hours) and elevated temperatures led to a noticeable decrease in yield of bis-tosylate **4.4** and an increased formation of the chlorinated 2,9-di(chloromethyl)-1,10-phenanthroline. This was attributed to the presence of the

electron-withdrawing phenanthroline unit in **4.4**, promoting the in situ nucleophilic substitution of the tosylate by Cl^-.[361]

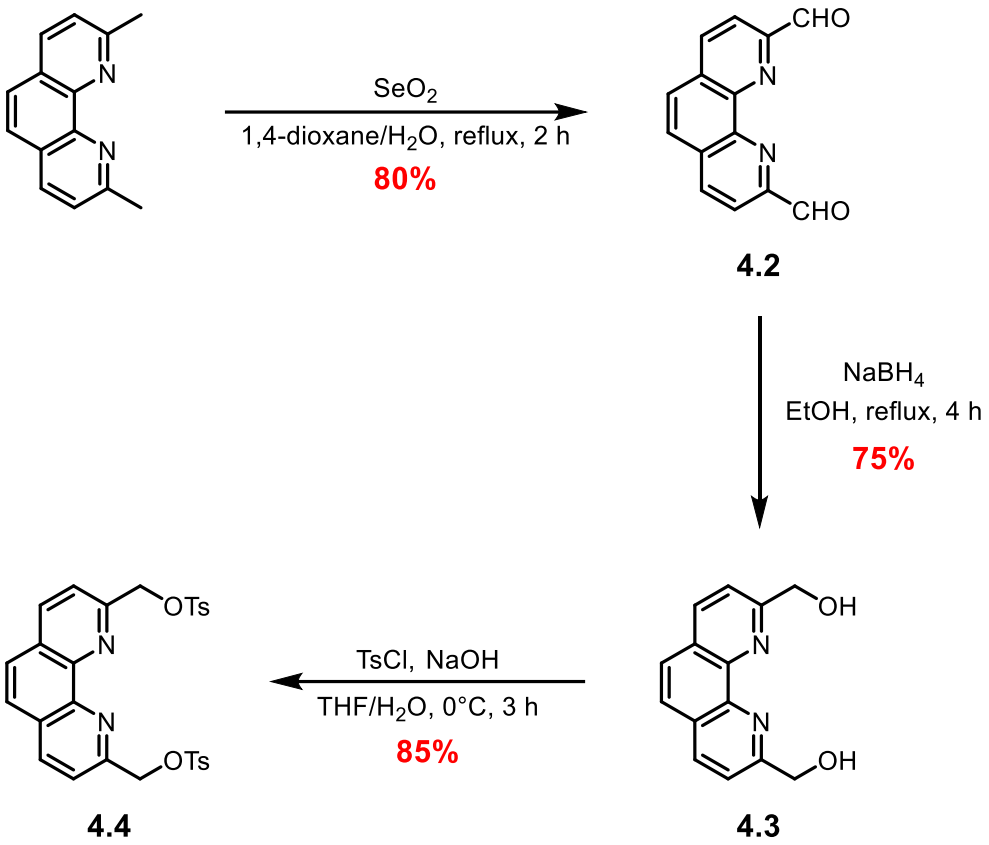

Scheme 4.2 Synthetic route to bis-tosylate phenanthroline precursor **4.4**.

To prepare the requisite azide precursor **4.7** (Scheme 4.3),[127] hydroquinone was initially mono-alkylated with 1,2-dibromoethane in the presence of KOH to give phenol **4.5** in 15% yield after purification by column chromatography. Azidation of compound **4.5** was achieved via nucleophilic substitution with NaN_3 in DMSO to afford **4.6** in 94% yield. To enhance its solubility in organic solvent, the phenol OH group of compound **4.6** was converted into the methoxymethyl (MOM) ether by reacting with MOM chloride in the presence of D*i*PEA in CH_2Cl_2 to obtain **4.7** in 95% yield.

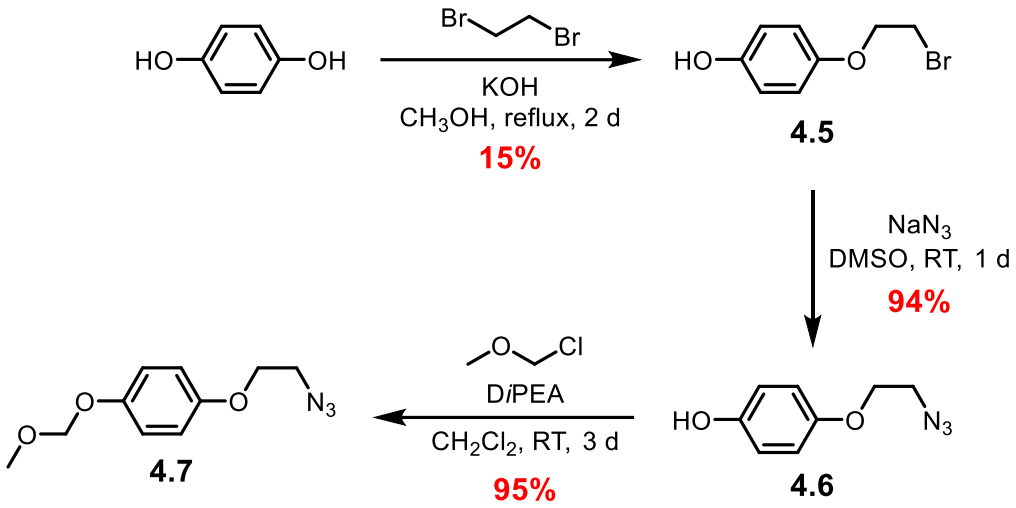

Scheme 4.3 Synthetic route to azido-functionalised hydroquinone linker **4.7**.

The multi-step synthesis of target phenanthroline-based XB/ChB heteroditopic macrocycles **4.1·I/Te^{Me}**, as well as the HB analogue **4.1·H**, is outlined in Scheme 4.4. CuAAC click reaction between the appropriately appended alkynyl precursors **2.3·I/Te^{Me}/H** (See Scheme 2.11 for synthesis) and two equivalents of azide **4.7** afforded the MOM-protected precursors **4.8**, which consist of the XB/ChB/HB anion binding sites. Deprotection of **4.8** via treatment with acidic methanolic solution gave the bis-phenol precursors **4.9** quantitatively. Target macrocycles **4.1·I**, **4.1·Te^{Me}** and **4.1·H** were prepared by cyclisation reaction between the appropriate bis-phenol **4.9** and phenanthroline-functionalised bis-tosylate **4.4** in the presence of basic Cs_2CO_3 in anhydrous DMF under high-dilution conditions (1.0 mM) in yields of up to 54%. All three receptors were characterised by ^{1}H, ^{13}C and ^{125}Te (where relevant) NMR spectroscopies and high-resolution ESI-MS.

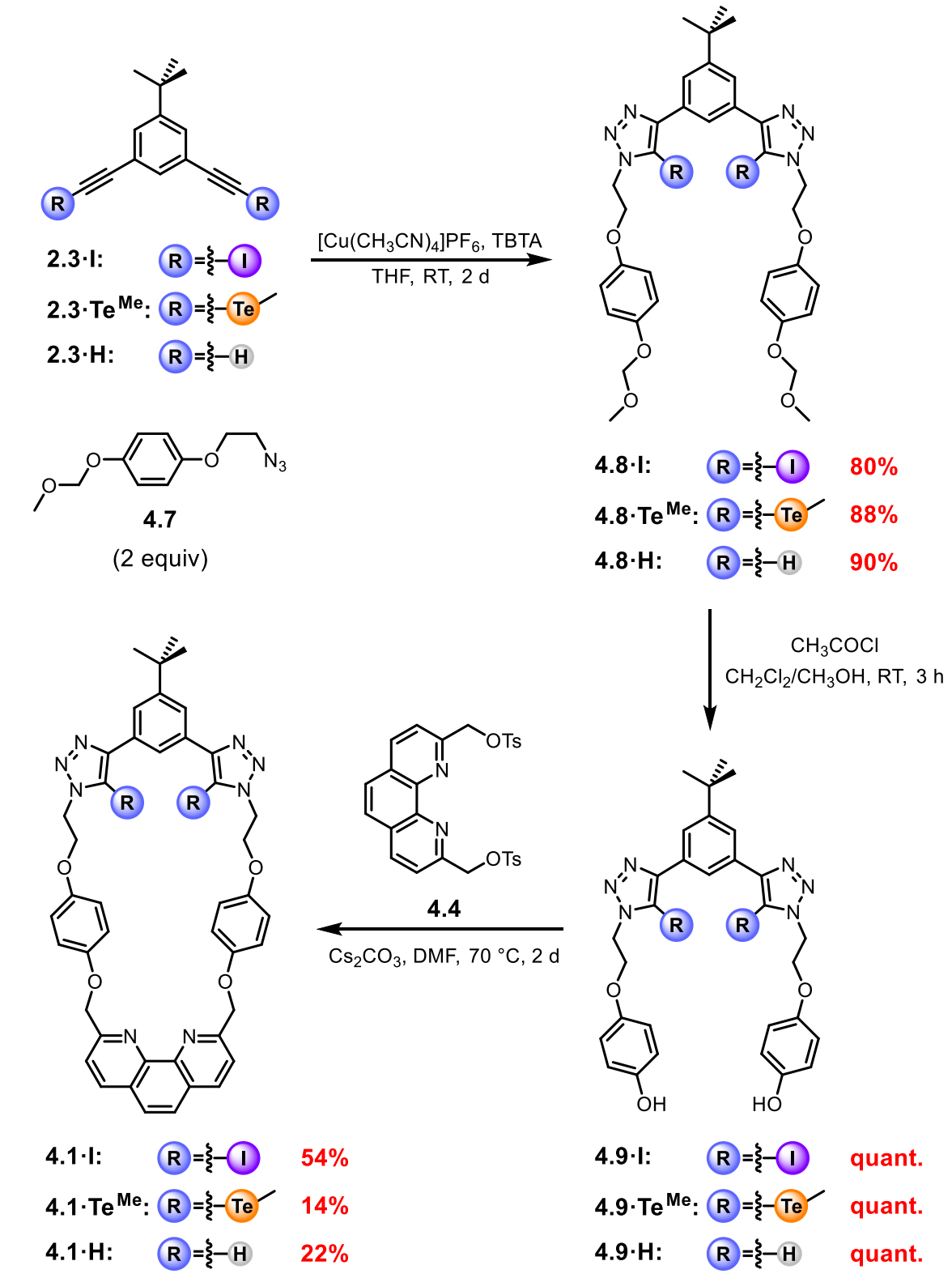

Scheme 4.4 Synthesis of XB/ChB/HB phenanthroline-based heteroditopic macrocycles **4.1·I/Te^{Me}/H**.

^{1}H NMR spectra of all three receptors in $CDCl_3$ are shown in Figure 4.6. Only minor shift differences were observed for the phenanthroline aromatic protons (*f*, *g*

and *h*) and external benzene spacer proton (*a*). Internal benzene proton *b* of **4.1·I/Te^{Me}**, however, appears significantly more downfield than that of **4.1·H**, attributed to the stronger electron-withdrawing ability of the iodine and tellurium atoms. Additional proton signals corresponding to $TeCH_3$ (i^{TeMe}) and proto-triazole (i^{Trz}) are observed at 1.90 ppm and 7.98 ppm respectively for **4.1·Te^{Me}** and **4.1·H**.

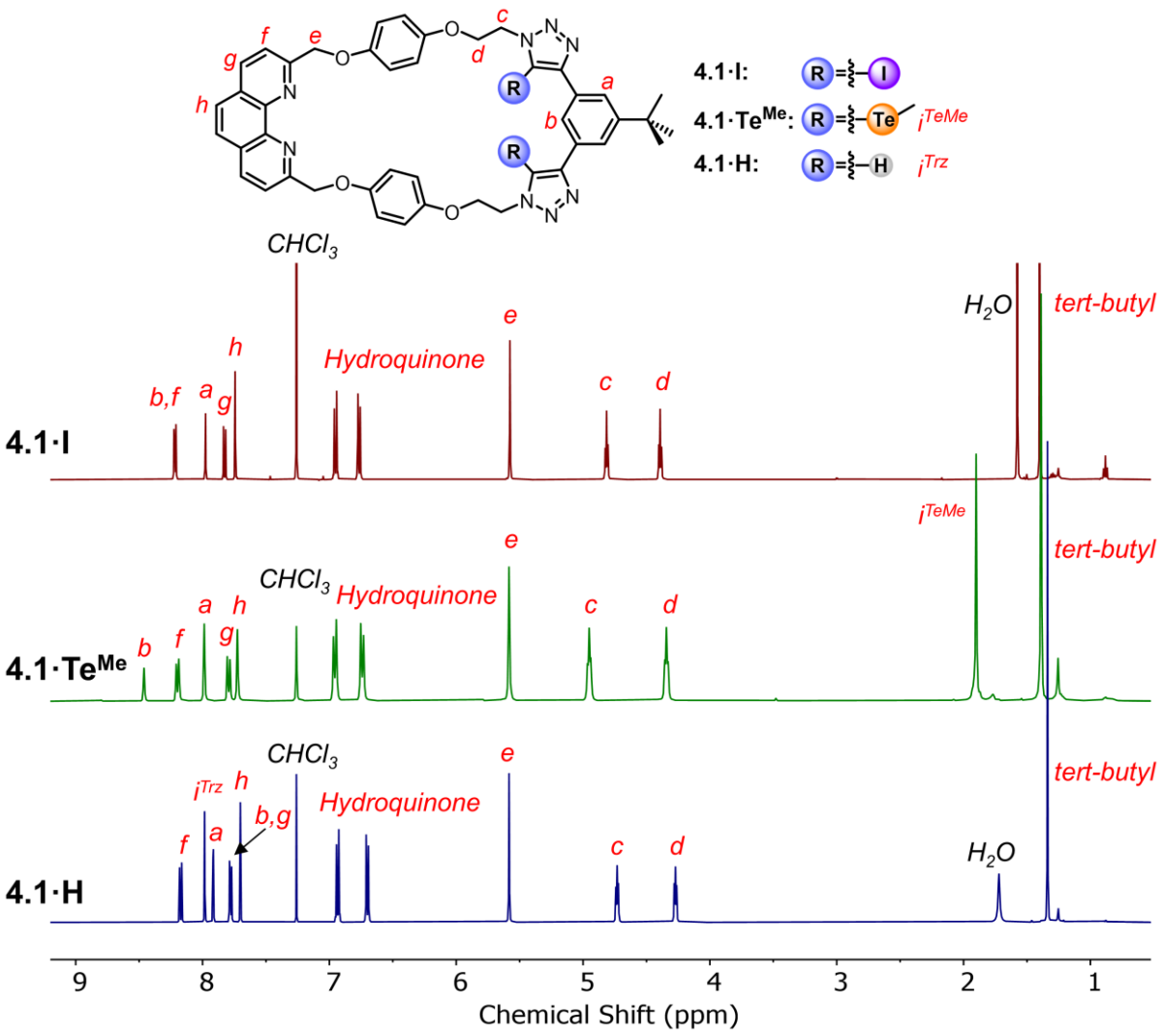

Figure 4.6 Stacked ^{1}H NMR spectra of **4.1·I** (top), **4.1·Te^{Me}** (middle) and **4.1·H** (bottom) (400 MHz, 298 K, $CDCl_3$).

Crystals suitable for X-ray diffraction analysis were obtained by slow evaporation of a $CHCl_3/CH_3OH$ solution of **4.1·I** and by vapour diffusion of pentane into a $CHCl_3$ solution of **4.1·H** (Figure 4.7). Compared to the proto-triazoles, the two iodo-triazoles are more twisted out of the plane of the central benzene spacer. In particular, one of the iodo-triazoles was observed to form a XB with a CH_3OH solvate molecule, demonstrating a I···O contact significantly shorter than the sum of their van der Waals radii (87%).

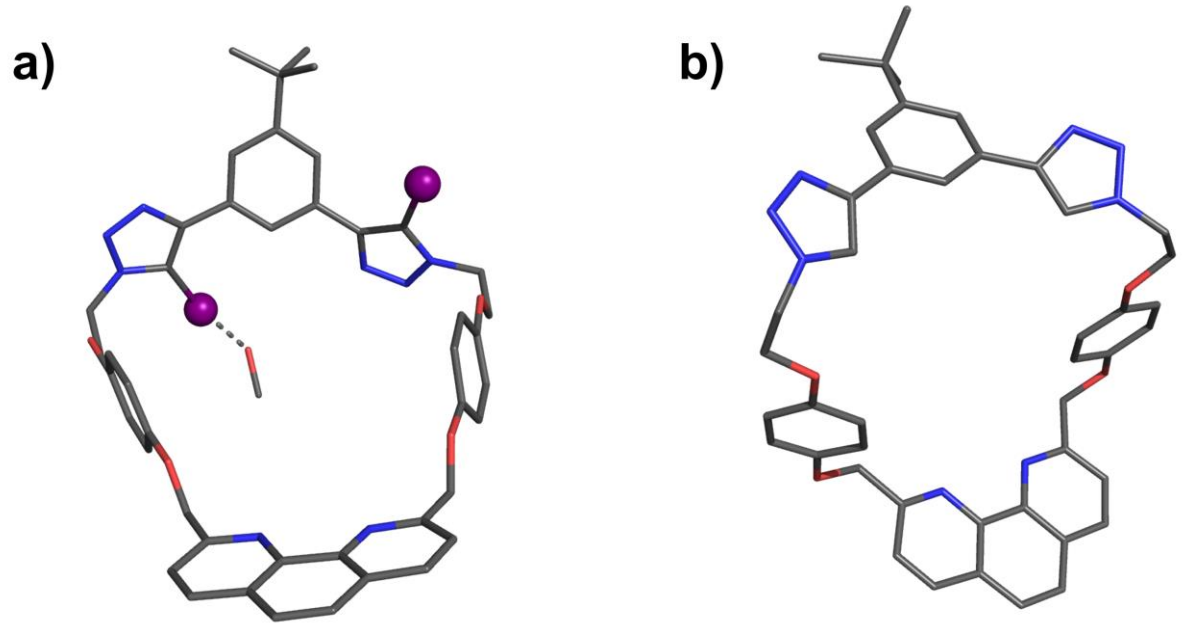

Figure 4.7 Crystal structure of a) **4.1·I** and b) **4.1·H**. XB interaction between an iodine atom (purple) and a methanol solvate is shown as grey dotted line in **4.1·I**. Hydrogen atoms are omitted for clarity. Gray = carbon, blue = nitrogen, and red = oxygen.

4.3.2 Ion-Pair Recognition Studies

To assess the ion-pair binding properties of the heteroditopic macrocycles, qualitative Li^+ cation complexation studies were conducted in 1:1 $CDCl_3/CD_3CN$. After establishing the capability of these receptors to chelate to the alkali metal cation, quantitative ^1H NMR anion titration experiments in the absence and presence of a co-bound Li^+ were undertaken to investigate the cooperativity effect in the binding of lithium halide salts as ion-pairs.

4.3.2.1 Lithium Cation Complexation Studies

In a typical experiment, a solution of $LiClO_4$ salt dissolved in CD_3CN (2.0 mM) was added slowly to a solution of the receptor dissolved in an equal-volume of $CDCl_3$ (2.0 mM), resulting in a final mixture concentration of 1.0 mM in 1:1 $CDCl_3/CD_3CN$. The mixture was thereafter sonicated for one hour to facilitate metal complexation.

The comparative ^1H NMR spectra of the receptors before and after complexation with $LiClO_4$ are shown in Figure 4.8. In all cases, general downfield perturbations of phenanthroline aromatic protons (*f*, *g* and *h*) were observed, suggestive of Li^+ binding. Furthermore, significant downfield shifts were seen for $TeCH_3$ (i^{TeMe}) (Figure 4.8b) and proto-triazole (i^{Trz}) (Figure 4.8c) signals respectively for **4.1·Te^{Me}** and **4.1·H**, which were likely result from conformational change of the macrocycles upon cation complexation.

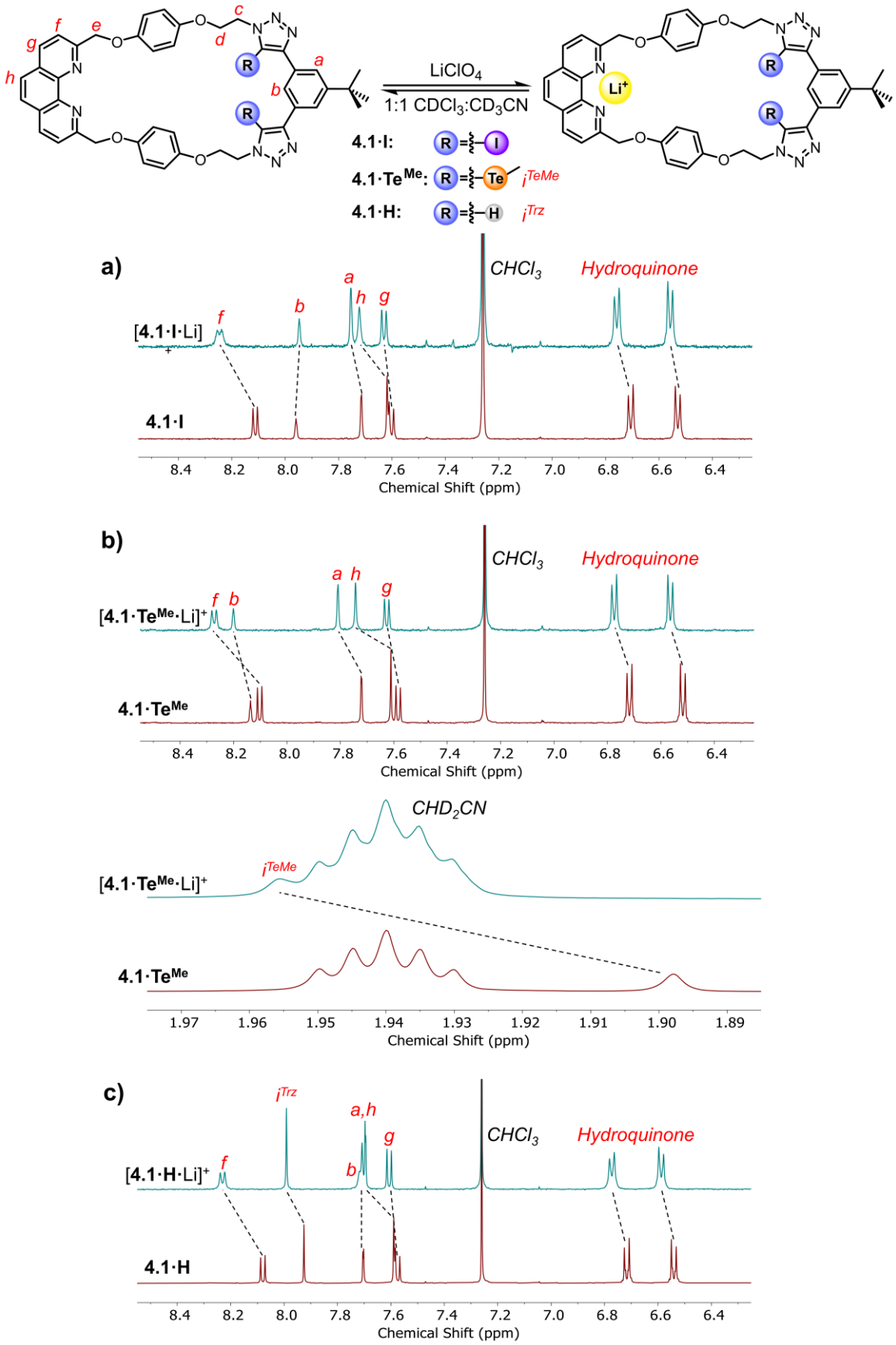

Figure 4.8 Truncated ^{1}H NMR spectra showing the a) aromatic region of **4.1·I**, b) aromatic region and $TeCH_3$ peak of **4.1·Te^{Me}**, and c) aromatic region of **4.1·H** in the absence and presence of one equivalent of $LiClO_4$ (500 MHz, 298 K, 1:1 $CDCl_3$/CD_3CN).

4.3.2.2 Anion Binding Studies

(A) Free Receptors

To investigate the halide anion binding properties of the receptors in the absence of Li^+, ^1H NMR anion titrations of the free receptors were conducted with TBA halide salts in 1:1 $CDCl_3/CD_3CN$. For all macrocycles, negligible shifts in the ^1H NMR spectra were observed upon increasing anion concentrations (up to 10 equivalents), indicating no halide binding in this mixed solvent system.

(B) Lithium Cation Complexed Receptors

To assess the capability of the macrocyclic receptors to simultaneously bind a Li^+ cation and halide anion, preliminary qualitative ^1H NMR binding studies were conducted in 1:1 $CDCl_3/CD_3CN$. The addition of one, two and five equivalents of halide anions (as their TBA salts) to the Li^+-complexed macrocycles (equimolar solutions $LiClO_4$ and macrocycle) strongly indicated the co-bound metal cation switched on the receptors' anion affinity. Figure 4.9 shows a representative example of the titration of XB receptor **4.1·I** with TBACl. Upon addition of Cl^- to [**4.1·I**·Li]$^+$, gradual downfield perturbations of internal benzene proton *b* were observed, attributable to chloride anion binding in the vicinity of the XB donors. Similar shifts in the ^1H NMR spectra were observed upon addition of Br^- and I^-, suggestive of concurrent binding of LiBr and LiI as ion-pairs.

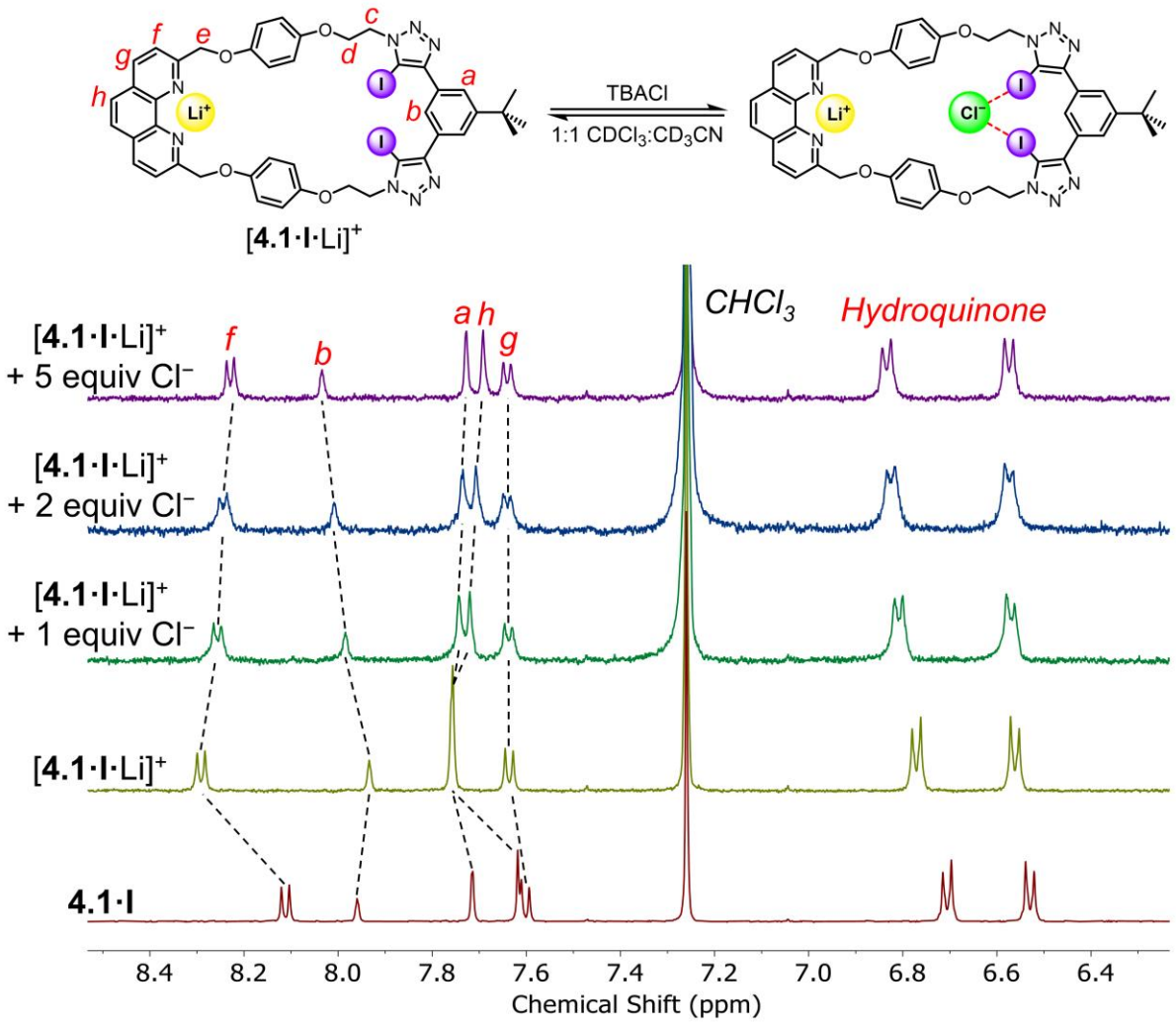

Figure 4.9 Truncated ^{1}H NMR spectra showing the aromatic regions of free receptor **4.1·I**, upon addition of 1 equivalent of LiClO4 and further addition of 1, 2 and 5 equivalents of TBACl (500 MHz, 298 K, 1:1 $CDCl_3/CD_3CN$).

Concomitant to the downfield perturbation of internal benzene proton *b*, addition of Br^- and I^- to the Li^+-complexed receptors **4.1·Te^{Me}** and **4.1·H** elicited significant downfield perturbations to the respective $TeCH_3$ (i^{TeMe}) (Figure 4.10a) and proto-triazole (i^{Trz}) proton signals (Figure 4.10b), providing further evidence of the ion-pair recognition of LiBr and LiI. However, addition of Cl^- to both of these Li^+-bound ChB/HB macrocycles led to decomplexation of the metal cation and subsequent precipitation of the LiCl salt.

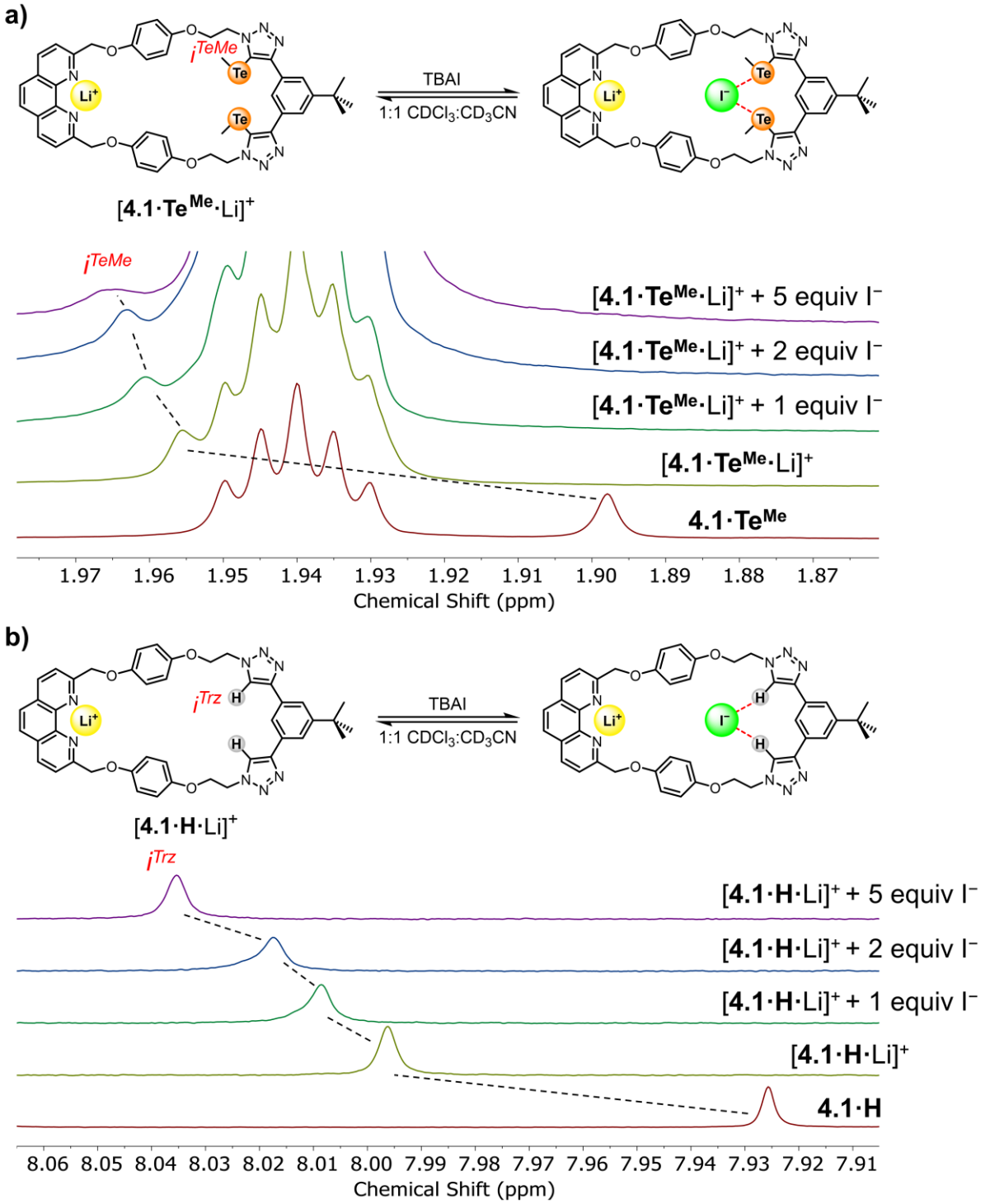

Figure 4.10 Truncated ^{1}H NMR spectra showing the a) $TeCH_3$ (i^{TeMe}) and b) proto-triazole (i^{Trz}) peaks of free receptor **4.1·Te^{Me}** and **4.1·H** respectively upon addition of 1 equivalent of $LiClO_4$ and further addition of 1, 2 and 5 equivalents of TBAI (500 MHz, 298 K, 1:1 $CDCl_3$/CD_3CN).

In order to evaluate the role of a co-bound Li^+ cation in the successful binding of Cl^- by the XB receptor **4.1·I**, analogous qualitative ^1H NMR binding studies with the anion were repeated in the presence of Na^+ or K^+. Upon sonicating a mixture of **4.1·I** and one equivalent of $NaClO_4$ or $KClO_4$ in 1:1 $CDCl_3/CD_3CN$ for one hour, significant perturbations of the phenanthroline aromatic proton signals were seen in the resulting ^1H NMR spectra, indicative of metal cation complexation (Figure 4.11). However, in stark contrast to the Li^+-complexed XB receptor, subsequent addition of TBACl to the solution of [**4.1·I**·Na]$^+$ or [**4.1·I**·K]$^+$ resulted in salt precipitation. This highlights the importance of Li^+ in the recognition of Cl^-, which is particularly impressive considering the high lattice energy of LiCl (834 kJ mol^{-1}) driving salt recombination.

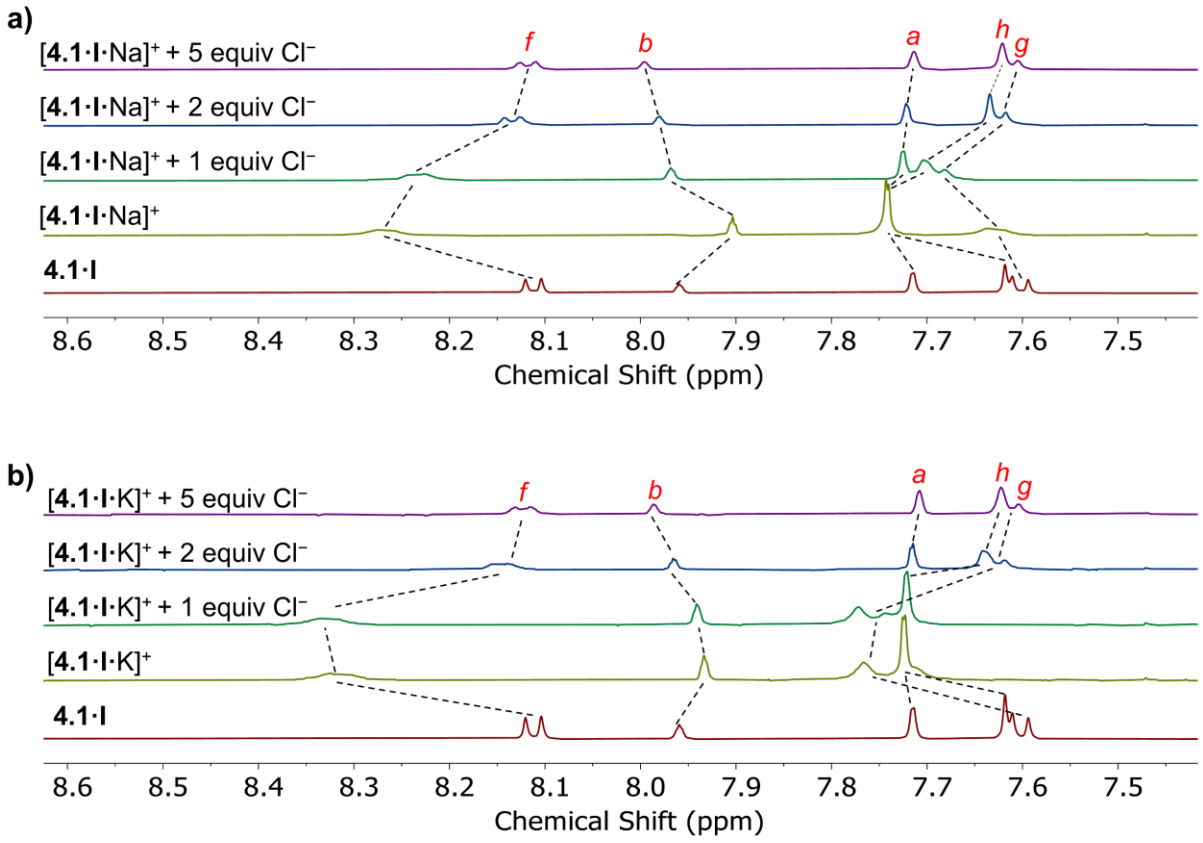

Figure 4.11 Truncated ^1H NMR spectra showing the aromatic regions of free receptor **4.1·I**, upon addition of 1 equivalent of either a) $NaClO_4$ or b) $KClO_4$, and further addition of 1, 2 and 5 equivalents of TBACl (500 MHz, 298 K, 1:1 $CDCl_3/CD_3CN$).

The quantitative ion-pair binding properties of the XB, ChB and HB receptors were investigated by ^{1}H NMR titrations of the Li^+-complexed macrocycles with TBA halide salts in the same solvent system. Bindfit[235,236] analysis of chemical shifts of proton signals as a function of anion concentration revealed 1:1 host-guest stoichiometric binding in all cases (Figure 4.12). The determined anion association constant values are tabulated in Table 4.1.

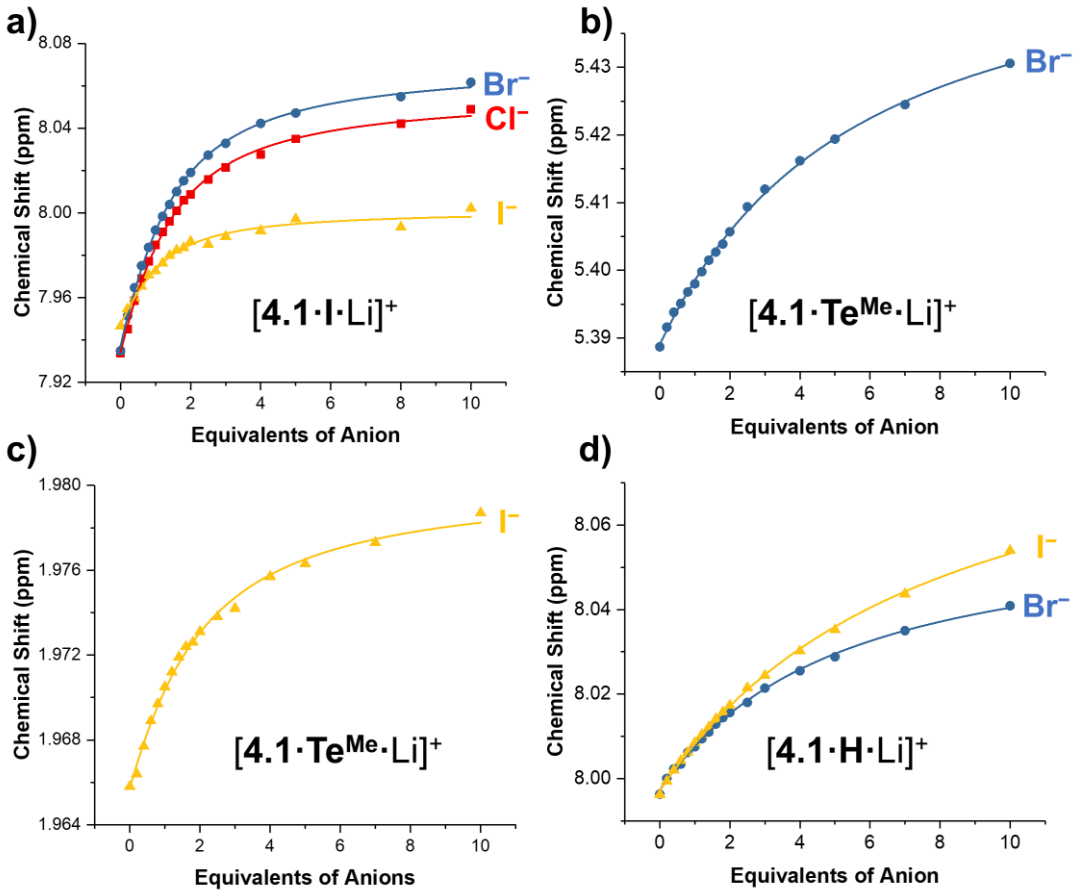

Figure 4.12 Binding isotherms of the macrocyclic receptors in the presence of one equivalent of $LiClO_4$ monitoring the chemical shift of a) internal benzene *b* ([**4.1·I·**Li]$^+$), b) methylene *e* ([**4.1·Te^{Me}·**Li]$^+$), c) $TeCH_3$ *i*^{TeMe} ([**4.1·Te^{Me}·**Li]$^+$) and d) proto-triazole *i*^{Trz} ([**4.1·H·**Li]$^+$) as a function of halide anion concentration (500 MHz, 298 K, [receptor] = 1.0 mM, 1:1 $CDCl_3/CD_3CN$).

Table 4.1: Anion association constants (K_a/M^{-1}) for **4.1·I**, **4.1·Te^{Me}** and **4.1·H** in the presence of 1 equivalent of $LiClO_4$ in 1:1 $CDCl_3/CD_3CN$.[a]

Anion	Cation	**4.1·XB**	**4.1·ChB**	**4.1·HB**
Cl^-	Li^+	1 150 (38)	–[b]	–[b]
Br^-	Li^+	1 210 (41)	186 (12)	211 (13)
I^-	Li^+	1 240 (166)[c]	662 (65)	121 (7)

[a]K_a values calculated using Bindfit software with a 1:1 host-guest binding model.[235,236] Errors (±) are in parentheses and are all <10% unless otherwise stated. Lithium cation added as $LiClO_4$. All anions added as their TBA salts. [Macrocycle] = 1.0 mM. Solvent = 1:1 $CDCl_3/CD_3CN$. T = 298 K. [b]Salt recombination. [c]Error = 13%.

In general, Table 4.1 reveals the significant cooperative recognition of lithium halide salts as ion-pairs, as no binding of halide anion was observed in the absence of a co-bound Li^+. This strong cooperativity is attributed to the favourable proximal electrostatic attractions between the endotopically chelated Li^+ and the anions. In particular, Li^+-complexed XB receptor [**4.1·I·**Li]$^+$ is the most potent ion-pair receptor, displaying 2- to 7-fold enhancement in the binding of Br^- and I^- compared to the ChB and HB analogues. This is further illustrated by its successful recognition of "hard" LiCl while salt precipitation was observed for the other two receptors. This could be rationalised by the strong I···Cl^- XB interaction, which significantly stabilises the basic anion and inhibits it from recombining with Li^+. Although XB receptor [**4.1·I·**Li]$^+$ demonstrates no selectivity preference towards halide anions, ChB congener **4.1·Te^{Me}** displays a marked preference towards "soft" LiI over LiBr, with $K_a(I^-)/K_a(Br^-)$ = 3.5. This improved halide guest selectivity of [**4.1·Te^{Me}·**Li]$^+$ is ascribed to both the size and shape complementarity between I^- and the macrocyclic cavity, as well as the favourable ChB interaction between telluromethyl-triazole donors and the anion.[127,234]

4.3.3 Extraction Studies

4.3.3.1 Solid-Liquid Extraction (SLE)

The promising ion-pair binding properties displayed by these receptors prompted an investigation into their ability to extract inorganic lithium salts. Specifically, solid-liquid extraction (SLE) experiments were conducted to investigate the capability of the macrocycles to solubilise lithium halide salts into organic solvents. In a typical study, an excess amount of the solid lithium salt was added to a macrocycle solution in $CDCl_3$ (600 μL) and the mixture was sonicated vigorously for an hour, followed by filtration to remove any excess solid. Subsequently, CD_3CN (200 μL) was added to improve the resolution of the post-extraction spectra. As shown in Figure 4.13, significant perturbations to the respective macrocycle proton signals were observed in the post-extraction spectra of all three receptors, confirming the successful extraction of the otherwise insoluble lithium halide salts into chloroform. Importantly, this demonstrates the potential of the σ-hole receptors (**4.1·I** and **4.1·Te^{Me}**) to function as solid-liquid extractants and lithium salt solubilising agents.

4.3.3.2 Liquid-Liquid Extraction (LLE)

The extraction properties of the heteroditopic macrocycles were also assessed in liquid-liquid extraction (LLE). A solution of the receptor dissolved in $CDCl_3$ (2 mM) was exposed to a D_2O solution of various LiX (X = Cl, Br, I) salts (5 mM), and the mixture was vigorously stirred for 30 minutes, whereupon precipitates were formed and the organic solution turned opaque. The $CDCl_3$ layer was separated from the LiX aqueous solution and a ^1H NMR spectrum was recorded. Unfortunately, no signals were observed in the post-extraction spectra, suggesting the receptor·LiX complexes were highly insoluble in $CDCl_3$.

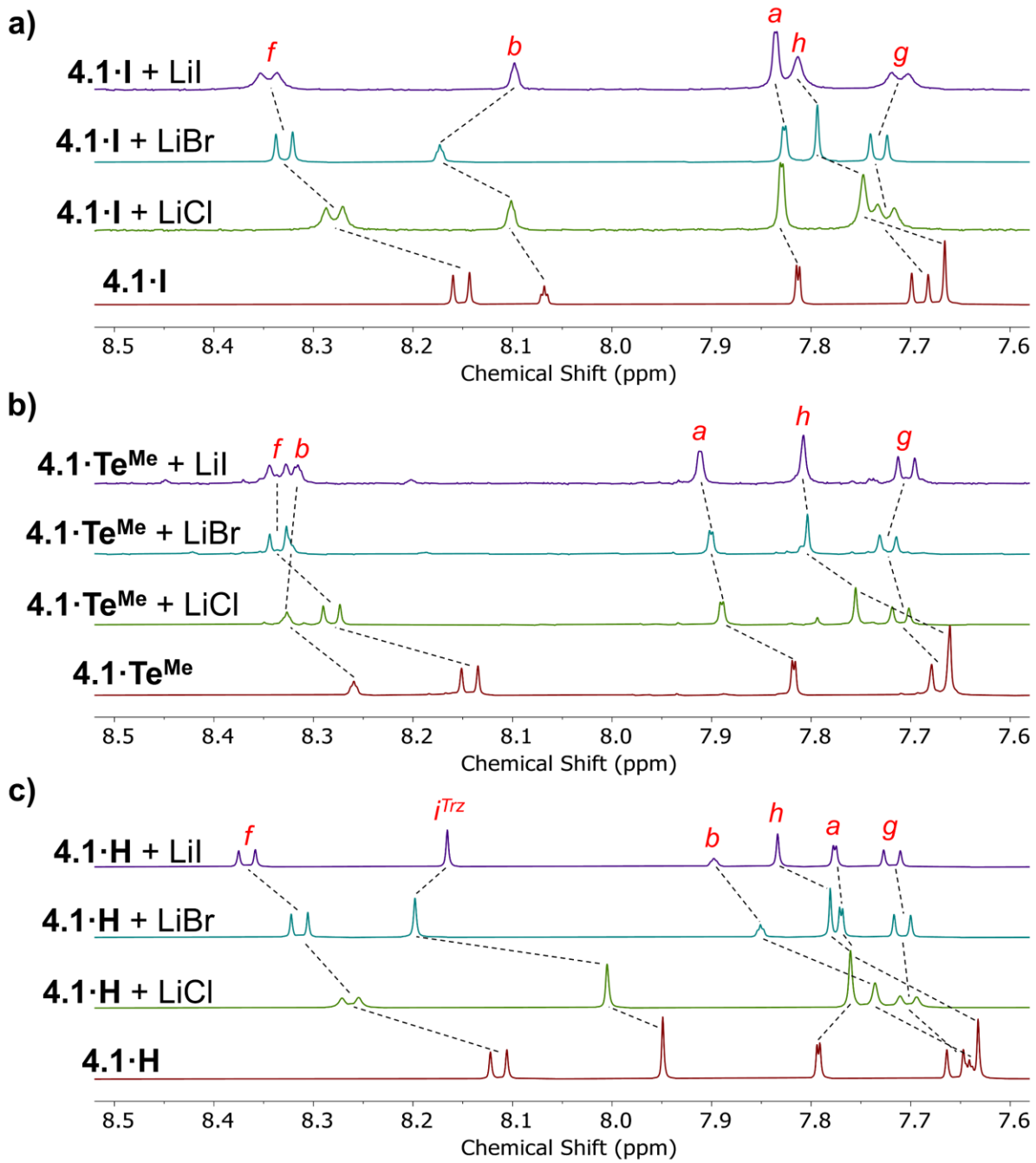

Figure 4.13 Comparative pre- and post-extraction ^{1}H NMR spectra of a) **4.1·I**, b) **4.1·Te^{Me}** and c) **4.1·H** with excess solid LiCl, LiBr and LiI (500 MHz, 298 K, 3:1 $CDCl_3/CD_3CN$).

4.3.4 Conclusion

In summary, a series of phenanthroline-based XB, ChB and HB heteroditopic macrocycles were synthesised for the ion-pair recognition of lithium halide salts. Notably, lithium cation complexation mediated by the phenanthroline ligand in these receptors concomitantly switches on their affinity for halide anions. Ion-pair binding studies conducted in 1:1 $CDCl_3/CD_3CN$ revealed that the XB macrocycle is the most potent receptor for lithium halide salts, capable of binding the "hard" LiCl ion-pair while addition of Cl^- to Li^+-complexed ChB and HB receptors led to salt recombination. Furthermore, ChB macrocycle consisting of the softer telluromethyl-triazole donors exhibited pronounced selectivity towards "soft" LiI over LiBr relative to the iodo-triazole-functionalised XB receptor. Both σ-hole receptors also display a superior binding affinity to the lithium salt ion-pair compared to the HB analogue. Lastly, preliminary solid-liquid extraction experiments demonstrated the ability of these heteroditopic macrocycles to solubilise solid lithium halide salts into organic solvents, showing their potential to function as extractants and solubilising agents of lithium salts. These results serve to highlight the potential of incorporating σ-hole donors into heteroditopic receptors to modulate both the affinity and selectivity of ion-pair binding.

4.3.5 Future Work

Future work of this project will entail the preparation of σ-hole heteroditopic [2]rotaxanes from the XB/ChB macrocycles **4.1·I/Te^{Me}** via a CuAAC-AMT procedure (Scheme 4.5).[340] As shown in Figure 4.14, the bound cation and anion are expected to exist as an axle-separated ion-pair in the rotaxane system. This is envisaged to enhance the host affinity to the ion-pair compared to the σ-hole macrocycles by virtue of the extra favourable interactions originating from axle triazole group with the co-bound cation (coordination to the triazole N donor) and anion (XB/ChB interactions from I/Te donors). Cation-induced polarisation of the axle σ-hole donors is also expected to further strengthen the receptors' anion affinity.

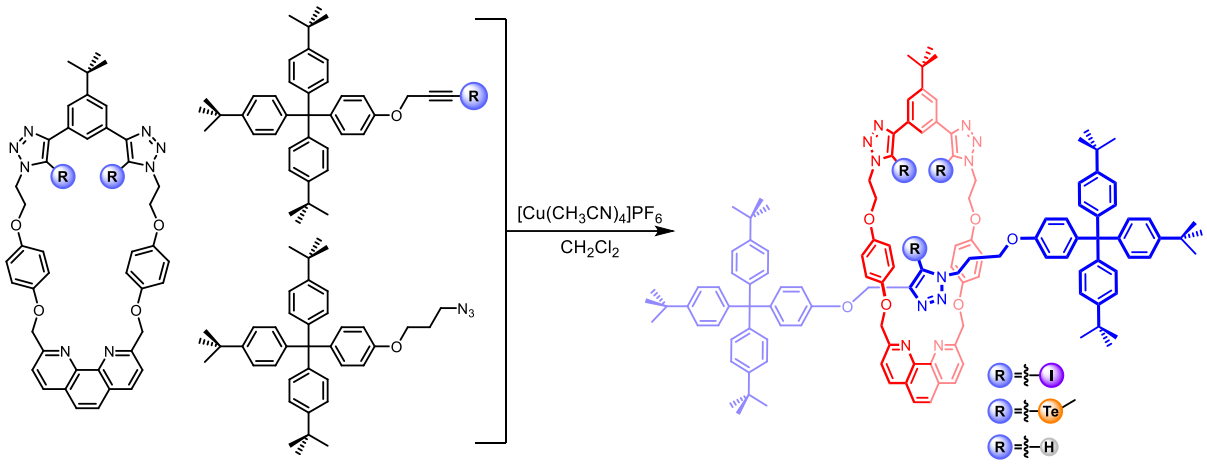

Scheme 4.5 Proposed synthesis of heteroditopic σ-hole [2]rotaxanes for the binding of ion-pairs.

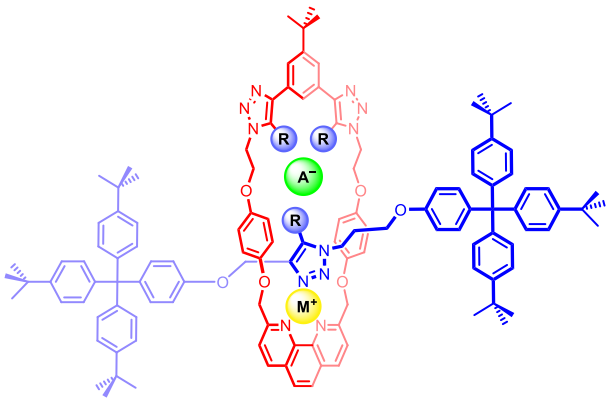

Figure 4.14 Proposed simultaneous binding of cation and anion as axle-separated ion-pair of the σ-hole [2]rotaxanes.

4.4 Halogen Bonding [2]Catenanes for Ion-Pair Recognition

Mimicking the unique shielded guest binding pockets of proteins and enzymes in Nature, MIM host systems have shown great promise in the molecular recognition and sensing of cations and anions.[201,202,215,237,258,280,362] However, the exploitation of rotaxanes[186,238,268,352,363,364] and catenanes[365] for ion-pair recognition is rare, potentially due to the synthetic challenge to functionalise MIM frameworks with multiple recognition sites for charged guests. Furthermore, the incorporation of XB donors into catenane receptors to mediate ion-pair recognition remains unprecedented. This project discusses the synthesis of the first examples of XB tritopic [2]catenanes, which display strong cooperative binding of sodium halide salts.

4.4.1 Design and Synthesis of [2]Catenanes

An alkali metal cation template strategy pioneered by Chiu and co-workers was adapted to synthesise the target XB [2]catenanes.[177–179,366,367] Group 1 metal cations have been widely utilised to template the formation of crown ethers, but are rarely exploited in the template-directed synthesis of interlocked structures.[178,368,369] In a seminal report by Chiu and co-workers in 2013,[179] the sodium cation was used to assemble two di(ethylene glycol) chains in an orthogonal manner, facilitating the formation of a [2]catenane in 81% yield after a double cyclisation reaction via imine formation (Scheme 4.6). This novel synthetic methodology was further extended by the same group to employ larger alkali metal cations such as K^+ and Rb^+ as templates in the synthesis of tri- and tetra(ethylene glycol)-based [2]catenane systems.[367] Inspired by this efficient way to form a mechanical bond, and the potential of the three-dimensional shielded polyether pocket in the resulting [2]catenanes to chelate to complementary alkali metal cations, this project entails the alkali metal cation template synthesis of tritopic all-XB [2]catenanes for ion-pair recognition applications.

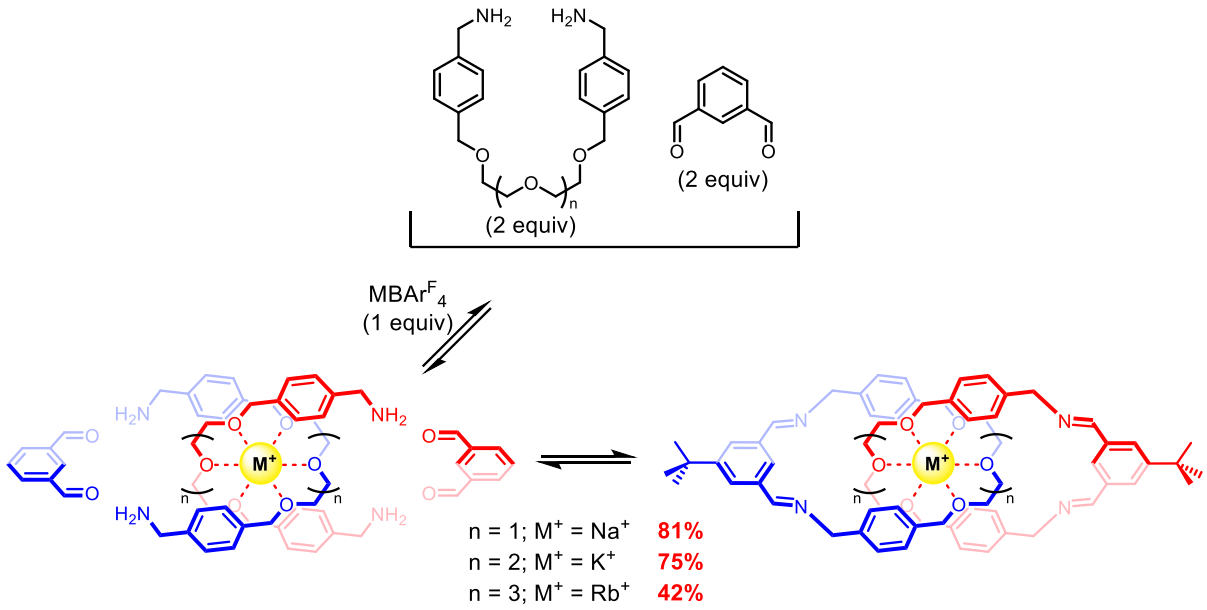

Scheme 4.6 Chiu's alkali metal cation template synthesis of [2]catenanes.[179,367]

Retrosynthetically, the target XB [2]catenane can be prepared by using an alkali metal cation to template the assembly of two oligo(ethylene glycol)-functionalised bis-azide precursor molecules in an orthogonal fashion, followed by CuAAC-mediated double cyclisation reactions with two equivalents of bis(iodo-alkyne) (Route b in Scheme 4.7). However, despite the high-yielding feature of CuAAC click reactions, a one-pot preparation of two macrocycles via the formation of four iodo-triazole groups could still be synthetically challenging. Therefore, one of the XB macrocycles was pre-formed and the alkali metal cation template assembly with the oligo(ethylene glycol)-based bis-azide in a pseudo-rotaxane manner (Route a in Scheme 4.7), would facilitate the subsequent CuAAC-mediated single cyclisation reaction with a bis(iodo-alkyne) to afford the target XB [2]catenane **4.10**.

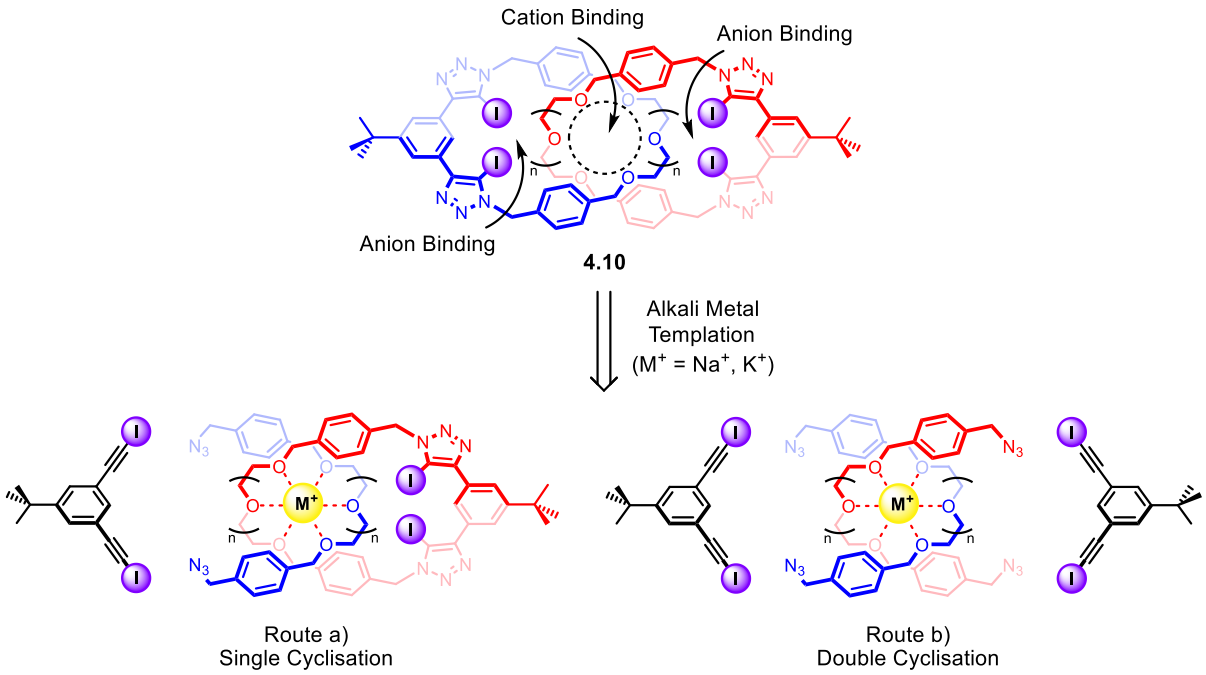

Scheme 4.7 Retrosynthesis of target all-XB [2]catenane via alkali metal cation templation.

4.4.1.1 Synthesis of Oligo(ethylene glycol)-based Bis-azide and XB Macrocycle

To prepare the target oligo(ethylene glycol)-functionalised bis-azides (Scheme 4.8), di- and tri(ethylene glycol) were initially alkylated with α,α'-dibromo-*p*-xylene in the presence of NaH in THF, affording the dibromides **4.11a** and **4.11b** in 38% and 18% respective yields after purification by column chromatography.[366] Quantitative azidation was achieved by stirring the dibromides **4.11a–b** with excess NaN_3 in DMSO, followed by aqueous work-up to give bis-azides **4.12a–b**. CuAAC-mediated cyclisation between **4.12a–b** and bis(iodo-alkyne) **2.3·I** (see Scheme 2.11 for synthesis) in the presence of $[Cu(CH_3CN)_4]PF_6$ and TBTA in CH_2Cl_2 afforded the target macrocycles **4.13a** and **4.13b** in 35% and 31% yields respectively.

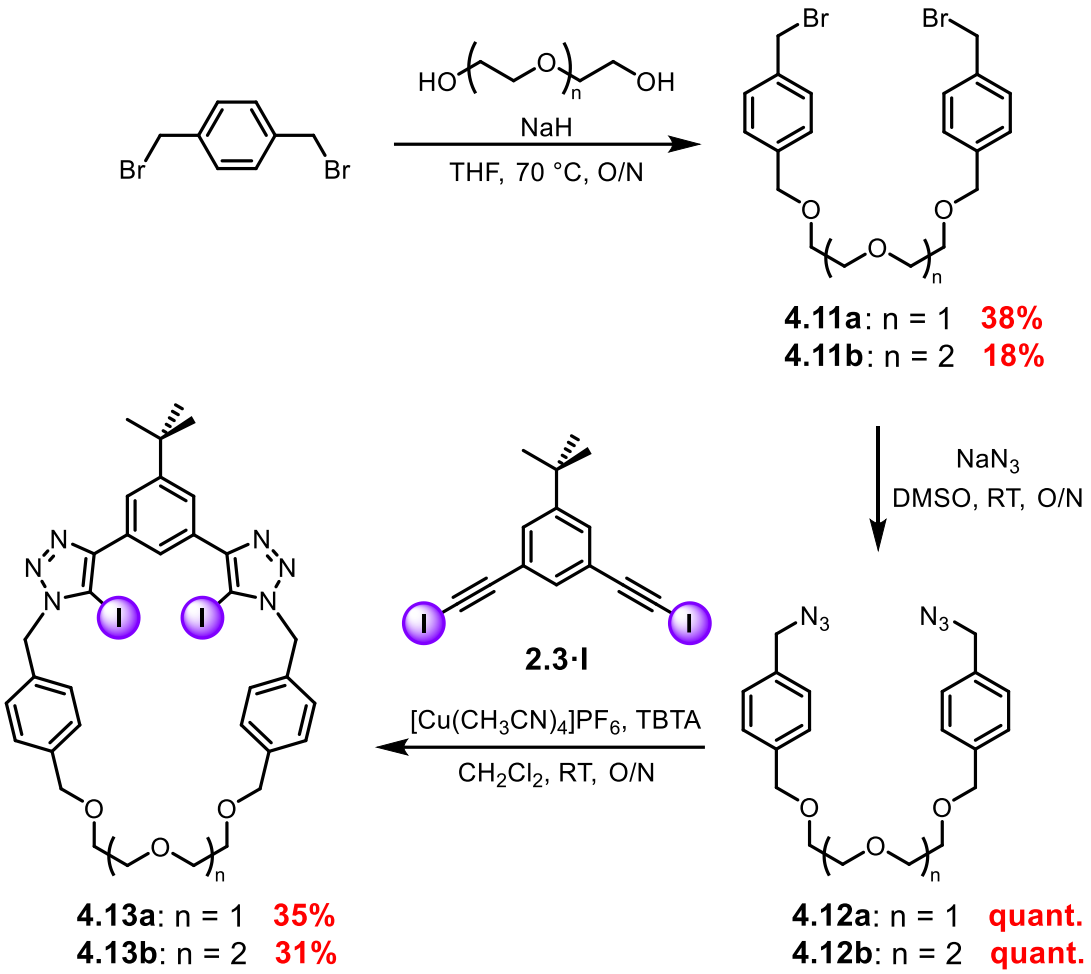

Scheme 4.8 Synthetic route to di- and tri-(ethylene glycol)-functionalised bis-azide **4.12** and XB macrocycle **4.13**.

4.4.1.2 Alkali-Metal Cation Templated Synthesis of XB [2]Catenanes

Given the efficiency of the Na^+ cation template-directed synthesis of both di- and tri(ethylene glycol)-based [2]catenanes (81% and 64% yields respectively) as reported by Chiu and co-workers,[367] this alkali metal cation was exploited in the synthesis of target XB homo-[2]catenanes **4.10a–b** (Scheme 4.9). In a typical reaction, macrocycle **4.13** and bis-azide **4.12** possessing the same length of polyether linkers were stirred in CH_2Cl_2 in the presence of one equivalent of $NaBAr^{F}{}_4$ salt for 30 minutes to facilitate the formation of the Na^+-templated pseudo-[2]rotaxane. Subsequently, one equivalent of bis(iodo-alkyne) **2.3·I** was added, followed by addition of $[Cu(CH_3CN)_4]PF_6$ and TBTA. The reaction mixture was allowed to stir at room temperature overnight. After

aqueous work-up with basic EDTA/NH_4OH and purification by preparative TLC, [2]catenanes **4.10a** and **4.10b** were isolated in 27% and 10% yields respectively. Notably, the higher yield obtained for **4.10a** was consistent with Chiu's finding, in which Na^+ is a more suitable template for di(ethylene glycol) chains. Both novel [2]catenanes were characterised by ^1H and ^{13}C NMR, and high-resolution ESI-MS (Figure 4.15).

A comparison of ^1H NMR spectra of [2]catenanes **4.10a** and **4.10b**, with their respective macrocycles **4.13a** and **4.13b**, is shown in Figure 4.16. In general, upfield shifts were observed for most of the proton signals in the respective [2]catenane relative to those of the free macrocycle, consistent with the shielding effect arising from the formation of the mechanical bond. Furthermore, relatively large upfield perturbations of the di- and tri(ethylene glycol) signals in **4.10a** and **4.10b** respectively were attributed to the proximity of these methylene protons to the shielding ring current generated by the aromatic xylene spacers of the interlocked macrocycles.

Crystal samples suitable for X-ray diffraction crystallography were obtained via slow evaporation of a 1:1 $CDCl_3/CD_3CN$ solution of **4.10a** in the presence of excess TBACl. Examination of the solid-state structure of **4.10a**·TBACl (Figure 4.17) reveals that each Cl^- is stabilised by four I···Cl^- XB interactions originating from two bis(iodotriazole)benzene motifs located on two neighbouring catenanes. The steric bulk of the *tert*-butyl groups appended on the central benzene spacer likely prevents the co-conformational inter-ring circumrotation necessary to bring the discrete XB donor motifs of the two interlocked macrocycles together for convergent tetradentate XB halide anion complexation.

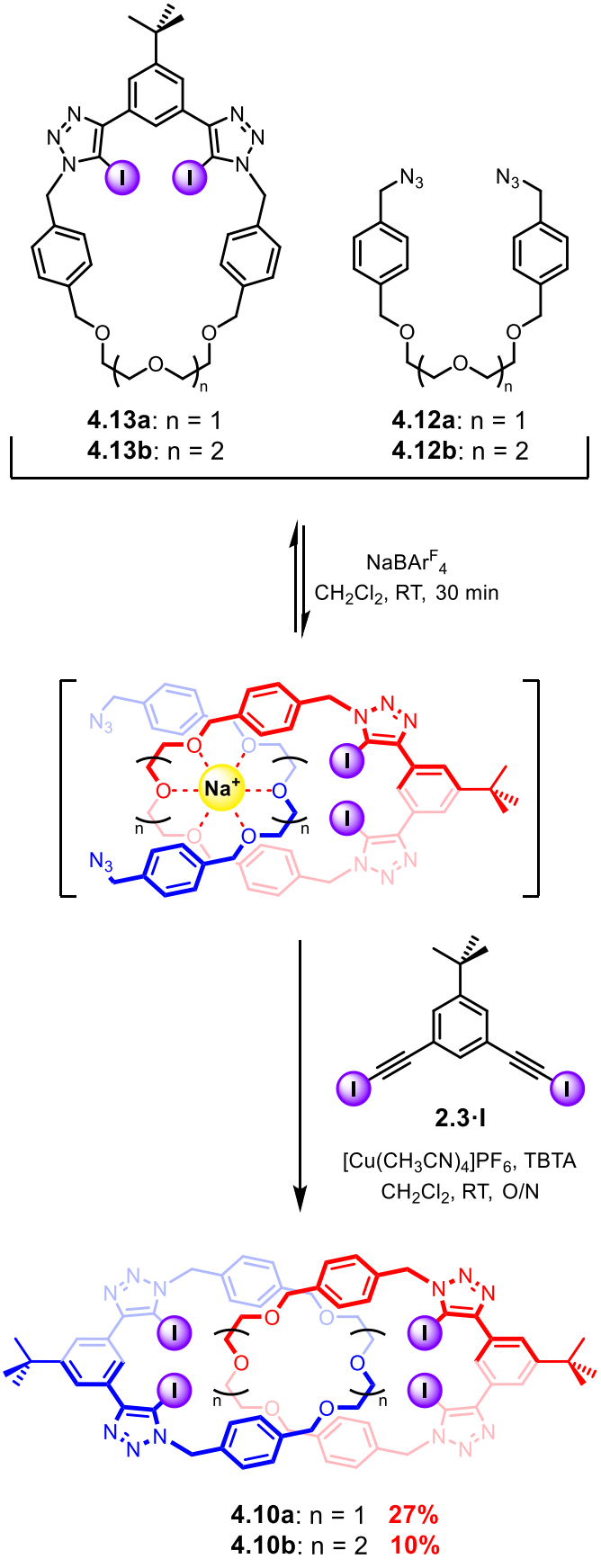

Scheme 4.9 Synthetic route to target XB [2]catenanes **4.10a–b** via Na^+ cation template strategy.

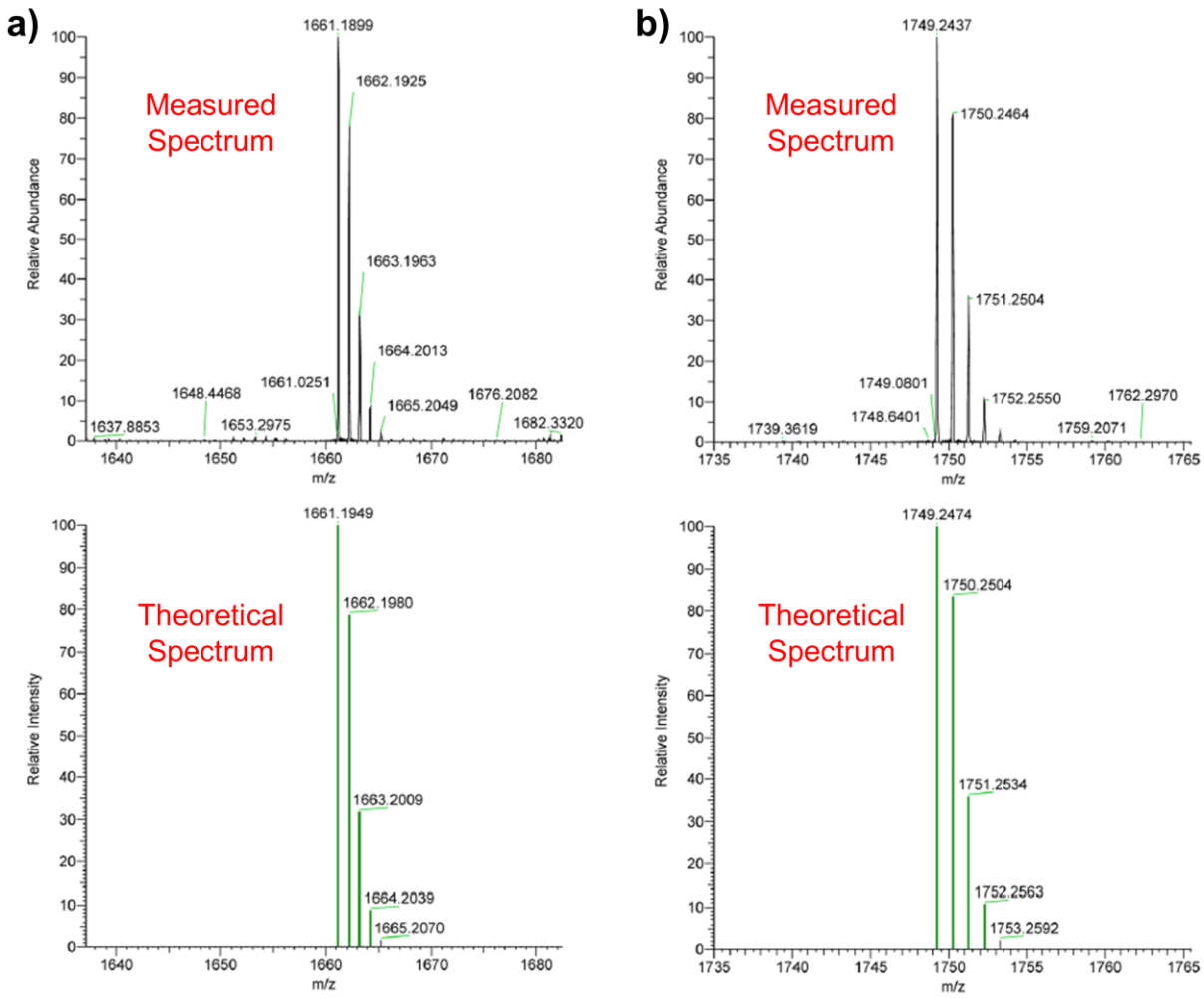

Figure 4.15 High-resolution electrospray ionisation (ESI) mass spectra of [2]catenanes a) **4.10a** and b) **4.10b**.

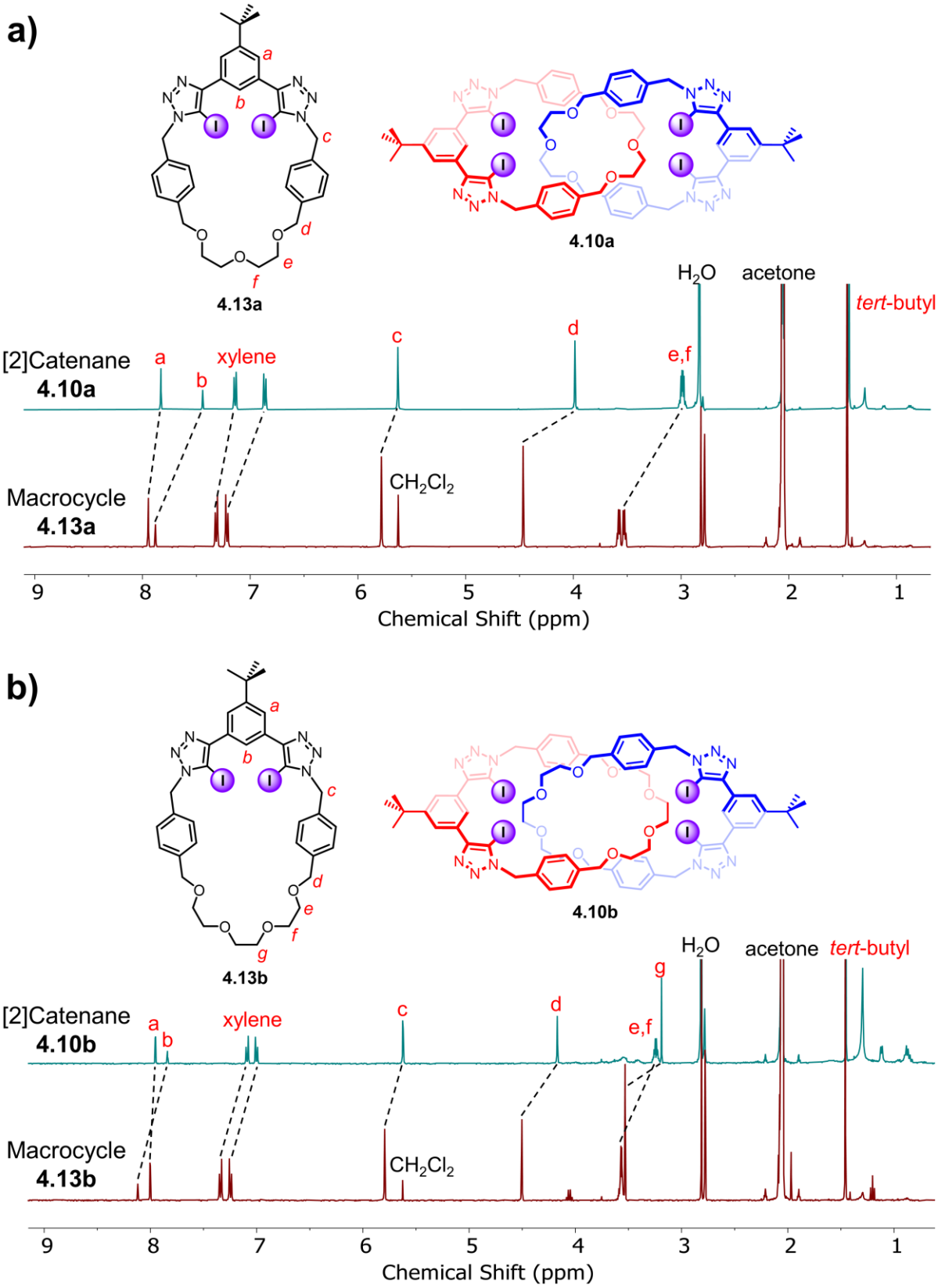

Figure 4.16 Comparative ^{1}H NMR spectra of [2]catenanes a) **4.10a** and b) **4.10b**, and their respective macrocycles (400 MHz, 298 K, acetone-d_6).

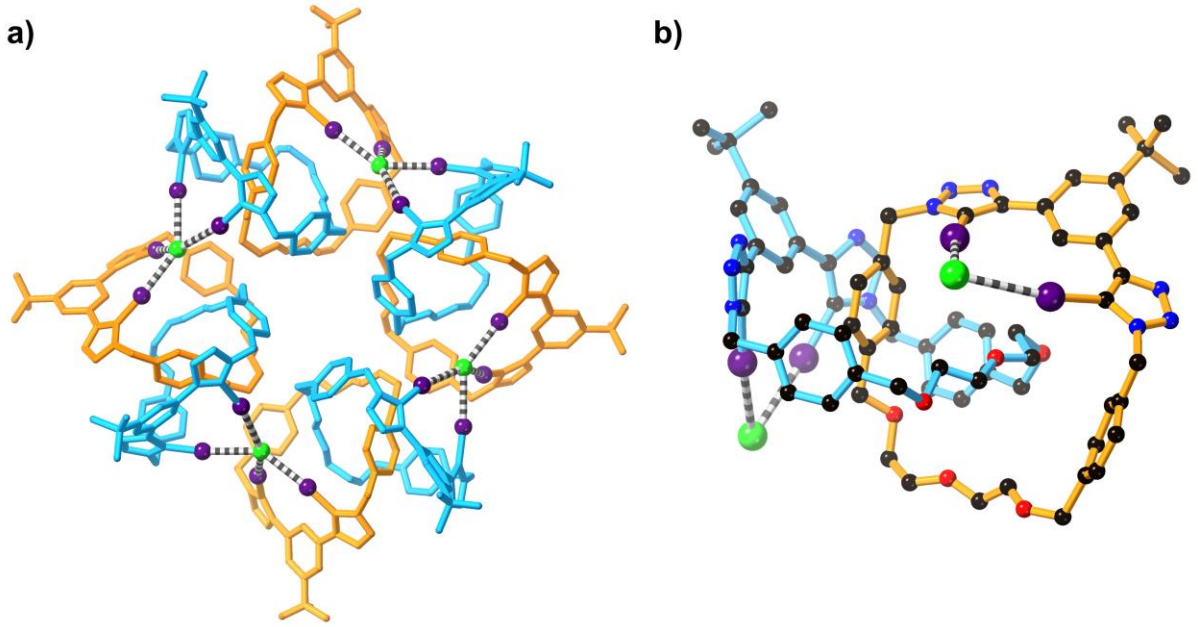

Figure 4.17 a) Solid-state structure and b) the truncated view of **4.10a**·TBACl. Hydrogen atoms and TBA^+ cation are omitted for clarity. Black = carbon, blue = nitrogen, red = oxygen, purple = iodine, green = chlorine.

4.4.2 Ion-Pair Recognition Studies

Following the successful synthesis of the all-XB [2]catenanes, attention turned to investigate their ability to recognise alkali metal halide salts as ion-pairs. In a preliminary study involving the smaller [2]catenane **4.10a**, the efficacy of the interlocked receptor to encapsulate the Na^+ cation was first established via a ^1H NMR titration experiment in 1:1 $CDCl_3/CD_3CN$. Thereafter, to probe the capability of **4.10a** to cooperatively bind sodium halide salts, the halide anion affinities of the [2]catenane in the absence and presence of a co-bound Na^+ cation were determined by conducting quantitative ^1H NMR anion titration experiments in the same mixed solvent system.

4.4.2.1 Sodium Cation Complexation Studies

To investigate the potential of [2]catenane **4.10a** to complex the Na^+ cation, aliquots of $NaClO_4$ were added to a 1:1 $CDCl_3/CD_3CN$ solution of the interlocked receptor. As shown in Figure 4.18a, ethylene glycol protons *e* and *f* experienced significant downfield and upfield shifts respectively upon increasing the cation

concentration. This suggested Na^+ cation complexation occurred at the polyether regions created by the two interlocked rings, which amplified the asymmetry of these two sets of methylene protons. Moreover, large upfield perturbations of internal benzene proton *b* was observed, which may be rationalised by structural rigidification of the [2]catenane upon cation binding and, as a result burying the aryl proton *b* deeper inside the interlocked architecture. Small downfield shifts were also observed for both xylene aryl protons, ascribed to a conformational change of the polyether binding pocket domain to accommodate the Na^+ cation. By monitoring the chemical shift of ethylene glycol proton *e*, Bindfit[235,236] analysis of the resulting titration isotherm using a 1:1 host-guest stoichiometric binding model determined the Na^+ cation association constant as 780 M^{-1} (Table 4.2).

For comparison, an analogous Na^+ cation titration experiment was conducted on macrocyclic receptor **4.13a**, which displayed no binding to the cation in this 1:1 $CDCl_3/CD_3CN$ solvent mixture (Figure 4.18b). This highlights the importance of saturating the coordination sphere of the Na^+ cation via encapsulation by the two di(ethylene glycol) chains. The presence of a more shielded cation binding environment in [2]catenane **4.10a** was also thought to play a role in assisting the desolvation of the metal cation, as stronger cation affinities are frequently observed for interlocked receptors compared to acyclic analogues.[176,370]

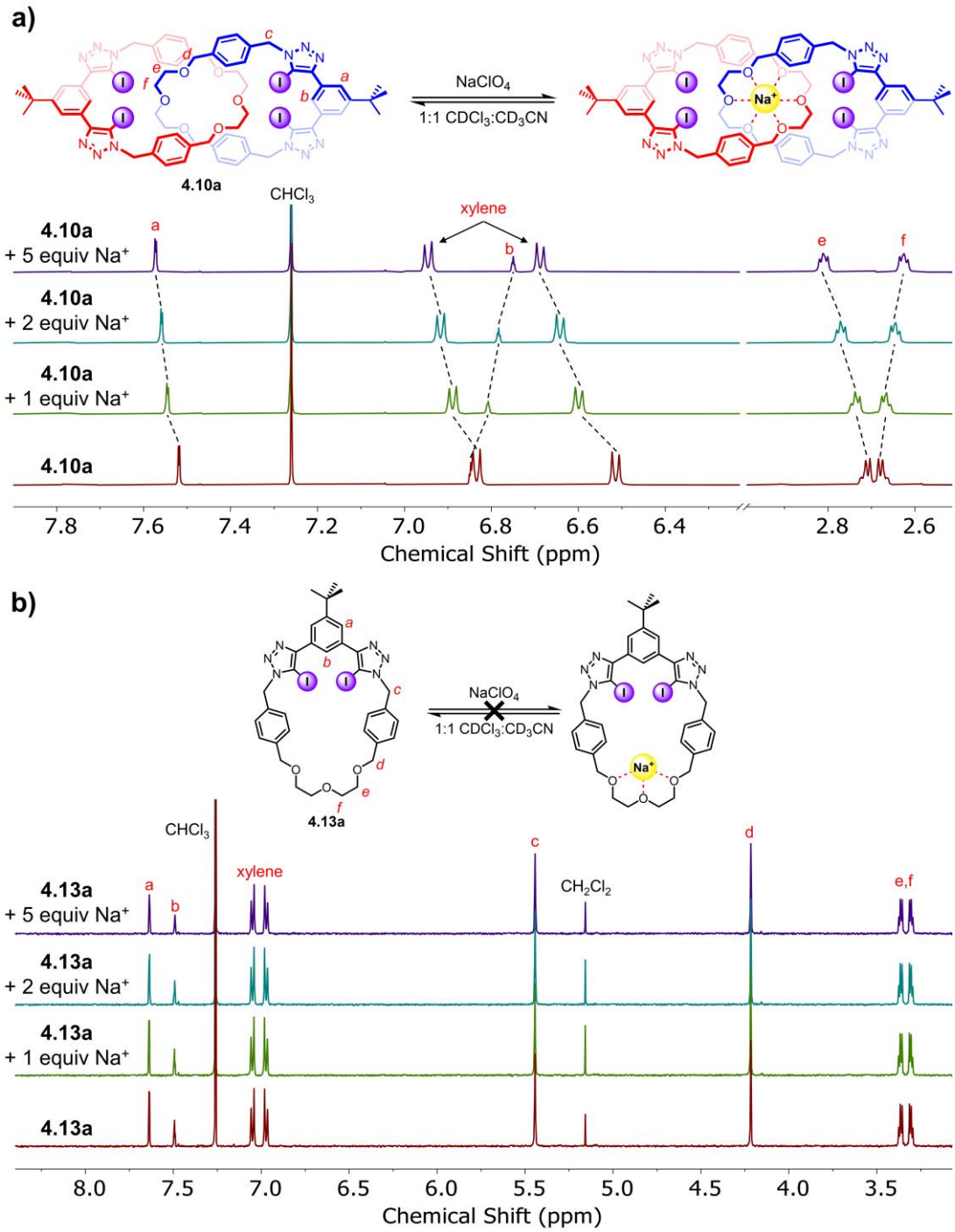

Figure 4.18 ^{1}H NMR spectra of a) [2]catenane **4.10a** and b) macrocycle **4.13a** upon addition of 1, 2 and 5 equivalents of $NaClO_4$ (500 MHz, 298 K, 1:1 $CDCl_3/CD_3CN$).

Table 4.2: Cation association constants (K_a/M^{-1}) for [2]catenane **4.10a** and macrocycle **4.13a** with $NaClO_4$ in 1:1 $CDCl_3/CD_3CN$ determined by ^{1}H NMR titrations.[a]

Cation	[2]Catenane 4.10a	Macrocycle 4.13a
Na^+	780 (14)	N.B.[b]

[a]K_a values calculated using Bindfit with a 1:1 host-guest binding model.[235,236] Errors (±) are in parentheses and are all <2%. Sodium cation added as $NaClO_4$. Solvent = 1:1 $CDCl_3/CD_3CN$. T = 298 K. [Receptor] = 1.0 mM. [b]N.B. = no binding.

4.4.2.2 Anion Binding Studies

(A) *Free Macrocycle and [2]Catenane*

The anion recognition properties of the free [2]catenane **4.10a** and macrocycle **4.13a** were investigated by ^{1}H NMR titrations with TBA halide salts in 1:1 $CDCl_3/CD_3CN$. For both receptors, increasing the halide anion concentration led to significant downfield shifts for the respective internal benzene proton *b* while negligible proton shifts were observed for the rest of the spectra (Figure 4.19). This suggested anion binding was mediated by the XB donors in the vicinity of the catenane or macrocycle cavities. By plotting the chemical shift of *b* as a function of anion concentration, the resulting isotherms were all fitted to a 1:1 host-guest binding model using Bindfit[235,236] and the calculated anion association constants for both receptors are summarised in Table 4.3. In general, both the [2]catenane **4.10a** and its constituting macrocycle **4.13a** displayed very similar binding constant values towards the halide anions (Cl^-, Br^- and I^-). This indicated that the two bis(iodo-triazole)benzene XB donor sites in [2]catenane **4.10a** were acting independently of each other. The presence of the two bulky *tert*-butyl groups conceivably prevented the interlocked rings from undergoing the co-conformational inter-ring circumrotation necessary to bring the two distant XB anion binding sites together for convergent tetradentate XB anion complexation. It is noteworthy that attempts to fit the halide titration data of [2]catenane **4.10a** to a 1:2 host-guest binding model were unsuccessful, suggesting the relatively weak binding of halide anions in this mixed solvent system renders the receptor incapable of overcoming the electrostatic repulsion for co-binding of the second anionic guest.

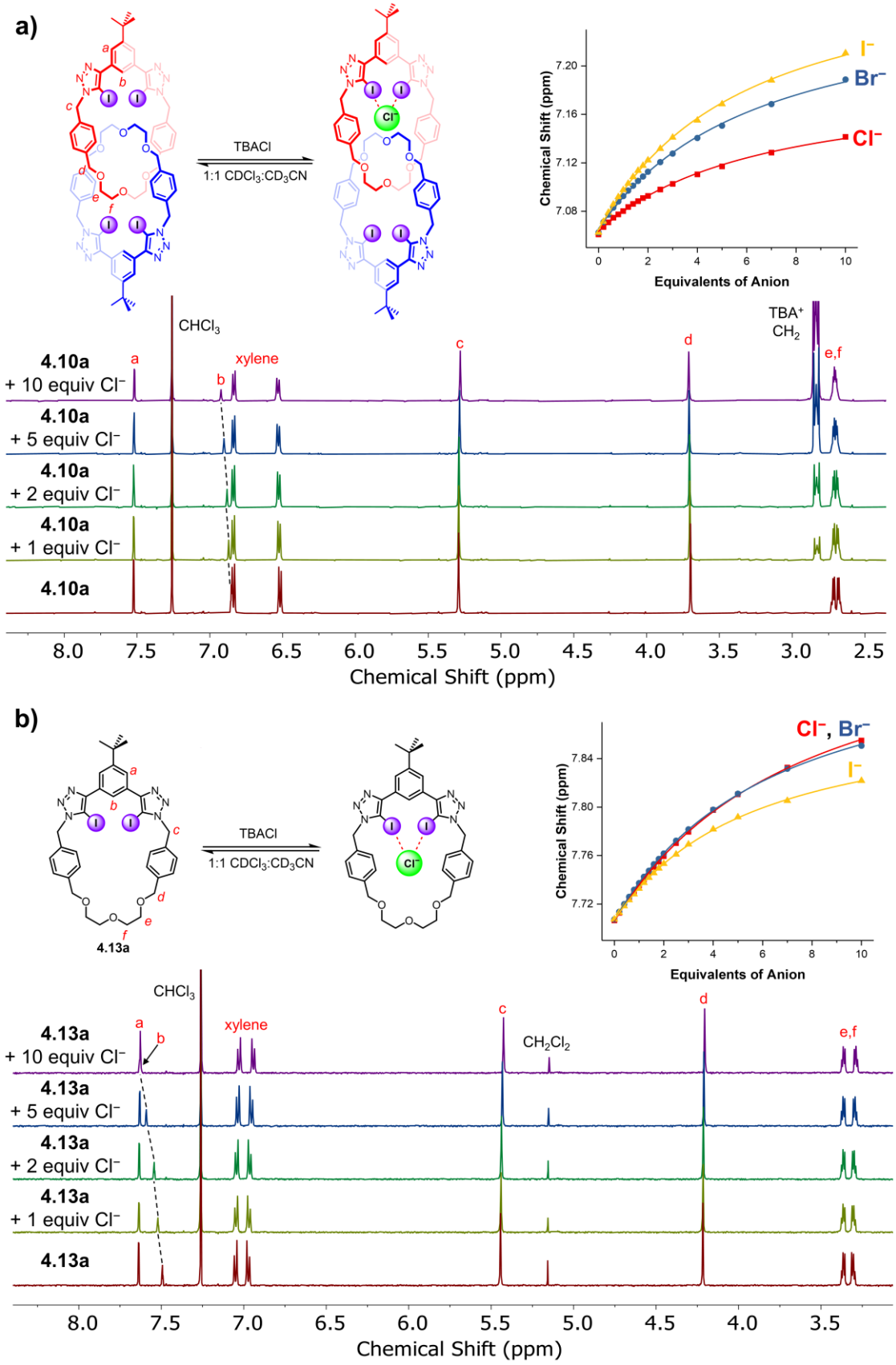

Figure 4.19 ^{1}H NMR spectra of a) [2]catenane **4.10a** and b) macrocycle **4.13a** upon addition of 1, 2, 5 and 10 equivalents of TBACl (500 MHz, 298 K, 1:1 $CDCl_3/CD_3CN$). Inset: Binding isotherms showing changes in chemical shift of internal benzene proton *b* upon increasing equivalents of halide anions.

Table 4.3: Anion association constants (K_a/M^{-1}) for [2]catenane **4.10a** and macrocycle **4.13a** with TBA halide salts in 1:1 $CDCl_3$/CD_3CN determined by ^{1}H NMR titrations.[a]

Anion	[2]Catenane 4.10a	Macrocycle 4.13a
Cl^-	132 (2)	125 (1)
Br^-	156 (3)	154 (1)
I^-	174 (3)	186 (2)

[a]K_a values calculated using Bindfit with a 1:1 host-guest binding model.[235,236] Errors (±) are in parentheses and are all <2%. All anions added as their TBA salts. Solvent = 1:1 $CDCl_3$/CD_3CN. T = 298 K. [**4.10a**] = [**4.13a**] = 1.0 mM.

(B) Sodium Cation Complexed [2]Catenane

After establishing the efficacy of [2]catenane **4.10a** to individually bind Na^+ cation (Section 4.4.2.1) and halide anions (Section 4.4.2.2 (A)), the potential of the interlocked receptor to recognise sodium halide salts as ion-pairs was investigated. In a typical ^{1}H NMR ion-pair titration experiment, TBA halide salts were added to a 1:1 $CDCl_3$/CD_3CN receptor solution in the presence of 1 equivalent of $NaClO_4$. A representative titration with TBAI is shown in Figure 4.20. Upon the addition of I^- anion, progressive downfield shifts of internal benzene proton *b* was observed, indicative of anion binding in the vicinity of the XB donors. In addition, ethylene glycol protons *e* and *f* diverged with increasing anion concentration. These observations, together with the downfield perturbations to xylene aryl protons, were attributed to the catenane undergoing a co-conformational change in order to accommodate both the Na^+ and I^- guest species as an ion-pair inside the respective polyether and XB catenane cavities. Similar shifts in the ^{1}H NMR titration spectra were observed upon addition of TBABr, suggestive of an analogous ion-pair binding conformation. However, in the case of Cl^-, addition of the anion to the Na^+-complexed [2]catenane resulted in salt recombination followed by precipitation of NaCl, potentially due to the relatively high lattice energy of NaCl.

By monitoring the chemical shift of proton *b* as a function of anion concentration, binding isotherms for the titrations with TBABr and TBAI in the presence of 1 equivalent of $NaClO_4$ were generated. The presence of two distinct anion binding sites in the tritopic [2]catenane **4.10a** necessitates a more detailed study into the ion-pair binding stoichiometry. Five possible binding models, including the simple 1:1, and four different variants of 1:2 host-guest models, were considered for the titrations.[235] As shown in Table 4.4, these four variants of 1:2 models differ in the relationships between K_1 and K_2 (step-wise binding constants), and between δ_1 and δ_2 (chemical shifts induced by formation of 1:1 and 1:2 host-guest complexes respectively).

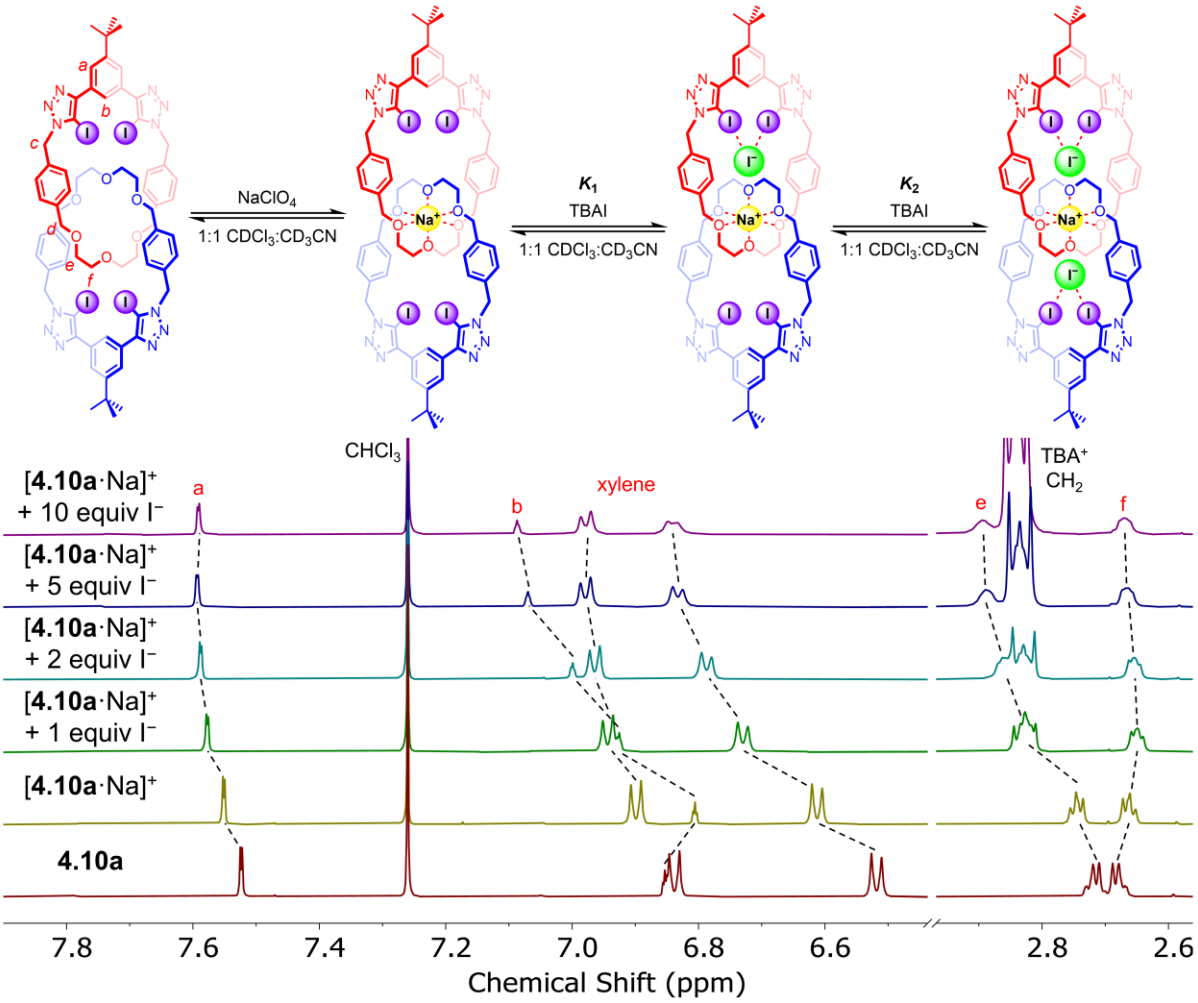

Figure 4.20 Truncated ^{1}H NMR spectra of free receptor **4.10a**, upon addition of 1 equivalent of $NaClO_4$ and further addition of 1, 2, 5 and 10 equivalents of TBAI (500 MHz, 298 K, 1:1 $CDCl_3/CD_3CN$).

Table 4.4: Possible binding models[235] involved in the ion-pair titration of **4.10a** and the difference in their respective relationships between K_1, K_2, δ_1 and δ_2.[a]

Binding Models (Host:Guest)	Relationship between K_1 & K_2	Relationship between δ_1 & δ_2
1:1	Not applicable[b]	Not applicable[b]
1:2 (Full)	$K_1 \neq 4K_2$	$\delta_1 \neq 2\delta_2$
1:2 (Non-cooperative)	$K_1 = 4K_2$	$\delta_1 \neq 2\delta_2$
1:2 (Additive)	$K_1 \neq 4K_2$	$\delta_1 = 2\delta_2$
1:2 (Statistical)	$K_1 = 4K_2$	$\delta_1 = 2\delta_2$

[a]K_1 and K_2 represent the step-wise binding constants. δ_1 and δ_2 represent the chemical shift induced by the formation of 1:1 and 1:2 host-guest complexes respectively. [b]Only K_1 and δ_1 are involved in 1:1 binding.

To determine the binding model that best describes or fits each titration data isotherm, an approach introduced by Thordarson and co-workers was employed.[139,371,372] This involves fitting the isotherms to each plausible binding model and compares the resulting covariance of the fit (cov_{fit}), where cov_{fit} is defined as the covariance of the residuals (difference between the calculated and experimental data) divided by the covariance of the experimental data.[235] The lower the value of cov_{fit}, the better the quality of the fit. However, as also pointed by Thordarson, complex models (e.g. 1:2 (Full) model) with higher number of fitted parameters usually appear to fit better than simpler models (e.g. 1:1 model). It is therefore suggested that a cov_{fit} of a more complicated model should be at least 3–5 times lower than that of a simpler model for it to be considered as valid.

With this in mind, Table 4.5 summarises the determined anion association constants, number of fitted parameters involved and cov_{fit} obtained by fitting the binding isotherms to the different binding models using Bindfit software.[235,236] In the case of Br^- titration, cov_{fit} of 1:2 (Full) and 1:2 (Non-cooperative) models are 21- and 16-times respectively lower than that of the simpler 1:1 model. Despite the slightly lower cov_{fit} of 1:2 (Full) fitting, its higher number of fitted parameters makes it difficult

to decide whether it is superior to the 1:2 (Non-cooperative) model. Therefore, both models are taken into consideration to describe the binding (Figure 4.21a–b). For I^-, cov_{fit} of 1:2 (Full) is significantly better (210 times lower) than that of 1:1 and all other variants of 1:2 binding models, and is therefore the best model to describe the titration data set (Figure 4.21c).

Table 4.5: Anion association constants (K_a/M^{-1}) for [2]catenane **4.10a** with TBA halide salts in the presence of one equivalent of $NaClO_4$ in 1:1 $CDCl_3/CD_3CN$ determined by ^1H NMR titrations and fitting of the isotherms with different binding models.[a]

Anion	Cation	Binding Model (Host:Guest)	No. of Fitted Parameters	K_1 (M^{-1})	K_2 (M^{-1})	cov_{fit} ($\times10^{-3}$)	cov_{fit} Factor[b]
Br^-	Na^+	1:1	3	1 180	/	0.59	1.0
		1:2 (Full)	**5**	**2 920**	**596**	**0.028**	**21**
		1:2 (Non-cooperative)	**4**	**2 150**	**536**	**0.038**	**16**
		1:2 (Additive)	4	920	<0	0.18	3.3
		1:2 (Statistical)	3	6	1	280	<0.1
I^-	Na^+	1:1	3	1 050	/	2.0	1.0
		1:2 (Full)	**5**	**4 440**	**933**	**0.0095**	**210**
		1:2 (Non-cooperative)	4	726	181	0.45	4.4
		1:2 (Additive)	4	665	<0	0.63	3.1
		1:2 (Statistical)	3	5	1	270	<0.1

[a]Step-wise K_1 and K_2 values calculated using Bindfit with different binding models.[235,236] Errors (±) are <5% for 1:1, 1:2 (Full), 1:2 (Non-cooperative) and 1:2 (Additive) fittings, and <30% for 1:2 (Statistical) fitting. Sodium cation added as $NaClO_4$. All anions added as their TBA salts. Solvent = 1:1 $CDCl_3/CD_3CN$. T = 298 K. [**4.10a**] = 1.0 mM. [b]cov_{fit} factor = cov_{fit} of 1:1 binding model divided by the cov_{fit} of the respective model. Binding models best fitted for the titration isotherms are highlighted in red.

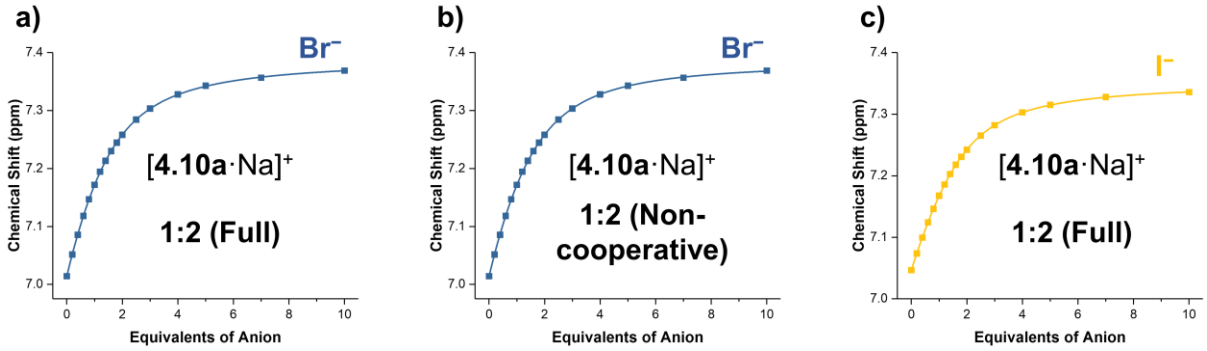

Figure 4.21 Binding isotherms of **4.10a** with a) TBABr (fitted to 1:2 (Full) model), b) TBABr (fitted to 1:2 (Non-cooperative) model) and c) TBAI (fitted to 1:2 (Full) model) in the presence of 1 equivalent of $NaClO_4$ (500 MHz, 298 K, 1:1 $CDCl_3/CD_3CN$).

Comparing the halide association constants of [2]catenane **4.10a** in the absence (Table 4.3) and presence (Table 4.5) of $NaClO_4$, the interlocked receptor demonstrates strong cooperative binding towards NaBr and NaI ion-pairs. Complexation of **4.10a** with one equimolar of Na^+ significantly enhanced its affinity towards Br^- (14–19-fold increase in K_1) and I^- (26-fold increase in K_1). Furthermore, while free [2]catenane could only bind one halide anion in a 1:1 stoichiometric fashion, Na^+-complexed [2]catenane was capable of fully exploiting its two discrete XB bis(iodo-triazole)benzene motifs to recognise up to two halide anions in a 1:2 host-guest manner. The cooperativity in anion binding observed, as well as the switching from 1:1 to 1:2 binding equilibria, is attributed to receptor preorganisation originating from cation chelation and favourable proximal electrostatics between the co-bound ions. Importantly, while no selectivity preference of halide anions was seen with the free catenane **4.10a**, complexation with Na^+ led to a marked preference of the interlocked receptor towards I^-.

4.4.3 Solid-Liquid Extraction Studies

Prompted by the potency of [2]catenane **4.10a** in the cooperative binding of NaI in 1:1 $CDCl_3/CD_3CN$, the potential of the receptor to function as a NaI salt extractant was evaluated by a preliminary solid-liquid extraction study. Upon sonicating a $CDCl_3$ solution of **4.10a** with excess solid NaI for 30 minutes, the post-extraction ^1H NMR spectrum showed shifts in proton signals consistent with those observed in ion-pair titration of **4.10a** with TBAI in the presence of 1 equivalent of $NaClO_4$ (Figure 4.20). Specifically, downfield shifts of internal benzene proton *b* and diverging of ethylene glycol protons *e* and *f* suggested the co-binding of Na^+ and I^- as an ion-pair. This indicated that receptor **4.10a** was capable of solubilising the otherwise insoluble NaI salt into $CDCl_3$. For the sake of comparison, macrocycle **4.13a** was also subjected to the same SLE conditions with NaI salt but negligible shifts in the resulting ^1H NMR spectrum indicated no extraction of the alkali metal salt.

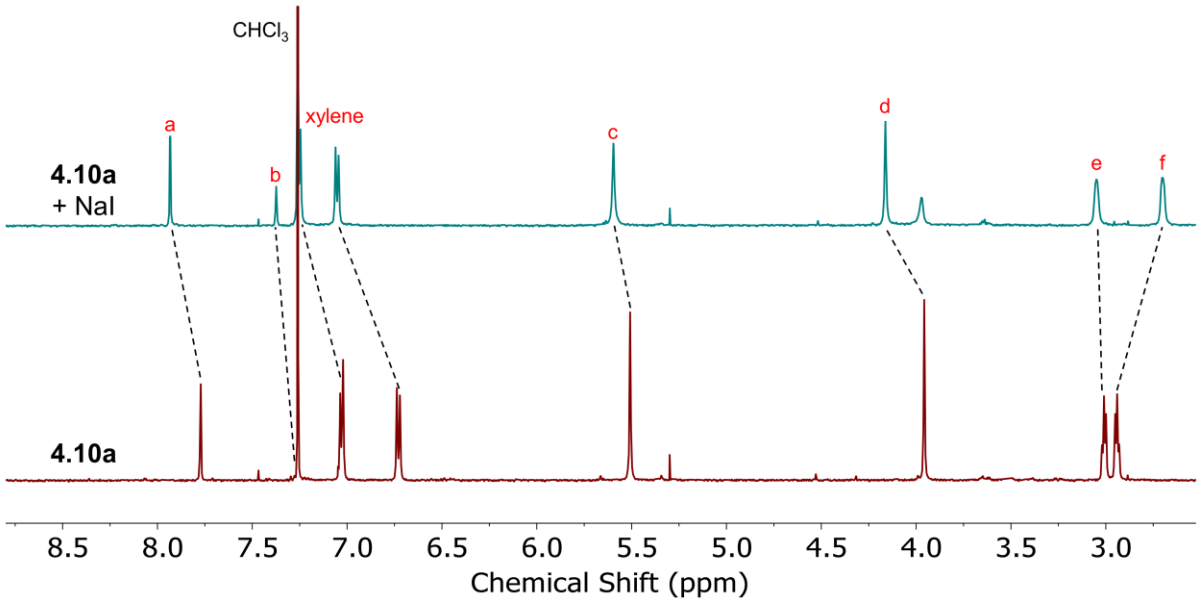

Figure 4.22 Comparative pre- and post-extraction ^1H NMR spectra of [2]catenane **4.10a** with excess solid NaI (500 MHz, 298 K, $CDCl_3$).

4.4.4 Conclusion

To summarise, first examples of all-XB tritopic [2]catenanes were successfully prepared via an alkali metal cation template protocol. ^{1}H NMR titrations revealed that Na^+ cation complexation at the three-dimensional polyether pocket of the interlocked host dramatically strengthened its XB-mediated recognition of halide anions and, impressively, induced a switch of anion binding equilibria from 1:1 to 1:2 host-guest stoichiometry. Furthermore, the presence of a co-bound Na^+ cation led to a pronounced binding selectivity towards I^- anion, a preference that was not observed for the free catenane receptor. Preliminary solid-liquid extraction study also illustrated the capability of the catenane host to function as an efficient extractant for alkali metal salts. Importantly, this work demonstrated the exciting potential of XB interlocked multitopic hosts in the recognition of ion-pairs.

4.4.5 Future Work

Exploiting the templating potential of heavier members of Group 1 metal cations, such as K^+ and Rb^+, future work of this project will first entail the synthesis of the larger, tetra(ethylene glycol)-functionalised XB [2]catenane via the alkali metal cation template synthesis (Scheme 4.10). Furthermore, inspired by the contrasting ion-pair affinity and selectivity demonstrated by XB and ChB heteroditopic receptors (Section 4.3), ChB analogues of the series of [2]catenanes could be prepared. A detailed study into the capabilities of this family of tritopic XB/ChB [2]catenanes, and their protic HB congeners, to recognise different alkali or alkaline earth metal salts as ion-pairs should lay the foundation for the future design of σ-hole multitopic MIMs.

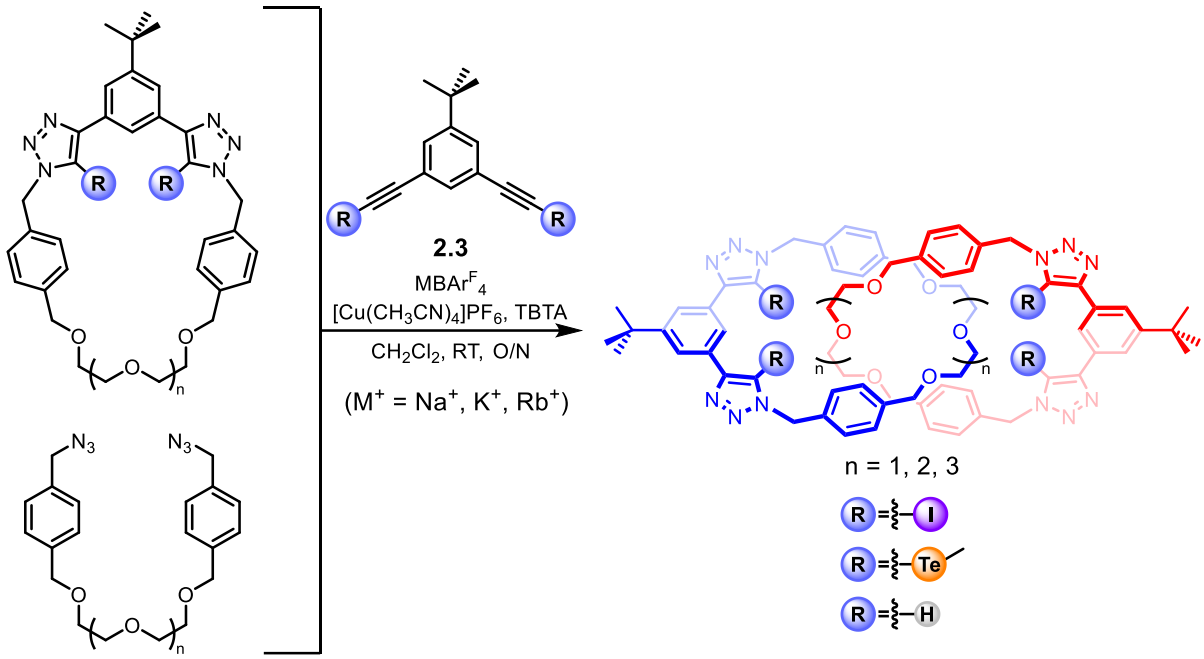

Scheme 4.10 Synthetic route to the series of tritopic XB, ChB and HB [2]catenanes functionalised with di-, tri- and tetra(ethylene glycol) linkers.

To further enhance the ion-pair recognition potency of the XB catenane systems, tetratopic [3]catenane consisting of two polyether cation binding pockets could be synthesised from bis-oligo(ethylene glycol)-based macrocycle, bis-azide and bis-alkyne precursors via modification of alkali metal cation template protocol as shown in Scheme 4.11. The complexation of up to two alkali metal cations in the oligo(ethylene glycol) domains is envisaged to substantially augment the anion affinity of the resulting dicationic [[3]catenane·M_2]$^{2+}$ host complex, as well as minimise the electrostatic penalty for the binding of the second anion (Figure 4.23).

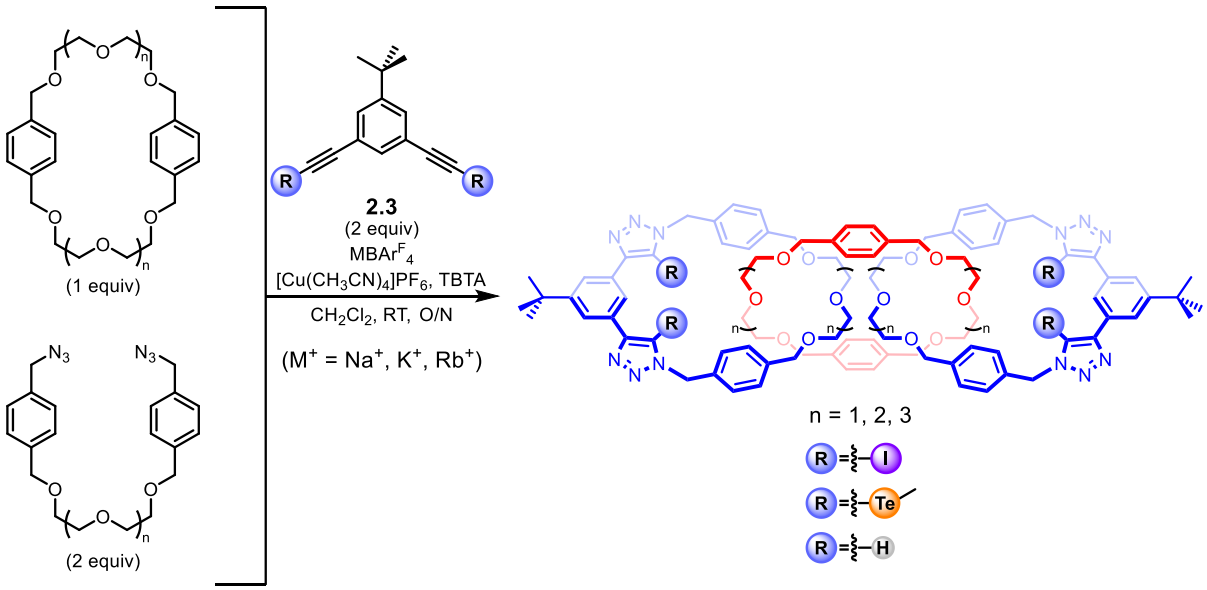

Scheme 4.11 Synthetic route to a series of XB/ChB/HB tetratopic [3]catenanes via alkali metal cation template methodology.

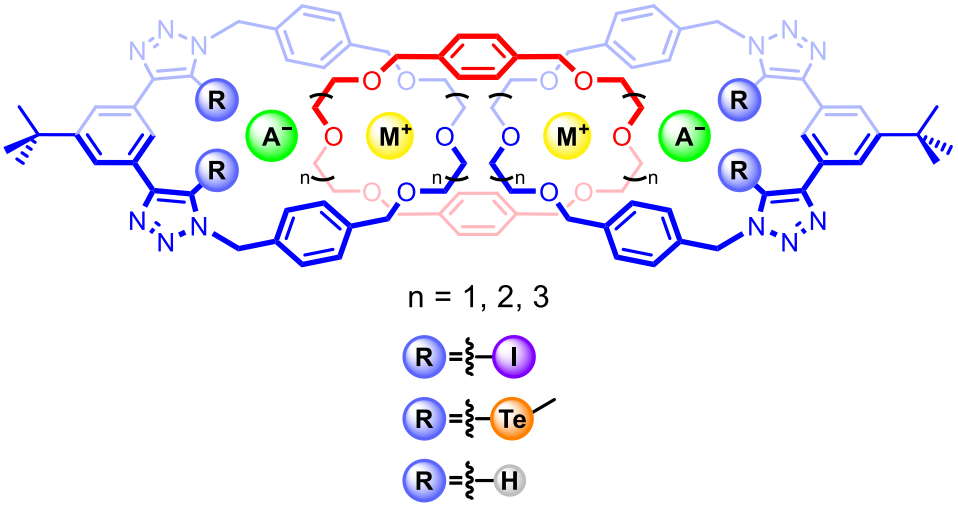

Figure 4.23 Proposed ion-pair binding mode of the tetratopic [3]catenane.

Chapter 5

Conclusion

Chapter 5 Conclusion

The main theme of this thesis is the incorporation of XB and ChB donor motifs into macrocyclic and interlocked host systems for the recognition of anions and ion-pair species.

Chapter 2 explores the fundamental charged guest recognition properties of a library of σ-hole [2]rotaxanes, including the unprecedented all-ChB and mixed XB/ChB interlocked receptors. Extensive ^{1}H NMR titration experiments reveal the significant influence of the nature, combination and disposition of XB and ChB donors on the anion recognition properties of the rotaxane hosts. Notably, the strength of Te···anion ChB interactions could be effectively fine-tuned by varying the electronic and steric nature of the substituents appended on the divalent tellurium atoms. Furthermore, the Lewis basic character of the tellurium atoms is demonstrated by the rotaxane hosts displaying exceptional binding to complementary "soft" metal cations. This unique manifestation of amphoteric character of anisotropically polarised tellurium atoms presents an exciting opportunity for the future design of charged guest receptors, in which the recognition of *both* cations and anions are mediated by the same set of donor atoms. In addition, a mixed XB/ChB [2]rotaxane was shown to be capable of the cooperative binding of lithium iodide as an axle-separated ion-pair.

Chapter 3 seeks to demonstrate the potential of XB host systems in anion sensing. Strapped zinc(II) metalloporphyrins incorporated with a potent bidentate XB donor motif display substantially augmented halide anion affinities and selectivity compared to strap-free zinc(II) tetraphenylporphyrin. Building on this work, dual optical- and redox-active BODIPY-porphyrin rotaxanes were prepared to further improve the anion sensing performance. In these interlocked systems, axle triazole coordination to the strapped zinc(II) metalloporphyrin macrocyclic component serves to enhance the

degree of receptor preorganisation. Fluorescence titrations demonstrate the optical halide and oxoanion (acetate and sulfate) sensing capability of these rotaxane hosts via quenching of the rotaxane axle BODIPY-centred emission bands in both organic and organic-aqueous media. Electrochemical studies further reveal large-magnitude cathodic shifts of the rotaxanes' porphyrin $P/P^{+\bullet}$ oxidation redox couples occurs upon anion binding.

In Chapter 4, XB and ChB interactions are exploited in lithium halide ion-pair recognition. Lithium complexation to a series of phenanthroline-based XB/ChB/HB heteroditopic macrocycles concomitantly switches on their halide anion affinity. In particular, the XB macrocycle proved to be the most potent ion-pair receptor studied and was the only macrocycle capable of recognising the "hard" LiCl ion-pair without salt recombination. In contrast, the ChB macrocyclic receptor displayed a marked preference towards the "soft" LiI ion-pair over LiBr. Solid-liquid extraction studies revealed the ability of these heteroditopic macrocycles to solubilise lithium halide salts into organic solvent media.

Inspired by the potency of XB-mediated ion-pair recognition, the first all-XB tritopic [2]catenane was synthesised via adaptation of an alkali metal cation template methodology. Sodium cation binding at the polyether domains of the catenane host dramatically enhanced bromide and iodide anion affinity and selectivity in the XB cavities. A switch of the host-guest anion binding stoichiometry from 1:1 in the absence of sodium, to 1:2 in the presence of the co-bound sodium cation allows for the receptor to overcome the energetic cost associated with the recognition of a second anion.

In conclusion, the results of these projects serve to highlight the exciting potential of utilising σ-hole interactions in supramolecular host-guest chemistry, in particular in the context of anion and ion-pair recognition. Importantly, the contrasting charged

guest coordination behaviour exhibited by XB and ChB donors can be exploited in future host design for modulation of receptor affinity and selectivity towards target anion, cation and ion-pair guest species.

Chapter 6

Experimental

Chapter 6 Experimental

6.1 General Considerations

6.1.1 Instrumentations

NMR spectra for the nuclei ^{1}H, $^{13}C\{^{1}H\}$ and $^{19}F\{^{1}H\}$ were recorded on Bruker Avance III HD nanobay NMR machines (Hg400 and Venus400) each equipped with a 9.4 T magnet, or Bruker Avance III NMR machine (AVD500) equipped with a 11.75 T magnet, or Bruker Avance NMR machine (AVC500) equipped with a 11.75 T magnet and a ^{13}C detect cryoprobe, or Bruker NEO 600 with broadband helium cryoprobe. ^{125}Te NMR spectra were recorded on the AVD500. All chemical shifts are reported in part per million (ppm) with signals splitting denoted as singlet (s), broad singlet (brs), doublet (d), triplet (t), quartet (q), quintet (quint.), septet (sept.) and multiplet (m). Coupling constants (J) are reported as 3-bond coupling (^{3}J) unless otherwise specified and are recorded to the nearest 0.1 ppm. ^{1}H and ^{13}C NMR spectra are calibrated to the residual solvent peak, or to the solvent with the higher number of deuterium atoms for mixed solvent systems, and are assigned with aid from 2D NMR spectroscopies including COSY and ROESY. Low resolution ESI mass spectra were recorded on a Waters LCT Premier XE bench-top orthogonal acceleration time-of-flight LC-MS system. High resolution ESI and MALDI spectra were recorded on a Bruker micrOTOF spectrometer and Autoflex™ speed MALDI-TOF(/TOF) spectrometer respectively. UV–visible absorption and emission spectra were recorded on a HORIBA Duetta™ absorbance and fluorescence spectrometer using quartz cuvettes with pathlength of 10 mm.

6.1.2 ^{1}H NMR Titration Protocols

^{1}H NMR titration experiments were performed on a Bruker Avance III NMR 500 MHz spectrometer (AVD500) at 298 K. In a typical experiment, aliquots of a 50 mM charged guest stock solution were added to 0.5 mL of a 1.0 mM host solution, where 1.0 equivalent of charged guest added corresponds to 10.0 μL of the stock solution. The samples were thoroughly mixed before recording the ^{1}H NMR spectra. 17 data points corresponding to 0.0, 0.2, 0.4, 0.6, 0.8, 1.0, 1.2, 1.4, 1.6, 1.8, 2.0, 2.5, 3.0, 4.0, 5.0, 7.0 and 10.0 equivalents of added charged guest were obtained. The binding of charged guest with all hosts were found to be fast on the NMR timescale. Stability constants were determined using BindFit[235,236] software, employing a 1:1 host-guest stoichiometric binding model unless otherwise specified.

6.1.3 Optical Titration Protocols

UV–visible absorption and fluorescence titration experiments were both performed on a HORIBA Duretta™ absorbance and fluorescence spectrophotometer at 298 K using 1.0 mL quartz cuvettes of pathlength 10 mm. The charged guest was dissolved in the host solution to maintain the same host concentration throughout the course of titration. In a typical experiment, aliquots of a charged guest stock solution of appropriate concentration were added to a 1.0 mL host solution. The samples were thoroughly mixed before recording the UV–visible absorption or emission spectra. Stability constants were determined by global fitting using OriginLab[235,236] software, employing a 1:1 host-guest stoichiometric binding model unless otherwise specified.

6.1.4 Solid-Liquid and Liquid-Liquid Extraction Protocols

In a typical solid-liquid extraction (SLE) experiment, excess (10 equiv) solid salt was added to 0.60 mL of a 2.0 mM host solution and the mixture was vigorously sonicated for 1 hour at ambient temperature. The excess salt was subsequently filtered

off and the ^{1}H NMR spectrum of the post-extraction solution was recorded and compared with that of the pre-extraction solution.

In a typical liquid-liquid extraction (LLE) experiment, 0.70 mL of a 2.0 mM host solution was added to a 0.70 mL D_2O solution of the salt of interest of appropriate concentration. The biphasic mixture was vigorously stirred for 1 hour at room temperature. The organic layer was separated from the aqueous layer and the ^{1}H NMR spectrum of the post-extraction organic solution was recorded and compared with that of the pre-extraction solution.

6.1.5 Electrochemical Experiments

All experiments were conducted on an Autolab potentiostat (Metrohm) in a three electrode set up. As working electrode a glassy carbon electrode was used (3 mm diameter, BASi), which was polished mechanically with alumina slurry (0.05 μm, Buehler) followed by sonication in EtOH/H_2O. The counter electrode was a Pt wire, while as reference electrode a leak-free Ag|AgCl electrode (Innovative Instruments Ltd.) or a non-aqueous Ag|$AgNO_3$ reference electrode (with an inner filling solution of 10 mM $AgNO_3$ in CH_3CN, 100 mM $TBAPF_6$) were used (the latter for all anion titrations). All potentials are reported with respect to Fc/Fc^+ as internal standard.

Cyclic voltammetry (CV) spectra were recorded using a step potential of 2.4 mV and at a scan rate of 100 mV/s, unless otherwise noted. The electrochemical reversibility was assessed by recording CVs at varying scan rates (25, 50, 75, 100, 200, 400, 600 and 800 mV/s). Square wave voltammetry (SWV) spectra were recorded using a step potential of 2 mV, a 20 mV amplitude and a frequency of 25 Hz. All electrochemical titrations were followed by SWV and half-wave potentials were obtained as the peak potential from SWV. In all cases 100 mM $TBAPF_6$ was used as supporting electrolyte. In anion sensing studies both the overall host concentration

(0.1 mM) as well as the total ionic strength was kept constant (100 mM; by titration of an initial host solution containing 100 mM $TBAPF_6$ titrated with a solution containing 100 mM TBA-anion and 0.1 mM host).

6.2 Synthetic Procedures

6.2.1 Chemicals and Solvents

All solvents and reagents used in this thesis were purchased from commercial suppliers and used as received unless otherwise stated. Dry organic solvents were degassed by purging with nitrogen and dehydrated by passing through an MBraun MPSP-800 column. Water was deionised and micro-filtered using a Milli-Q® Millipore machine. TBA salts and $[Cu(CH_3CN)_4]PF_6$ were stored in vacuum desiccators containing anhydrous P_2O_5 powder in between usage. TBTA was synthesised according to a reported procedure[373] and stored at room temperature. Et_3N was distilled from KOH and stored over the same base prior to use. Ratios of solvent mixtures are reported by volume. Brine refers to a saturated aqueous solution of NaCl, and basic $EDTA_{(aq.)}$ refers to an aqueous solution of 0.02 M EDTA with 1% NH_3 (28–30%) solution. Thin layer chromatography (TLC) analysis was performed using Merck silica Kieselgel 60 F_{254} 0.25 mm or Fluka 60 Å aluminium oxide matrix on precoated aluminium plates, with spots visualised under UV light (254 nm) and/or staining with basic $KMnO_4$ solution/iodine vapour (only for silica TLC). Column chromatography was carried out on Merck silica gel 60 under a positive pressure of nitrogen, and preparative TLC was performed on 20 × 20 cm plates with a silica layer of thickness 1 mm. Microwave-assisted reactions were performed in a Biotage® Initiator 2.0 reactor using sealed standard Biotage pyrex-glass microwave vials with caps containing rubber septa.

6.2.2 Synthetic Procedures and Characterisations of Novel Compounds from Chapter 2

XB Macrocycle (2.1·I)

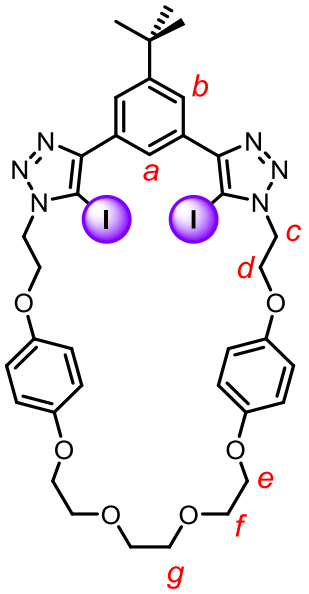

General Procedure for CuAAC-mediated Macrocyclisation

$[Cu(CH_3CN)_4]PF_6$ (86 mg, 0.23 mmol, 0.5 equiv) and TBTA (61 mg, 0.12 mmol, 0.25 equiv) were added to dry and degassed CH_2Cl_2 (130 mL), and allowed to stir at room temperature for 15 minutes under N_2. Bis-azide **2.6** (218 mg, 0.46 mmol, 1 equiv) dissolved in dry and degassed CH_2Cl_2 (10 mL) was added to the Cu(I)-TBTA mixture, followed by a solution of bis(iodoalkyne) **2.3·I** (200 mg, 0.46 mmol, 1 equiv) in dry and degassed CH_2Cl_2 (10 mL). The reaction mixture was allowed to stir at room temperature in dark overnight. The solvent was removed *in vacuo* and the solid residue was redissolved in CH_2Cl_2 (100 mL) and washed with aqueous basic EDTA (30 mL x 2). The organic layer was dried over $MgSO_4$, filtered and concentrated on the rotary evaporator. Further purification with silica gel column chromatography (60% EtOAc in CH_2Cl_2) afforded the target macrocycle **2.1·I** as white powder (129 mg, 31%).

^{1}H NMR (400 MHz, $CDCl_3$) δ (ppm): 8.12 (t, J = 1.6 Hz, 1H; *a*), 7.96 (d, J = 1.6 Hz, 2H; *b*), 6.78 (d, J = 9.2 Hz, 4H; *hydroquinone ArH*), 6.71 (d, J = 9.2 Hz, 4H; *hydroquinone ArH*), 4.86 (t, J = 4.9 Hz, 4H; *c*), 4.43 (t, J = 4.9 Hz, 4H; *d*), 4.02 (t, J = 4.8 Hz, 4H; *e*), 3.78 (t, J = 4.8 Hz, 4H; *f*), 3.67 (s, 4H; *g*), 1.43 (s, 9H; *tert*-butyl *H*).

^{13}C NMR (126 MHz, $CDCl_3$) δ (ppm): 153.68, 152.41, 152.23, 150.53, 130.29, 125.61, 124.42, 78.73, 70.97, 69.85, 68.35, 67.74, 50.16, 35.30, 31.52, 29.85, 1.17.

HRMS (ESI +ve) m/z: 907.1168 ($[M+H]^+$, $C_{36}H_{41}O_6N_6I_2$ requires 907.1171)

ChB Macrocycle (2.1·Te^{Me})

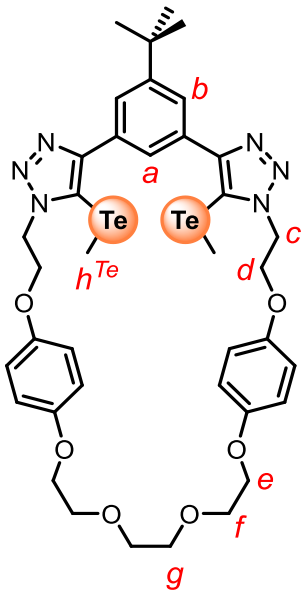

Following the general procedure for CuAAC-mediated macrocyclisation between bis(telluromethylalkyne) **2.3·Te^{Me}** (250 mg, 0.54 mmol, 1 equiv) and bis-azide **2.6** (254 mg, 0.54 mmol, 1 equiv), the crude was purified by silica gel column chromatography (60% EtOAc in CH_2Cl_2) to give the target macrocycle **2.1·Te^{Me}** as white powder (218 mg, 43%).

^{1}H NMR (400 MHz, $CDCl_3$) δ (ppm): 8.41 (t, J = 1.6 Hz, 1H; *a*), 7.92 (d, J = 1.6 Hz, 2H; *b*), 6.80 (d, J = 9.2 Hz, 4H; *hydroquinone ArH*), 6.74 (d, J = 9.2 Hz, 4H; *hydroquinone ArH*), 5.00 (t, J = 4.8 Hz, 4H; *c*), 4.36 (t, J = 4.8 Hz, 4H; *d*), 4.03 (t, J = 4.8 Hz, 4H; *e*), 3.81 (t, J = 4.8 Hz, 4H; *f*), 3.70 (s, 4H; *g*), 1.85 (s, 6H; h^{Te}), 1.42 (s, 9H, *tert*-butyl *H*).

^{13}C NMR (126 MHz, $CDCl_3$) δ (ppm): 153.80, 153.46, 152.31, 152.02, 131.58, 125.78, 124.78, 115.95, 115.74, 102.35, 71.00, 69.83, 68.38, 68.15, 50.44, 35.20, 31.52, -12.69.

HRMS (ESI +ve) m/z: 941.1650 ($[M+H]^+$, $C_{38}H_{47}O_6N_6Te_2$ requires 941.1658)

HB Macrocycle (2.1·H)

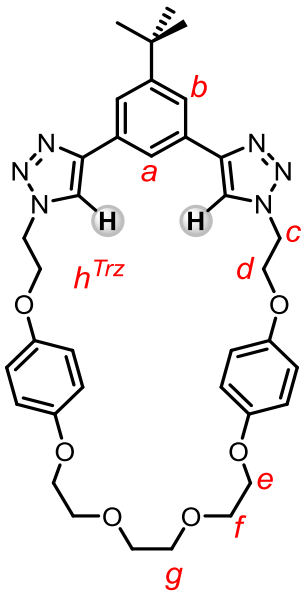

Following the general procedure for CuAAC-mediated macrocyclisation between bis(iodoalkyne) **2.3·H** (200 mg, 1.10 mmol, 1 equiv) and bis-azide **2.6** (518 mg, 1.10 mmol, 1 equiv), the crude was purified by silica gel column chromatography (15:15:70 EtOAc/Acetone/CH_2Cl_2) to give the target macrocycle **2.1·H** as white powder (154 mg, 21%).

^{1}H NMR (400 MHz, acetone-d_6) δ (ppm): 8.53 (s, 2H; h^{Trz}), 8.09 (d, J = 1.6 Hz, 2H; *b*), 8.00 (t, J = 1.6 Hz, 1H; *a*), 6.89 (d, J = 9.2 Hz, 4H; *hydroquinone ArH*), 6.83 (d, J = 9.2 Hz, 4H; *hydroquinone ArH*), 4.86 (t, J = 4.6 Hz, 4H; *c*), 4.42 (t, J = 4.6 Hz, 4H; *d*), 4.03 (t, J = 4.6 Hz, 4H; *e*), 3.77 (t, J = 4.6 Hz, 4H; *f*), 3.63 (s, 4H; *g*), 1.42 (s, 9H; *tert*-butyl *H*).

^{13}C NMR (126 MHz, acetone-d_6) δ (ppm): 154.69, 153.45, 153.07, 148.16, 132.59, 122.51, 121.23, 116.64, 116.48, 71.54, 70.34, 69.02, 68.33, 50.69, 35.53, 31.66, 26.22.

HRMS (ESI +ve) m/z: 655.3234 ($[M+H]^+$, $C_{36}H_{43}O_6N_6$ requires 655.3239).

5-*tert*-Butyl-1,3-bis(telluromethylalkynyl)benzene (2.3·Te^{Me})

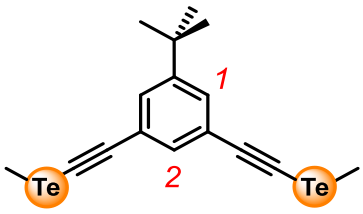

1,3-bis[(trimethylsilyl)ethynyl]-5-*tert*butylbenzene (200 mg, 0.61 mmol, 1 equiv) was dissolved in CH_3OH (3 mL) and a suspension of AgF (159 mg, 1.25 mmol, 2.05 equiv) in CH_3OH (12 mL) was added dropwise. The mixture was stirred for 10 minutes at room temperature to give the silver acetylide, to which dry THF (12 mL) was added to form a suspension. In a separate flask, $(CH_3)_2Te_2$ (175 mg, 0.61 mmol, 1 equiv) was added to dry THF (4 mL) and cooled to 0 °C. 1 M Br_2 in CH_2Cl_2 (0.61 mL) was then added at 0 °C to generate CH_3TeBr. After warming to room temperature, CH_3TeBr solution was added to silver acetylide suspension slowly and the reaction mixture was stirred for 30 minutes. The crude was then filtered through celite, and solvent was removed *in vacuo*. Product was purified by silica gel column chromatography (10% CH_2Cl_2 in *n*-hexane) to give the product as yellow oil (219 mg, 77%).

^{1}H NMR (400 MHz, $CDCl_3$) δ (ppm): 7.35 (d, J = 1.5 Hz, 2H; *1*), 7.29 (t, J = 1.5 Hz, 1H; *2*), 2.21 (s, 6H, $TeCH_3$), 1.28 (s, 9H, *tert*-butyl H)

^{13}C NMR (101 MHz, $CDCl_3$) δ (ppm): 151.33, 132.19, 128.98, 123.34, 110.30, 44.81, 34.73, 31.09, -14.42

^{125}Te NMR (126 MHz, $CDCl_3$) δ (ppm): 165.27

HRMS (MALDI-TOF) m/z: 495.942 ($[M]^{\bullet+}$, $C_{16}H_{18}Te_2$ requires 465.950)

Stopper telluromethyl-alkyne (2.8·Te^{Me})

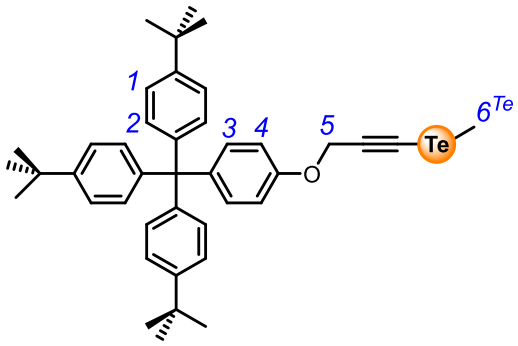

General Procedure for Stopper Telluroalkyne Synthesis

$AgNO_3$ (158 mg, 0.98 mmol, 1.01 equiv) and catalytic amount of freshly distilled Et_3N (0.1 mL) were added to a solution of stopper proto-alkyne **2.7·H** (500 mg, 0.92 mmol, 1 equiv) dissolved in 1:1 CH_2Cl_2:CH_3CN (40 mL). The mixture was stirred at room temperature for 30 minutes in dark to generate the corresponding stopper silver acetylide. The solvent was removed *in vacuo* and the isolated acetylide was suspended in dry THF (18 mL). In a separate flask, $(CH_3)_2Te_2$ (263 mg, 0.92 mmol, 1 equiv) was dissolved in dry THF (6 mL), to which was added 1.0 M Br_2 solution in CH_2Cl_2 (0.92 mL) at 0 °C to generate the corresponding CH_3TeBr. After warming to room temperature, the CH_3TeBr solution was added to the stopper silver acetylide suspension dropwise and the reaction mixture was stirred for 30 minutes. The crude was then filtered through celite, and concentrated on rotary evaporator. Product was purified by silica gel column chromatography (20% CH_2Cl_2 in *n*-hexane) to give the product as white powder (410 mg, 65%).

^{1}H NMR (400 MHz, acetone-d_6) δ (ppm): 7.32 (d, J = 8.6 Hz, 6H; *2*), 7.12 (d, J = 8.6 Hz, 6H; *1*), 7.11 (d, J = 9.0 Hz, 2H; *3*), 6.90 (d, J = 9.0 Hz, 2H; *4*), 4.94 (s, 2H; *5*), 2.11 (s, 3H; 6^{Te}), 1.30 (s, 27H; *tert*-butyl H).

^{13}C NMR (126 MHz, $CDCl_3$) δ (ppm): 155.78, 148.48, 144.22, 140.50, 132.37, 130.89, 124.19, 113.61, 106.44, 63.23, 57.34, 43.28, 34.44, 31.53, -14.92.

Stopper Phenyl Telluroalkyne (2.8·Te^{Ph})

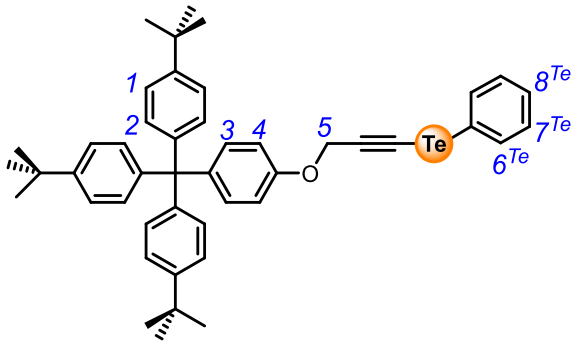

Following the general procedure for stopper telluroalkyne synthesis using stopper proto-alkyne **2.7·H** (500 mg, 0.92 mmol, 1 equiv) and Ph_2Te_2 (377 mg, 0.92 mmol, 1 equiv) as starting materials, the crude was purified with silica gel column chromatography (20% CH_2Cl_2 in *n*-hexane) to give the target **2.8·Te^{Ph}** as white powder (468 mg, 68%).

^{1}H NMR (400 MHz, acetone-d_6) δ (ppm): 7.76 – 7.70 (m, 2H; *6Te*), 7.32 (d, J = 8.6 Hz, 6H; *2*), 7.29 – 7.24 (m, 1H; *8Te*), 7.24 – 7.17 (m, 2H; *7Te*), 7.16 – 7.08 (m, 8H; *3* + *1*), 6.94 (d, J = 9.0 Hz, 2H; *4*), 5.05 (s, 2H; *5*), 1.30 (s, 27H; *tert*-butyl H).

^{13}C NMR (126 MHz, $CDCl_3$) δ (ppm): 155.66, 148.51, 144.21, 140.57, 135.64, 132.39, 130.91, 129.88, 128.20, 124.20, 113.66, 112.58, 110.27, 63.24, 57.28, 46.76, 34.44, 31.54.

Stopper *para*-Trifluoromethyl Telluroalkyne (2.8·Te^{pCF3})

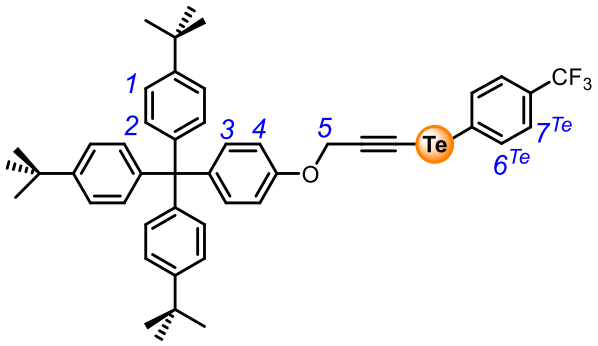

Following the general procedure for stopper telluroalkyne synthesis using stopper proto-alkyne **2.7·H** (500 mg, 0.92 mmol, 1 equiv) and (*para*-CF_3-Ph)$_2$Te$_2$ (502 mg, 0.92 mmol, 1 equiv) as starting materials, the crude was purified with silica gel column chromatography (10% CH_2Cl_2 in *n*-hexane) to give the target **2.8·Te^{pCF3}** as white powder (420 mg, 56%).

^{1}H NMR (400 MHz, acetone-d_6) δ (ppm): 7.98 (d, J = 8.0 Hz, 2H; 7^{Te}), 7.55 (d, J = 8.0 Hz, 2H; 6^{Te}), 7.31 (d, J = 8.7 Hz, 6H; *2*), 7.17 – 7.08 (m, 8H; *3* + *1*), 6.96 (d, J = 9.0 Hz, 2H; *4*), 5.10 (s, 2H; *5*), 1.30 (s, 27H; *tert*-butyl H).

^{13}C NMR (126 MHz, $CDCl_3$) δ (ppm): 155.62, 148.57, 144.17, 140.82, 134.81, 132.46, 130.89, 126.34 (q, $^4J_{C-F}$ = 3.9 Hz), 124.22, 124.05 (q, $^1J_{C-F}$ = 273 Hz), 118.47, 113.62, 111.65, 63.26, 57.26, 45.86, 34.45, 31.52, 22.49.

Stopper Telluromethyl-triazole-functionalised Azide (2.9·Te^{Me})

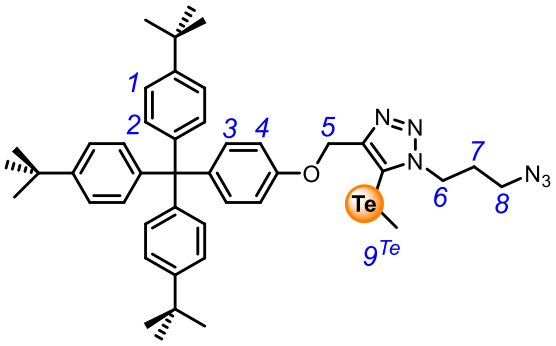

[Cu(CH$_3$CN)$_4$]PF$_6$ (54 mg, 0.15 mmol, 0.5 equiv) and TBTA (78 mg, 0.15 mmol, 0.5 equiv) were added to dry and degassed CH$_2$Cl$_2$ (5 mL) and the mixture was stirred at room temperature for 20 minutes. CH$_2$Cl$_2$ solutions of 1,3-diazido-propane (295 mg, 2.34 mmol, 8 equiv) and stopper telluromethyl-alkyne **2.8·Te^{Me}** (200 mg, 0.29 mmol, 1 equiv) were added sequentially. The reaction mixture was left stirring at room temperature in dark overnight. The crude was washed with basic EDTA (30 mL) and deionised water (30 mL × 3). The organic layer was dried over anhydrous MgSO4, filtered and concentrated *in vacuo*. Further purification with silica gel column chromatography (60% CH$_2$Cl$_2$ in *n*-hexane) gave the product as white powder (201 mg, 85%).

^{1}H NMR (600 MHz, acetone-*d*$_6$) δ (ppm): (d, *J* = 8.4 Hz, 6H; *2*), 7.13 (d, *J* = 8.4 Hz, 6H; *1*), 7.12 (d, *J* = 8.9 Hz, 2H; *3*), 6.99 (d, *J* = 8.9 Hz, 2H; *4*), 5.21 (s, 2H; *5*), 4.68 (t, *J* = 7.0 Hz, 2H; *6*), 3.48 (t, *J* = 6.5 Hz, 2H; *8*), 2.23 (q, *J* = 6.7Hz, 2H; *7*), 2.09 (s, 3H; *9Te*), 1.31 (s, 27H; *tert*-butyl H).

^{13}C NMR (151 MHz, acetone-*d*$_6$) δ (ppm): 157.59, 152.05, 149.22, 145.24, 140.69, 132.87, 131.47, 125.08, 114.53, 106.03, 63.95, 63.76, 49.13, 49.03, 34.88, 31.66, 30.59, -13.25.

HRMS (ESI +ve) m/z: 811.3474 ([M+H]$^+$, C$_{44}$H$_{55}$N$_6$OTe requires 811.3476).

Tridentate All-ChB [2]Rotaxane (2.11·ChB$_3$)

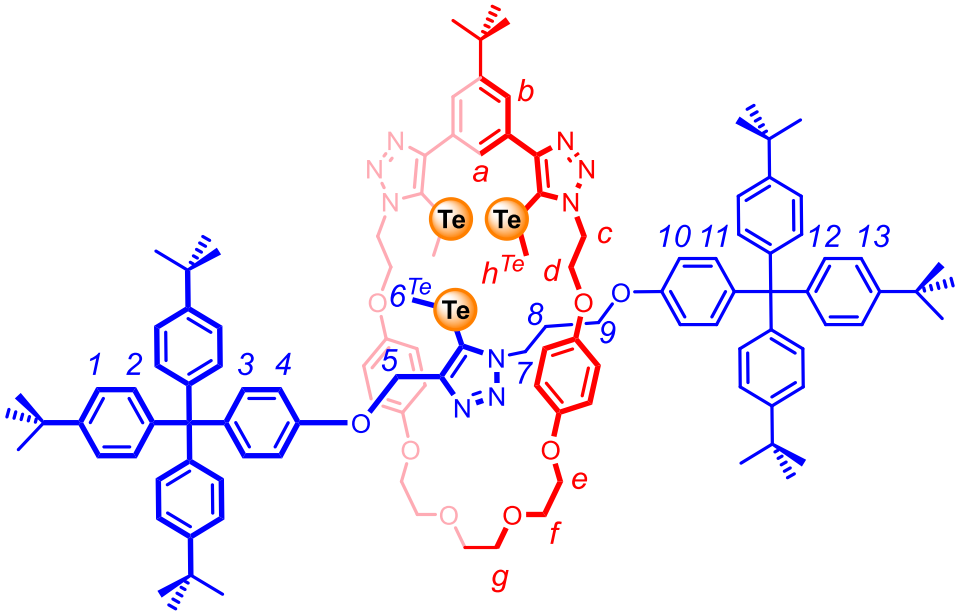

General Procedure for CuAAC-AMT Synthesis of [2]Rotaxanes

Macrocycle **2.1·Te^{Me}** (10 mg, 0.011 mmol, 1 equiv) and [Cu(CH$_3$CN)$_4$]PF$_6$ (4 mg, 0.011 mmol, 1 equiv) were dissolved in dry and degassed CH$_2$Cl$_2$ (0.7 mL) in a sealed vial, and the mixture was allowed to stir at room temperature under N$_2$ for 30 minutes. Stopper azide **2.10** (31 mg, 0.053 mmol, 5 equiv) and stopper alkyne **2.8·Te^{Me}** (36 mg, 0.053 mmol, 5 equiv), each dissolved in dry and degassed CH$_2$Cl$_2$ (0.7 mL), were sequentially added to the vial. The reaction mixture was left stirring at room temperature for 2 days, if after which time TLC analysis of the crude indicated the persistence of azide/alkyne precursors, additional portion of [Cu(CH$_3$CN)$_4$]PF$_6$ (4 mg, 0.011 mmol, 1 equiv) was added. This process was repeated until complete consumption of azide/alkyne was observed. Afterwards, the crude was diluted with CH$_2$Cl$_2$ (20 mL) and washed with aqueous 0.02 M NH$_4$OH/EDTA (20 mL), dried with MgSO$_4$, filtered and concentrated on rotary evaporator. Further purification with preparative TLC (10% EtOAc in CH$_2$Cl$_2$) afforded the target tridentate [2]rotaxane **2.11·ChB$_3$** as white powder (5.7 mg, 24%).

^{1}H NMR (500 MHz, acetone-d_6) δ (ppm): 8.62 (t, J = 1.6 Hz, 1H; *a*), 8.09 (d, J = 1.6 Hz, 2H; *b*), 7.32 (m, 12H; *2, 12*), 7.15 (m, 12H; *1, 13*), 7.08 (d, J = 8.8 Hz, 2H; *3*), 7.02 (d, J = 8.8 Hz, 2H; *11*), 6.81 (d, J = 8.8 Hz, 2H; *4*), 6.50 (d, J = 8.8 Hz, 2H; *10*), 6.47 (d, J = 9.1 Hz, 4H; hydroquinone ArH), 6.39 (d, J = 9.1 Hz, 4H; hydroquinone ArH), 5.01 (t, J = 4.7 Hz, 4H; *c*), 4.85 (s, 2H; *5*), 4.29 (t, J = 4.7 Hz, 4H; *d*), 4.16 (t, J = 7.4 Hz, 2H; *7*), 3.84 (t, J = 5.0 Hz, 4H; *e*), 3.60 (t, J = 5.0 Hz, 4H; *f*), 3.54 – 3.47 (m, 6H; *g*, *9*), 1.98 (s, 6H; h^{Te}), 1.56 (s, 3H; 6^{Te}), 1.42 (s, 9H; macrocycle ^{t}Bu), 1.30 (s, 54H; axle ^{t}Bu).

^{13}C NMR (151 MHz, acetone-d_6) δ (ppm): 157.44, 157.39, 154.06, 153.28, 153.03, 151.71, 151.64, 149.09, 149.05, 145.49, 145.40, 140.27, 139.96, 132.93, 132.66, 132.59, 131.48, 125.79, 125.36, 125.11, 125.10, 116.22, 115.93, 114.50, 114.23, 105.58, 103.20, 71.32, 70.13, 68.79, 68.54, 65.18, 63.96, 63.31, 54.96, 51.30, 48.64, 35.70, 34.90, 34.89, 31.79, 31.72, 31.70, 30.34, -12.66, -13.05.

HRMS (ESI +ve) m/z: 2210.8261 ($[M]^{+\bullet}$, $C_{119}H_{143}O_8N_9Te_3$ requires 2210.8228).

Tridentate All-XB [2]Rotaxane (2.11·XB3)

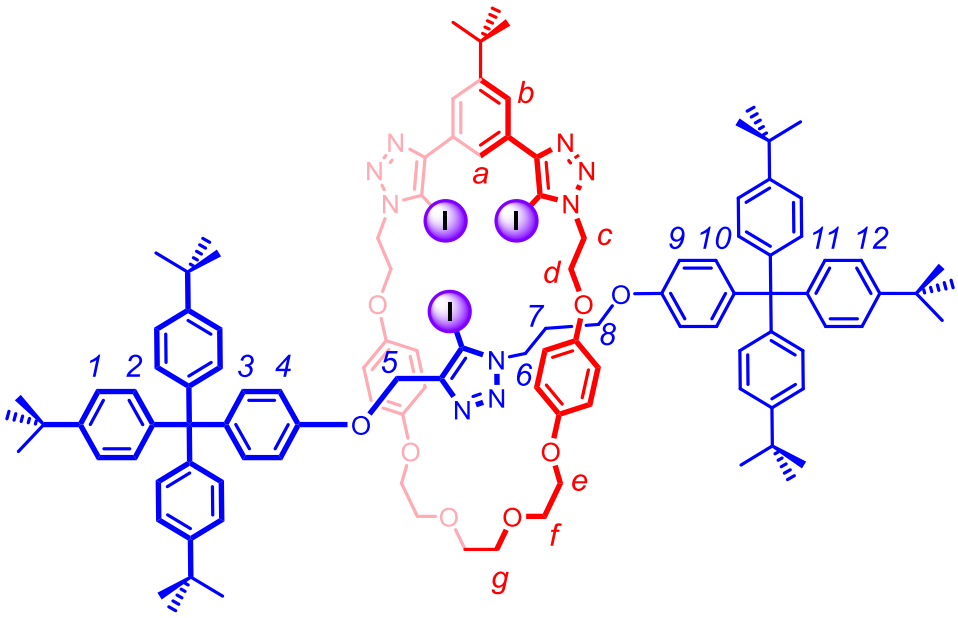

Following the general procedure for CuAAC-AMT synthesis of [2]rotaxanes between macrocycle **2.1·I** (10 mg, 0.011 mmol, 1 equiv), stopper azide **2.10** (32 mg, 0.055 mmol, 5 equiv) and stopper alkyne **2.8·I** (37 mg, 0.055 mmol, 5 equiv), the product was purified by preparative TLC (acetone/EtOAc/CH_2Cl_2 2:6:92) to give the target tridentate [2]rotaxane **2.11·XB3** as white powder (7.4 mg, 31%).

^{1}H NMR (400 MHz, acetone-d_6) δ (ppm): 8.32 (t, J = 1.6 Hz, 1H; *a*), 8.02 (d, J = 1.6 Hz, 2H; *b*), 7.37 – 7.27 (m, 12H; *2, 11*), 7.18 – 7.11 (m, 12H; *1, 12*), 7.09 (d, J = 8.9 Hz, 2H; *3*), 6.98 (d, J = 8.9 Hz, 2H; *10*), 6.86 (d, J = 8.9 Hz, 2H; *4*), 6.45 (apparent s, 8H; *hydroquinone ArH*), 6.36 (d, J = 8.9 Hz, 2H; *9*), 4.88 (t, J = 4.7 Hz, 4H; *c*), 4.82 (s, 2H; *5*), 4.42 – 4.23 (m, 4H; *d*), 3.93 – 3.79 (m, 6H; *6, e*) 3.61 (t, J = 4.7 Hz, 4H; *f*), 3.52 (s, 4H; *g*), 3.35 (t, J = 5.9 Hz, 2H; *8*), 1.70 (q, J = 5.9 Hz, 2H; *7*), 1.42 (s, 9H; *macrocycle tert*-butyl *H*), 1.31 (s, 57H; axle *tert*-butyl *H*).

^{13}C NMR (151 MHz, acetone-d_6) δ (ppm): 157.38, 157.27, 154.07, 153.11, 152.29, 150.40, 149.15, 149.06, 147.68, 145.47, 145.32, 140.58, 139.98, 132.77, 132.64, 131.95,

131.53, 131.49, 125.38, 125.27, 125.12, 125.11, 116.18, 116.06, 114.54, 114.07, 82.81, 80.22, 71.41, 70.25, 68.56, 68.21, 64.81, 63.96, 62.22, 50.96, 48.16, 35.75, 34.91, 34.89, 31.79, 31.74, 31.70, 23.34.

HRMS (ESI +ve) m/z: 2163.7530 ($[M+H]^+$, $C_{116}H_{135}O_8N_9I_3$ requires 2163.7594).

Tridentate Mixed XB/ChB [2]Rotaxane (2.11·XB$_2$ChB^{Me})

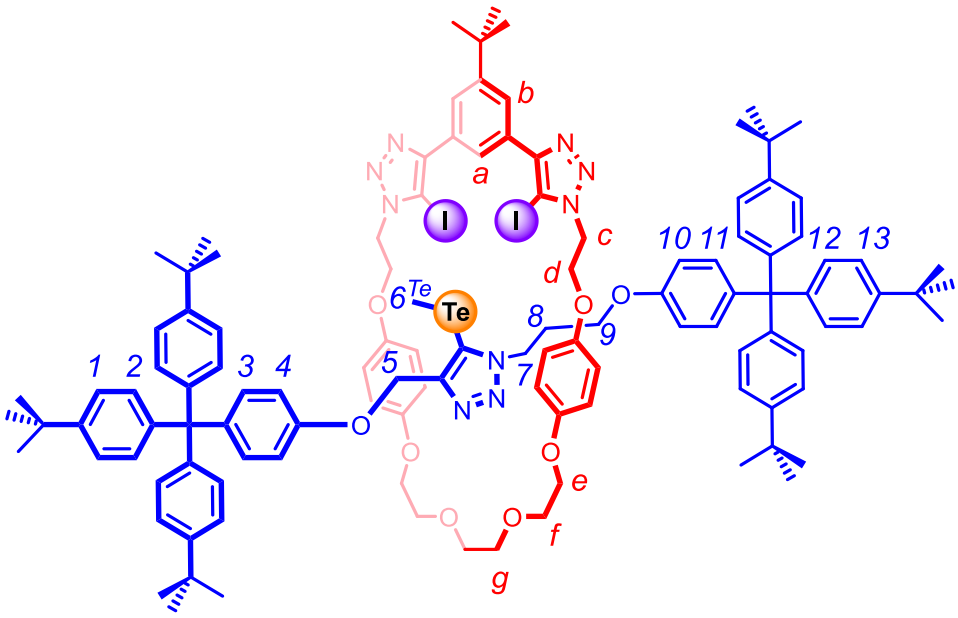

Following the general procedure for CuAAC-AMT synthesis of [2]rotaxanes between macrocycle **2.1·I** (10 mg, 0.011 mmol, 1 equiv), stopper azide **2.10** (32 mg, 0.055 mmol, 5 equiv) and stopper alkyne **2.8·Te^{Me}** (38 mg, 0.055 mmol, 5 equiv), the product was purified by preparative TLC (10% EtOAc in CH_2Cl_2) to give the target tridentate [2]rotaxane **2.11·XB$_2$ChB^{Me}** as white powder (6.0 mg, 25%).

^{1}H NMR (600 MHz, acetone-d_6) δ (ppm): 8.25 (t, J = 1.6 Hz, 1H; *a*), 8.01 (d, J = 1.6 Hz, 2H; *b*), 7.36 – 7.27 (m, 12H; *2, 12*), 7.14 – 7.10 (m, 12H; *1, 13*), 7.06 (d, J = 8.8 Hz, 2H; *3*), 6.93 (d, J = 8.8 Hz, 2H; *11*), 6.81 (d, J = 8.8 Hz, 2H; *4*), 6.49 (d, J = 8.8 Hz, 4H; *hydroquinone ArH*), 6.42 (d, J = 8.8 Hz, 4H; *hydroquinone ArH*), 6.31 (d, J = 8.8 Hz, 2H; *10*), 4.95 (s, 2H; *5*), 4.89 (t, J = 4.9 Hz, 4H; *c*), 4.34 (t, J = 5.0 Hz, 4H; *d*), 4.23 (t, J = 6.5 Hz, 2H; *7*), 3.88 – 3.80 (m, 4H; *e*), 3.60 (t, J = 5.0 Hz, 4H; *f*), 3.54 – 3.48 (m, 4H; *g*), 3.39 (t, J = 6.5 Hz, 2H; *9*), 1.85 (q, J = 6.5 Hz, 2H; *8*), 1.65 (s, 3H; *6Te*), 1.42 (s, 9H; macrocycle *tert*-butyl H), 1.31 (s, 54H; axle *tert*-butyl H).

^{13}C NMR (151 MHz, acetone-d_6) δ(ppm): 157.43, 157.27, 154.09, 153.11, 152.24, 151.69, 150.45, 149.13, 149.05, 145.48, 145.36, 140.37, 139.82, 132.73, 132.64, 131.92, 131.56, 131.49, 125.39, 125.11, 116.17, 116.11, 114.53, 114.00, 105.73, 80.24, 71.35, 70.20, 68.54, 68.23, 64.85, 63.96, 63.93, 63.42, 50.96, 48.57, 34.91, 34.90, 31.78, 31.75, 31.71, 30.35, 23.34, 14.36, -12.87.

HRMS (ESI +ve) m/z: 2178.7774 ($[M]^{\bullet+}$, $C_{117}H_{137}O_8N_9TeI_2$ requires 2178.7752).

Tridentate Mixed XB/ChB [2]Rotaxane (2.11·XB$_2$ChB^{Ph})

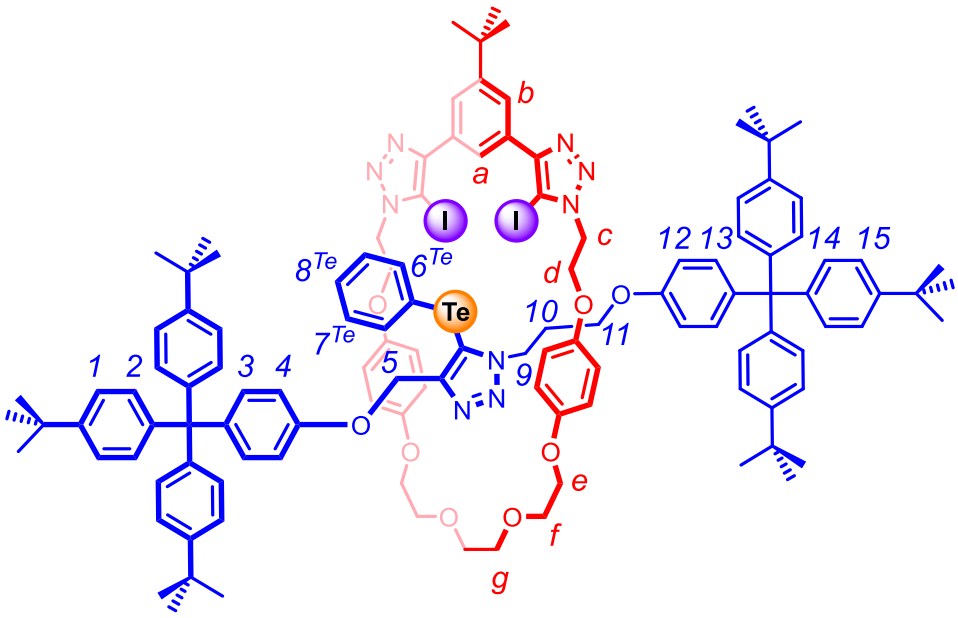

Following the general procedure for CuAAC-AMT synthesis of [2]rotaxanes between macrocycle **2.1·I** (10 mg, 0.011 mmol, 1 equiv), stopper azide **2.10** (32 mg, 0.055 mmol, 5 equiv) and stopper alkyne **2.8·Te^{Ph}** (41 mg, 0.055 mmol, 5 equiv), the product was purified by preparative TLC (10% EtOAc in CH_2Cl_2) to give the target tridentate [2]rotaxane **2.11·XB$_2$ChB^{Ph}** as white powder (4.9 mg, 20%).

^{1}H NMR (600 MHz, acetone-d_6) δ (ppm): 8.26 (t, J = 1.6 Hz, 1H; *a*), 8.00 (d, J = 1.6 Hz, 2H; *b*), 7.35 (d, J = 7.5 Hz, 2H; 7^{Te}), 7.34 – 7.29 (m, 12H; *2, 14*), 7.14 – 7.10 (m, 13H; *1, 15, 8Te*), 7.04 (d, J = 7.5 Hz, 2H; *6Te*), 7.02 (d, J = 8.9 Hz, 4H; *3*), 6.94 (d, J = 8.9 Hz, 2H; *13*), 6.76 (d, J = 8.9 Hz, 2H; *4*), 6.49 (d, J = 8.9 Hz, 4H; *hydroquinone ArH*), 6.40 (d, J = 8.9 Hz, 4H; *hydroquinone ArH*), 6.32 (d, J = 8.9 Hz, 4H; *10*), 4.99 (s, 2H; *5*), 4.88 (t, J = 4.9 Hz, 4H; *c*), 4.42 – 4.29 (m, 4H; *d*), 4.22 (t, J = 6.5 Hz, 2H; *9*), 3.86 – 3.79 (m, 4H; *e*), 3.59 (t, J = 5.0 Hz, 4H; *f*), 3.54 – 3.48 (m, 4H; *g*), 3.38 (t, J = 6.5 Hz, 2H; *11*), 1.77 (q, J = 6.5 Hz, 2H; *10*), 1.41 (s, 9H; *macrocycle tert*-butyl *H*), 1.31 (s, 54H; axle *tert*-butyl *H*).

^{13}C NMR (151 MHz, acetone-d_6) δ(ppm): 157.37, 157.27, 154.13, 153.10, 152.23, 150.40, 149.11, 149.04, 145.48, 145.36, 140.33, 139.87, 137.46, 132.69, 132.61, 131.85, 131.54, 131.49, 130.54, 128.94, 125.36, 125.11, 125.10, 116.26, 116.23, 115.17, 114.46, 114.09, 108.19, 80.19, 71.33, 70.16, 68.56, 68.25, 65.02, 63.94, 63.10, 50.92, 48.81, 35.72, 34.91, 34.89, 31.77, 31.74, 31.71, 23.33, 14.35, 1.40.

HRMS (ESI +ve) m/z: 2240.7954 ($[M]^{\cdot+}$, $C_{122}H_{139}O_8N_9TeI_2$ requires 2240.7909).

Tridentate Mixed XB/ChB [2]Rotaxane (2.11·XB$_2$ChB^{pCF3})

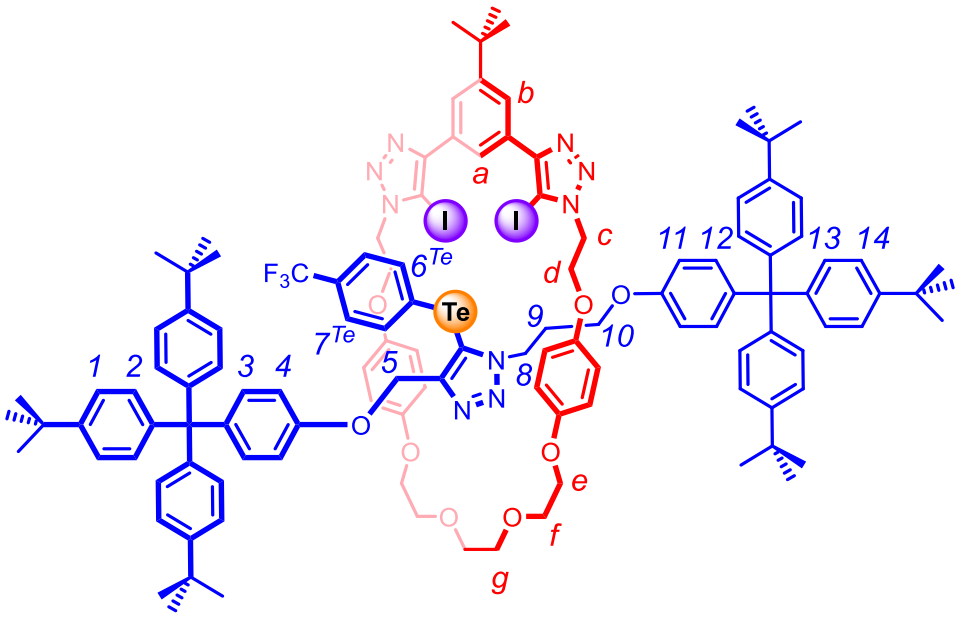

Following the general procedure for CuAAC-AMT synthesis of [2]rotaxanes between macrocycle **2.1·I** (10 mg, 0.011 mmol, 1 equiv), stopper azide **2.10** (32 mg, 0.055 mmol, 5 equiv) and stopper alkyne **2.8·Te^{pCF3}** (45 mg, 0.055 mmol, 5 equiv), the product was purified by preparative TLC (6% EtOAc in CH_2Cl_2) to give the target tridentate [2]rotaxane **2.11·XB$_2$ChB^{pCF3}** as white powder (3.3 mg, 13%).

^{1}H NMR (600 MHz, acetone-d_6) δ (ppm): 8.29 (t, J = 1.6 Hz, 1H; *a*), 8.00 (d, J = 1.6 Hz, 2H; *b*), 7.47 – 7.40 (m, 2H; *7Te*), 7.35 – 7.33 (m, 2H; *6Te*), 7.33 – 7.28 (m, 12H; *2, 13*), 7.15 – 7.08 (m, 12H; *1, 14*), 7.03 (d, J = 8.2 Hz, 2H; *3*), 6.97 (s, 2H), 6.47 (d, J = 9.1 Hz, 4H; *hydroquinone ArH*), 6.38 (d, J = 9.1 Hz, 4H; *hydroquinone ArH*), 4.99 – 4.92 (brs, 2H; *5*), 4.89 (t, J = 4.8 Hz, 4H; *c*), 4.38 – 4.31 (m, 4H; *d*), 4.24 – 4.14 (m, 2H; *8*), 3.84 – 3.77 (m, 4H; *e*), 3.58 (t, J = 5.2 Hz, 5H; *f*), 3.51 (s, 4H; *g*), 3.43 – 3.36 (m, 2H; *10*), 1.62 – 1.55 (m, 2H; *9*), 1.40 (s, 9H; *macrocycle ^{t}Bu H*), 1.30 (s, 54H; *axle ^{t}Bu H*).

^{13}C NMR (151 MHz, acetone-d_6) δ (ppm): 157.29, 154.11, 153.09, 152.70, 152.29, 150.36, 149.12, 149.05, 145.46, 145.34, 136.75, 132.68, 132.65, 131.85, 131.52, 131.47, 126.74 (q, $^4J_{C-F}$ = 4.0 Hz), 125.31, 125.11, 125.09, 116.19, 116.15, 114.39, 114.13, 80.44, 76.07, 71.32, 70.15, 68.51, 68.27, 65.02, 63.94, 63.05, 50.97, 48.87, 46.76, 35.72, 34.90, 34.89, 32.65, 31.75, 31.73, 31.70, 30.35, 23.34, 14.35, 12.29, 1.41 (signal of CF_3 missing due to poor signal-to-noise ratio).

^{19}F NMR (377 MHz, acetone-d_6) δ (ppm): −63.02.

HRMS (ESI +ve) m/z: 2308.7802 ($[M+H]^+$, $C_{123}H_{139}O_8N_9TeI_2F_3$ requires 2308.7827).

Tridentate All-HB [2]Rotaxane (2.11·HB3)

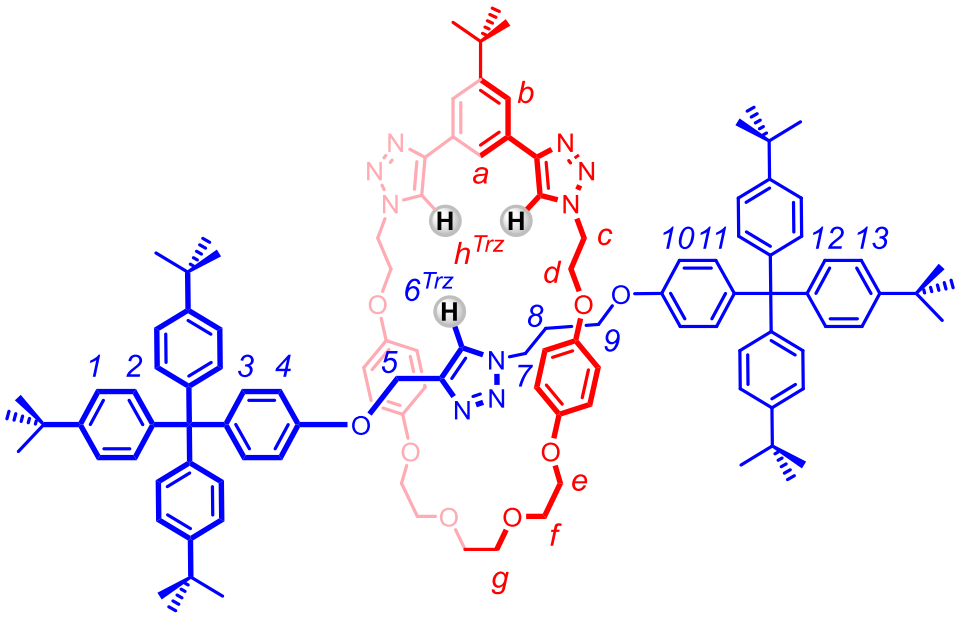

Following the general procedure for CuAAC-AMT synthesis of [2]rotaxanes between macrocycle **2.1·H** (10 mg, 0.015 mmol, 1 equiv), stopper azide **2.10** (45 mg, 0.076 mmol, 5 equiv) and stopper alkyne **2.7·H** (41 mg, 0.076 mmol, 5 equiv), the product was purified by preparative TLC (25% EtOAc in CH_2Cl_2) to give the target tridentate [2]rotaxane **2.11·HB3** as white powder (5.0 mg, 18%).

^{1}H NMR (400 MHz, acetone-d_6) δ (ppm): 8.30 (s, 2H; H^{Trz}), 8.03 (d, J = 1.6 Hz, 2H; *b*), 7.95 (t, J = 1.6 Hz, 1H; *a*), 7.47 (s, 1H; 6^{Trz}), 7.36 – 7.23 (m, 12H; *2, 12*), 7.16 – 7.07 (m, 12H; *1, 13*), 7.06 – 7.00 (m, 4H; *3, 11*), 6.80 (d, J = 8.9 Hz, 2H; *4*), 6.59 – 6.46 (m, 10H; *10, hydroquinone ArH*), 4.85 (s, 2H; *5*), 4.71 (t, J = 4.8 Hz, 4H; *c*), 4.30 (t, J = 4.8 Hz, 4H; *d*), 3.93 (t, J = 6.5 Hz, 2H; *7*), 3.90 – 3.85 (m, 4H; *e*), 3.62 (t, J = 4.6 Hz, 4H; *f*), 3.54 (s, 4H; *g*), 3.48 (t, J = 6.5 Hz, 2H; *9*), 1.36 (s, 9H; *macrocycle ^{t}Bu H*), 1.30 (s, 54H; *axle ^{t}Bu H*).

^{13}C NMR (151 MHz, acetone-d_6) δ (ppm): 157.41, 157.27, 154.27, 153.02, 152.97, 149.12, 149.10, 148.11, 145.36, 145.28, 144.01, 140.53, 140.30, 132.78, 132.69, 132.56, 131.43,

125.11, 125.09, 124.87, 122.84, 122.24, 121.36, 116.70, 116.22, 114.33, 114.09, 71.44, 70.27, 68.77, 68.07, 64.95, 63.93, 61.93, 50.42, 47.39, 35.53, 34.89, 31.75, 31.70, 31.69, 23.34, 14.36, 1.42.

HRMS (ESI +ve) m/z: 1786.0609 ($[M+H]^+$, $C_{116}H_{138}O_8N_9$ requires 1786.0696).

Tetradentate All-ChB [2]Rotaxane (2.12·ChB$_4$)

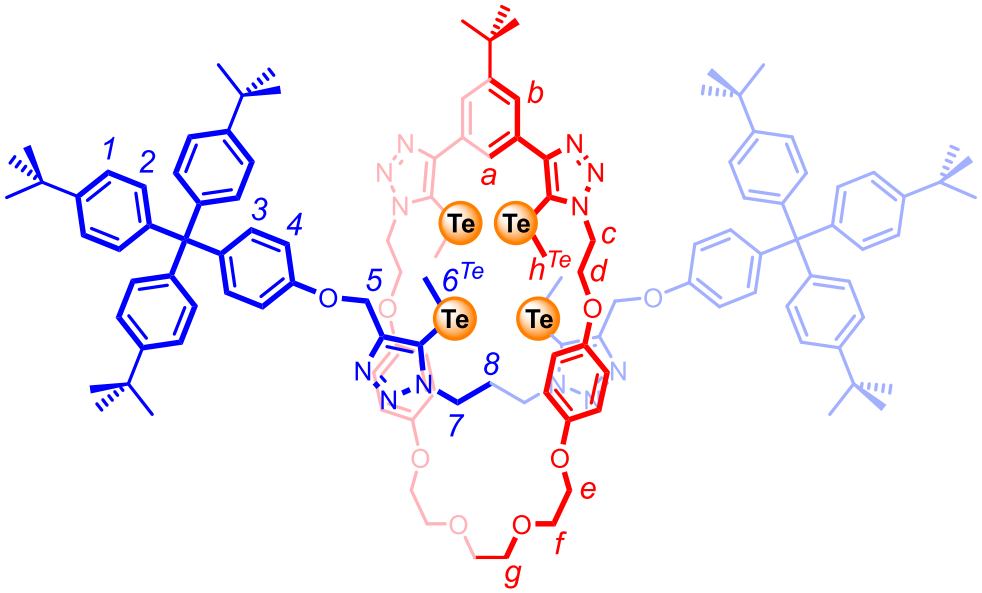

Following the general procedure for CuAAC-AMT synthesis of [2]rotaxanes between macrocycle **2.1·Te^{Me}** (10 mg, 0.011 mmol, 1 equiv), stopper azide **2.9·Te^{Me}** (43 mg, 0.053 mmol, 5 equiv) and stopper alkyne **2.8·Te^{Me}** (36 mg, 0.053 mmol, 5 equiv), the product was purified by preparative TLC (acetone/EtOAc/CH_2Cl_2 2:20:78) to give the target tetradentate [2]rotaxane **2.12·ChB$_4$** as white powder (4.7 mg, 18%).

^{1}H NMR (600 MHz, acetone-d_6) δ (ppm): 8.62 (t, J = 1.6 Hz, 1H; *a*), 8.06 (d, J = 1.6 Hz, 2H; *b*), 7.30 (d, J = 8.6 Hz, 12H; *2*), 7.14 (d, J = 8.6 Hz, 12H; *1*), 7.10 (d, J = 8.9 Hz, 4H; *3*), 6.87 (d, J = 8.9 Hz, 4H; *4*), 6.45 (d, J = 9.1 Hz, 4H; *hydroquinone ArH*), 6.29 (d, J = 9.1 Hz, 4H; *hydroquinone ArH*), 5.01 (t, J = 4.6 Hz, 4H; *c*), 4.97 (s, 4H; *5*), 4.31 – 4.25 (m, 8H; *d, 7*), 3.86 (t, J = 4.8 Hz, 4H; *e*), 3.64 (t, J = 4.8 Hz, 4H; *f*), 3.59 (s, 4H; *g*), 2.01 (s, 6H; h^{Te}), 1.65 (s, 6H; 6^{Te}), 1.43 (s, 9H; *macrocycle tert*-butyl *H*), 1.30 (s, 54H; *axle tert*-butyl *H H*).

^{13}C NMR (151 MHz, acetone-d_6) δ (ppm): 157.40, 153.95, 153.35, 152.83, 151.96, 151.70, 149.10, 145.38, 140.35, 132.91, 132.75, 132.71, 131.47, 125.40, 125.09, 115.98,

115.73, 114.52, 105.75, 103.51, 71.28, 70.21, 68.64, 68.32, 63.96, 63.32, 51.34, 48.82, 34.89, 31.78, 31.71, 23.34, 14.36, -12.61, -12.69.

HRMS (ESI +ve) m/z: 2435.7847 ($[M]^{\cdot+}$, $C_{123}H_{148}N_{12}O_8Te_4$ requires 2435.7773).

Tetradentate Mixed XB/ChB [2]Rotaxane (2.12·XB$_2$ChB$_2$)

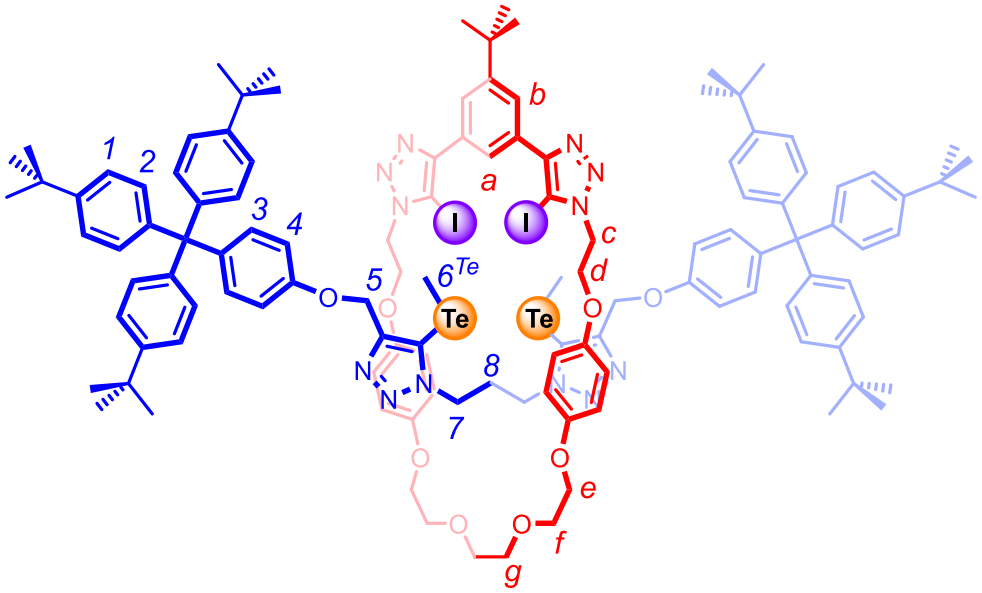

Following the general procedure for CuAAC-AMT synthesis of [2]rotaxanes between macrocycle **2.1·I** (10 mg, 0.011 mmol, 1 equiv), stopper azide **2.9·Te^{Me}** (45 mg, 0.055 mmol, 5 equiv) and stopper alkyne **2.8·Te^{Me}** (38 mg, 0.055 mmol, 5 equiv), the product was purified by preparative TLC (30% EtOAc in CH_2Cl_2) to give the target tetradentate [2]rotaxane **2.12·XB$_2$ChB$_2$** as white powder (2.6 mg, 10%).

^{1}H NMR (400 MHz, acetone-*d*$_6$) δ (ppm): 8.34 (t, *J* = 1.6 Hz, 1H; *a*), 8.01 (d, *J* = 1.6 Hz, 2H; *b*), 7.30 (d, *J* = 8.6 Hz, 12H; *2*), 7.12 (d, *J* = 8.6 Hz, 12H; *1*), 7.08 (d, *J* = 8.9 Hz, 4H; *3*), 6.85 (d, *J* = 8.9 Hz, 4H; *4*), 6.45 (d, *J* = 9.1 Hz, 4H; *hydroquinone ArH*), 6.32 (d, *J* = 9.1 Hz, 4H; *hydroquinone ArH*), 5.00 (s, 4H; *5*), 4.88 (t, *J* = 4.8 Hz, 4H; *c*), 4.31 (t, *J* = 4.8 Hz, 4H; *d*), 4.25 (t, *J* = 7.4 Hz, 4H; *7*), 3.87 (t, *J* = 4.9 Hz, 4H; *e*), 3.65 (t, *J* = 4.9 Hz, 4H; *f*), 3.61 (s, 4H; *g*), 1.69 (s, 6H; *6Te*), 1.43 (s, 9H; *macrocycle tert*-butyl *H*), 1.30 (s, 54H; axle *tert*-butyl *H*). (Proton signal *8* missing due to signal overlapping).

^{13}C NMR (151 MHz, acetone-*d*$_6$) δ (ppm): 157.38, 153.96, 152.90, 152.38, 151.98, 150.45, 149.12, 145.34, 140.42, 132.77, 131.49, 131.47, 125.10, 115.97, 115.91, 114.53,

105.66, 80.68, 71.33, 70.27, 68.33, 68.03, 63.95, 63.33, 50.96, 48.76, 35.77, 34.89, 32.65, 31.71, 23.34, 14.35, 1.41, -12.67.

HRMS (ESI +ve) m/z: 2403.7405 ($[M]^{\cdot+}$, $C_{121}H_{142}I_2N_{12}O_8Te_2$ requires 2403.7298).

Tetradentate Mixed XB/ChB [2]Rotaxane (2.12·XB$_3$ChB)

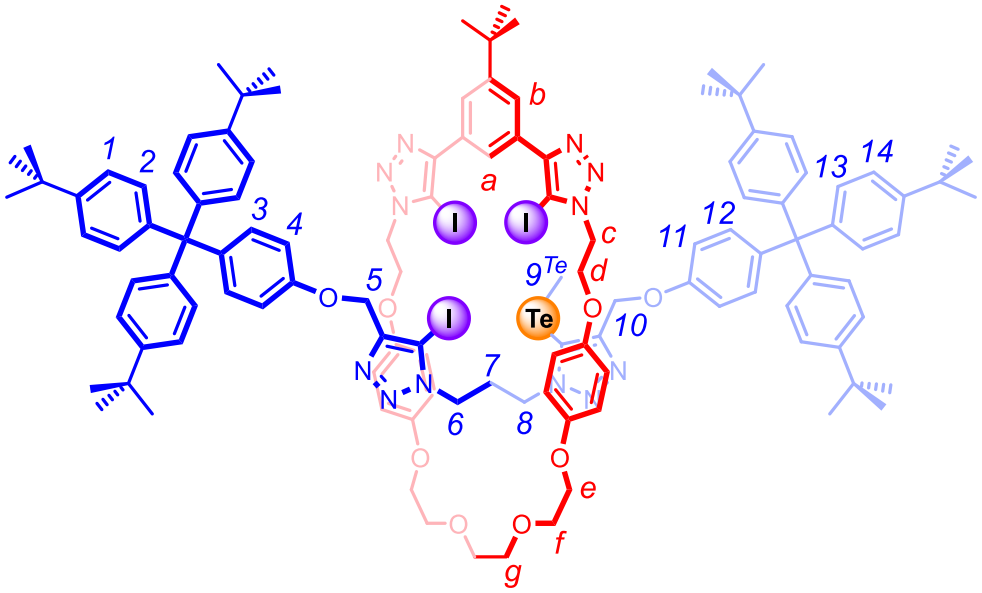

Following the general procedure for CuAAC-AMT synthesis of [2]rotaxanes between macrocycle **2.1·I** (10 mg, 0.011 mmol, 1 equiv), stopper azide **2.9·I** (44 mg, 0.055 mmol, 5 equiv) and stopper alkyne **2.8·Te^{Me}** (38 mg, 0.055 mmol, 5 equiv), the product was purified by preparative TLC (acetone/EtOAc/CH_2Cl_2 2:20:78) to give the target tetradentate [2]rotaxane **2.12·XB$_3$ChB** as white powder (4.5 mg, 17%).

^{1}H NMR (600 MHz, acetone-d_6) δ (ppm): 8.37 (t, J = 1.6 Hz, 1H; *a*), 8.01 (d, J = 1.6 Hz, 2H; *b*), 7.30 (d, J = 8.6 Hz, 12H; *2, 13*), 7.12 (d, J = 8.6 Hz, 12H; *1, 14*), 7.10 – 7.06 (m, 4H; *3, 12*), 6.90 – 6.83 (m, 4H; *4, 11*), 6.46 (d, J = 9.1 Hz, 4H; *hydroquinone ArH*), 6.37 (d, J = 9.1 Hz, 4H; *hydroquinone ArH*), 5.00 (s, 2H; *5*), 4.88 (t, J = 4.7 Hz, 4H; *c*), 4.86 (s, 2H; *10*), 4.32 (t, J = 4.7 Hz, 4H; *d*), 4.22 (t, J = 7.3 Hz, 2H; *6*), 4.03 (t, J = 7.3 Hz, 2H; *8*), 3.88 (t, J = 4.7 Hz, 4H; *e*), 3.65 (t, J = 4.7 Hz, 4H; *f*), 3.59 (s, 4H; *g*), 1.65 (s, 3H; *9Te*), 1.43 (s, 9H; *macrocycle ^{t}Bu H*), 1.30 (s, 54H; *axle ^{t}Bu H*).

^{13}C NMR (151 MHz, acetone-d_6) δ (ppm): 157.40, 157.33, 153.96, 152.95, 152.36, 151.96, 150.51, 149.13, 147.97, 145.33, 145.31, 140.59, 140.43, 132.79, 131.96, 131.49, 125.51, 125.42, 125.10, 116.00, 115.97, 114.56, 114.53, 105.69, 82.88, 80.58, 71.36, 70.28,

68.38, 68.03, 63.95, 63.34, 62.14, 50.98, 48.55, 48.35, 35.75, 34.89, 31.78, 31.71, 30.73, 30.47, 23.34, 14.36, 1.41, -12.75 (peaks missing due to signal overlapping).

HRMS (ESI +ve) m/z: 2388.7104 ($[M+H]^+$, $C_{120}H_{140}I_3N_{12}O_8Te$ requires 2388.7141).

Tetradentate Mixed XB/ChB [2]Rotaxane (2.12·ChB$_3$XB)

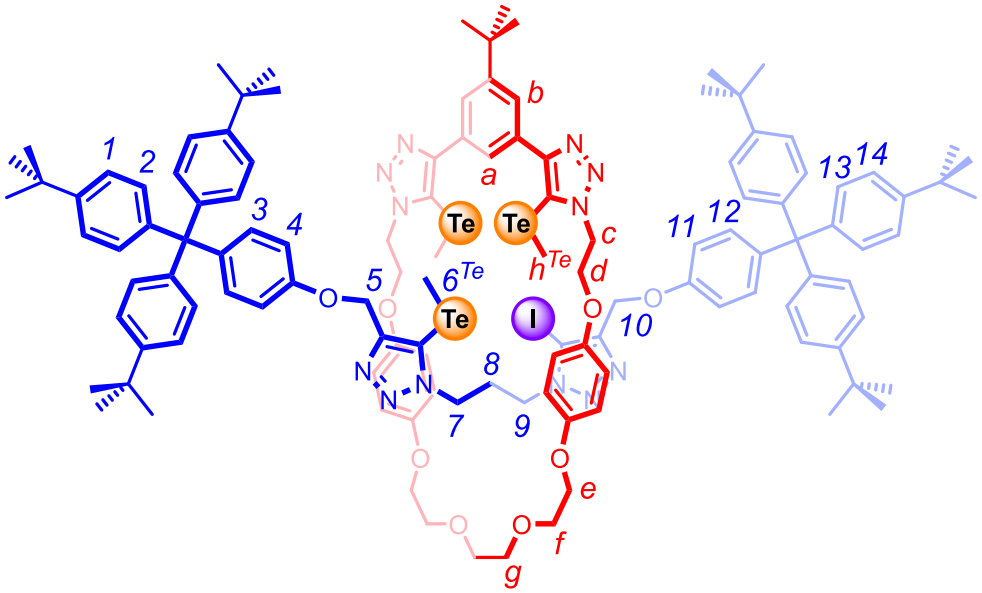

Following the general procedure for CuAAC-AMT synthesis of [2]rotaxanes between macrocycle **2.1·Te^{Me}** (10 mg, 0.011 mmol, 1 equiv), stopper azide **2.9·I** (42 mg, 0.053 mmol, 5 equiv) and stopper alkyne **2.8·Te^{Me}** (36 mg, 0.053 mmol, 5 equiv), the product was purified by preparative TLC (acetone/EtOAc/CH_2Cl_2 2:20:78) to give the target tetradentate [2]rotaxane **4·ChB$_3$XB** as white powder (5.9 mg, 23%).

^{1}H NMR (600 MHz, acetone-d_6) δ (ppm): 8.62 (d, J = 1.6 Hz, 1H; *a*), 8.07 (d, J = 1.6 Hz, 2H; *b*), 7.33 – 7.27 (m, 12H; *2, 13*), 7.16 – 7.12 (m, 12H; *1, 14*), 7.12 – 7.09 (m, 4H; *3, 12*), 6.92 – 6.87 (m, 4H; *4, 11*), 6.44 (d, J = 8.8 Hz, 4H; *hydroquinone ArH*), 6.33 (d, J = 8.8 Hz, 4H; *hydroquinone ArH*), 5.00 (t, J = 4.8 Hz, 4H; *c*), 4.98 (s, 2H; *10*), 4.87 (s, 2H; *5*), 4.28 (t, J = 4.8 Hz, 4H; *d*), 4.23 (t, J = 7.4 Hz, 2H; *9*), 4.03 (t, J = 7.4 Hz, 2H; *7*), 3.88 (d, J = 4.1 Hz, 4H; *e*), 3.65 (t, J = 4.1 Hz, 4H; *f*), 3.60 (s, 4H; *g*), 2.00 (s, 6H; h^{Te}), 1.61 (s, 3H; 6^{Te}), 1.43 (s, 9H; *macrocycle ^{t}Bu H*), 1.30 (s, 54H; *axle ^{t}Bu H*).

^{13}C NMR (151 MHz, acetone-d_6) δ (ppm): 157.42, 157.36, 153.95, 153.39, 152.87, 151.95, 151.73, 149.13, 149.11, 147.94, 145.36, 145.32, 140.57, 140.39, 132.94, 132.75, 132.73, 131.47, 126.05, 125.46, 125.09, 115.99, 115.77, 114.54, 114.52, 105.73, 103.47,

82.93, 71.33, 70.25, 68.62, 68.37, 63.96, 63.34, 62.16, 51.35, 48.61, 48.39, 35.70, 34.88, 31.79, 31.70, 30.35, 23.34, 14.36, -12.60, -12.74 (peaks missing due to signal overlapping).

HRMS (ESI +ve) m/z: 2417.7587 ($[M]^{\bullet+}$, $C_{122}H_{145}IN_{12}O_8Te_3$ requires 2417.7521).

6.2.3 Synthetic Procedures and Characterisations of Novel Compounds from Chapter 3

XB Strapped Porphyrin (3.1a·H_2)

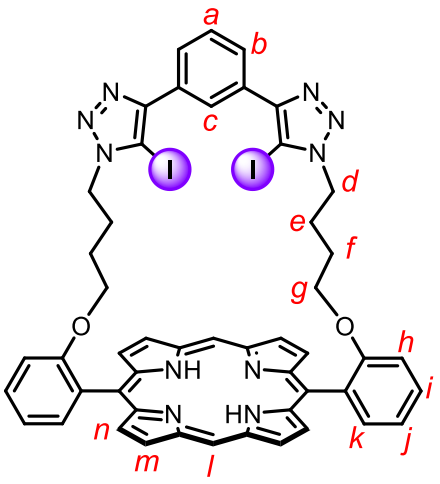

General Procedure for Porphyrin Formation by Pyrrole-Aldehyde Condensation

Dialdehyde **3.5a** (400 mg, 0.49 mmol, 1 equiv) and dipyrromethane (143 mg, 0.98 mmol, 2 equiv) were dissolved in dry and degassed CH_2Cl_2 (100 mL). Trifluoroacetic acid (TFA) (28 μL, 0.30 mmol, 0.6 equiv) was added and the reaction mixture was stirred at room temperature under N_2 overnight. DDQ (167 mg, 0.74 mmol, 1.5 equiv) was added and the mixture was stirred at room temperature overnight. Et_3N (69 μL, 0.49 mmol, 1 equiv) was added and the crude was filtered thorugh filter paper to remove black polymeric side products. The filtrate was washed with saturated aqueous $NaHCO_3$ (50 mL × 3), dried over anhydrous $MgSO_4$, filtered and concentrated *in vacuo*. Further purification with silica gel column chromatography (10% EtOAc in CH_2Cl_2) gave the product **3.1a·H_2** as purple powder (240 mg, 43%).

^{1}H NMR (500 MHz, $CDCl_3$) δ(ppm): 10.04 (s, 2H; *l*), 9.22 (d, J = 4.5 Hz, 4H; *m*), 8.97 (d, J = 4.5 Hz, 4H; *n*), 7.90 (dd, J = 7.7, 1.7 Hz, 2H; *b*), 7.77 (ddd, J = 8.8, 7.3, 1.7 Hz, 2H; *i*), 7.62 (dd, J = 7.3, 1.7 Hz, 2H; *k*), 7.51 (t, J = 7.7 Hz, 1H; *a*), 7.45 (d, J = 8.8 Hz,

2H; *h*), 7.29 (t, *J* = 7.3 Hz, 2H; *j*), 7.17 (t, *J* = 1.7 Hz, 1H; *c*), 4.27 (t, *J* = 5.9 Hz, 4H; *d*), 4.05 (t, *J* = 7.2 Hz, 4H; *g*), 1.72 (q, *J* = 7.2Hz, 4H; *f*), 1.48 (q, *J* = 5.9Hz, 4H; *e*), –3.09 (s, 2H; *pyrrole NH*).

^{13}C NMR (126 MHz, $CDCl_3$) δ (ppm): 157.76, 149.08, 147.60, 145.15, 137.67, 131.66, 131.30, 130.12, 130.01, 129.95, 129.53, 127.78, 124.05, 119.91, 115.74, 111.74, 104.97, 67.80, 50.24, 29.85, 26.52, 25.30.

HRMS (ESI +ve) m/z: 1067.14824 ($[M+H]^+$, $C_{50}H_{41}O_2N_{10}I_2$ requires 1067.14978).

XB Strapped Porphyrin (3.1b·H$_2$)

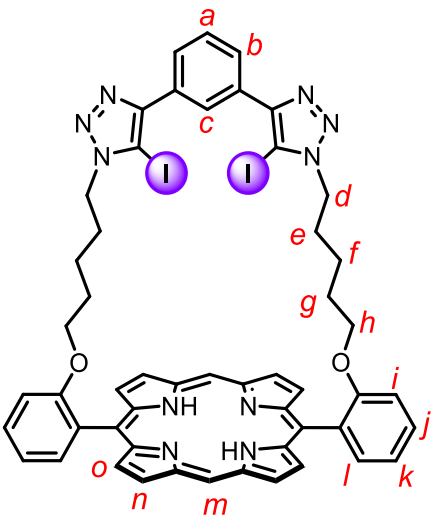

Following the general procedure for porphyrin formation by pyrrole-aldehyde condensation reaction between bis-aldehyde **3.5b** (500 mg, 0.59 mmol, 1 equiv) and dipyrromethene (173 mg, 1.18 mmol, 2 equiv), purification by silica gel column chromatography (10% EtOAc in CH_2Cl_2) afforded strapped porphyrin **3.1b·H$_2$** as purple powder (136 mg, 21%).

^{1}H NMR (500 MHz, $CDCl_3$) δ (ppm): 10.21 (s, 2H; *m*), 9.33 (d, J = 4.5 Hz, 4H; *n*), 9.02 (d, J = 4.5 Hz, 4H; *o*), 7.78 (m, 4H; *b*, j), 7.71 (dd, J = 7.6, 1.8 Hz, 2H; *l*), 7.42 (d, J = 7.7 Hz, 2H; *i*), 7.40 (d, J = 7.2 Hz, 1H; *a*), 7.32 (t, J = 7.4 Hz, 2H; *k*), 7.29 (d, J = 1.9 Hz, 1H; *c*), 4.06 (t, J = 6.9 Hz, 4H; *d*), 3.90 (t, J = 6.5 Hz, 4H; *h*), 1.50 (p, J = 6.5 Hz, 4H; *g*), 1.33 (p, J = 6.9 Hz, 4H; *e*), 0.87 (p, J = 7.8 Hz, 4H; *f*), −3.11 (s, 2H; *pyrrole NH*).

^{13}C NMR (126 MHz, $CDCl_3$) δ (ppm): 158.06, 149.18, 147.61, 145.18, 136.87, 131.58, 131.30, 130.37, 130.08, 130.00, 129.42, 127.91, 125.09, 119.71, 115.87, 112.12, 104.92, 68.06, 50.03, 29.86, 29.30, 28.10, 22.73.

HRMS (ESI +ve) m/z: 1095.17706 ([M+H]$^+$, $C_{52}H_{45}O_2N_{10}I_2$ requires 1095.18108).

XB Strapped Zinc(II) Metalloporphyrin (3.1a·Zn)

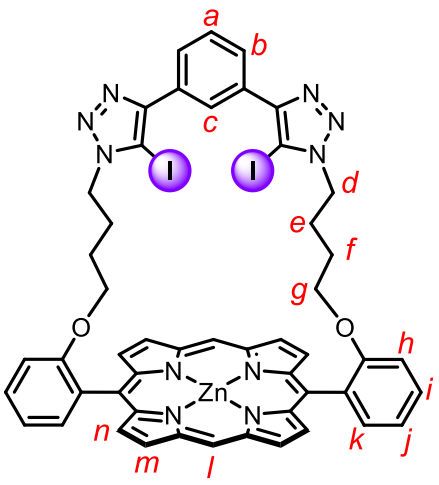

General Procedure for Porphyrin Metalation Reaction

Free-base porphyrin **3.1a·H₂** (130 mg, 0.12 mmol, 1 equiv) was dissolved in 1:1 $CHCl_3$:CH_3OH (20 mL). $Zn(CH_3COO)_2$•$2H_2O$ (112 mg, 0.61 mmol, 5 equiv) was added and the reaction mixture was stirred at room temperature overnight. The organic solvent was removed *in vacuo* and the solid residue was redissolved in CH_2Cl_2 (50 mL) and washed with H_2O (30 mL × 3). The combined organic layer was dried over anhydrous $MgSO_4$, filtered and concentrated on rotary evaporator to give the product **3.1a·Zn** as shiny purple-red powder (138 mg, quant.).

^{1}H NMR (500 MHz, $CDCl_3$) δ (ppm): 10.01 (s, 2H; *l*), 9.24 (d, J = 4.5 Hz, 4H; *m*), 9.03 (d, J = 4.5 Hz, 4H; *n*), 7.98 (dd, J = 7.7, 1.7 Hz, 2H; *b*), 7.78 (ddd, J = 8.8, 7.3, 1.7 Hz, 2H; *i*), 7.67 (dd, J = 7.3, 1.7 Hz, 2H; *k*), 7.60 (t, J = 7.7 Hz, 1H; *a*), 7.46 (d, J = 8.8 Hz, 2H; *h*), 7.31 (t, J = 1.7 Hz, 1H, *c*), 7.29 (t, J = 7.3 Hz, 2H; *j*), 4.23 (t, J = 5.9 Hz, 4H; *d*), 4.05 (t, J = 7.2 Hz, 4H; *g*), 1.70 (m, 4H; *e*), 1.49 (m, 4H; *f*).

^{13}C NMR (126 MHz, $CDCl_3$) δ (ppm): 157.83, 150.53, 149.50, 149.23, 137.42, 132.63, 131.92, 131.38, 130.33, 129.76, 129.63, 127.88, 124.80, 119.71, 116.63, 111.68, 106.05, 67.81, 50.24, 29.86, 26.75, 25.37.

HRMS (ESI +ve) m/z: 1151.04192 ([M+Na]$^+$, $C_{50}H_{38}O_2N_{10}I_2NaZn$ requires 1151.04522).

XB Strapped Zinc(II) Metalloporphyrin (3.1b·Zn)

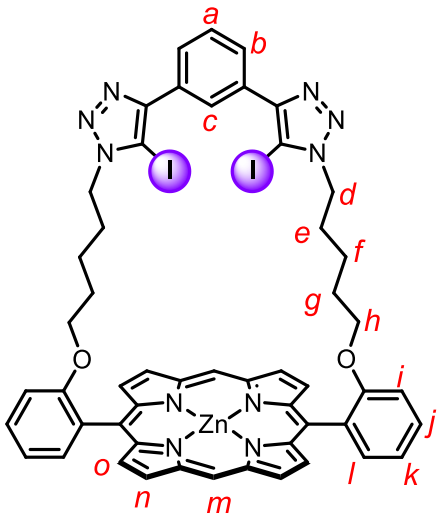

Following the general procedure for porphyrin metalation reaction between free base porphyrin **3.1b·H₂** (132 mg, 0.12 mmol, 1 equiv) and $Zn(CH_3COO)_2{\cdot}2H_2O$ (111 mg, 0.60 mmol, 5 equiv), aqueous work-up afforded the product **3.1b·Zn** as purple powder (140 mg, quant.).

^{1}H NMR (500 MHz, $CDCl_3$) δ (ppm): 10.16 (s, 2H; *m*), 9.35 (d, J = 4.4 Hz, 4H; *n*), 9.04 (d, J = 4.4 Hz, 4H; *o*), 7.84 (dd, J = 7.2, 1.7 Hz, 2H; *b*), 7.76 (ddd, J = 9.1, 7.6, 1.8 Hz, 2H; *j*), 7.46 (dd, J = 8.0, 1.7 Hz, 2H; *l*), 7.42 – 7.37 (m, 3H; *a, i*), 7.31 (td, J = 7.4, 1.1 Hz, 2H; *k*), 6.95 (t, J = 1.6 Hz, 1H; *c*), 4.01 (t, J = 6.3 Hz, 4H; *d*), 3.91 (t, J = 6.7 Hz, 4H; *h*), 1.50 (p, J = 6.7 Hz, 2H; *g*), 1.30 – 1.26 (m, 4H; *e*), 0.80 (p, J = 7.7 Hz, 4H; *f*).

^{13}C NMR (126 MHz, $CDCl_3$) δ (ppm): 158.21, 150.45, 149.48, 149.40, 136.75, 132.36, 131.98, 131.74, 129.74, 129.60, 129.30, 128.07, 126.02, 119.54, 116.44, 112.09, 105.96, 67.98, 50.14, 29.86, 28.99, 28.07, 22.31.

HRMS (ESI +ve) m/z: 1157.09234 ([M+H]$^+$, $C_{52}H_{43}O_2N_{10}I_2Zn$ requires 1157.09458).

Benzaldehyde-appended XB Bis(iodo-triazole)benzene (3.5a)

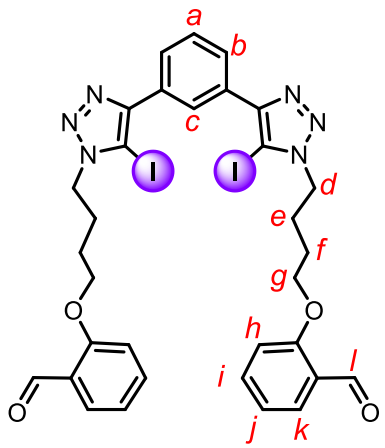

General Procedure for CuAAC Click Reaction

$[Cu(CH_3CN)_4]PF_6$ (99 mg, 0.26 mmol, 0.2 equiv) and TBTA (140 mg, 0.26 mmol, 0.2 equiv) were added to dry and degassed THF (7 mL) and the mixture was stirred at room temperature for 20 minutes until all solid dissolved, upon which a pale yellow solution was obtained. A solution of azide **3.4a** (870 mg, 3.97 mmol, 3 equiv) in dry and degassed THF (2 mL) was added, followed by a slow addition of bis(iodoalkyne) **3.2** (500 mg, 1.32 mmol, 1 equiv) in dry and degassed THF (2 mL). The reaction mixture turned green immediately upon the addition of **3.2** and was allowed to stir at room temperature under N_2 in dark for 3 days. The crude mixture was diluted with $CHCl_3$ (50 mL) and washed with basic EDTA (20 mL x 2) and brine (20 mL). The solvent was removed *in vacuo* and further purification with silica gel column chromatography (neat CH_2Cl_2 gradient to 20% EtOAc in CH_2Cl_2) gave the product **3.5a** as white foam (1.01 g, 93%).

^{1}H NMR (400 MHz, $CDCl_3$) δ (ppm): 10.52 (d, J = 0.8 Hz, 2H; *l*), 8.55 (t, J = 1.8 Hz, 1H; *c*), 7.99 (dd, J = 7.8, 1.8 Hz, 2H; *b*), 7.83 (dd, J = 7.6, 1.9 Hz, 2H; *k*), 7.58 (t, J =

7.8 Hz, 1H; *a*), 7.53 (ddd, *J* = 8.4, 7.4, 1.9 Hz, 2H; *i*), 7.02 (t, *J* = 7.6 Hz, 2H; *j*), 6.97 (d, *J* = 8.4 Hz, 2H; *h*), 4.59 (t, *J* = 7.0 Hz, 4H; *d*), 4.15 (t, *J* = 6.0 Hz, 4H; *g*), 2.31 – 2.19 (q, *J* = 6.0 Hz, 4H; *f*), 2.04 – 1.92 (q, *J* = 7.0Hz, 4H; *e*).

^{13}C NMR (126 MHz, $CDCl_3$) δ (ppm): 189.82, 161.15, 149.71, 136.26, 130.60, 129.20, 128.62, 127.82, 125.99, 124.79, 120.97, 112.40, 76.65, 67.34, 50.57, 26.61, 26.09.

HRMS (ESI +ve) m/z: 817.04841 ($[M+H]^+$, $C_{32}H_{31}O_4N_6I_2$ requires 817.04907).

Benzaldehyde-appended XB Bis(iodo-triazole)benzene (3.5b)

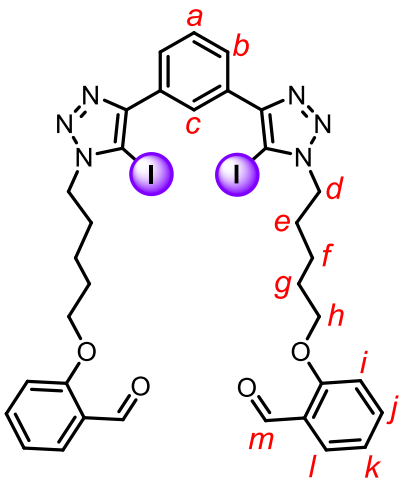

Following the general procedure for CuAAC click reaction between bis-iodoalkyne **3.2** (500 mg, 1.32 mmol, 1 equiv) and azide **3.4b** (981 mg, 3.97 mmol, 3 equiv), purification by silica gel column chromatography (20% EtOAc in CH_2Cl_2) afforded compound **3.5b** as white powder (0.85 g, 76%).

^{1}H NMR (400 MHz, $CDCl_3$) δ (ppm): 10.51 (d, J = 0.9 Hz, 2H; *m*), 8.55 (t, J = 1.8 Hz, 2H; *c*), 8.00 (dd, J = 7.8, 1.7 Hz, 2H; *b*), 7.83 (ddd, J = 7.7, 1.9, 0.9 Hz, 2H; *l*), 7.58 (t, J = 7.8 Hz, 2H; *a*), 7.53 (d, J = 7.9 Hz, 2H; *j*), 7.02 (td, J = 7.5, 1.0 Hz, 2H; *k*), 6.96 (d, J = 8.4 Hz, 2H; *i*), 4.51 (t, J = 7.2 Hz, 4H; *d*), 4.10 (t, J = 6.3 Hz, 4H; *h*), 2.09 (q, J = 7.2 Hz, 4H; *e*), 1.95 (q, J = 6.3 Hz, 4H; *g*), 1.64 (p, J = 8.2 Hz, 4H; *f*).

^{13}C NMR (126 MHz, $CDCl_3$) δ (ppm): 189.97, 161.38, 149.56, 136.20, 130.70, 129.11, 128.48, 127.76, 126.24, 124.84, 120.81, 112.49, 76.77, 68.03, 50.81, 29.72, 28.68, 23.21.

HRMS (ESI +ve) m/z: 845.07991 ($[M+H]^+$, $C_{34}H_{35}O_4N_6I_2$ requires 845.08037).

Terphenyl-Stoppered XB Strapped Porphyrin [2]Rotaxane (3.9·Zn)

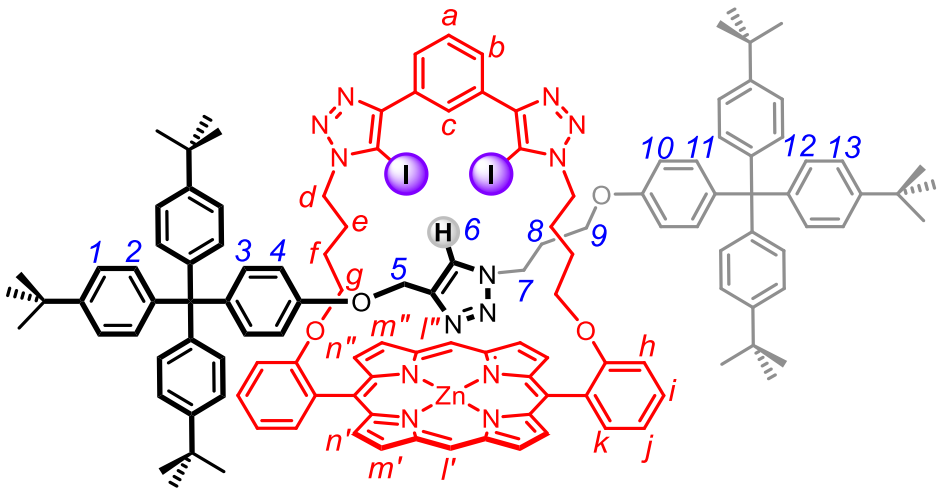

Following the general procedure for CuAAC-AMT synthesis of [2]rotaxanes, strapped porphyrin **3.1a·Zn** (10 mg, 0.009 mmol, 1 equiv) was reacted with terphenyl-stoppered azide **3.8** (26 mg, 0.044 mmol, 5 equiv) and terphenyl-stoppered alkyne **3.7** (24 mg, 0.044 mmol, 5 equiv), the product was purified by preparative TLC (2% EtOAc in CH_2Cl_2) to give the target [2]rotaxane **3.9·Zn** as shiny red powder (13 mg, 63%).

^{1}H NMR (400 MHz, acetone-d_6) δ (ppm): 10.03 (s, 1H; *l'*), 9.63 (s, 1H, *l''*), 9.18 (d, J = 4.5 Hz, 2H; *m'*), 8.97 (d, J = 4.5 Hz, 2H; *m''*), 8.84 (d, J = 4.3 Hz, 2H; *n'*), 8.78 (d, J = 4.3 Hz, 2H; *n''*), 7.96 (dd, J = 7.3, 1.7 Hz, 2H; *b*), 7.70 (d, J = 8.2 Hz, 2H; *i*), 7.62 (dd, J = 7.7, 1.8 Hz, 2H; *k*), 7.59 (t, J = 1.8 Hz, 1H; *c*), 7.49 – 7.40 (m, 12H; *2,12*), 7.36 (t, J = 7.3 Hz, 1H; *a*), 7.31 (d, J = 5.6 Hz, 2H; *h*), 7.30 – 7.24 (m, 14H; *1,13,j*), 7.13 (d, J = 8.7 Hz, 2H; *3*), 6.89 (d, J = 8.7 Hz, 2H; *11*), 6.43 (d, J = 8.6 Hz, 2H; *4*), 6.24 (s, 1H; 6^{Trz}), 5.22 (d, J = 8.6 Hz, 2H; *10*), 4.22 – 4.04 (m, 4H; *d*), 3.65 – 3.43 (m, 4H; *g*), 2.92 (t, J = 6.2 Hz, 2H; *7*), 2.55 (t, J = 5.2 Hz, 2H; *9*), 1.58 – 1.49 (m, 4H; *f*), 1.06 (p, J = 6.2 Hz, 2H; *8*), 0.76 – 0.55 (m, 4H; *e*). (Signal of proton *5* missing due to peaks overlap).

^{13}C NMR (126 MHz, $CDCl_3$) δ (ppm): 158.91, 156.26, 154.72, 150.15, 150.06, 149.57, 149.02, 148.83, 148.51, 148.49, 144.52, 144.47, 139.71, 139.40, 139.35, 137.19, 132.59,

132.25, 131.83, 131.77, 131.67, 131.42, 131.32, 130.94, 130.90, 130.19, 129.19, 128.87, 127.20, 126.30, 124.37, 124.34, 121.70, 119.71, 115.31, 113.42, 113.08, 112.99, 105.55, 68.77, 63.28, 63.26, 62.99, 56.85, 50.18, 45.51, 34.55, 34.52, 31.66, 31.62, 25.67.

HRMS (ESI +ve) m/z: 2260.8035 ($[M+H]^+$, $C_{130}H_{134}I_2N_{13}O_4Zn$ requires 2260.8088).

Stopper BODIPY Alkyne (3.12)

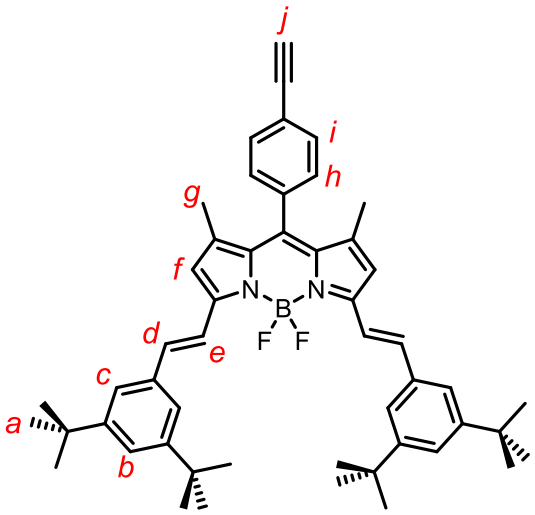

General Procedure for Knoevenagel Condensation

To a mixture of **3.11** (100 mg, 0.23 mmol, 1 equiv) in CH_3CN (10 mL), $MgSO_4$ (275 mg, 2.3 mmol, 10 equiv), 3,5-di-*tert*-butylbenzaldehyde (200 mg, 0.91 mmol, 4 equiv), pyrrolidine (163 mg, 2.3 mmol, 10 equiv) and glacial acetic acid (132 µL, 2.3 mmol, 10 equiv) were added. The reaction was immersed in an oil bath at 60 °C, upon which a colour change from orange to blue was observed, for 1 hour. The solvent was removed *in vacuo* and the crude dissolved in CH_2Cl_2 (10 mL) and washed with 0.05 M HCl (10 mL), saturated $NaHCO_3$ solution (10 mL) and brine (10 mL). The combined organics were dried over $MgSO_4$, filtered and the solvents removed *in vacuo*. Purification was achieved by column chromatography (CH_2Cl_2/*n*-hexane 3:2) to afford the product **3.12** as blue powder (58 mg, 30%).

^{1}H NMR (400 MHz, $CDCl_3$) δ (ppm): 7.77 (d, J = 16.3 Hz, 2H; *e*), 7.65 (d, J = 8.3 Hz; *i*), 7.45 (d, J = 1.8 Hz, 4H; *c*), 7.41 (t, J = 1.8 Hz, 2H; *b*), 7.35 (d, J = 8.3 Hz, 2H; *h*), 7.29 (d, J = 16.3 Hz, 2H; *d*), 6.65 (s, 2H; *f*), 3.19 (s, 1H; *j*), 1.48 (s, 6H; *g*), 1.37 (s, 36H; *a*).

^{13}C NMR (101 MHz, $CDCl_3$) δ (ppm): 153.03, 151.25, 141.84, 137.44, 136.01, 135.96, 133.02, 132.93, 128.83, 123.71, 122.93, 121.95, 118.98, 117.87, 83.10, 78.68, 35.01, 31.55, 22.82, 15.04.

^{19}F NMR (376 MHz, $CDCl_3$) δ (ppm): -138.56 (q, J = 32.1 Hz).

HRMS (ESI +ve) m/z: 748.4748 ($[M+H]^+$, $C_{51}H_{59}N_2B_1F_2$ requires 748.4752).

Azido-tetrafluorophenyl-appended BODIPY (3.13)

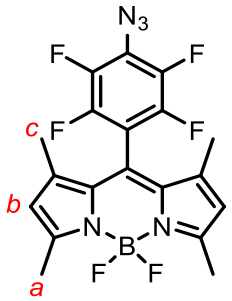

4-Azido-tetrafluorobenzaldehyde (500 mg, 2.28 mmol, 1 equiv) and 2,4-dimethylpyrrole (472 μL, 4.68 mmol, 2.05 equiv) were dissolved in dry degassed CH_2Cl_2 (150 mL) at room temperature. A catalytic amount of TFA (10 μL) was added and the reaction left to stir for 16 hours. A solution of *p*-chloranil (561 mg, 2.28 mmol, 1.1 equiv) dissolved in dry and degassed CH_2Cl_2 (20 mL) was then added and the reaction left to stir for a further 1 hour. Distilled NEt_3 (2.22 mL, 16.0 mmol, 7 equiv) and $BF_3{\cdot}OEt_2$ (2.25 mL, 18.2 mmol, 8 equiv) were added sequentially and the mixture left to stir for another 2 hours. The solution was then washed with H_2O (3 × 50 mL) and brine (50 mL) and dried over Na_2SO_4, filtered and the solvent removed *in vacuo*. The crude product was purified via column chromatography (CH_2Cl_2/*n*-hexane 2:3) and the desired product **3.13** was isolated as a red solid (356 mg, 35%).

^{1}H NMR (400 MHz, $CDCl_3$) δ (ppm): 6.05 (s, 2H; *b*), 2.57 (s, 6H; *a*), 1.64 (s, 6H; *c*).

^{13}C NMR (151 MHz, $CDCl_3$) δ (ppm): 157.78, 144.04 (dm, $^1J_{C-F}$ = 252 Hz, 2C), 141.73, 141.18 (dm, $^1J_{CF}$ = 252 Hz, 2C), 131.21, 123.44, 122.30, 32.08, 29.85, 14.94, 13.81.

^{19}F NMR (376 MHz, $CDCl_3$) δ (ppm): -139.77 – -139.91 (m), -146.16 (q, $^1J_{F-B}$ = 32.2 Hz), -149.95 – -150.14 (m).

HRMS (ESI +ve) m/z: 438.1317 ($[M+H]^+$, $C_{19}H_{15}N_5B_1F_6$ requires 438.1321).

Stopper BODIPY Azide (3.14)

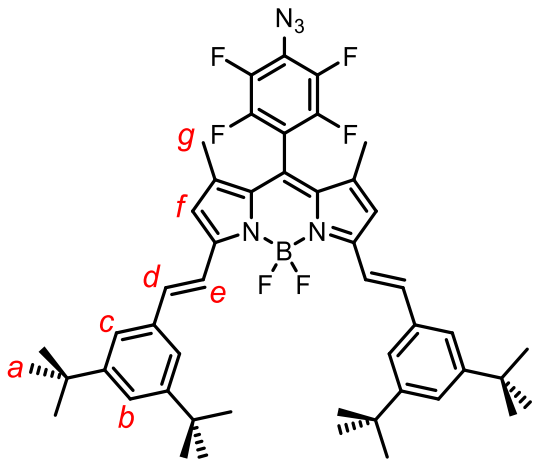

Following general procedure for Knoevenagel condensation with **3.13** (100 mg, 0.23 mmol, 1 equiv) and 3,5-di-*tert*-butylbenzaldehyde (200 mg, 0.91 mmol, 4 equiv), product **3.14** was obtained after silica gel column chromatography (CH_2Cl_2/*n*-hexane 3:2) as a blue powder (58 mg, 30%).

^{1}H NMR (400 MHz, $CDCl_3$) δ (ppm): 7.76 (d, J = 16.3 Hz, 2H; *d*), 7.48 – 7.41 (m, 6H; *b,c*), 7.33 (d, J = 16.3 Hz, 2H; *e*), 6.71 (s, 2H; *f*), 1.72 (s, 6H; *h*), 1.38 (s, 36H; *a*).

^{13}C NMR (126 MHz, $CDCl_3$) δ (ppm): 154.09, 151.27, 140.07, 138.59, 135.77, 132.99, 123.97, 122.01, 119.38, 118.73, 118.52, 34.90, 31.95, 31.42, 29.72, 29.38, 22.71, 14.14, 13.94.

^{19}F NMR (376 MHz, $CDCl_3$) δ (ppm): -138.57 (q, $^1J_{F-B}$ = 32.3 Hz), -139.17 – -139.32 (m), -150.16 – -150.32 (m).

HRMS (ESI +ve) m/z: 838.4439 ($[M+H]^+$, $C_{49}H_{55}N_5B_1F_6$ requires 838.4457).

BODIPY-Stoppered XB Strapped Porphyrin [2]Rotaxane (3.15·Zn)

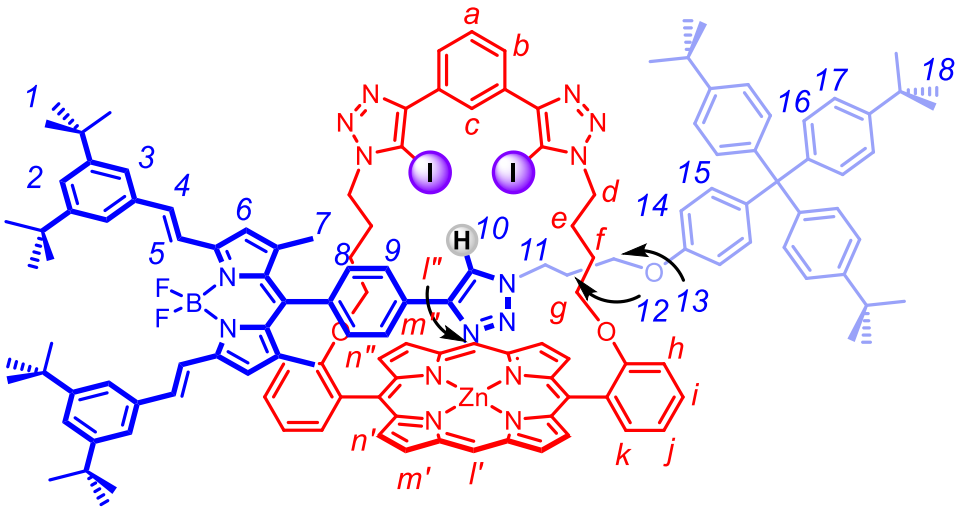

Following the general procedure for CuAAC-AMT synthesis of [2]rotaxanes, strapped porphyrin **3.1a·Zn** (10 mg, 0.009 mmol, 1 equiv) was reacted with BODIPY-stoppered alkyne **3.12** (33 mg, 0.044 mmol, 5 equiv) and terphenyl-stoppered azide **3.8** (26 mg, 0.044 mmol, 5 equiv). The crude was purified by preparative TLC (4% EtOAc in CH_2Cl_2) to give the product [2]rotaxane **3.15·Zn** as blue powder (7.6 mg, 35%).

^{1}H NMR (500 MHz, $CDCl_3$) δ (ppm): 10.10 (s, 1H; *l'*), 9.77 (s, 1H; *l''*), 9.26 (d, *J* = 4.4 Hz, 2H; *m'*), 9.11 (d, *J* = 4.4 Hz, 2H; *m''*), 8.98 (d, *J* = 4.4 Hz, 2H; *n'*), 8.95 (d, *J* = 4.4 Hz, 2H; *n''*), 8.02 (dd, *J* = 7.3, 1.8 Hz, 2H; *b*), 7.80 (d, *J* = 16.2 Hz, 2H; *4*), 7.76 (t, *J* = 8.0 Hz, 2H; *i*), 7.56 (dd, *J* = 7.7, 1.8 Hz, 2H; *k*), 7.47 (d, *J* = 1.8 Hz, 4H; *3*), 7.42 (t, *J* = 1.8 Hz, 2H; *2*), 7.38 (t, *J* = 7.6 Hz, 1H; *a*), 7.35 (d, *J* = 8.5 Hz, 2H; *h*), 7.33 – 7.29 (m, 9H; *c*,*5*,*16*), 7.28 (d, *J* = 9.0 Hz, 2H; *15*), 7.24 – 7.14 (m, 4H; *j*,*14*), 7.12 – 7.06 (m, 6H; *17*), 6.66 (s, 2H; *6*), 6.56 (s, 1H; *10*^{Trz}), 6.37 (d, *J* = 8.3 Hz, 2H; *8*), 4.22 – 4.13 (m, 2H; *9*), 4.09 – 3.99 (m, 4H; *d*), 3.79 – 3.69 (m, 4H; *g*), 1.73 – 1.57 (m, 4H, *e*), 1.47 (s, 6H; *7*) 1.39 (s, 36H; *1*), 1.36 (s, 27H; *18*), 0.86 – 0.76 (m, 4H, *f*). (Signals of proton *11–13* missing due to peaks overlap).

^{13}C NMR (126 MHz, $CDCl_3$) δ (ppm): 158.80, 152.91, 151.30, 150.33, 150.13, 149.48, 149.38, 148.53, 148.33, 144.46, 142.03, 137.24, 137.04, 136.15, 134.52, 133.37, 132.16, 132.08, 131.99, 131.76, 131.57, 130.88, 130.80, 130.06, 129.61, 128.97, 128.86, 127.05, 125.88, 125.65, 124.37, 123.64, 121.96, 119.99, 119.20, 117.75, 115.78, 113.37, 112.85, 105.95, 105.84, 68.87, 63.05, 53.57, 49.98, 44.65, 35.04, 34.54, 31.66, 31.59, 29.86, 25.82, 25.61, 22.85, 15.20, 14.28.

HRMS (ESI +ve) m/z: 2466.94248 ($[M+H]^+$, $C_{141}H_{148}O_3N_{15}BF_2I_2Zn$ requires 2466.93668)

BODIPY-Stoppered XB Strapped Porphyrin [2]Rotaxane (3.16·Zn)

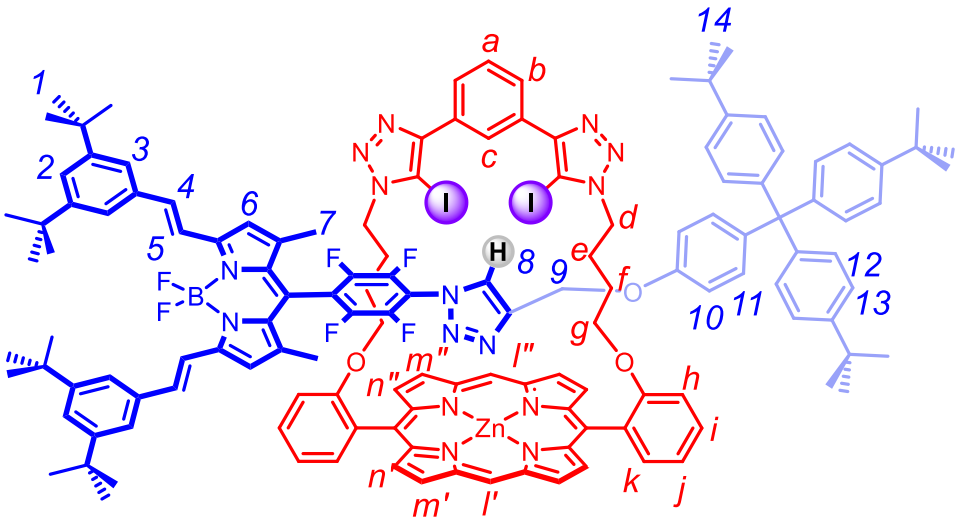

Following the general procedure for CuAAC-AMT synthesis of [2]rotaxanes, strapped porphyrin **3.1a·Zn** (10 mg, 0.009 mmol, 1 equiv) was reacted with BODIPY-stoppered azide **3.14** (37 mg, 0.044 mmol, 5 equiv) and terphenyl-stoppered alkyne **3.7** (24 mg, 0.044 mmol, 5 equiv). The crude was purified by preparative TLC (0.5% EtOAc in CH_2Cl_2) to give the product [2]rotaxane **3.16·Zn** as blue powder (8 mg, 37%).

^{1}H NMR (400 MHz, CD_2Cl_2) δ (ppm): 9.98 (s, 1H; *l'*), 9.57 (s, 1H; *l"*), 9.21 (d, *J* = 4.5 Hz, 2H; *m'*), 9.03 (d, *J* = 4.5 Hz, 2H; *m"*), 8.93 (d, *J* = 4.4 Hz, 2H; *n'*), 8.91 (d, *J* = 4.4 Hz, 2H; *n"*), 7.92 (d, *J* = 6.5 Hz, 2H; *b*), 7.80 (t, *J* = 7.5 Hz, 2H; *i*), 7.75 (d, *J* = 16.3 Hz, 2H; *4*), 7.51 – 7.46 (m, 7H; *2,3,a*), 7.45 – 7.34 (m, 12H; *5,12,h,k*), 7.25 (d, *J* = 8.6 Hz, 6H; *13*), 7.21 (d, *J* = 7.8 Hz, 2H; *j*), 7.13 (t, *J* = 1.8 Hz, 1H; *c*), 6.76 (s, 2H; *6*), 6.70 (d, *J* = 8.8 Hz, 2H; *11*), 6.15 (s, 1H; *8*), 4.61 (d, *J* = 8.7 Hz, 2H; *10*), 4.25 – 4.03 (m, 4H; *d*), 3.96 – 3.73 (m, 4H; *g*), 1.63 (s, 6H; *7*), 1.39 (s, 36H; *1*), 1.38 (s, 27H; *14*), 0.56 (s, 2H; *9*).

^{13}C NMR (126 MHz, $CDCl_3$) δ (ppm): 158.74, 154.38, 151.42, 150.29, 150.08, 149.52, 149.19, 149.08, 148.38, 148.17, 144.46, 140.07, 139.73, 138.91, 137.31, 135.89, 132.61,

132.36, 131.99, 131.71, 131.47, 131.18, 130.78, 130.68, 129.43, 128.65, 127.33, 126.54, 124.40, 124.17, 123.12, 122.19, 119.92, 118.82, 118.77, 118.55, 115.54, 113.14, 112.93, 105.63, 105.58, 68.72, 63.15, 50.28, 35.04, 34.55, 31.67, 31.56, 29.85, 25.96, 25.74, 25.65, 14.01, 1.17.

^{19}F NMR (376 MHz, CD_2Cl_2) δ (ppm): -137.70 – -137.87 (m), -138.35 (q, $^{1}J_{F-B}$ = 32.6 Hz), -145.01 – -145.18 (m).

HRMS (ESI +ve) m/z: 2510.8677 ($[M+H]^+$ $C_{139}H_{140}BF_6I_2N_{15}O_3Zn$ requires 2510.8670).

6.2.4 Synthetic Procedures and Characterisations of Novel Compounds from Chapter 4

Heteroditopic Phenanthroline-based XB Macrocycle (4.1·I)

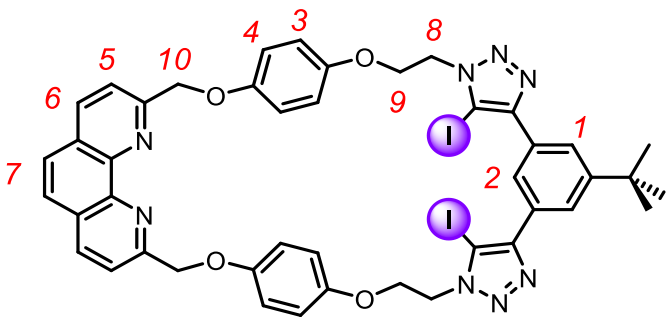

General Procedure for Williamson Ether Condensation-Mediated Macrocyclisation

Bis-phenol **4.9·I** (398 mg, 0.50 mmol, 1 equiv) and bis-tosylate **4.4** (276 mg, 0.50 mmol, 1 equiv) were dissolved in dry DMF (502 mL) and Cs_2CO_3 (655 mg, 2.01 mmol, 4 equiv) was added. The reaction mixture was heated at 70 °C in dark under N_2 for 2 days. The solvent was removed *in vacuo* and the crude solid was redissolved in $CHCl_3$ (50 mL) and washed with H_2O (50 mL) and brine (50 mL). The organic solvent was dried with excess anhydrous $MgSO_4$, filtered and concentrated on rotary evaporator. Purification by iterative repeated silica gel column chromatography (5% CH_3OH in CH_2Cl_2, then 2% CH_3OH in CH_2Cl_2) gave the macrocycle **4.1·I** as white powder (269 mg, 54%).

^{1}H NMR (400 MHz, $CDCl_3$) δ (ppm): 8.22 (t, J = 1.6 Hz, 1H; *2*), 8.21 (d, J = 8.3 Hz, 2H; *5*), 7.98 (d, J = 1.6 Hz, 2H; *1*), 7.83 (d, J = 8.3 Hz, 2H; *6*), 7.74 (s, 2H; *7*), 6.95 (d, J = 9.1 Hz, 4H; *3*), 6.77 (d, J = 9.1 Hz, 4H; *4*), 5.58 (s, 4H; *10*), 4.81 (t, J = 5.5 Hz, 4H, H_8), 4.39 (t, J = 5.5 Hz, 4H, H_9), 1.40 (s, 9H, *tert*-butyl H)

^{13}C NMR (126 MHz, $CDCl_3$) δ (ppm): 158.61, 153.34, 152.31, 150.25, 145.44, 137.16, 130.17, 128.34, 126.50, 125.57, 123.42, 121.39, 116.45, 116.06, 78.32, 72.81, 67.36, 49.77, 35.29, 31.49, 22.50

HRMS (ESI +ve) m/z: 997.1165 ($[M+H]^+$, $C_{44}H_{39}I_2N_8O_4$ requires 997.1178)

Heteroditopic Phenanthroline-based ChB Macrocycle (4.1·Te^{Me})

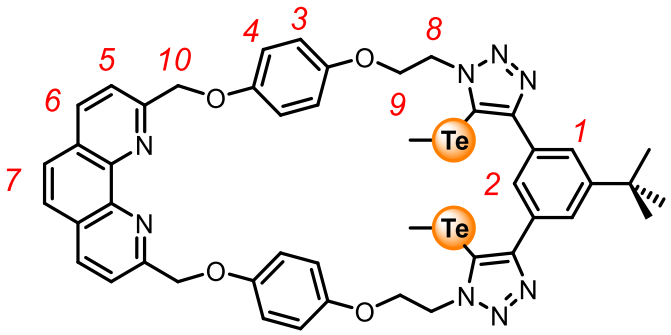

Following general procedure for Williamson ether condensation-mediated macrocyclisation between bis-phenol **4.9·Te^{Me}** (164 mg, 0.20 mmol, 1 equiv) and bis-tosylate **4.4** (109 mg, 0.20 mmol, 1 equiv), the product was purified by iterative repeated preparative TLC (2% EtOH in CH_2Cl_2) to give the macrocycle **4.1·Te^{Me}** as white powder (45 mg, 22%).

^{1}H NMR (400 MHz, $CDCl_3$) δ (ppm): 8.46 (t, *J* = 1.6 Hz, 1H; *2*), 8.20 (d, *J* = 8.3 Hz, 2H; *5*), 7.99 (d, *J* = 1.6 Hz, 2H; *1*), 7.80 (d, *J* = 8.3 Hz, 2H; *6*), 7.73 (s, 2H; *7*), 6.96 (d, *J* = 8.6 Hz, 4H; *3*), 6.74 (d, *J* = 8.6 Hz, 4H; *4*), 5.58 (s, 4H; *10*), 4.95 (t, *J* = 5.4 Hz, 4H; *8*), 4.34 (t, *J* = 5.5 Hz, 4H; *9*), 1.90 (s, 6H; *TeCH$_3$*), 1.39 (s, 9H, *tert*-butyl *H*)

^{13}C NMR (126 MHz, $CDCl_3$) δ (ppm): 158.60, 153.31, 153.25, 152.39, 151.83, 137.23, 131.36, 128.32, 126.49, 125.55, 124.26, 121.39, 116.52, 115.93, 101.45, 72.60, 67.93, 50.22, 35.21, 31.49, 29.85

^{125}Te NMR (158 MHz, $CDCl_3$) δ (ppm): 113.50

HRMS (ESI +ve) m/z: 1029.1659 ($[M+H]^+$, $C_{46}H_{45}O_4N_8{}^{126}Te^{130}Te$ requires 1029.1654)

Heteroditopic Phenanthroline-based HB Macrocycle (4.1·H)

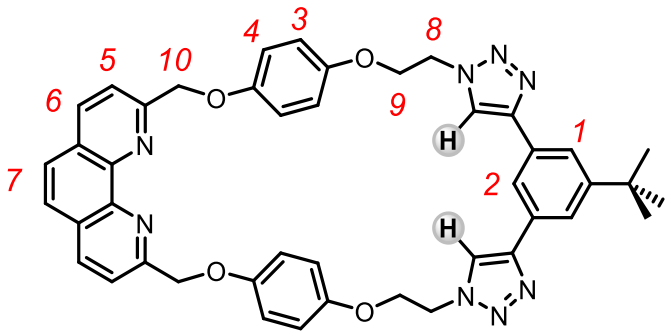

Following general procedure for Williamson ether condensation-mediated macrocyclisation between bis-phenol **4.8·H** (286 mg, 0.53 mmol, 1 equiv) and bis-tosylate **4.4** (291 mg, 0.53 mmol, 1 equiv), the product was purified by iterative repeated preparative TLC (2% EtOH in CH_2Cl_2) to give the macrocycle **4.1·H** as white powder (45 mg, 22%).

^{1}H NMR (400 MHz, $CDCl_3$) δ(ppm): 8.16 (d, J = 8.3 Hz, 2H; *5*), 8.02 (s, 2H; Triazole *H*), 7.91 (d, J = 1.6 Hz, 2H; *1*), 7.81 (t, J = 1.6 Hz, 1H; *2*), 7.77 (d, J = 8.3 Hz, 2H; *6*), 7.69 (s, 2H; *7*), 5.57 (s, 4H; *10*), 4.69 (t, J = 4.8 Hz, 4H; *3*), 4.23 (t, J = 4.8 Hz, 4H; *4*), 1.28 (s, 9H, *tert*-butyl *H*).

^{13}C NMR (126 MHz; $CDCl_3$) δ(ppm): 158.67, 153.36, 152.80, 152.30, 147.96, 145.43, 137.13, 130.84, 128.32, 126.46, 122.87, 121.43, 121.23, 120.51, 116.59, 116.30, 72.61, 67.96, 50.17, 35.10, 31.42.

HRMS (ESI +ve) m/z: 745.3245 ($[M+H]^+$, $C_{44}H_{41}O_4N_8$ requires 745.3237)

MOM-protected XB Bis(iodo-triazole)benzene (4.8·I)

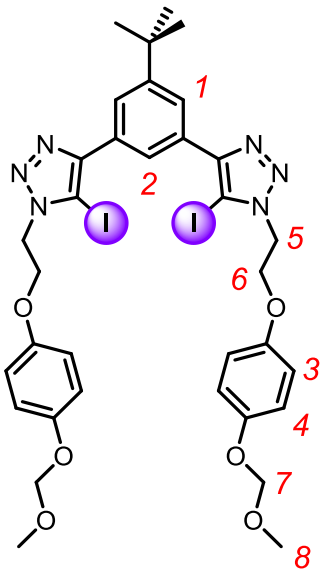

Following the general procedure for CuAAC click reaction between bis-iodoalkyne **2.3·I** (300 mg, 0.69 mmol, 1 equiv) and azide **4.7** (386 mg, 1.73 mmol, 2.5 equiv), purification by silica gel column chromatography (10% EtOAc in CH_2Cl_2) afforded compound **4.8·I** as white solid (488 mg, 80%).

^{1}H NMR (400 MHz, $CDCl_3$) δ (ppm): 8.32 (t, J = 1.6 Hz, 1H; *2*), 8.02 (d, J = 1.6 Hz, 2H; *1*), 6.96 (d, J = 9.0 Hz, 4H; *3*), 6.82 (d, J = 9.0 Hz, 4H; *4*), 5.09 (s, 4H; *7*), 4.84 (t, J = 5.8 Hz, 4H; *5*), 4.44 (t, J = 5.8 Hz, 4H; *6*), 3.45 (s, 6H; *8*), 1.43 (s, 9H; *tert*-butyl *H*)

^{13}C NMR (126 MHz, $CDCl_3$) δ (ppm): 153.13, 152.06, 152.02, 150.16, 130.28, 125.38, 123.75, 117.73, 115.73, 95.30, 78.07, 66.88, 56.01, 50.01, 35.34, 31.50

HRMS (ESI +ve) m/z: 881.1006 ($[M+H]^+$, $C_{34}H_{39}I_2N_6O_6$ requires 881.1015)

MOM-protected ChB Bis(telluromethyl-triazole)benzene (4.8·Te^{Me})

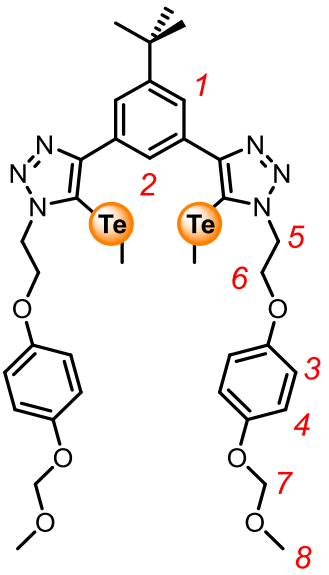

Following general procedure for CuAAC click reaction between azide **4.7** (126 mg, 0.56 mmol, 2.5 equiv) and bis-telluroalkyne **2.3·Te^{Me}** (105 mg, 0.23 mmol, 1 equiv), the product was purified by silica gel column chromatography (20% EtOAc in CH_2Cl_2) to give **4.8·Te^{Me}** as yellow solid (182 mg, 88%). Due to instability of **4.8·Te^{Me}**, only the ^{1}H NMR spectrum was recorded and the compound was used immediately in the next step without any further characterisation.

^{1}H NMR (400 MHz, $CDCl_3$) δ (ppm): 8.47 (t, J = 1.6 Hz, 1H; *2*), 8.11 (d, J = 1.6 Hz, 2H; *1*), 6.95 (d, J = 9.0Hz, 4H; *3*), 6.80 (d, J = 9.0 Hz, 4H; *4*), 5.08 (s, 4H; *7*), 5.08 (t, J = 5.4 Hz, 4H; *3*) 4.39 (t, J = 5.4 Hz, 4H; *4*), 3.45 (s, 6H; *8*), 1.95 (s, 6H; *TeCH$_3$*), 1.43 (s, 9H; *tert*-butyl *H*).

MOM-protected HB Bis(proto-triazole)benzene (4.8·H)

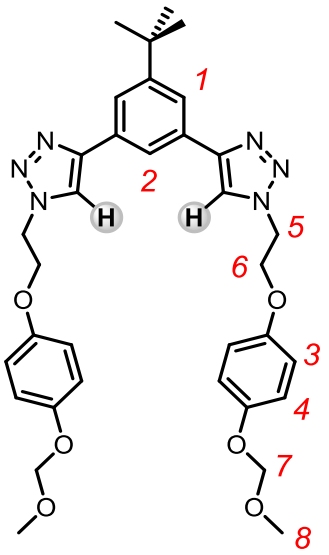

Following general procedure for CuAAC click reaction between azide **4.7** (396 mg, 1.78 mmol, 2.5 equiv) and bis-protoalkyne **2.3·H** (110 mg, 0.71 mmol, 1 equiv), the product was purified by silica gel column chromatography (10-20% EtOAc in CH_2Cl_2) to give **4.8·H** as white foam (342 mg, 90%).

^{1}H NMR (400 MHz, $CDCl_3$) δ (ppm): 8.03 (s, 2H; triazole *H*), 8.02 (t, *J* = 1.6 Hz, 1H; *2*), 7.89 (d, *J*=1.6 Hz, 2H; *1*), 6.97 (d, *J*=9.0 Hz, 4H; *3*), 6.83 (d, *J*=9.0 Hz, 4H; *4*), 5.09 (s, 4H; *7*), 4.80 (t, *J*=5.0 Hz, 4H; *5*), 4.37 (t, *J*=5.0 Hz, 4H; *6*), 3.45 (s, 6H; *8*), 1.41 (s, 9H; *tert*-butyl *H*)

^{13}C NMR (126 MHz, $CDCl_3$) δ (ppm): 153.07, 152.72, 152.21, 148.17, 130.96, 122.92, 121.18, 120.69, 117.81, 115.85, 95.27, 67.36, 56.03, 50.15, 35.13, 31.50

HRMS (ESI +ve) m/z: 629.3082 ($[M+H]^+$, $C_{34}H_{41}N_6O_6$ requires 629.3082)

Phenol-appended XB Bis(iodo-triazole)benzene (4.9·I)

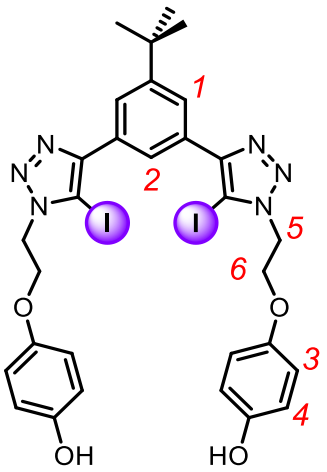

General Procedure for MOM-deprotection

Acetyl chloride (1.07 mL, 15.1 mmol, 30 equiv) was added to CH_3OH (5 mL) slowly at 0 °C. The solution was stirred at 0 °C for 5 minutes and stirred at room temperature for a further 15 minutes. A solution of **4.8·I** (442 mg, 0.50 mmol, 1 equiv) in CH_2Cl_2 (5 mL) was added to the acidic methanol solution slowly and the reaction mixture was stirred at room temperature for 2 hours. After the reaction was complete (monitored by TLC), the crude mixture was concentrated on rotary evaporator and the product was dried on high vacuum for 1 day to yield the product **4.9·I** as white powder in excellent purity (286 mg, quant.).

^{1}H NMR (400 MHz, d_6-acetone) δ (ppm): 8.45 (t, J = 1.6 Hz, 1H; *2*), 8.09 (d, J = 1.6 Hz, 2H; *1*), 6.81 (d, J = 9.0 Hz, 2H; *3*), 6.74 (d, J = 9.0 Hz, 2H; *4*), 4.91 (t, J = 5.4 Hz, 2H; *5*), 4.50 (t, J = 5.4 Hz, 2H; *6*), 2.85 (brs, 2H, *hydroquinone OH*), 1.45 (s, 9H, *tert*-butyl *H*)

^{13}C NMR (126 MHz, d_6-acetone) δ (ppm): 154.24, 152.65, 152.45, 150.09, 131.94, 125.28, 124.16, 116.65, 116.60, 79.99, 67.92, 50.94, 35.77, 31.66

HRMS (ESI +ve) m/z: 793.0484 ($[M+H]^+$, $C_{30}H_{31}N_6O_4I_2$ requires 793.0491)

Phenol-appended ChB Bis(telluromethyl-triazole)benzene (4.9·Te^{Me})

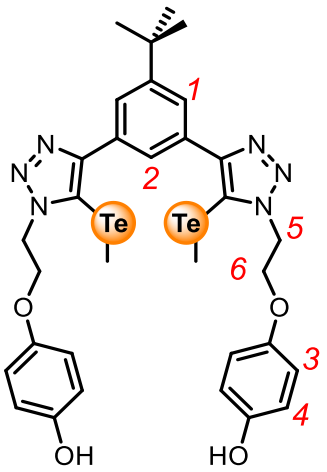

Following general procedure for MOM-deprotection of **4.8·Te^{Me}** (182 mg, 0.20 mmol, 1 equiv), the product bis-phenol **4.9·Te^{Me}** was isolated as yellow foam (164 mg, quant.). Due to instability of **4.9·Te^{Me}**, only the ^{1}H NMR spectrum was recorded and the compound was used immediately in the next step without any further characterisation.

^{1}H NMR (400 MHz, CD_3OD) δ (ppm): 8.16 (t, J = 1.6 Hz, 1H; *2*), 8.12 (d, J = 1.6 Hz, 2H; *1*), 6.73 (d, J = 8.7 Hz, 4H; *3*), 6.64 (d, J = 8.7 Hz, 4H; *4*), 5.16 (t, J = 4.9 Hz, 4H; *5*), 4.46 (t, J = 4.9 Hz, 4H; *6*), 1.97 (s, 6H; *TeCH$_3$*), 1.43 (s, 9H; *tert*-butyl *H*)

Phenol-appended HB Bis(proto-triazole)benzene (4.9·H)

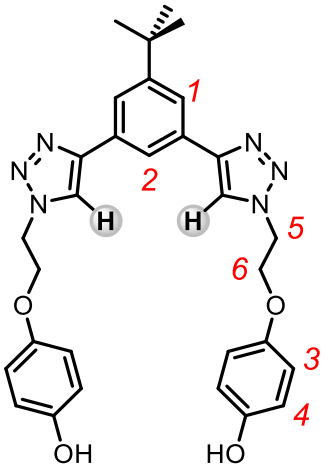

Following general procedure for MOM-deprotection of **4.8·H** (333 mg, 0.53 mmol, 1 equiv), the product bis-phenol **4.9·H** was isolated as white foam (164 mg, quant.).

^{1}H NMR (400 MHz, d_6-acetone) δ(ppm): 8.65 (s, 2H; *triazole H*), 8.33 (t, J = 1.6 Hz, 1H; *2*), 8.01 (t, J = 1.6Hz, 2H; *1*), 6.83 (d, J = 9.0 Hz, 4H; *3*), 6.74 (d, J = 9.0 Hz, 4H; *4*), 4.89 (t, J = 5.1 Hz, 4H; *5*), 4.45 (t, J = 5.1 Hz, 4H; *6*), 3.30 (brs, 1H; *hydroquinone OH*), 1.41 (s, 9H; *tert*-butyl *H*)

^{13}C NMR (126 MHz, d_6-acetone) δ(ppm): 153.32, 152.73, 152.44, 147.57, 131.86, 123.27, 122.98, 121.18, 116.83, 116.61, 68.05, 51.02, 35.58, 31.59

HRMS (ESI +ve) m/z: 541.2554 ([M+H]$^+$, $C_{30}H_{33}N_6O_4$ requires 541.2558)

Di(ethylene glycol)-based Bis-azide (4.12a)

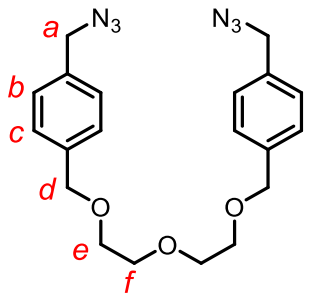

General Procedure for Azidation

Bromide **4.11a** (2.00 g, 4.24 mmol, 1 equiv) and NaN_3 (1.10 g, 16.9 mmol, 4 equiv) were added into DMSO (40 mL) and the reaction mixture was stirred at room temperature overnight. The crude was then diluted with H_2O (50 mL) and extracted with Et_2O (50 mL × 3). The combined organic layer was washed with brine (50 mL), dried over anhydrous $MgSO_4$, filtered and concentrated on the rotary evaporator to afford the bis-azide **4.12a** as yellow oil (1.68 g, quant.).

^{1}H NMR (400 MHz, $CDCl_3$) δ (ppm): 7.40–7.34 (m, 4H, *b*), 7.30—7.27 (m, 4H, *c*), 4.58 (s, 4H, *a*), 4.32 (s, 4H, *d*), 3.75—3.60 (m, 12H, *e* + *f*)

^{13}C NMR (126 MHz; $CDCl_3$) δ (ppm): 138.70, 134.78, 128.43, 128.27, 72.98, 70.86, 69.76, 54.69.

HRMS (ESI +ve) m/z: 419.1793 ($[M+Na]^+$, $C_{20}H_{24}O_3N_6Na$ requires 419.1802).

Tri(ethylene glycol)-based Bis-azide (4.12b)

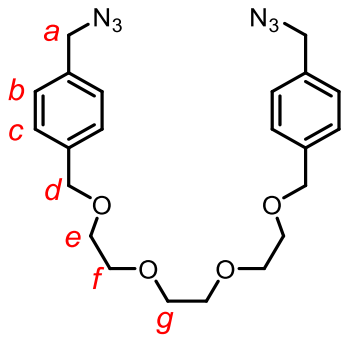

Following general procedure azidation, bromide **4.11b** (2.00 g, 3.87 mmol, 1 equiv) was reacted with NaN_3 (1.01 g, 15.5 mmol, 4 equiv) and the product bis-azide **4.12b** was isolated as yellow oil (1.71 g, quant.).

^{1}H NMR (400 MHz, acetone-d_6) δ(ppm): 7.38 (m, J = 8.3 Hz, 8H, b + c), 4.56 (s, 4H, a), 4.42 (s, 4H, d), 3.69 – 3.57 (m, 12H, e + f + g) ppm.

^{13}C NMR (126 MHz; acetone-d_6) δ(ppm): 140.21, 135.89, 129.34, 128.79, 73.18, 71.48, 71.42, 70.71, 54.97.

HRMS (ESI +ve) m/z: 463.2057 ([M+Na]$^+$, $C_{22}H_{28}O_3N_6Na$ requires 463.2064).

Di(ethylene glycol)-based XB Macrocycle (4.13a)

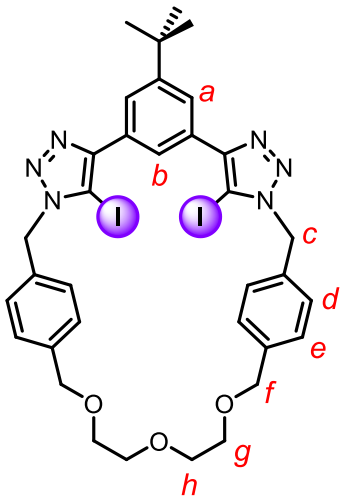

Following the general procedure for CuAAC-mediated macrocyclisation between bis(iodoalkyne) **2.3·I** (394 mg, 0.91 mmol, 1 equiv) and bis-azide **4.12a** (360 mg, 0.91 mmol, 1 equiv), the product was purified by silica gel column chromatography (15% EtOAc in CH_2Cl_2) to give the target macrocycle **4.13a** as white powder (264 mg, 35%).

^{1}H NMR (400 MHz, acetone-d_6) δ (ppm): 7.94 (d, J = 1.6 Hz, 2H; *a*), 7.88 (t, J = 1.6 Hz, 1H; *b*), 7.31 (d, J = 8.0 Hz, 4H; *d*), 7.21 (d, J = 8.0 Hz, 4H; *e*), 5.78 (s, 4H; *c*), 4.46 (s, 4H; *f*), 3.61 – 3.56 (m, 4H; *g*), 3.55 – 3.49 (m, 4H; *h*), 1.45 (s, 9H; *tert*-butyl H).

^{13}C NMR (126 MHz; acetone-d_6) δ (ppm): 153.14, 152.29, 139.68, 135.66, 131.92, 129.20, 128.63, 125.99, 125.44, 79.01, 73.33, 71.26, 70.60, 35.72, 31.75 (Peak missing due to merging with acetone residual solvent peak).

HRMS (ESI +ve) m/z: 831.1000 ($[M+H]^+$, $C_{34}H_{37}O_3N_6I_2$ requires 831.1011).

Tri(ethylene glycol)-based XB Macrocycle (4.13b)

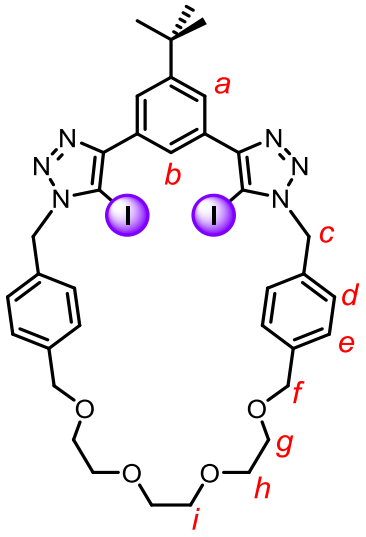

Following the general procedure for CuAAC-mediated macrocyclisation between bis(iodoalkyne) **2.3·I** (384 mg, 0.89 mmol, 1 equiv) and bis-azide **4.12b** (390 mg, 0.89 mmol, 1 equiv), the product was purified by silica gel column chromatography (30% EtOAc in CH_2Cl_2) to give the target macrocycle **4.13b** as white powder (240 mg, 31%).

^{1}H NMR (400 MHz, acetone-d_6) δ (ppm): 8.12 (t, J = 1.6 Hz, 1H; *b*), 8.00 (d, J = 1.6 Hz, 2H; *a*), 7.34 (d, J = 8.0 Hz, 4H; *d*), 7.24 (d, J = 8.0 Hz, 4H; *e*), 5.79 (s, 4H; *c*), 4.50 (s, 4H; *f*), 3.61 – 3.53 (m, 8H; *g* + *h*), 3.53 (s, 4H; *i*), 1.45 (s, 9H; *tert*-butyl H).

^{13}C NMR (126 MHz; acetone-d_6) δ (ppm): 152.92, 151.69, 140.05, 135.57, 131.96, 128.84, 128.44, 125.84, 124.84, 79.32, 79.28, 73.16, 71.51, 71.40, 70.86, 35.78, 31.76.

HRMS (ESI +ve) m/z: 875.1256 ($[M+H]^+$, $C_{36}H_{41}O_4N_6I_2$ requires 875.1273).

Di(ethylene glycol)-based All-XB [2]Catenane (4.10a)

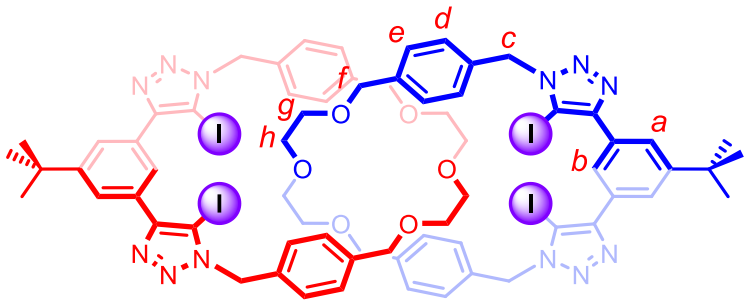

General Procedure for Alkali Metal Cation Template Synthesis of [2]Catenane

Macrocycle **4.13a** (10.0 mg, 0.012 mmol, 1 equiv), bis-azide **4.12a** (4.8 mg, 0.012 mmol, 1 equiv) and $NaBAr^{F}{}_{4}$ (10.7 mg, 0.012 mmol, 1 equiv) were added to dry and degassed CH_2Cl_2 (1.0 mL) and the mixture was stirred at room temperature for 30 minutes under N_2. A CH_2Cl_2 (0.4 mL) solution of bis(iodoalkyne) **2.3·I** (5.2 mg, 0.012 mmol, 1 equiv) was added to the mixture, followed by a solution of 1:1 mixture of $[Cu(CH_3CN)_4]PF_6$ (2.2 mg, 0.006 mmol, 0.5 equiv) and TBTA (3.2 mg, 0.006 mmol, 0.5 equiv) dissolved in CH_2Cl_2 (1.0 mL). The reaction mixture was left stirring at room temperature overnight. The crude was diluted with CH_2Cl_2 (30 mL) and washed with aqueous 0.01 M NH_4OH/EDTA (20 mL), dried with $MgSO_4$, filtered and concentrated on rotary evaporator. Further purification with iterative preparative TLC (0.5% CH_3OH in EtOAc/CH_2Cl_2 1:1) afforded the target [2]catenane **4.10a** as white powder (5.4 mg, 27%).

^{1}H NMR (400 MHz, acetone-d_6) δ (ppm): 7.83 (d, J = 1.6 Hz, 4H; *a*), 7.44 (t, J = 1.6 Hz, 2H; *b*), 7.14 (d, J = 8.1 Hz, 8H; *d*), 6.86 (d, J = 8.1 Hz, 8H; *e*), 5.62 (s, 8H; *c*), 3.98 (s, 8H; *f*), 3.04 – 2.92 (m, 16H; *g* + *h*), 1.44 (s, 18H; *tert*-butyl H).

^{13}C NMR (151 MHz; acetone-d_6) δ (ppm): 152.66, 152.49, 139.96, 135.21, 132.08, 129.40, 129.01, 126.66, 126.01, 80.17, 73.02, 70.79, 70.02, 35.74, 32.80, 31.82.

HRMS (ESI +ve) m/z: 1661.1899 ($[M+H]^+$, $C_{68}H_{73}O_6N_{12}I_4$ requires 1661.1949).

Tri(ethylene glycol)-based All-XB [2]Catenane (4.10b)

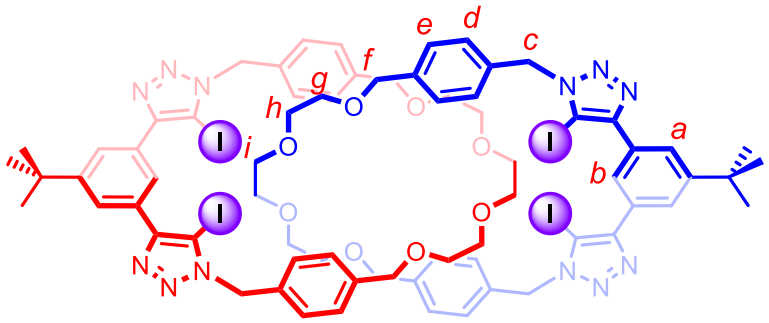

Following the general procedure for alkali metal cation template synthesis of [2]catenane, macrocycle **4.13b** (10.0 mg, 0.011 mmol, 1 equiv) was reacted with bis-azide **4.12b** (5.0 mg, 0.011 mmol, 1 equiv), $NaBAr^{F}{}_{4}$ (10.1 mg, 0.011 mmol, 1 equiv) and bis(iodo-alkyne) **2.3·I** (5.0 mg, 0.011 mmol, 1 equiv). The crude was purified by iterative preparative TLC (1% CH_3OH in EtOAc/CH_2Cl_2 7:3) to give the target [2]catenane **4.10b** as white powder (2.0 mg, 10%).

^{1}H NMR (400 MHz, acetone-d_6) δ (ppm): 7.95 (d, J = 1.6 Hz, 4H; *a*), 7.84 (t, J = 1.6 Hz, 2H; *b*), 7.09 (d, J = 8.0 Hz, 8H; *d*), 7.00 (d, J = 8.0 Hz, 8H; *e*), 5.62 (s, 8H; *c*), 4.17 (s, 8H; *f*), 3.31 – 3.19 (m, 16H; *g* + *h*), 3.18 (s, 8H; *i*), 1.45 (s, 18H; *tert*-butyl H).

^{13}C NMR (151 MHz; acetone-d_6) δ (ppm): 152.67, 151.66, 140.02, 135.21, 131.97, 128.80, 128.77, 125.75, 125.26, 79.93, 73.09, 71.34, 71.16, 70.75, 35.81, 31.84, 23.49.

HRMS (ESI +ve) m/z: 1749.2437 ($[M+H]^+$, $C_{72}H_{81}O_8N_{12}I_4$ requires 1749.2474).

References

References

1 Supramolecular Chemistry, 2nd Edition | Wiley, https://www.wiley.com/en-gb/Supramolecular+Chemistry%2C+2nd+Edition-p-9780470512340.

2 The Nobel Prize in Chemistry 1987, https://www.nobelprize.org/prizes/chemistry/1987/press-release/.

3 The Nobel Prize in Chemistry 2016, https://www.nobelprize.org/prizes/chemistry/2016/press-release/.

4 N. Koumura, R. W. J. Zijlstra, R. A. van Delden, N. Harada, B. L. Feringa, *Nature* **1999**, *401*, 152.

5 J. D. Badjic, *Science* **2004**, *303*, 1845.

6 Y. Liu, A. H. Flood, P. A. Bonvallet, S. A. Vignon, B. H. Northrop, H.-R. Tseng, J. O. Jeppesen, T. J. Huang, B. Brough, M. Baller, S. Magonov, S. D. Solares, W. A. Goddard, C.-M. Ho, J. F. Stoddart, *J. Am. Chem. Soc.* **2005**, *127*, 9745.

7 T. Kudernac, N. Ruangsupapichat, M. Parschau, B. Maciá, N. Katsonis, S. R. Harutyunyan, K.-H. Ernst, B. L. Feringa, *Nature* **2011**, *479*, 208.

8 F. P. Schmidtchen, *Angewandte Chemie International Edition in English* **1977**, *16*, 720.

9 E. Arunan, G. R. Desiraju, R. A. Klein, J. Sadlej, S. Scheiner, I. Alkorta, D. C. Clary, R. H. Crabtree, J. J. Dannenberg, P. Hobza, H. G. Kjaergaard, A. C. Legon, B. Mennucci, D. J. Nesbitt, *Pure and Applied Chemistry* **2011**, *83*.

10 J. L. Cook, C. A. Hunter, C. M. R. Low, A. Perez-Velasco, J. G. Vinter, *Angewandte Chemie International Edition* **2007**, *46*, 3706.

11 C. A. Hunter, *Angewandte Chemie International Edition* **2004**, *43*, 5310.

12 P. Politzer, J. S. Murray, T. Clark, *Phys. Chem. Chem. Phys.* **2010**, *12*, 7748.

13 P. Politzer, J. S. Murray, T. Clark, *Phys. Chem. Chem. Phys.* **2013**, *15*, 11178.

14 P. Politzer, J. S. Murray, T. Clark, G. Resnati, *Phys. Chem. Chem. Phys.* **2017**, *19*, 32166.

15 T. Clark, M. Hennemann, J. S. Murray, P. Politzer, *Journal of Molecular Modeling* **2007**, *13*, 291.

16 G. R. Desiraju, P. S. Ho, L. Kloo, A. C. Legon, R. Marquardt, P. Metrangolo, P. Politzer, G. Resnati, K. Rissanen, *Pure and Applied Chemistry* **2013**, *85*.

17 J. S. Murray, P. Lane, T. Clark, P. Politzer, *J Mol Model* **2007**, *13*, 1033.

18 J. S. Murray, P. Lane, P. Politzer, *Int. J. Quantum Chem.* **2007**, *107*, 2286.

19 J. S. Murray, P. Lane, P. Politzer, *J Mol Model* **2009**, *15*, 723.

20 A. Bauzá, A. Frontera, *Angew. Chem. Int. Ed.* **2015**, *54*, 7340.

21 P. Metrangolo, H. Neukirch, T. Pilati, G. Resnati, *Acc. Chem. Res.* **2005**, *38*, 386.

22 P. Metrangolo, F. Meyer, T. Pilati, G. Resnati, G. Terraneo, *Angew. Chem. Int. Ed.* **2008**, *47*, 6114.

23 A. Mukherjee, S. Tothadi, G. R. Desiraju, *Acc. Chem. Res.* **2014**, *47*, 2514.

24 Y. Lu, T. Shi, Y. Wang, H. Yang, X. Yan, X. Luo, H. Jiang, W. Zhu, *J. Med. Chem.* **2009**, *52*, 2854.

25 R. Wilcken, M. O. Zimmermann, A. Lange, A. C. Joerger, F. M. Boeckler, *J. Med. Chem.* **2013**, *56*, 1363.

26 L. Mendez, G. Henriquez, S. Sirimulla, M. Narayan, *Molecules* **2017**, *22*, 1397.

27 H. Wang, H. K. Bisoyi, A. M. Urbas, T. J. Bunning, Q. Li, *Chem. Eur. J.* **2019**, *25*, 1369.

28 M. Saccone, L. Catalano, *J. Phys. Chem. B* **2019**, *123*, 9281.

29 G. Cavallo, P. Metrangolo, T. Pilati, G. Resnati, M. Sansotera, G. Terraneo, *Chem. Soc. Rev.* **2010**, *39*, 3772.

30 J. Pancholi, P. D. Beer, *Coordination Chemistry Reviews* **2020**, *416*, 213281.

31 R. L. Sutar, S. M. Huber, *ACS Catal.* **2019**, *9*, 9622.

32 H. Yang, M. W. Wong, *Molecules* **2020**, *25*, 1045.

33 A. Bundhun, P. Ramasami, J. S. Murray, P. Politzer, *J Mol Model* **2013**, *19*, 2739.

34 C. B. Aakeroy, D. L. Bryce, G. R. Desiraju, A. Frontera, A. C. Legon, F. Nicotra, K. Rissanen, S. Scheiner, G. Terraneo, P. Metrangolo, G. Resnati, *Pure and Applied Chemistry* **2019**, *91*, 1889.

35 A. F. Cozzolino, P. S. Whitfield, I. Vargas-Baca, *J. Am. Chem. Soc.* **2010**, *132*, 17265.

36 K. T. Mahmudov, M. N. Kopylovich, M. F. C. Guedes da Silva, A. J. L. Pombeiro, *Dalton Trans.* **2017**, *46*, 10121.

37 P. C. Ho, J. Z. Wang, F. Meloni, I. Vargas-Baca, *Coordination Chemistry Reviews* **2020**, *422*, 213464.

38 S. Benz, M. Macchione, Q. Verolet, J. Mareda, N. Sakai, S. Matile, *J. Am. Chem. Soc.* **2016**, *138*, 9093.

39 M. Macchione, M. Tsemperouli, A. Goujon, A. R. Mallia, N. Sakai, K. Sugihara, S. Matile, *Helv. Chim. Acta* **2018**, *101*, e1800014.

40 L. M. Lee, M. Tsemperouli, A. I. Poblador-Bahamonde, S. Benz, N. Sakai, K. Sugihara, S. Matile, *J. Am. Chem. Soc.* **2019**, *141*, 810.

41 B. Zhou, F. P. Gabbaï, *Chem. Sci.* **2020**, *11*, 7495.

42 Y. Nagao, T. Hirata, S. Goto, S. Sano, A. Kakehi, K. Iizuka, M. Shiro, *J. Am. Chem. Soc.* **1998**, *120*, 3104.

43 C. A. Hunter, J. K. M. Sanders, *J. Am. Chem. Soc.* **1990**, *112*, 5525.

44 C. R. Patrick, G. S. Prosser, *Nature* **1960**, *187*, 1021.

45 J. C. Ma, D. A. Dougherty, *Chem. Rev.* **1997**, *97*, 1303.

46 B. L. Schottel, H. T. Chifotides, K. R. Dunbar, *Chem. Soc. Rev.* **2008**, *37*, 68.

47 C. Garau, A. Frontera, D. Quiñonero, P. Ballester, A. Costa, P. M. Deyà, *ChemPhysChem* **2003**, *4*, 1344.

48 H. Liu, Q. Zhang, M. Wang, *Angew. Chem. Int. Ed.* **2018**, *57*, 6536.

49 N. T. Southall, K. A. Dill, A. D. J. Haymet, *J. Phys. Chem. B* **2002**, *106*, 521.

50 M. Lisbjerg, B. E. Nielsen, B. O. Milhøj, S. P. A. Sauer, M. Pittelkow, *Org. Biomol. Chem.* **2015**, *13*, 369.

51 F. Ahad, S. A. Ganie, *Indian J Endocrinol Metab* **2010**, *14*, 13.

52 C. Reiners, R. Schneider, *Radiat Environ Biophys* **2013**, *52*, 189.

53 G. R. Cutting, *Nat Rev Genet* **2015**, *16*, 45.

54 N. H. de Leeuw, *J. Phys. Chem. B* **2004**, *108*, 1809.

55 D. W. Schindler, *Limnol. Oceanogr.* **2006**, *51*, 356.

56 C. A. Johnson, *Applied Geochemistry* **2015**, *57*, 194.

57 E. A. Katayev, G. V. Kolesnikov, J. L. Sessler, *Chemical Society Reviews* **2009**, *38*, 1572.

58 *Arsenic in drinking water*, ed. by National Research Council (U.S.), National Academy Press, Washington, D.C, **1999**.

59 P. Ravenscroft, H. Brammer, K. S. Richards, *Arsenic pollution: a global synthesis*, Wiley-Blackwell, Chichester, U.K. ; Malden, MA, **2009**.

60 R. Quansah, F. A. Armah, D. K. Essumang, I. Luginaah, E. Clarke, K. Marfoh, S. J. Cobbina, E. Nketiah-Amponsah, P. B. Namujju, S. Obiri, M. Dzodzomenyo, *Environmental Health Perspectives* **2015**, *123*, 412.

61 N. H. Evans, P. D. Beer, *Angew. Chem. Int. Ed.* **2014**, *53*, 11716.

62 N. Busschaert, C. Caltagirone, W. Van Rossom, P. A. Gale, *Chem. Rev.* **2015**, *115*, 8038.

63 P. Molina, F. Zapata, A. Caballero, *Chem. Rev.* **2017**, *117*, 9907.

64 C. H. Park, H. E. Simmons, *J. Am. Chem. Soc.* **1968**, *90*, 2431.

65 R. D. Shannon, *Acta Crystallographica Section A* **1976**, *32*, 751.

66 Y. Marcus, *J. Chem. Soc., Faraday Trans.* **1991**, *87*, 2995.

67 F. Hofmeister, *Archiv für experimentelle Pathologie und Pharmakologie* **1888**, *24*, 247.

68 B. Hribar, N. T. Southall, V. Vlachy, K. A. Dill, *J. Am. Chem. Soc.* **2002**, *124*, 12302.

69 A. S. Thomas, A. H. Elcock, *J. Am. Chem. Soc.* **2007**, *129*, 14887.

70 R. Mancinelli, A. Botti, F. Bruni, M. A. Ricci, A. K. Soper, *Phys. Chem. Chem. Phys.* **2007**, *9*, 2959.

71 R. L. Baldwin, *Biophys J* **1996**, *71*, 2056.

72 Y. Zhang, P. Cremer, *Current Opinion in Chemical Biology* **2006**, *10*, 658.

73 C. L. D. Gibb, B. C. Gibb, *Journal of the American Chemical Society* **2011**, *133*, 7344.

74 R. S. Carnegie, C. L. D. Gibb, B. C. Gibb, *Angew. Chem. Int. Ed.* **2014**, *53*, 11498.

75 *CRC handbook of chemistry and physics: a ready-reference book of chemical and physical data*, 90. ed., 2009th–2010th ed. , ed. by David R. Lide, Chemical Rubber Company, CRC Press, Boca Raton, FLa., **2009**.

76 J. W. Pflugrath, F. A. Quiocho, *Nature* **1985**, *314*, 257.

77 H. Luecke, F. A. Quiocho, *Nature* **1990**, *347*, 402.

78 K. Kavallieratos, S. R. de Gala, D. J. Austin, R. H. Crabtree, *J. Am. Chem. Soc.* **1997**, *119*, 2325.

79 S. Kubik, R. Goddard, R. Kirchner, D. Nolting, J. Seidel, *Angewandte Chemie International Edition* **2001**, *40*, 2648.

80 S. Kubik, R. Goddard, *Proc Natl Acad Sci USA* **2002**, *99*, 5127.

81 V. Amendola, L. Fabbrizzi, L. Mosca, *Chem. Soc. Rev.* **2010**, *39*, 3889.

82 S. J. Brooks, P. R. Edwards, P. A. Gale, M. E. Light, *New J. Chem.* **2006**, *30*, 65.

83 V. Blažek Bregović, N. Basarić, K. Mlinarić-Majerski, *Coordination Chemistry Reviews* **2015**, *295*, 80.

84 P. G. Young, J. K. Clegg, M. Bhadbhade, K. A. Jolliffe, *Chem. Commun.* **2011**, *47*, 463.

85 D. Quiñonero, R. Prohens, C. Garau, A. Frontera, P. Ballester, A. Costa, P. M. Deyà, *Chemical Physics Letters* **2002**, *351*, 115.

86 G. Picci, M. Kubicki, A. Garau, V. Lippolis, R. Mocci, A. Porcheddu, R. Quesada, P. C. Ricci, M. A. Scorciapino, C. Caltagirone, *Chem. Commun.* **2020**, *56*, 11066.

87 L. Qin, A. Hartley, P. Turner, R. B. P. Elmes, K. A. Jolliffe, *Chem. Sci.* **2016**, *7*, 4563.

88 A. Portell, R. Barbas, D. Braga, M. Polito, C. Puigjaner, R. Prohens, *CrystEngComm* **2009**, *11*, 52.

89 R. Prohens, A. Portell, C. Puigjaner, S. Tomàs, K. Fujii, K. D. M. Harris, X. Alcobé, M. Font-Bardia, R. Barbas, *Crystal Growth & Design* **2011**, *11*, 3725.

90 N. Busschaert, R. B. P. Elmes, D. D. Czech, X. Wu, I. L. Kirby, E. M. Peck, K. D. Hendzel, S. K. Shaw, B. Chan, B. D. Smith, K. A. Jolliffe, P. A. Gale, *Chem. Sci.* **2014**, *5*, 3617.

91 D.-W. Yoon, D. E. Gross, V. M. Lynch, J. L. Sessler, B. P. Hay, C.-H. Lee, *Angew. Chem. Int. Ed.* **2008**, *47*, 5038.

92 Y. Li, A. H. Flood, *Angew. Chem. Int. Ed.* **2008**, *47*, 2649.

93 Y. Li, A. H. Flood, *J. Am. Chem. Soc.* **2008**, *130*, 12111.

94 S. Lee, C.-H. Chen, A. H. Flood, *Nature Chem* **2013**, *5*, 704.

95 S. Lee, B. E. Hirsch, Y. Liu, J. R. Dobscha, D. W. Burke, S. L. Tait, A. H. Flood, *Chemistry – A European Journal* **2016**, *22*, 560.

96 Y. Liu, W. Zhao, C.-H. Chen, A. H. Flood, *Science* **2019**, *365*, 159.

97 M. A. Yawer, V. Havel, V. Sindelar, *Angewandte Chemie International Edition* **2015**, *54*, 276.

98 J. Svec, M. Necas, V. Sindelar, *Angewandte Chemie International Edition* **2010**, *49*, 2378.

99 P. Mateus, N. Bernier, R. Delgado, *Coordination Chemistry Reviews* **2010**, *254*, 1726.

100 M. W. Hosseini, J.-M. Lehn, *Helvetica Chimica Acta* **1988**, *71*, 749.

101 T. H. Wirth, Norman. Davidson, *J. Am. Chem. Soc.* **1964**, *86*, 4325.

102 B. Dietrich, T. M. Fyles, J.-M. Lehn, L. G. Pease, D. L. Fyles, *J. Chem. Soc., Chem. Commun.* **1978**, 934.

103 C. Bazzicalupi, A. Bencini, A. Bianchi, M. Cecchi, B. Escuder, V. Fusi, E. Garcia-España, C. Giorgi, S. V. Luis, G. Maccagni, V. Marcelino, P. Paoletti, B. Valtancoli, *J. Am. Chem. Soc.* **1999**, *121*, 6807.

104 H. Zhou, Y. Zhao, G. Gao, S. Li, J. Lan, J. You, *J. Am. Chem. Soc.* **2013**, *135*, 14908.

105 J. Cai, B. P. Hay, N. J. Young, X. Yang, J. L. Sessler, *Chem. Sci.* **2013**, *4*, 1560.

106 A. Mele, P. Metrangolo, H. Neukirch, T. Pilati, G. Resnati, *J. Am. Chem. Soc.* **2005**, *127*, 14972.

107 M. G. Chudzinski, C. A. McClary, M. S. Taylor, *J. Am. Chem. Soc.* **2011**, *133*, 10559.

108 S. H. Jungbauer, D. Bulfield, F. Kniep, C. W. Lehmann, E. Herdtweck, S. M. Huber, *J. Am. Chem. Soc.* **2014**, *136*, 16740.

109 J. E. Hein, J. C. Tripp, L. B. Krasnova, K. B. Sharpless, V. V. Fokin, *Angew. Chem. Int. Ed.* **2009**, *48*, 8018.

110 R. Tepper, B. Schulze, H. Görls, P. Bellstedt, M. Jäger, U. S. Schubert, *Org. Lett.* **2015**, *17*, 5740.

111 D. Mungalpara, S. Stegmüller, S. Kubik, *Chem. Commun.* **2017**, *53*, 5095.

112 L. C. Gilday, N. G. White, P. D. Beer, *Dalton Transactions* **2013**, *42*, 15766.

113 A. M. S. Riel, D. A. Decato, J. Sun, C. J. Massena, M. J. Jessop, O. B. Berryman, *Chem. Sci.* **2018**, *9*, 5828.

114 F. Zapata, A. Caballero, N. G. White, T. D. W. Claridge, P. J. Costa, V. Félix, P. D. Beer, *J. Am. Chem. Soc.* **2012**, *134*, 11533.

115 S. M. Walter, F. Kniep, L. Rout, F. P. Schmidtchen, E. Herdtweck, S. M. Huber, *J. Am. Chem. Soc.* **2012**, *134*, 8507.

116 F. Zapata, A. Caballero, P. Molina, I. Alkorta, J. Elguero, *J. Org. Chem.* **2014**, *79*, 6959.

117 R. Tepper, S. Bode, R. Geitner, M. Jäger, H. Görls, J. Vitz, B. Dietzek, M. Schmitt, J. Popp, M. D. Hager, U. S. Schubert, *Angew. Chem. Int. Ed.* **2017**, *56*, 4047.

118 T. Chivers, R. S. Laitinen, *Chem. Soc. Rev.* **2015**, *44*, 1725.

119 G. E. Garrett, G. L. Gibson, R. N. Straus, D. S. Seferos, M. S. Taylor, *J. Am. Chem. Soc.* **2015**, *137*, 4126.

120 P. Wonner, L. Vogel, M. Düser, L. Gomes, F. Kniep, B. Mallick, D. B. Werz, S. M. Huber, *Angew. Chem. Int. Ed.* **2017**, *56*, 12009.

121 G. E. Garrett, E. I. Carrera, D. S. Seferos, M. S. Taylor, *Chem. Commun.* **2016**, *52*, 9881.

122 A. Borissov, I. Marques, J. Y. C. Lim, V. Félix, M. D. Smith, P. D. Beer, *J. Am. Chem. Soc.* **2019**, *141*, 4119.

123 S. Benz, J. López-Andarias, J. Mareda, N. Sakai, S. Matile, *Angew. Chem. Int. Ed.* **2017**, *56*, 812.

124 S. Benz, A. I. Poblador-Bahamonde, N. Low-Ders, S. Matile, *Angew. Chem. Int. Ed.* **2018**, *57*, 5408.

125 H. Zhao, F. P. Gabbaï, *Nature Chem* **2010**, *2*, 984.

126 B. Zhou, F. P. Gabbaï, *J. Am. Chem. Soc.* **2021**, *143*, 8625.

127 J. Y. C. Lim, I. Marques, A. L. Thompson, K. E. Christensen, V. Félix, P. D. Beer, *Journal of the American Chemical Society* **2017**, *139*, 3122.

128 R. Shukla, T. Kida, B. D. Smith, *Org. Lett.* **2000**, *2*, 3099.

129 A. Arduini, E. Brindani, G. Giorgi, A. Pochini, A. Secchi, *J. Org. Chem.* **2002**, *67*, 6188.

130 V. Böhmer, A. Dalla Cort, L. Mandolini, *J. Org. Chem.* **2001**, *66*, 1900.

131 J. L. Sessler, D. E. Gross, W.-S. Cho, V. M. Lynch, F. P. Schmidtchen, G. W. Bates, M. E. Light, P. A. Gale, *J. Am. Chem. Soc.* **2006**, *128*, 12281.

132 P. A. Gale, *Coordination Chemistry Reviews* **2003**, *240*, 191.

133 M. M. Naseer, K. Jurkschat, *Chem. Commun.* **2017**, *53*, 8122.

134 F. Y. Mihan, S. Bartocci, M. Bruschini, P. De Bernardin, G. Forte, I. Giannicchi, A. D. Cort, *Aust. J. Chem.* **2012**, *65*, 1638.

135 S. K. Kim, J. L. Sessler, *Acc. Chem. Res.* **2014**, *47*, 2525.

136 A. J. McConnell, P. D. Beer, *Angew. Chem. Int. Ed.* **2012**, *51*, 5052.

137 Q. He, G. I. Vargas-Zúñiga, S. H. Kim, S. K. Kim, J. L. Sessler, *Chem. Rev.* **2019**, *119*, 9753.

138 A. McConnell, A. Docker, P. Beer, *ChemPlusChem* **2020**, cplu.202000484.

139 E. N. W. Howe, M. Bhadbhade, P. Thordarson, *J. Am. Chem. Soc.* **2014**, *136*, 7505.

140 L. K. S. von Krbek, C. A. Schalley, P. Thordarson, *Chem. Soc. Rev.* **2017**, *46*, 2622.

141 B. Qiao, A. Sengupta, Y. Liu, K. P. McDonald, M. Pink, J. R. Anderson, K. Raghavachari, A. H. Flood, *J. Am. Chem. Soc.* **2015**, *137*, 9746.

142 S. K. Kim, J. L. Sessler, *Chem. Soc. Rev.* **2010**, *39*, 3784.

143 J. M. Mahoney, A. M. Beatty, B. D. Smith, *J. Am. Chem. Soc.* **2001**, *123*, 5847.

144 S. K. Ray, A. Homberg, M. Vishe, C. Besnard, J. Lacour, *Chem. Eur. J.* **2018**, *24*, 2944.

145 J. L. Sessler, S. K. Kim, D. E. Gross, C.-H. Lee, J. S. Kim, V. M. Lynch, *J. Am. Chem. Soc.* **2008**, *130*, 13162.

146 I.-W. Park, J. Yoo, B. Kim, S. Adhikari, S. K. Kim, Y. Yeon, C. J. E. Haynes, J. L. Sutton, C. C. Tong, V. M. Lynch, J. L. Sessler, P. A. Gale, C.-H. Lee, *Chem. Eur. J.* **2012**, *18*, 2514.

147 X. Ni, X. Zeng, C. Redshaw, T. Yamato, *J. Org. Chem.* **2011**, *76*, 5696.

148 D.-H. Wang, Z. Gong, R. Sun, D.-Z. Zhao, *New J. Chem.* **2015**, *39*, 5991.

149 J. Hu, L. Chen, J. Shen, J. Luo, P. Deng, Y. Ren, H. Zeng, W. Feng, L. Yuan, *Chem. Commun.* **2014**, *50*, 8024.

150 V. Valderrey, E. C. Escudero-Adán, P. Ballester, *Angew. Chem. Int. Ed.* **2013**, *52*, 6898.

151 M. Karbarz, J. Romański, *Inorg. Chem.* **2016**, *55*, 3616.

152 R. Gotor, A. M. Costero, S. Gil, P. Gaviña, K. Rurack, *Eur. J. Org. Chem.* **2014**, *2014*, 4005.

153 D. J. White, N. Laing, H. Miller, S. Parsons, P. A. Tasker, S. Coles, *Chem. Commun.* **1999**, 2077.

154 M. Zakrzewski, N. Kwietniewska, W. Walczak, P. Piątek, *Chem. Commun.* **2018**, *54*, 7018.

155 P. Breccia, M. Van Gool, R. Pérez-Fernández, S. Martín-Santamaría, F. Gago, P. Prados, J. de Mendoza, *J. Am. Chem. Soc.* **2003**, *125*, 8270.

156 J. H. Lee, J. H. Lee, Y. R. Choi, P. Kang, M.-G. Choi, K.-S. Jeong, *J. Org. Chem.* **2014**, *79*, 6403.

157 C. J. Bruns, J. F. Stoddart, *The nature of the mechanical bond: from molecules to machines*, **2017**.

158 J. Rotzler, M. Mayor, *Chem. Soc. Rev.* **2013**, *42*, 44.

159 N. H. Evans, C. J. Serpell, P. D. Beer, *Angew. Chem. Int. Ed.* **2011**, *50*, 2507.

160 W. Liu, C. L. Stern, J. F. Stoddart, *J. Am. Chem. Soc.* **2020**, *142*, 10273.

161 C. D. Pentecost, K. S. Chichak, A. J. Peters, G. W. V. Cave, S. J. Cantrill, J. F. Stoddart, *Angew. Chem. Int. Ed.* **2007**, *46*, 218.

162 K. S. Chichak, *Science* **2004**, *304*, 1308.

163 E. Wasserman, *J. Am. Chem. Soc.* **1960**, *82*, 4433.

164 E. Wasserman, *Scientific American* **1962**, *207*, 94.

165 G. Schill, A. Lüttringhaus, *Angewandte Chemie International Edition in English* **1964**, *3*, 546.

166 G. Schill, C. Zürcher, *Angewandte Chemie International Edition in English* **1969**, *8*, 988.

167 L. Steemers, M. J. Wanner, A. W. Ehlers, H. Hiemstra, J. H. van Maarseveen, *Org. Lett.* **2017**, *19*, 2342.

168 C. O. Dietrich-Buchecker, J. P. Sauvage, J. P. Kintzinger, *Tetrahedron Letters* **1983**, *24*, 5095.

169 B. Taghavi Shahraki, S. Maghsoudi, Y. Fatahi, N. Rabiee, S. Bahadorikhalili, R. Dinarvand, M. Bagherzadeh, F. Verpoort, *Coordination Chemistry Reviews* **2020**, *423*, 213484.

170 D. Sluysmans, J. F. Stoddart, *Trends in Chemistry* **2019**, *1*, 185.

171 J. E. M. Lewis, P. D. Beer, S. J. Loeb, S. M. Goldup, *Chem. Soc. Rev.* **2017**, *46*, 2577.

172 N. H. Evans, P. D. Beer, *Chem. Soc. Rev.* **2014**, *43*, 4658.

173 J. E. Beves, B. A. Blight, C. J. Campbell, D. A. Leigh, R. T. McBurney, *Angew. Chem. Int. Ed.* **2011**, *50*, 9260.

174 F. Aricó, J. D. Badjic, S. J. Cantrill, A. H. Flood, K. C.-F. Leung, Y. Liu, J. F. Stoddart, in *Templates in Chemistry II*, ed. by Christoph A. Schalley, Fritz Vögtle, Karl Heinz Dötz, Springer Berlin Heidelberg, Berlin, Heidelberg, **2005**, Vol. 249, pp. 203–259.

175 J. C. Loren, P. Gantzel, A. Linden, J. S. Siegel, *Org. Biomol. Chem.* **2005**, *3*, 3105.

176 D. A. Leigh, P. J. Lusby, S. J. Teat, A. J. Wilson, J. K. Y. Wong, *Angewandte Chemie International Edition* **2001**, *40*, 1538.

177 A. Inthasot, S.-T. Tung, S.-H. Chiu, *Acc. Chem. Res.* **2018**, *51*, 1324.

178 Y.-H. Lin, C.-C. Lai, Y.-H. Liu, S.-M. Peng, S.-H. Chiu, *Angew. Chem. Int. Ed.* **2013**, *52*, 10231.

179 S.-T. Tung, C.-C. Lai, Y.-H. Liu, S.-M. Peng, S.-H. Chiu, *Angew. Chem. Int. Ed.* **2013**, *52*, 13269.

180 G. M. Hübner, J. Gläser, C. Seel, F. Vögtle, *Angewandte Chemie International Edition* **1999**, *38*, 383.

181 J. A. Wisner, P. D. Beer, M. G. B. Drew, M. R. Sambrook, *J. Am. Chem. Soc.* **2002**, *124*, 12469.

182 M. R. Sambrook, P. D. Beer, J. A. Wisner, R. L. Paul, A. R. Cowley, *J. Am. Chem. Soc.* **2004**, *126*, 15364.

183 T. Bunchuay, A. Docker, A. J. Martinez-Martinez, P. D. Beer, *Angew. Chem. Int. Ed.* **2019**, *58*, 13823.

184 B. Qiao, Y. Liu, S. Lee, M. Pink, A. H. Flood, *Chem. Commun.* **2016**, *52*, 13675.

185 M. J. Barrell, D. A. Leigh, P. J. Lusby, A. M. Z. Slawin, *Angew. Chem. Int. Ed.* **2008**, *47*, 8036.

186 D.-H. Li, B. D. Smith, *J. Org. Chem.* **2019**, *84*, 2808.

187 V. Aucagne, K. D. Hänni, D. A. Leigh, P. J. Lusby, D. B. Walker, *Journal of the American Chemical Society* **2006**, *128*, 2186.

188 S. M. Goldup, D. A. Leigh, T. Long, P. R. McGonigal, M. D. Symes, J. Wu, *J. Am. Chem. Soc.* **2009**, *131*, 15924.

189 S. M. Goldup, D. A. Leigh, R. T. McBurney, P. R. McGonigal, A. Plant, *Chem. Sci.* **2010**, *1*, 383.

190 J. J. Danon, D. A. Leigh, P. R. McGonigal, J. W. Ward, J. Wu, *J. Am. Chem. Soc.* **2016**, *138*, 12643.

191 J. Berná, J. D. Crowley, S. M. Goldup, K. D. Hänni, A.-L. Lee, D. A. Leigh, *Angewandte Chemie* **2007**, *119*, 5811.

192 J. D. Crowley, K. D. Hänni, A.-L. Lee, D. A. Leigh, *Journal of the American Chemical Society* **2007**, *129*, 12092.

193 S. M. Goldup, D. A. Leigh, P. J. Lusby, R. T. McBurney, A. M. Z. Slawin, *Angewandte Chemie* **2008**, *120*, 3429.

194 J. D. Crowley, K. D. Hänni, D. A. Leigh, A. M. Z. Slawin, *J. Am. Chem. Soc.* **2010**, *132*, 5309.

195 M. Asakawa, P. R. Ashton, V. Balzani, A. Credi, C. Hamers, G. Mattersteig, M. Montalti, A. N. Shipway, N. Spencer, J. F. Stoddart, M. S. Tolley, M. Venturi, A. J. P. White, D. J. Williams, *Angewandte Chemie International Edition* **1998**, *37*, 333.

196 A. M. Brouwer, *Science* **2001**, *291*, 2124.

197 D. A. Leigh, V. Marcos, M. R. Wilson, *ACS Catal.* **2014**, *4*, 4490.

198 V. Blanco, D. A. Leigh, U. Lewandowska, B. Lewandowski, V. Marcos, *J. Am. Chem. Soc.* **2014**, *136*, 15775.

199 M. J. Chmielewski, J. J. Davis, P. D. Beer, *Org. Biomol. Chem.* **2009**, *7*, 415.

200 M. J. Langton, P. D. Beer, *Acc. Chem. Res.* **2014**, *47*, 1935.

201 K. M. Bąk, K. Porfyrakis, J. J. Davis, P. D. Beer, *Mater. Chem. Front.* **2020**, *4*, 1052.

202 H. M. Tay, P. Beer, *Org. Biomol. Chem.* **2021**, *19*, 4652.

203 M. Cirulli, A. Kaur, J. E. M. Lewis, Z. Zhang, J. A. Kitchen, S. M. Goldup, M. M. Roessler, *J. Am. Chem. Soc.* **2019**, *141*, 879.

204 M. Nandi, S. Bej, T. K. Ghosh, P. Ghosh, *Chem. Commun.* **2019**, *55*, 3085.

205 J. Y. C. Lim, P. D. Beer, *Chem* **2018**, *4*, 731.

206 N. A. Semenov, A. V. Lonchakov, N. A. Pushkarevsky, E. A. Suturina, V. V. Korolev, E. Lork, V. G. Vasiliev, S. N. Konchenko, J. Beckmann, N. P. Gritsan, A. V. Zibarev, *Organometallics* **2014**, *33*, 4302.

207 J. Y. C. Lim, J. Y. Liew, P. D. Beer, *Chem. Eur. J.* **2018**, *24*, 14560.

208 E. Navarro-García, B. Galmés, M. D. Velasco, A. Frontera, A. Caballero, *Chem. Eur. J.* **2020**, *26*, 4706.

209 R. Parra, *Molecules* **2014**, *19*, 1069.

210 X. Yang, P.-P. Zhou, D.-G. Zhou, P.-J. Zheng, Y. Dai, C.-X. Yan, Z. Yang, *Computational and Theoretical Chemistry* **2016**, *1076*, 32.

211 A. M. S. Riel, R. K. Rowe, E. N. Ho, A.-C. C. Carlsson, A. K. Rappé, O. B. Berryman, P. S. Ho, *Acc. Chem. Res.* **2019**, *52*, 2870.

212 S. Yu, P. Kumar, J. S. Ward, A. Frontera, K. Rissanen, *Chem* **2021**, *7*, 948.

213 N. Al-Salim, T. A. Hamor, W. R. McWhinnie, *J. Chem. Soc., Chem. Commun.* **1986**, 453.

214 S. Panda, H. B. Singh, R. J. Butcher, *Chem. Commun.* **2004**, 322.

215 J. E. M. Lewis, M. Galli, S. M. Goldup, *Chem. Commun.* **2017**, *53*, 298.

216 J. D. Crowley, S. M. Goldup, A.-L. Lee, D. A. Leigh, R. T. McBurney, *Chemical Society Reviews* **2009**, *38*, 1530.

217 K. D. Hänni, D. A. Leigh, *Chem. Soc. Rev.* **2010**, *39*, 1240.

218 M. Denis, S. M. Goldup, *Nat Rev Chem* **2017**, *1*, 0061.

219 S. Saito, E. Takahashi, K. Nakazono, *Organic Letters* **2006**, *8*, 5133.

220 J. D. Crowley, S. M. Goldup, N. D. Gowans, D. A. Leigh, V. E. Ronaldson, A. M. Z. Slawin, *J. Am. Chem. Soc.* **2010**, *132*, 6243.

221 V. Aucagne, J. Berná, J. D. Crowley, S. M. Goldup, K. D. Hänni, D. A. Leigh, P. J. Lusby, V. E. Ronaldson, A. M. Z. Slawin, A. Viterisi, D. B. Walker, *Journal of the American Chemical Society* **2007**, *129*, 11950.

222 H. Lahlali, K. Jobe, M. Watkinson, S. M. Goldup, *Angew. Chem. Int. Ed.* **2011**, *50*, 4151.

223 M. J. Langton, Y. Xiong, P. D. Beer, *Chemistry - A European Journal* **2015**, *21*, 18910.

224 X. Li, J. Y. C. Lim, P. D. Beer, *Faraday Discuss.* **2017**, *203*, 245.

225 J. Y. C. Lim, T. Bunchuay, P. D. Beer, *Chem. Eur. J.* **2017**, *23*, 4700.

226 J. Y. C. Lim, I. Marques, V. Félix, P. D. Beer, *J. Am. Chem. Soc.* **2017**, *139*, 12228.

227 J. Y. C. Lim, P. D. Beer, *Eur. J. Org. Chem.* **2019**, *2019*, 3433.

228 X. Li, J. Y. C. Lim, P. D. Beer, *Chem. Eur. J.* **2018**, *24*, 17788.

229 D. A. Shultz, H. Lee, R. K. Kumar, K. P. Gwaltney, *J. Org. Chem.* **1999**, *64*, 9124.

230 T. Nishikawa, S. Shibuya, S. Hosokawa, M. Isobe, *Synlett* **1994**, *1994*, 485.

231 Y. C. Tse, A. Docker, Z. Zhang, P. D. Beer, *Chem. Commun.* **2021**, *57*, 4950.

232 Y. Tobe, J. Kishi, I. Ohki, M. Sonoda, *J. Org. Chem.* **2003**, *68*, 3330.

233 N. L. Kilah, M. D. Wise, C. J. Serpell, A. L. Thompson, N. G. White, K. E. Christensen, P. D. Beer, *Journal of the American Chemical Society* **2010**, *132*, 11893.

234 A. Docker, C. Guthrie, H. Kuhn, P. D. Beer, *Angewandte Chemie International Edition n/a*.

235 P. Thordarson, *Chem. Soc. Rev.* **2011**, *40*, 1305.

236 Supramolecular.org - Binding Constant Calculators | Supramolecular, http://supramolecular.org/.

237 M. J. Langton, P. D. Beer, *Accounts of Chemical Research* **2014**, *47*, 1935.

238 R. C. Knighton, P. D. Beer, *Chem. Commun.* **2014**, *50*, 1540.

239 R. Tepper, B. Schulze, P. Bellstedt, J. Heidler, H. Görls, M. Jäger, U. S. Schubert, *Chem. Commun.* **2017**, *53*, 2260.

240 R. A. Bissell, E. Córdova, A. E. Kaifer, J. F. Stoddart, *Nature* **1994**, *369*, 133.

241 D. B. Amabilino, C. O. Dietrich-Buchecker, A. Livoreil, L. Pérez-García, J.-P. Sauvage, J. F. Stoddart, *J. Am. Chem. Soc.* **1996**, *118*, 3905.

242 C. A. Stanier, S. J. Alderman, T. D. W. Claridge, H. L. Anderson, *Angewandte Chemie International Edition* **2002**, *41*, 1769.

243 J. M. Spruell, W. F. Paxton, J.-C. Olsen, D. Benítez, E. Tkatchouk, C. L. Stern, A. Trabolsi, D. C. Friedman, W. A. Goddard, J. F. Stoddart, *J. Am. Chem. Soc.* **2009**, *131*, 11571.

244 D. A. Leigh, P. J. Lusby, A. M. Z. Slawin, D. B. Walker, *Chem. Commun.* **2012**, *48*, 5826.

245 J. E. M. Lewis, R. J. Bordoli, M. Denis, C. J. Fletcher, M. Galli, E. A. Neal, E. M. Rochette, S. M. Goldup, *Chem. Sci.* **2016**, *7*, 3154.

246 P. Thordarson, E. J. A. Bijsterveld, A. E. Rowan, R. J. M. Nolte, *Nature* **2003**, *424*, 915.

247 Y. Tachibana, N. Kihara, T. Takata, *J. Am. Chem. Soc.* **2004**, *126*, 3438.

248 N. Miyagawa, M. Watanabe, T. Matsuyama, Y. Koyama, T. Moriuchi, T. Hirao, Y. Furusho, T. Takata, *Chem. Commun.* **2010**, *46*, 1920.

249 J. Berná, M. Alajarín, R.-A. Orenes, *J. Am. Chem. Soc.* **2010**, *132*, 10741.

250 V. Blanco, A. Carlone, K. D. Hänni, D. A. Leigh, B. Lewandowski, *Angew. Chem. Int. Ed.* **2012**, *51*, 5166.

251 V. Blanco, D. A. Leigh, V. Marcos, J. A. Morales-Serna, A. L. Nussbaumer, *J. Am. Chem. Soc.* **2014**, *136*, 4905.

252 M. Galli, J. E. M. Lewis, S. M. Goldup, *Angew. Chem. Int. Ed.* **2015**, *54*, 13545.

253 K. Eichstaedt, J. Jaramillo-Garcia, D. A. Leigh, V. Marcos, S. Pisano, T. A. Singleton, *J. Am. Chem. Soc.* **2017**, *139*, 9376.

254 Y.-J. Lee, K.-S. Liu, C.-C. Lai, Y.-H. Liu, S.-M. Peng, R. P. Cheng, S.-H. Chiu, *Chem. Eur. J.* **2017**, *23*, 9756.

255 A. G. Cheetham, M. G. Hutchings, T. D. W. Claridge, H. L. Anderson, *Angew. Chem. Int. Ed.* **2006**, *45*, 1596.

256 A. Fernandes, A. Viterisi, F. Coutrot, S. Potok, D. A. Leigh, V. Aucagne, S. Papot, *Angew. Chem. Int. Ed.* **2009**, *48*, 6443.

257 T. Kench, P. A. Summers, M. K. Kuimova, J. E. M. Lewis, R. Vilar, *Angew. Chem.* **2021**, *133*, 11023.

258 G. T. Spence, P. D. Beer, *Accounts of Chemical Research* **2013**, *46*, 571.

259 M. J. Langton, P. D. Beer, *Chem. Eur. J.* **2012**, *18*, 14406.

260 A. Caballero, F. Zapata, N. G. White, P. J. Costa, V. Félix, P. D. Beer, *Angew. Chem.* **2012**, *124*, 1912.

261 L. M. Hancock, E. Marchi, P. Ceroni, P. D. Beer, *Chem. Eur. J.* **2012**, *18*, 11277.

262 M. J. Langton, O. A. Blackburn, T. Lang, S. Faulkner, P. D. Beer, *Angew. Chem. Int. Ed.* **2014**, *53*, 11463.

263 B. R. Mullaney, A. L. Thompson, P. D. Beer, *Angewandte Chemie International Edition* **2014**, *53*, 11458.

264 J. M. Mercurio, A. Caballero, J. Cookson, P. D. Beer, *RSC Adv.* **2015**, *5*, 9298.

265 M. J. Langton, I. Marques, S. W. Robinson, V. Félix, P. D. Beer, *Chem. Eur. J.* **2016**, *22*, 185.

266 A. Brown, T. Lang, K. M. Mullen, P. D. Beer, *Org. Biomol. Chem.* **2017**, *15*, 4587.

267 J. Y. C. Lim, I. Marques, V. Félix, P. D. Beer, *Angew. Chem. Int. Ed.* **2018**, *57*, 584.

268 M. Denis, L. Qin, P. Turner, K. A. Jolliffe, S. M. Goldup, *Angew. Chem. Int. Ed.* **2018**, *57*, 5315.

269 J. M. Van Raden, B. M. White, L. N. Zakharov, R. Jasti, *Angew. Chem. Int. Ed.* **2019**, *58*, 7341.

270 A. Brown, M. J. Langton, N. L. Kilah, A. L. Thompson, P. D. Beer, *Chemistry - A European Journal* **2015**, *21*, 17664.

271 T. A. Barendt, S. W. Robinson, P. D. Beer, *Chemical Science* **2016**, *7*, 5171.

272 T. A. Barendt, A. Docker, I. Marques, V. Félix, P. D. Beer, *Angew. Chem. Int. Ed.* **2016**, *55*, 11069.

273 T. A. Barendt, L. Ferreira, I. Marques, V. Félix, P. D. Beer, *J. Am. Chem. Soc.* **2017**, *139*, 9026.

274 T. A. Barendt, I. Rašović, M. A. Lebedeva, G. A. Farrow, A. Auty, D. Chekulaev, I. V. Sazanovich, J. A. Weinstein, K. Porfyrakis, P. D. Beer, *J. Am. Chem. Soc.* **2018**, *140*, 1924.

275 N. H. Evans, C. J. Serpell, P. D. Beer, *Chem. Commun.* **2011**, *47*, 8775.

276 N. H. Evans, C. J. Serpell, N. G. White, P. D. Beer, *Chemistry - A European Journal* **2011**, *17*, 12347.

277 N. H. Evans, H. Rahman, A. V. Leontiev, N. D. Greenham, G. A. Orlowski, Q. Zeng, R. M. J. Jacobs, C. J. Serpell, N. L. Kilah, J. J. Davis, P. D. Beer, *Chem. Sci.* **2012**, *3*, 1080.

278 A. Brown, P. D. Beer, *Dalton Trans.* **2012**, *41*, 118.

279 J. Y. C. Lim, M. J. Cunningham, J. J. Davis, P. D. Beer, *Dalton Trans.* **2014**, *43*, 17274.

280 R. Hein, P. D. Beer, J. J. Davis, *Chem. Rev.* **2020**, *120*, 1888.

281 *The porphyrin handbook*, ed. by Karl M. Kadish, Kevin M. Smith, Roger Guilard, Academic Press, San Diego, **2000**.

282 M. Biesaga, *Talanta* **2000**, *51*, 209.

283 L. B. Josefsen, R. W. Boyle, *Metal-Based Drugs* **2008**, *2008*, 1.

284 P. Rothemund, A. R. Menotti, *J. Am. Chem. Soc.* **1941**, *63*, 267.

285 A. D. Adler, F. R. Longo, J. D. Finarelli, J. Goldmacher, J. Assour, L. Korsakoff, *J. Org. Chem.* **1967**, *32*, 476.

286 J. S. Lindsey, H. C. Hsu, I. C. Schreiman, *Tetrahedron Letters* **1986**, *27*, 4969.

287 P. D. Beer, M. G. B. Drew, R. Jagessar, *J. Chem. Soc., Dalton Trans.* **1997**, 881.

288 C. Lee, D. H. Lee, J.-I. Hong, *Tetrahedron Letters* **2001**, *42*, 8665.

289 C. Bucher, C. H. Devillers, J.-C. Moutet, G. Royal, E. Saint-Aman, *New J. Chem.* **2004**, *28*, 1584.

290 D. P. Cormode, S. S. Murray, A. R. Cowley, P. D. Beer, *Dalton Transactions* **2006**, 5135.

291 D. P. Cormode, M. G. B. Drew, R. Jagessar, P. D. Beer, *Dalton Transactions* **2008**, 6732.

292 C.-H. Lee, S. Lee, H. Yoon, W.-D. Jang, *Chemistry - A European Journal* **2011**, *17*, 13898.

293 H. Yoon, C.-H. Lee, Y.-H. Jeong, H.-C. Gee, W.-D. Jang, *Chem. Commun.* **2012**, *48*, 5109.

294 J. M. M. Rodrigues, A. S. F. Farinha, P. V. Muteto, S. M. Woranovicz-Barreira, F. A. Almeida Paz, M. G. P. M. S. Neves, J. A. S. Cavaleiro, A. C. Tomé, M. T. S. R. Gomes, J. L. Sessler, J. P. C. Tomé, *Chem. Commun.* **2014**, *50*, 1359.

295 K.-I. Hong, H. Yoon, W.-D. Jang, *Chem. Commun.* **2015**, *51*, 7486.

296 W. Lin, T.-Y. Cen, S.-P. Wang, Z. Zhang, J. Wu, J. Huang, S. Li, *Chinese Chemical Letters* **2018**, *29*, 1372.

297 C.-H. Lee, H. Yoon, P. Kim, S. Cho, D. Kim, W.-D. Jang, *Chem. Commun.* **2011**, *47*, 4246.

298 L. C. Gilday, N. G. White, P. D. Beer, *Dalton Trans.* **2012**, *41*, 7092.

299 J. Zhang, Y. Li, W. Yang, S.-W. Lai, C. Zhou, H. Liu, C.-M. Che, Y. Li, *Chemical Communications* **2012**, *48*, 3602.

300 M. J. Gunter, S. M. Farquhar, K. M. Mullen, *New J. Chem.* **2004**, 10.1039.b411583j.

301 S. W. Hewson, K. M. Mullen, *Eur. J. Org. Chem.* **2019**, *2019*, 3358.

302 T. Kowada, H. Maeda, K. Kikuchi, *Chem. Soc. Rev.* **2015**, *44*, 4953.

303 M. Poddar, R. Misra, *Coordination Chemistry Reviews* **2020**, *421*, 213462.

304 Y. Qin, X. Liu, P.-P. Jia, L. Xu, H.-B. Yang, *Chem. Soc. Rev.* **2020**, *49*, 5678.

305 A. Loudet, K. Burgess, *Chem. Rev.* **2007**, *107*, 4891.

306 N. Boens, V. Leen, W. Dehaen, *Chem. Soc. Rev.* **2012**, *41*, 1130.

307 T. E. Wood, A. Thompson, *Chem. Rev.* **2007**, *107*, 1831.

308 L. Wang, H. Ding, X. Ran, H. Tang, D. Cao, *Dyes and Pigments* **2020**, *172*, 107857.

309 M. Rajeswara Rao, M. Ravikanth, *J. Org. Chem.* **2011**, *76*, 3582.

310 Q. Li, Y. Guo, S. Shao, *Analyst* **2012**, *137*, 4497.

311 Y. Yu, N. Bogliotti, J. Tang, J. Xie, *Eur. J. Org. Chem.* **2013**, *2013*, 7749.

312 S. Dixit, N. Agarwal, *Journal of Photochemistry and Photobiology A: Chemistry* **2017**, *343*, 66.

313 Y. Li, J. Chen, T.-S. Chu, *J. Comput. Chem.* **2018**, *39*, 1639.

314 P. Ashokkumar, H. Weißhoff, W. Kraus, K. Rurack, *Angew. Chem. Int. Ed.* **2014**, *53*, 2225.

315 J. Yao, H. Li, Y.-N. Xu, Q.-C. Wang, D.-H. Qu, *Chem. Asian J.* **2014**, *9*, 3482.

316 N. Sun, X. Xiao, W. Li, J. Jiang, *Adv. Sci.* **2015**, *2*, 1500082.

317 J. Yao, X. Fu, X.-L. Zheng, Z.-Q. Cao, D.-H. Qu, *Dyes and Pigments* **2015**, *121*, 13.

318 B. Nisanci, S. Sahinoglu, E. Tuner, M. Arik, İ. Kani, A. Dastan, Ö. A. Bozdemir, *Chem. Commun.* **2017**, *53*, 12418.

319 N. Yesilgul, O. Seven, R. Guliyev, E. U. Akkaya, *J. Org. Chem.* **2018**, *83*, 13228.

320 S.-M. Chan, F.-K. Tang, C.-S. Kwan, C.-Y. Lam, S. C. K. Hau, K. C.-F. Leung, *Mater. Chem. Front.* **2019**, *3*, 2388.

321 Y. Wu, M. Frasconi, W.-G. Liu, R. M. Young, W. A. Goddard, M. R. Wasielewski, J. F. Stoddart, *J. Am. Chem. Soc.* **2020**, *142*, 11835.

322 M. Rémy, I. Nierengarten, B. Park, M. Holler, U. Hahn, J. Nierengarten, *Chem. Eur. J.* **2021**, *27*, 8492.

323 R. Arumugaperumal, V. Srinivasadesikan, M. V. Ramakrishnam Raju, M.-C. Lin, T. Shukla, R. Singh, H.-C. Lin, *ACS Appl. Mater. Interfaces* **2015**, *7*, 26491.

324 D. Aldakov, P. Anzenbacher, *J. Am. Chem. Soc.* **2004**, *126*, 4752.

325 P. Anzenbacher, M. A. Palacios, K. Jursíková, M. Marquez, *Org. Lett.* **2005**, *7*, 5027.

326 Q.-Y. Cao, Y.-M. Han, P.-S. Yao, W.-F. Fu, Y. Xie, J.-H. Liu, *Tetrahedron Letters* **2014**, *55*, 248.

327 M. Alfonso, A. Espinosa Ferao, A. Tárraga, P. Molina, *Inorg. Chem.* **2015**, *54*, 7461.

328 F. Bettazzi, D. Voccia, A. Bencini, C. Giorgi, I. Palchetti, B. Valtancoli, L. Conti, *Eur. J. Inorg. Chem.* **2018**, *2018*, 2675.

329 R. Kaur, G. Dhaka, P. Singh, S. Rana, N. Kaur, *Arabian Journal of Chemistry* **2020**, *13*, 6931.

330 C. Bejger, J. S. Park, E. S. Silver, J. L. Sessler, *Chem. Commun.* **2010**, *46*, 7745.

331 P. D. Beer, F. Szemes, V. Balzani, C. M. Salà, M. G. B. Drew, S. W. Dent, M. Maestri, *J. Am. Chem. Soc.* **1997**, *119*, 11864.

332 A. Borissov, J. Y. C. Lim, A. Brown, K. E. Christensen, A. L. Thompson, M. D. Smith, P. D. Beer, *Chem. Commun.* **2017**, *53*, 2483.

333 S. Purushothaman, R. Prasanna, R. Raghunathan, *Tetrahedron* **2013**, *69*, 9742.

334 S. B. Mane, C.-H. Hung, *Chem. Eur. J.* **2015**, *21*, 4825.

335 M. Nappa, J. S. Valentine, *Journal of the American Chemical Society* **1978**, *100*, 5075.

336 M. Kimura, Y. Nakano, N. Adachi, Y. Tatewaki, H. Shirai, N. Kobayashi, *Chem. Eur. J.* **2009**, *15*, 2617.

337 A. Eggenspiller, A. Takai, M. E. El-Khouly, K. Ohkubo, C. P. Gros, C. Bernhard, C. Goze, F. Denat, J.-M. Barbe, S. Fukuzumi, *J. Phys. Chem. A* **2012**, *116*, 3889.

338 D. A. Roberts, T. W. Schmidt, M. J. Crossley, S. Perrier, *Chemistry - A European Journal* **2013**, *19*, 12759.

339 H. S. Prakash Rao, M. Kamalraj, M. Prabakaran, *RSC Adv.* **2019**, *9*, 4499.

340 Y. Miyazaki, C. Kahlfuss, A. Ogawa, T. Matsumoto, J. A. Wytko, K. Oohora, T. Hayashi, J. Weiss, *Chemistry - A European Journal* **2017**, *23*, 13579.

341 Z. Li, R. Bittman, *J. Org. Chem.* **2007**, *72*, 8376.

342 J. F. W. Keana, S. X. Cai, *J. Org. Chem.* **1990**, *55*, 3640.

343 M. J. Langton, C. J. Serpell, P. D. Beer, *Angewandte Chemie International Edition* **2016**, *55*, 1974.

344 S. Kubik, *Chem. Soc. Rev.* **2010**, *39*, 3648.

345 S. Kubik, R. Kirchner, D. Nolting, J. Seidel, *J. Am. Chem. Soc.* **2002**, *124*, 12752.

346 Y. Hua, Y. Liu, C.-H. Chen, A. H. Flood, *J. Am. Chem. Soc.* **2013**, *135*, 14401.

347 A. Schaly, R. Belda, E. García-España, S. Kubik, *Org. Lett.* **2013**, *15*, 6238.

348 F. Sommer, S. Kubik, *Org. Biomol. Chem.* **2014**, *12*, 8851.

349 M. Lisbjerg, B. M. Jessen, B. Rasmussen, B. E. Nielsen, A. Ø. Madsen, M. Pittelkow, *Chem. Sci.* **2014**, *5*, 2647.

350 M. J. Langton, S. W. Robinson, I. Marques, V. Félix, P. D. Beer, *Nature Chem* **2014**, *6*, 1039.

351 A. J. McConnell, A. Docker, P. D. Beer, *ChemPlusChem* **2020**, *85*, 1824.

352 A. Brown, K. M. Mennie, O. Mason, N. G. White, P. D. Beer, *Dalton Trans.* **2017**, *46*, 13376.

353 P. Sabater, F. Zapata, B. López, I. Fernández, A. Caballero, P. Molina, *Dalton Trans.* **2018**, *47*, 15941.

354 T. Bunchuay, A. Docker, U. Eiamprasert, P. Surawatanawong, A. Brown, P. D. Beer, *Angew. Chem. Int. Ed.* **2020**, anie.202001125.

355 A. Docker, T. Bunchuay, M. Ahrens, A. J. Martinez-Martinez, P. D. Beer, *Chem. Eur. J.* **2021**, chem.202100579.

356 T. Tozawa, Y. Misawa, S. Tokita, Y. Kubo, *Tetrahedron Letters* **2000**, *41*, 5219.

357 S. Roelens, A. Vacca, O. Francesconi, C. Venturi, *Chem. Eur. J.* **2009**, *15*, 8296.

358 J. D. Megiatto, D. I. Schuster, *J. Am. Chem. Soc.* **2008**, *130*, 12872.

359 C. J. Chandler, L. W. Deady, J. A. Reiss, *Journal of Heterocyclic Chemistry* **1981**, *18*, 599.

360 T. Wang, J. S. Bradshaw, P. Huszthy, X. Kou, N. K. Dalley, R. M. Izatt, *Journal of Heterocyclic Chemistry* **1994**, *31*, 1.

361 R. Ding, Y. He, X. Wang, J. Xu, Y. Chen, M. Feng, C. Qi, *Molecules* **2011**, *16*, 5665.

362 M. J. Chmielewski, J. J. Davis, P. D. Beer, *Org. Biomol. Chem.* **2009**, *7*, 415.

363 M. J. Deetz, R. Shukla, B. D. Smith, *Tetrahedron* **2002**, *58*, 799.

364 J. R. Romero, G. Aragay, P. Ballester, *Chem. Sci.* **2017**, *8*, 491.

365 R. C. Knighton, P. D. Beer, *Org. Chem. Front.* **2021**, *8*, 2468.

366 Y.-H. Lin, C.-C. Lai, S.-H. Chiu, *Org. Biomol. Chem.* **2014**, *12*, 2907.

367 Y.-J. Lee, T.-H. Ho, C.-C. Lai, S.-H. Chiu, *Org. Biomol. Chem.* **2016**, *14*, 1153.

368 G. Kaiser, T. Jarrosson, S. Otto, Y.-F. Ng, A. D. Bond, J. K. M. Sanders, *Angew. Chem. Int. Ed.* **2004**, *43*, 1959.

369 S. A. Vignon, T. Jarrosson, T. Iijima, H.-R. Tseng, J. K. M. Sanders, J. F. Stoddart, *J. Am. Chem. Soc.* **2004**, *126*, 9884.

370 A. M. Albrecht-Gary, Z. Saad, C. O. Dietrich-Buchecker, J. P. Sauvage, *J. Am. Chem. Soc.* **1985**, *107*, 3205.

371 P. Thordarson, R. G. E. Coumans, J. A. A. W. Elemans, P. J. Thomassen, J. Visser, A. E. Rowan, R. J. M. Nolte, *Angewandte Chemie International Edition* **2004**, *43*, 4755.

372 J. E. A. Webb, M. J. Crossley, P. Turner, P. Thordarson, *J. Am. Chem. Soc.* **2007**, *129*, 7155.

373 J. E. Hein, L. B. Krasnova, M. Iwasaki, V. V. Fokin, in *Organic Syntheses*, ed. by John Wiley & Sons, Inc., John Wiley & Sons, Inc., Hoboken, NJ, USA, **2011**, pp. 238–246.

Appendices

Appendices

Single Crystal X-ray Diffraction Studies

Single crystal X-ray diffraction experiments in this thesis were conducted by fellow graduate students Zongyao Zhang and Hui Min Tay.

Single crystals of **3.1a·Zn**, **3.1b·Zn**, **4.1·I**, **4.1·H** and **4.10a** suitable for X-ray analysis were each coated with Paratone-N oil, suspended in a small fibre loop, and placed in a cold gaseous nitrogen stream on a Oxford Diffraction Supernova X-ray diffractometer performing ϕ- and ω-scans at 150(2) K. Diffraction intensities were measured using graphite monochromated Cu Kα radiation (λ = 0.71073 and 1.54056 Å). Data collection, indexing, initial cell refinements, frame integration, final cell refinements and absorption corrections were accomplished using the program Crysalispro. Scattering factors and anomalous dispersion corrections were taken from the *International Tables for X-ray Crystallography*. All structures were solved by direct methods using SHELXS and refined against F^2 on all data by full-matrix least squares with SHELXL following established refinement strategies.[1] All non-hydrogen atoms were refined anisotropically. All hydrogen atoms binding to carbon were included into the model at geometrically calculated positions and refined using a riding model. The isotropic displacement parameters of all hydrogen atoms were fixed to 1.2 times the U value of the atoms they are linked to (1.5 times for methyl groups). Details of the data quality and a summary of the residual values for the refinements are listed in Table A1–5.

Deposition Numbers 2095235 (for **3.1a·Zn**), 2095236 (for **3.1b·Zn**), 2069372 (for **4.1·I**) and 2068373 (for **4.1·H**) contain the supplementary crystallographic data

for this thesis. These data are provided free of charge by the joint Cambridge Crystallographic Data Centre and Fachinformationszentrum Karlsruhe.

Table A1: Crystal data and structure refinement for **3.1a·Zn**.

Identification code	**3.1a·Zn**
Empirical formula	C52 H42 Cl4 I2 N10 O2 Zn
Formula weight	1299.92
Temperature	150(2) K
Wavelength	1.54184 Å
Crystal system	Monoclinic
Space group	$P2_1/c$
Unit cell dimensions	a = 23.4412(2) Å α = 90°. b = 11.38600(10) Å β = 93.3872(10)°. c = 18.6576(2) Å γ = 90°.
Volume	4971.04(8) $Å^3$
Z	4
Density (calculated)	1.737 Mg/m^3
Absorption coefficient	12.850 mm^{-1}
F(000)	2576
Crystal size	0.25 x 0.25 x 0.25 mm^3
Theta range for data collection	3.778 to 76.424°.
Index ranges	-29<=h<=28, -12<=k<=13, -23<=l<=22
Reflections collected	56701
Independent reflections	10299 [R(int) = 0.0716]
Completeness to theta = 67.684°	100.0 %
Absorption correction	Sphere
Max. and min. transmission	0.08027 and 0.00973
Refinement method	Full-matrix least-squares on F^2
Data / restraints / parameters	10299 / 0 / 640
Goodness-of-fit on F^2	1.066
Final R indices [I>2sigma(I)]	R1 = 0.0699, wR2 = 0.1677
R indices (all data)	R1 = 0.0715, wR2 = 0.1716
Extinction coefficient	n/a
Largest diff. peak and hole	3.033 and -0.870 $e.Å^{-3}$

Table A2: Crystal data and structure refinement for **3.1b·Zn**.

Identification code	**3.1b·Zn**
Empirical formula	C57 H51 Cl3 I2 N10 O3 Zn
Formula weight	1349.59
Temperature	150(2) K
Wavelength	1.54184 Å
Crystal system	Orthorhombic
Space group	$Cmc2_1$
Unit cell dimensions	a = 23.6933(3) Å α = 90°. b = 12.4738(2) Å β = 90°. a = 18.4605(3) Å γ = 90°.
Volume	5455.92(14) $Å^3$
Z	4
Density (calculated)	1.643 Mg/m^3
Absorption coefficient	11.306 mm^{-1}
F(000)	2696
Crystal size	0.400 x 0.400 x 0.400 mm^3
Theta range for data collection	3.731 to 76.151°.
Index ranges	-27<=h<=29, -15<=k<=15, -23<=l<=23
Reflections collected	29380
Independent reflections	5495 [R(int) = 0.0502]
Completeness to theta = 67.684°	100.0 %
Absorption correction	Sphere
Max. and min. transmission	0.08756 and 0.01250
Refinement method	Full-matrix least-squares on F^2
Data / restraints / parameters	5495 / 1 / 355
Goodness-of-fit on F^2	1.088
Final R indices [I>2sigma(I)]	R1 = 0.0674, wR2 = 0.1530
R indices (all data)	R1 = 0.0680, wR2 = 0.1541
Absolute structure parameter	0.001(3)
Extinction coefficient	n/a
Largest diff. peak and hole	3.317 and -0.415 $e.Å^{-3}$

Table A3: Crystal data and structure refinement for **4.1·I**.

Identification code	**4.1·I**
Empirical formula	C45 H42 I2 N8 O6.20
Formula weight	1047.86
Temperature	150(2) K
Wavelength	1.54178 Å
Crystal system	Monoclinic
Space group	C2/c
Unit cell dimensions	a = 25.3739(2) Å α = 90°. b = 27.4143(2) Å β = 90°. a = 14.36510(10) Å γ = 90°.
Volume	9642.95(13) $Å^3$
Z	8
Density (calculated)	1.444 Mg/m^3
Absorption coefficient	10.681 mm^{-1}
F(000)	4189
Crystal size	0.300 x 0.300 x 0.200 mm^3
Theta range for data collection	3.606 to 76.207°.
Index ranges	-31<=h<=25, -34<=k<=34, -18<=l<=17
Reflections collected	59983
Independent reflections	10028 [R(int) = 0.0334]
Completeness to theta = 67.679°	100.0 %
Absorption correction	Semi-empirical from equivalents
Max. and min. transmission	0.08176 and 0.01028
Refinement method	Full-matrix least-squares on F^2
Data / restraints / parameters	10028 / 6 / 561
Goodness-of-fit on F^2	1.099
Final R indices [I>2sigma(I)]	R1 = 0.0810, wR2 = 0.2274
R indices (all data)	R1 = 0.0830, wR2 = 0.2347
Extinction coefficient	n/a
Largest diff. peak and hole	3.051 and -0.462 $e.Å^{-3}$

Table A4: Crystal data and structure refinement for **4.1·H**.

Identification code	**4.1·H**
Empirical formula	C45.67 H41.67 Cl5 N8 O4
Formula weight	943.78
Temperature	150(2) K
Wavelength	0.71073 Å
Crystal system	Triclinic
Space group	P-1
Unit cell dimensions	a = 15.8391(5) Å α = 90°. b = 15.8758(4) Å β = 90°. a = 33.8664(12) Å γ = 90°.
Volume	7952.3(5) $Å^3$
Z	6
Density (calculated)	1.182 Mg/m^3
Absorption coefficient	0.319 mm^{-1}
F(000)	2932
Crystal size	0.4 x 0.3 x 0.25 mm^3
Theta range for data collection	2.876 to 30.411°.
Index ranges	-21<=h<=21, -22<=k<=18, -44<=l<=48
Reflections collected	101936
Independent reflections	41553 [R(int) = 0.1030]
Completeness to theta = 25.242°	99.8 %
Absorption correction	Semi-empirical from equivalents
Max. and min. transmission	1.00000 and 0.67982
Refinement method	Full-matrix least-squares on F^2
Data / restraints / parameters	41553 / 30 / 1722
Goodness-of-fit on F^2	1.106
Final R indices [I>2sigma(I)]	R1 = 0.1411, wR2 = 0.3578
R indices (all data)	R1 = 0.2966, wR2 = 0.4529
Extinction coefficient	n/a
Largest diff. peak and hole	2.008 and -1.184 $e.Å^{-3}$

Table A5: Crystal data and structure refinement for **4.10a**.	
Identification code	**4.10a**
Empirical formula	C83 H84 Cl I4 N13 O6
Formula weight	1902.68
Temperature	150.01(10) K
Wavelength	1.54184 Å
Crystal system	Tetragonal
Space group	P4/n
Unit cell dimensions	a = 36.7665(5) Å α = 90°. b = 36.7665(5) Å β = 90°. c = 13.8705(4) Å γ = 90°.
Volume	18749.8(7) $Å^3$
Z	8
Density (calculated)	1.348 Mg/m^3
Absorption coefficient	11.120 mm^{-1}
F(000)	7600
Crystal size	0.273 x 0.235 x 0.035 mm^3
2Θ range for data collection	7.224 to 153.956°.
Index ranges	-45<=h<=46, -46<=k<=40, -16<=l<=17
Reflections collected	154321
Independent reflections	19574 [R(int) = 0.1414, R(sigma) = 0.0630]
Refinement method	Full-matrix least-squares on F^2
Data / restraints / parameters	19574 / 68 / 1024
Goodness-of-fit on F^2	1.036
Final R indices [I>2sigma(I)]	R1 = 0.0712, wR2 = 0.1955
R indices (all data)	R1 = 0.0999, wR2 = 0.2214
Largest diff. peak and hole	1.66 and -0.72 $e.Å^{-3}$

References

1 G. M. Sheldrick, *Acta. Cryst.* **2008**, *A64*, 112.